Universidad Autónoma de Madrid | Escuela de Doctorado

Precision event shapes with massive quarks

Alejandro Bris Cuerpo

Supervised by Dr. Vicent Mateu

Programa de Doctorado en Física Teórica
Instituto de Física Teórica UAM-CSIC
Departamento de Física Teórica

Madrid, 2024

Agradecimientos/Acknowledgments

En primer lugar, me gustaría destacar que este trabajo se ha podido llevar a cabo gracias a mi supervisor, el doctor Vicent Mateu, no solo por su guía y ayuda durante el proceso sino porque fue él quien en primera instancia me ofreció la oportunidad de realizar el doctorado.

Durante dicho periodo he tenido la oportunidad de coincidir con muy buenos compañeros que han contribuido a su catalogación como una gran etapa de mi vida. En este apartado querría hacer especial mención al doctor Néstor González, del cual he podido aprender mucho tanto dentro como fuera del aspecto académico.

Todo ello fue posible por la hospitalidad con la que la Universidad de Salamanca me trató durante mis estancias en la institución.

I would like to thank also to Dr. Andreas Maier because I learned a lot from him during my scientific visit at DESY making it worth travelling despite the restrictions caused by the Covid emergency. He is still helping me.

También estoy agradecido a la Universidad Autónoma de Madrid, que además de haber hecho posible el desarrollo de mi tesis, cuenta con una escuela de doctorado cuyo apoyo y comprensión, en especial por parte de la secretaría y dirección, han permitido junto a mi tutor el doctor Agustín Sabio la conclusión de la misma.

Finalmente, dado que el refrán no especifica, he de reconocer que, si el fruto de mi trabajo se puede considerar ciencia, será debido a la paciencia de mi familia.

This work was based on the following publications:

- Alejandro Bris, Néstor G. Gracia, and Vicent Mateu. Oriented Event Shapes for massive Quarks. EPJ Web Conf., 274:03001, 2022.
- Alejandro Bris, Néstor G. Gracia, and Vicent Mateu. NLO oriented event-shape distributions for massive quarks. JHEP, 02:247, 2023.
- Alejandro Bris, Vicent Mateu, and Fernando Gil. Massive lighter quark corrections to boosted-top cross section. EPJ Web Conf., 274:04002, 2022.
- Alejandro Bris, Vicent Mateu, and Moritz Preisser. Massive event-shape distributions at N2LL. JHEP, 09:132, 2020.
- Alejandro Bris and Vicent Mateu, Secondary massive quarks with the Mellin-Barnes expansion. To appear soon in arXiv.
- Alejandro Bris, Vicent Mateu and Fernando Gil, Secondary massive quark corrections to boosted-top cross sections. To appear soon in arXiv.

Abstract

In the quest of searching for physics beyond the Standard Model, increasing the control and precision on the theoretical predictions is of utmost importance to understand the origin of the discrepancies found when comparing to experimental data. In this sense, QCD is the sector in which more effort has to be invested due to the slow convergence of the associated perturbative series and its non-perturbative aspects, which are always present no matter how large the energy is.

The differential cross section distributions in terms of observables called event shapes, which contain information about the geometric properties of the particles' momenta in the final state, are very sensitive to QCD dynamics and therefore have been studied for many years to determine the parameters involved in these interactions.

In high-energy experiments, most of the time it is sufficient to use the approximation that all particles in the final state are massless, but for high-precision calculations or if one is interested in cases where the quark mass is a dominant effect, this approximation is no longer valid. While the theoretical computation for massless quarks at e^+e^- colliders has been pushed to unprecedented precision in recent years, computations for massive quarks remain at a lower precision and therefore the goal of this thesis is to fill in that gap.

Considering non-vanishing masses opens the possibility to varying the scheme in the definition of an event shape, so we first study each of the possible schemes in the collinear limit and obtain the corresponding distribution for different observables. Next, we analyze the production of heavy quarks when measuring also the orientation of the final state with respect to the beam axis. Then the computation of the effects of this parameter on virtual quantum corrections is presented through the standard method, and finally the development of a simpler procedure based on series expansions is discussed.

Resumen

En la búsqueda de física más allá del Modelo Estándar, incrementar el control y la precisión de las predicciones teóricas es fundamental para entender el origen de las discrepancias encontradas en la comparación con respecto a los datos experimentales. En este sentido, QCD es el sector en el que mayor esfuerzo se ha de invertir debido a la lenta convergencia de las series pertubativas asociadas y de sus aspectos no perturbativos, los cuales están siempre presentes sin importar cómo de alta sea la energía.

Las distribuciones de probabilidad en término de los observables llamados *formas de evento*, que contienen información acerca de las propiedades geométricas de los momentos de las partículas en el estado final, son muy sensibles a la dinámica de QCD y por tanto se han estudiado durante muchos años para determinar los parámetros involucrados en estas interacciones.

En los experimentos de alta energía, la mayor parte de las veces es suficiente con usar la aproximación de que todas las partículas en el estado final no tienen masa, pero para cálculos de gran precisión o si uno está interesado en casos donde la masa del quark es un efecto dominante, esta aproximación ya no es válida. Mientras que su cálculo teórico para quarks sin masa en colisionadores e^+e^- se ha impulsado a una precisión sin precedentes en los últimos años, los cálculos para quarks masivos permanecen con una precisión inferior, por tanto en este trabajo se persigue disminuir dicha separación.

La consideración de masas no nulas abre la posibilidad a la variación de esquema en la definición de una *forma de evento*, por lo que inicialmente estudiamos cada uno de los posibles esquemas en el límite colinear y obtenemos la distribucion correspondiente para distintos observables. Después, analizamos la producción de quarks pesados cuando se mide también la orientación del estado final con respecto al eje del haz. A continuación el cálculo de los efectos de este parámetro en las correcciones cuánticas virtuales es presentado a través del método estándar y finalmente se discute el desarrollo de un procedimiento más simple basado en series de expansiones.

Contents

Chapter 1

Introduction

1.1 Motivation

The establishment of the Standard Model (SM for short) was one of the biggest achievements in the 20th century particle physics community, worth a Nobel prize [62]. A comprehensive review can be found in Ref. [55]. It was not only able to explain the outcome of all the experiments carried out at that time (and most of the ones running nowadays) but it served to unify three of the four fundamental interactions in nature under the desirable mathematical property of symmetry [26, 64].

After its formulation, the development of a new generation of colliders brought a huge amount of very accurate data, signaling the beginning of the current search for new physics (NP for short) aiming to explain the tensions that appeared between the analysis of these experimental results and the SM predictions. A number of conceptual and phenomenological problems also triggered the efforts of scientists to find a more fundamental theory: neutrino masses, dark matter and energy, the hierarchy problem, the large number of free parameters in the SM, the existence of three and only three flavor replicas, matter-antimatter asymmetry, quantization of gravity, etc [57, 16].

Reducing theoretical uncertainties would help clarifying the discrepancies between theory and experiment and will in addition constrain NP models. In order to achieve this goal, the strategy with the largest impact would be increasing the precision of Quantum Chromo-Dynamics (QCD) predictions, given the slow convergence of perturbative series in powers of α_s —caused by the large value of the strong coupling— and the presence of non-perturbative effects within this sector.

Additionally, since many of the Beyond Standard Model (BSM for short) theories modify the Higgs [33, 21] sector of the SM and the coupling to this boson is proportional to the particle's mass, the top quark is a prominent gate being used to explore such extensions [19]. The top quark is only colored particle not subject to confinement, since it decays before hadronization can take place, and therefore is quasi-free. Measuring its properties (notable its very large mass) is then carried out at collider experiments, studding high-energy observables which most of the time involve jets. Jets are very colimated sprays of energetic particles that travel nearly in the same direction. They have their origin in the peculiar perturbative radiation pattern exhibit by the strong interactions, which favors the emission of additional hard colored partons in the same direction as the parent quark or gluon, or soft partons in any direction.

Let us discuss in more detail the formation and evolution of jets: when a final-state quark is prop-

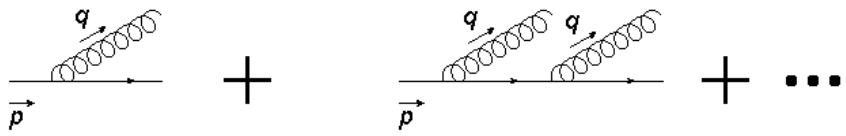

Figure 1.1: Gluon radiation from a quark

agating, the configuration for gluon emission is similar to the one shown in Fig. 1.1 and the probability is given in perturbative QCD by a power series in the coupling constant. In the case of massless quarks, and under the simplifying assumption of all gluons having the same momentum q (which does not affect the argumentation), we have:

$$\text{Prob} \sim \sum_n \mathcal{O}\left[\left(\frac{\alpha_s}{(p+n\,q)^2}\right)^n\right] \sim \sum_n \mathcal{O}\left[\left(\frac{\alpha_s}{2n\,p\cdot q}\right)^n\right], \tag{1.1}$$

where p is the momentum of the final-state quark and n is the number of radiated gluons. Therefore, the result will be significantly enhanced when $p \cdot q \ll 1$ and there are two different cases for which this happens:

- q^μ is soft: $(q^\mu \sim \lambda^2;\, \lambda \ll 1) \Rightarrow p \cdot q \sim \lambda^2$.
- q^μ is collinear to p^μ: $(\vec{q} \parallel \vec{p}) \Rightarrow p \cdot q \sim \lambda^2$.

Under the assumption $\alpha_s \sim \lambda^2$, these enhancements make all terms in the expansion equally important, breaking down the convergence of the perturbative series and signaling the necessity of accounting for all collinear and soft gluon radiations at once, which gives rise to the aforementioned jet.

For a massive quark the situation is similar and the probability behaves in the following way:

$$\text{Prob} \sim \sum_n \mathcal{O}\left[\left(\frac{\alpha_s}{(p+n\,q)^2-m^2}\right)^n\right] \sim \sum_n \mathcal{O}\left[\left(\frac{\alpha_s}{2n\,p\cdot q}\right)^n\right], \tag{1.2}$$

being m the quark mass. Soft emission enhancement remains as for massless quarks:

- q soft: $(q^\mu \sim \lambda^2;\, \lambda \ll 1) \Rightarrow p \cdot q \ll 1$.

whereas collinear gluons now satisfy:

- q collinear: $(\vec{q} \parallel \vec{p}) \Rightarrow p \cdot q \sim \mathcal{O}\left(\frac{m^2}{|\vec{p}|^2}\right)$.

Provided $m/|\vec{p}| \sim \lambda$, collinear radiation in the propagation of heavy quarks with high momentum is still favored leading again to a jet which now will be sensitive to the quark mass. In real-life computations, these enhancements manifest themselves as large logarithms that slow down or even invalidate fixed-order perturbation expansions. Since the nature of these logarithms is related to the incomplete cancellation of real- and virtual-radiation singularities, one gets two powers of log per each power of α_s. Such pathological logarithms go under the name of "Sudakov logs".

Led by the discussion above, heavy quarks and jets initiated by those will be the main focus of this thesis. We confine our study to the case of massive event shapes in e^+e^- collisions, using fixed-order perturbation theory to include higher order effects, and effective field theories (EFTs for short) to sum up to all orders in perturbation theory (such summation is normally dubbed "resummation")

the large (double) logarithms that appear in the dijet kinematic regime. EFTs provide a nice framework for resummation: solving the renormalization group evolution of Wilson coefficients will do the job.

These advanced Quantum Field Theory (QFT for short) concepts are introduced in the remaining of this Chapter. In Chapter 2, we will explore the sensitivity of generic event-shape distributions to the mass of the (**primary**) quark (that is, the quark from which the jet emerges) through different choices in their definition, called massive schemes (which should not be confused with QFT mass schemes such as pole, $\overline{\text{MS}}$, MSR...), and compute the NLO jet function, the missing piece to achieve $\text{N}^2\text{LL} + \mathcal{O}(\alpha_s)$ precision. In Chapter 3 we consider the orientation of the event with respect to the beam axis, carrying out the NLO fixed-order computation of oriented event-shape distributions for massive quarks, as well as the total oriented cross section. In Chapter 4 we analyze secondary massive quark corrections affecting jet cross sections with highly boosted heavy quarks, computing the two-loop contributions for the hard and jet function, and developing a full-fledged variable-flavor number scheme (VFNS) for final state boosted tops. Finally, in Chapter 5, the development of a new technique designed to effortlessly compute the corrections due to massive quark bubbles and massive gauge bosons shall be presented. These will be applied to a variety of matrix elements, recovering known results (including those first time obtained in Chapter 4) and obtaining optimal expansions for various hierarchies of the masses with respect to the relevant kinematic variables.

1.2 $e^+e^- \to$ hadrons

In this section we lay out the theoretical foundations for the process we are mostly interested: high-energy hadron production in e^+e^- collisions, whose cross section can be written as:

$$\sigma = \frac{1}{2\Lambda^{\frac{1}{2}}(Q^2, m_e, m_e)} \sum_X \int \mathrm{d}\Phi_X \, (2\pi)^d \, \delta^{(d)}\left(q - \sum_{i\in X} p_i\right) \left|\mathcal{M}(e^+e^- \to X)\right|^2 , \tag{1.3}$$

$$\mathrm{d}\Phi_X \equiv \prod_{i\in X} \frac{\mathrm{d}^{d-1}p_i}{(2\pi)^{d-1}} \frac{1}{2p_i^0} ,$$

with Λ the Källén function, $Q = \sqrt{(p_{e^+} + p_{e^-})^2}$ the center of mass (COM for short) energy, m_e the electron mass, q the total momentum of the final state particles and d the number of dimensions.[1] In the high-energy regime we are interested in, the mass of the electron can be neglected ($Q \gg m_e$) leading to the following flux factor:

$$2\Lambda^{\frac{1}{2}}(Q^2, m_e, m_e) \simeq 2\Lambda^{\frac{1}{2}}(Q^2, 0, 0) = 2Q^2 . \tag{1.4}$$

Since the couplings satisfy the hierarchy $\alpha_{em} \ll \alpha_s$, we can limit ourselves to leading order in α_{em} —that is, to the tree level— (even though we will capture the main electroweak corrections to the Z-boson propagator through a Breit-Wigner, accounting for the fact that it is unstable) but consider many QCD quantum corrections in powers of α_s, leading to the splitting of this kind of matrix elements into both parts (see Fig. 1.2):[2]

$$\left|\mathcal{M}(e^+e^- \to X)\right|^2 = \sum_{C=V,A} L^C_{\mu\nu} \, H^{\mu\nu}_C . \tag{1.5}$$

[1] We will use $d = 4 - 2\varepsilon$ in dimensional regularization, which will serve the purpose of regularizing both infrared and collinear (denoted globally as IR), as well as ultraviolet (UV) divergences.

[2] The average in the initial and sum over the final degrees of freedom is implicit.

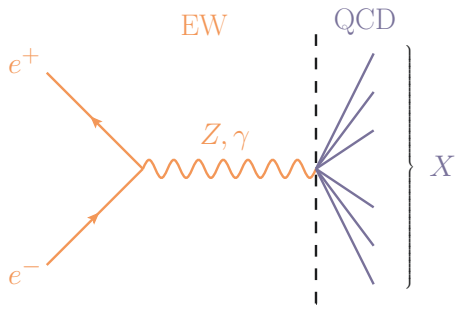

Figure 1.2: Sketch of the EW-QCD matrix element splitting: orange shows the EW part while blue stands for the colored (QCD) sector.

The leptonic tensor $L^C_{\mu\nu}$ is given by:

$$
\begin{aligned}
L^C_{\mu\nu} &= L^C \, l_{\mu\nu} \,, \\
l_{\mu\nu} &= p^\mu_{e^-} p^\nu_{e^+} + p^\nu_{e^-} p^\mu_{e^+} - \frac{Q^2}{2} g^{\mu\nu} \,, \\
L_V &= \frac{\alpha^2_{em}(4\pi)^2}{Q^4} \left[Q_q^2 - \frac{2Q^2 Q_q v_e v_q (Q^2 - m_Z^2)}{(Q^2 - m_Z^2)^2 + \left(\frac{Q^2 \Gamma_Z}{m_Z}\right)^2} + \frac{Q^4 (v_e^2 + a_e^2) v_q^2}{(Q^2 - m_Z^2)^2 + \left(\frac{Q^2 \Gamma_Z}{m_Z}\right)^2} \right] \,, \\
L_A &= \frac{\alpha^2_{em}(4\pi)^2 (v_e^2 + a_e^2) a_q^2}{(Q^2 - m_Z^2)^2 + \left(\frac{Q^2 \Gamma_Z}{m_Z}\right)^2} \,,
\end{aligned}
\tag{1.6}
$$

where m_Z and Γ_Z are the mass and the decay width of the Z-boson, respectively, C labels the vector V and axial-vector A currents, Q_q is the electric charge of the quark being produced, and $v_{q,e}$ and $a_{q,e}$ are the vector and axial charges for the corresponding fermion:

$$
v_f = \frac{T_f^3 - 2Q_f \sin^2\theta_W}{2 \sin\theta_W \cos\theta_W} \,, \qquad a_f = \frac{T_f^3}{2 \sin\theta_W \cos\theta_W} \,. \tag{1.7}
$$

Here T_f^3 is the third component of weak isospin and θ_W is the weak mixing angle. On the other hand, the hadronic part has the following form:

$$
H = \langle 0 | \mathcal{J}_C^{\mu\dagger} | X \rangle \langle X | \mathcal{J}_C^\nu | 0 \rangle \,, \tag{1.8}
$$

being $\mathcal{J}^\mu_{V,A}$ the vector and axial-vector quark currents, defined as follows:[3]

$$
\mathcal{J}^\mu_C = \overline{q}^a_f \Gamma^\mu_C q^a_f \,, \qquad \begin{aligned} \Gamma^\mu_V &= \gamma^\mu \\ \Gamma^\mu_A &= \gamma^\mu \gamma^5 \end{aligned} \,, \tag{1.9}
$$

In the previous formula, the flavor f (which is not used as a label in the current itself) is fixed and a sum over colors a is understood.

[3]These two QCD quark currents are ultraviolet finite and do not need multiplicative renormalization. All currents are defined in terms of bare fields, which is the way they appear in the theoretical expressions for the relevant matrix elements.

Finally, if one is not interested in the orientation of the final-state with respect to the beam (an exception to this case is Chapter 3), an angular average with respect to the incoming leptons can be taken:

$$\int \frac{\mathrm{d}^{d-2}\Omega}{\Omega_{\rm tot}^{d-2}}\, l_{\mu\nu} = Q^2 \frac{1-\varepsilon}{3-2\varepsilon}\tilde{l}_{\mu\nu}\,, \tag{1.10}$$
$$\Omega_{\rm tot}^{d-2} = (4\pi)^{1-\varepsilon}\frac{\Gamma(1-\varepsilon)}{\Gamma(2-2\varepsilon)}\,,$$
$$\tilde{l}_{\mu\nu} \equiv \frac{q_\mu q_\nu}{Q^2} - g_{\mu\nu}\,.$$

Since $q^\mu = p_{e^+}^\mu + p_{e^-}^\mu$ is the momentum of the mediating (virtual) boson (see Fig. 1.2), we obtain in this way an expression for the cross section that will simplify the computations due to the Ward identity satisfied by vector current, as well as the axial-vector current in the chiral limit (that is, for zero quark mass):

$$\sigma = \frac{1}{2Q^2}\tilde{\sum}_X \int \mathrm{d}^d x\, e^{iq\cdot x} \sum_{C=V,A} \tilde{L}_C\, \tilde{l}_{\mu\nu}\, \langle 0|\mathcal{J}_C^{\mu\dagger}(x)|X\rangle\langle X|\mathcal{J}_C^{\nu}(0)|0\rangle\,, \tag{1.11}$$

where we also combined the Fourier representation of the momentum conservation delta with the space-time evolution of the current operator, and defined:

$$\tilde{\sum}_X \equiv \sum_X \int \mathrm{d}\Phi_X\,, \tag{1.12}$$
$$\tilde{L}_C \equiv L^C\, Q^2 \frac{1-\varepsilon}{3-2\varepsilon}\,.$$

1.3 Event shapes

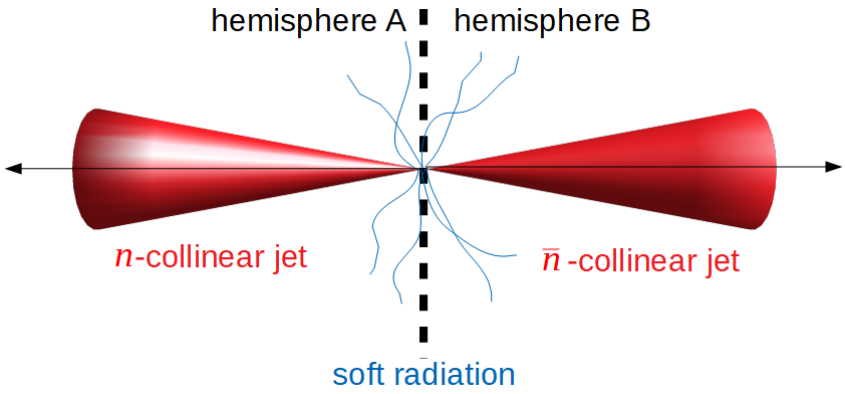

Figure 1.3: Dijet-type event in the COM frame. These events are characterized by the COM energy Q, the collinear $p_n^2 \sim p_{\bar{n}}^2 \sim Q^2\lambda^2$ and soft $p_s^2 \sim Q^2\lambda^4$ scales, with $\lambda \ll 1$. In the case of jets initiated by massive quarks, the parameter λ is assumed to be of the order of its reduced mass $\lambda \sim \hat{m} \equiv m/Q$.

We refer to event shapes as a type of observables containing information about the geometric distribution of the final-state particle energy and momenta. Cross sections differential in the value of a given event-shapes are very sensitive to QCD dynamics, and therefore have been extensively used by

the scientific community to study QCD properties and determine its parameters (specially α_s) for many years, mostly in Deep Inelastic Scattering (DIS) and e^+e^- collisions (which will be our case), although in recent years they have been adapted to the scenario of pp and $p\bar{p}$ colliders. For a review see Refs. [17, 45]

We will focus on events whose final state, in the center of mass frame, consists of two back-to-back narrow jets (see Fig. 1.3). These are dubbed dijet-type event shapes, which attain their minimum value in this kinematic regime, and are the most suitable to describe it. Moreover, their value in this region can be decomposed into the sum of collinear (in two back-to-back directions) and soft contributions [4, 52], that is:

$$\overline{e} \;=\; e_n + e_{\overline{n}} + e_s \,, \tag{1.13}$$

where $\overline{e}$ is the measurement function for the event-shape e at leading power in λ. This is a key feature for the factorization of the event-shape distribution within the corresponding effective field theory (EFT for short). Additionally, even for cases in which the event-shape definition involves non-linear correlations among final-state momenta, in the dijet limit each sector e_n, $e_{\overline{n}}$ and e_s can be written as a sum over single-particle contributions. We will study the previous decomposition for several event-shapes in Chapter 2.

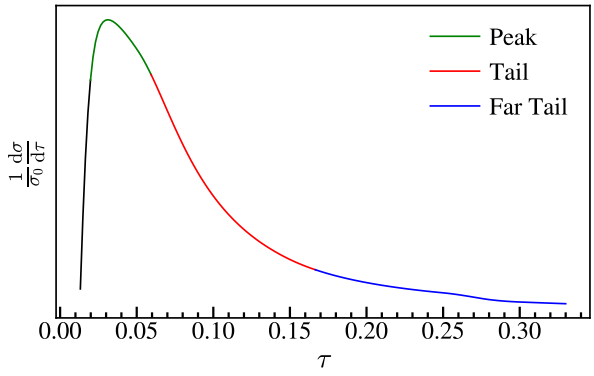

Figure 1.4: Different regions for an example thrust distribution

For a given dijet-type event-shape differential cross-section one may distinct the following regions (see Fig. 1.4):

- Peak: pure dijet configuration. Hadronization due to soft effects is $\mathcal{O}(1)$.
- Tail: transition between 2- and 3-jet events. Soft hadronization is a correction tractable with an OPE.
- Far-tail: multi-jet (isotropic) events. Hadronization involves multiple scales.

Some of the most common event-shapes are:

- **Thrust** [22]:

$$\tau = \frac{1}{Q_P}\min_{\hat{t}} \sum_i (|\vec{p}_i\,| - |\hat{t}\cdot\vec{p}_i\,|)\,. \tag{1.14}$$

  where $\hat{t}$ is the thrust axis, a unitary vector chosen to minimize the sum, and the normalization is given by $Q_P \equiv \sum_i |\vec{p}_i\,|$.

- **C-parameter** [20, 54]:

$$C = \frac{3}{2}\left[1 - \frac{1}{Q_P^2}\sum_{i,j}\frac{(\vec{p}_i \cdot \vec{p}_j)^2}{|\vec{p}_i\,||\vec{p}_j\,|}\right]. \tag{1.15}$$

  where

- **Hemisphere Jet Mass** [9, 13, 14]:

$$s = \left(\sum_{i\in h} p_i\right)^2, \tag{1.16}$$

  where h is one of the hemispheres delimited by the plane normal to the thrust axis $\hat{t}$.

1.4 Effective Field Theories

EFTs are useful to tackle problems with a strong hierarchy between the involved scales. They describe the dynamics of the light degrees of freedom of a system, that is, the physics at a scale much lower than some ultraviolet scale related to the problem under study, and exploit symmetries that emerge only in certain kinematic regimes. There are two different ways to build an EFT:

- **Top-down:** The EFT is obtained from another theory, called full (or UV) theory, describing a wider range of degrees of freedom. In a first step, one identifies the kinematic region of interest and characterizes it by a small and dimensionless parameter, usually referred as λ, that sets the power counting. Integrating out the hard modes of the fields in the full theory action and expanding the resulting operators in the small parameter λ yields the EFT Lagrangian, which is by itself an expansion in terms of increasing-dimension operators.
- **Bottom-up:** In this case the full theory is unknown (or it is known but the system undergoes a phase transition such that the degrees of freedom in both theories do not coincide) and therefore all operators consistent with the physical assumptions must be taken into account. The unspecified coefficients (couplings) can be determined comparing theoretical predictions to experimental data (or in some cases, to numerical data obtained from lattice simulations). The set of operators is constrained by considering the relevant degrees of freedom, symmetries, equations of motion and integration by parts relating the different terms. They can be ordered according to the power counting parameter, so not all of them are equally important, and there is a finite set at each order.

Therefore, results from a top-down EFT truncated to some power correspond to an approximation up to a certain power of λ of the full-theory prediction. At first sight, it seems there is no reason for considering EFTs other than making computations easier (obviously in a bottom-up EFT there is no other possibility). Nevertheless, matching and running within the EFTs framework pulls apart the different scales and sums up large logarithms appearing in the full theory that can invalidate the perturbative expansion. The procedure consists in the following steps:

1) Pick a physical process (in general, the simplest possible) that only has light degrees of freedom as external states.

2) Compute this process in both theories (full & EFT) and, within the order one is working, set to zero the difference at some (high) scale (in this context, setting means imposing).

3) From the previous condition, extract the connection (**matching**) between the coefficients of both theories at this scale.

4) Using renormalization group equations evolve (**running**) the EFT Wilson coefficients (low energy constants) down to the low scale.

5) Compute the renormalization-group (RG) improved observable using the EFT.

The virtue of this procedure is that the matching coefficient does not depend on the particular process one is studying, but it is a property of the operator itself. Therefore, once the coefficient has been determined (with the simplest possible process, and with the simplest regularization procedure), the operator can be used to compute a plethora of observables.

Due to the fact that both theories agree in the description of infrared physics, the matching can only depend on the hard scales whereas the EFT operators lead to matrix elements for which the low scale is natural (and hence choosing the renormalization scale of the same order as the low scale minimizes logarithms). Hence, by means of matching, we obtain a result factorized in terms of a (high-energy) matching coefficient times a (low-energy) matrix element with different natural scales. Then one just needs to use renormalization group evolution (RGE) on the Wilson coefficient to evaluate all parts of the factorization at the same (low) scale. In Ref. [15], a very clear explanation with simple examples about the way scales become separated can be found. For another review on effective field theories, deepening in their physical meaning, see Ref. [50].

In this work we will deal with two EFTs: Soft Collinear Effective Theory (SCET), used to carry out the resummation of (double) large logarithms appearing in QCD in the peak and tail regions of the distributions for massless quarks, or the tail region for massive quarks, and boosted Heavy Quark Effective Theory (bHQET) necessary to describe the peak region in the case of massive primary quarks.

1.4.1 SCET

Soft-Collinear Effective theory is an EFT built top-down from QCD to describe, as the name suggest, the soft and collinear degrees of freedom relevant in situations involving jets. This kinematic region is better characterized expressing the momenta in a light-cone basis, which is defined by two light-like four-vectors $\{n_1^\mu, n_2^\mu\}$ satisfying $n_1^2 = n_2^2 = 0$ and the basis of the (space-like) perpendicular subspace. Here we will adopt the usual convention $n_1^\mu = n^\mu \equiv (1,0,0,-1)$; $n_2^\mu = \overline{n}^\mu \equiv (1,0,0,1)$ and the perpendicular standard unit vectors in the x and y directions. With this choice we have:

$$\begin{aligned} p^\mu &= n\cdot p\,\frac{\overline{n}^\mu}{2} + \overline{n}\cdot p\,\frac{n^\mu}{2} + p_\perp^\mu \equiv p^+\frac{\overline{n}^\mu}{2} + p^-\frac{n^\mu}{2} + p_\perp^\mu\,, \\ p\cdot q &= \frac{1}{2}\,p^+q^- + \frac{1}{2}\,q^+p^- - \vec{p}_\perp\cdot\vec{q}_\perp\,, \end{aligned} \tag{1.17}$$

and specify the corresponding components with the following short-hand notation $p^\mu = (p^+, p^-, p_\perp^\mu)$.

In a dijet situation the collinear scaling is $p_n \sim Q\left(\lambda^2, 1, \lambda\right)$, and $p_{\overline{n}} \sim Q\left(1, \lambda^2, \lambda\right)$, both with virtuality $p_n^2 \sim p_{\bar{n}}^2 \sim Q^2\lambda^2$ where Q is the energy in the COM frame. As for the soft modes, there are two different versions of the theory: $\mathrm{SCET_I}$ accounting for soft momenta that satisfy $p_{us} \sim Q\left(\lambda^2, \lambda^2, \lambda^2\right)$ (also called ultrasoft) and $\mathrm{SCET_{II}}$ with $p_s \sim Q\left(\lambda, \lambda, \lambda\right)$, with virtualities $p_{us}^2 \sim Q^2\lambda^4$ and $p_s^2 \sim Q^2\lambda^2$, respectively.

Hereinafter, we will refer to $\mathrm{SCET_I}$ just as SCET since it is the relevant one for the observables under study (see the caption in Fig. 1.3), and will denote the ultrasoft momenta simply by p_s. Furthermore one can get $\mathrm{SCET_{II}}$ from $\mathrm{SCET_I}$ by integrating out also the modes resulting from the sum of collinear and soft momenta, since these are off the theory shell: $p \equiv p_s + p_n \sim Q\left(\lambda, 1, \lambda\right) \to p^2 \sim Q^2\lambda \gg Q^2\lambda^2$

(the sum is neither soft, nor collinear), and therefore it can be obtained just from matching the soft Wilson lines in SCET to the corresponding ones.

Leading Order Lagrangian

As mentioned before, once we established the kinematic region of the theory, the EFT fields are given by the mode restriction of those in the full theory to the EFT sectors, which can be done in the Fourier representation. For instance the QCD quark field:

$$\psi(x) = \int \frac{\mathrm{d}^4 p}{(2\pi)^4} \delta(p^2)\theta(p^0)[u(p)a(p)e^{-ip\cdot x} + v(p)b^\dagger(p)e^{ip\cdot x}]\,, \tag{1.18}$$

leads to SCET quark n-collinear field if we just consider the corresponding momentum scaling:

$$\psi_n(x) = \int \frac{\mathrm{d}^4 p_n}{(2\pi)^4} \delta(p_n^2)\theta(p_n^0)[u(p_n)a(p_n)e^{-ip_n\cdot x} + v(p_n)b^\dagger(p_n)e^{ip_n\cdot x}]\,, \tag{1.19}$$

and the same holds for the soft fields as well as for the gluon $A^a_\mu(x)$. The existence of a preferential direction affects also the spinor components, therefore we have to distinguish the large and small contributions and grade the operators appearing in the SCET Lagrangian in terms of the power counting parameter. The splitting can be done by introducing the following projectors:

$$P_n \equiv \frac{\not{n}\bar{\not{n}}}{4}\,, \qquad P_{\bar{n}} \equiv \frac{\bar{\not{n}}\not{n}}{4}\,, \tag{1.20}$$

which satisfy the following properties:

$$\begin{aligned} &P_n + P_{\bar{n}} = I\,, \qquad P_n^2 = P_n\,, \qquad P_{\bar{n}}^2 = P_{\bar{n}}\,, \\ &\frac{P_{\bar{n}}\,u(p_n)}{P_n\,u(p_n)} \sim \frac{P_{\bar{n}}\,v(p_n)}{P_n\,v(p_n)} \sim \lambda\,. \end{aligned} \tag{1.21}$$

The first line can be shown using the properties of the Dirac gamma matrices and the second one applying any of the projectors to the Dirac's equation for the spinors. Using these projectors, we define the large and small projections of the QCD quark field:

$$P_n\,\psi_n(x) \equiv \hat{\xi}_n(x)\,, \qquad P_{\bar{n}}\,\psi_n(x) \equiv \hat{\varphi}_n(x)\,. \tag{1.22}$$

Therefore, given a collinear direction n, the SCET Lagrangian is obtained from the QCD action[4]

$$\begin{aligned} \mathcal{L}_{\mathrm{QCD}} &= \overline{\psi}\left[i\not{D}\right]\psi - \frac{1}{2}\mathrm{Tr}\left\{G^{\mu\nu}G_{\mu\nu}\right\}\,. \\ D_\mu &= \partial_\mu - igA_\mu\,, \\ G_{\mu\nu} &= \frac{i}{g}[D^\mu, D^\nu]\,. \end{aligned} \tag{1.23}$$

by making the replacements:

$$\begin{aligned} \psi &\to \hat{\xi}_n + \hat{\varphi}_n + \psi_s\,, \\ A^\mu &\to \hat{A}^\mu_n + A^\mu_s\,. \end{aligned} \tag{1.24}$$

[4]We start from the massless case and will discuss later the inclusion of a quark mass. We also omit the gauge-fixing and ghost terms to make the presentation simple. More details can be found on the SCET review of Ref. [60].

and carrying out the corresponding expansion as a series in λ. This procedure yields some operators containing different powers in their various components. The label formalism helps performing this last separation of scales in terms of derivatives acting on the SCET fields. It consists in expressing the collinear momentum p_n^μ as a sum of label and residual contributions:

$$\begin{aligned} p_n^\mu &= p_l^\mu + p_r^\mu \,, \\ p_l^\mu &\sim Q(0,1,\lambda) \,, \\ p_r^\mu &\sim Q(\lambda^2,\lambda^2,\lambda^2) \,, \end{aligned} \tag{1.25}$$

in such a way that any SCET collinear field $\hat{\phi}_n$ can be decomposed as the sum of labeled fields with only residual momenta:

$$\begin{aligned} \hat{\phi}_n(x) &\equiv \int \frac{\mathrm{d}^4 p_n}{(2\pi)^4} \left[\hat{\phi}^+(p_n)\, e^{-ip_n\cdot x} + \hat{\phi}^-(p_n)\, e^{ip_n\cdot x}\right] \\ &= \sum_{p_l\neq 0} \int \frac{\mathrm{d}^4 p_r}{(2\pi)^4} \left[\hat{\phi}^+_{p_l}(p_r)\, e^{-i(p_l+p_r)\cdot x} + \hat{\phi}^-_{p_l}(p_r)\, e^{i(p_l+p_r)\cdot x}\right] \\ &= \sum_{p_l\neq 0} \left[\hat{\phi}^+_{p_l}(x)\, e^{-ip_l\cdot x} + \hat{\phi}^-_{p_l}(x)\, e^{ip_l\cdot x}\right] . \end{aligned} \tag{1.26}$$

As can be seen explicitly in the previous equation, all collinear fields are defined with the exclusion of the zero label momentum region, since that regime is covered by the soft fields. This will lead to the necessity of using 0-bin subtractions in the collinear loop integrals to get the right result. The procedure consists in subtracting, at the corresponding order of the power counting parameter we are working, the contribution of the collinear loop integral but considering the loop momentum scales as if it were soft, in order to avoid double counting

$$\begin{aligned} &\tilde{I} \equiv \int \mathrm{d}^d\ell\, f(\ell^\mu, p_i^\mu) \Longrightarrow I^{0-\mathrm{bin}} = \int \underbrace{\mathrm{d}^d\ell}_{\sim\lambda^{2d}}\; f(\underbrace{\ell^\mu}_{\sim\lambda^2}, p_i^\mu) = \int \mathrm{d}^d\ell \sum_{n=0} \underbrace{f^n(\ell^\mu, p_i^\mu)}_{\sim\lambda^{n-2d}} , \\ &I = \tilde{I} - I^{0-\mathrm{bin}} \underset{\mathrm{LO}}{\longrightarrow} \int \mathrm{d}^d\ell\, \left[f(\ell^\mu, p_i^\mu) - f^0(\ell^\mu, p_i^\mu)\right] , \end{aligned} \tag{1.27}$$

where LO stands for leading order. It is worth mentioning that the contribution of the 0-bin can be scaleless (and therefore vanishes in dimensional regularization) or start at an order higher than the one one is working, in such a way that there is no need for subtractions. In this case we will omit their discussion.

From Eq. (1.26), defining the label momentum operator $\mathcal{P}^\mu \hat{\phi}_{p_l} = p_l^\mu \hat{\phi}_{p_l}$ with $\mathcal{P}^\mu = (0, \mathcal{P}^-, \mathcal{P}_\perp^\mu)$, we obtain:[5]

$$\hat{\phi}_n(x) = e^{-ix\cdot\mathcal{P}} \sum_{p_l\neq 0} \left[\hat{\phi}^+_{p_l}(x) + \hat{\phi}^-_{-p_l}(x)\right] \equiv e^{-ix\cdot\mathcal{P}} \sum_{p_l\neq 0} \phi_{n,p_l}(x) \equiv e^{-ix\cdot\mathcal{P}} \phi_n(x) \,. \tag{1.28}$$

Obviously, soft momenta are pure residual and soft fields are not labeled, even though one can regard them as carrying a zero label: $p_l = 0$ field:[6]

$$\phi_s(x) = e^{-ix\cdot\mathcal{P}} \phi_s(x) = \phi_{p_l=0}(x) \,. \tag{1.29}$$

[5] $\mathcal{P}$ always acts to the right, satisfying for Dirac adjoint fields: $\mathcal{P}^\mu \overline{\hat{\phi}}_{p_l} = -p_l^\mu \overline{\hat{\phi}}_{p_l}$. Since $p_\ell^- > 0$, one can extend the sum over positive and negative values of p_ℓ^- and use the sign of p_ℓ^- to distinguish between positive and negative frequency modes.

[6] Notice that we did not need to use the hat notation for these.

Now we see that the action of a "full-theory" derivative on a SCET collinear field is:

$$i\partial_\mu \hat{\phi}_n(x) = e^{-ix\cdot\mathcal{P}}(i\partial_\mu + \mathcal{P}_\mu)\phi_n(x)\,, \tag{1.30}$$

so in terms of label formalism fields (those without the hat notation) the derivative scalings are clear:

$$\begin{aligned} \mathcal{P}_\mu \phi_n &\sim Q(0,1,\lambda)\phi_n\,, \\ \partial_\mu \phi_s &\sim Q\lambda^2 \phi_s\,, \end{aligned} \tag{1.31}$$

and their scaling in powers of λ can be deduced from the kinetic terms in the Lagrangian imposing an $\mathcal{O}(\lambda^0)$ leading-order action to properly describe these degrees of freedom in SCET. Furthermore, the position and momentum commutation relation must hold. All in all:

$$\begin{aligned} S_{\text{kin}} &= \int d^4x\, \mathcal{L}_{\text{kin}} \sim \mathcal{O}\left(\lambda^0\right), \\ [p,x] = i &\to x\cdot p \sim \mathcal{O}\left(\lambda^0\right). \end{aligned} \tag{1.32}$$

And the previous conditions lead to:

$$\begin{aligned} &\xi_n \sim Q\lambda\,, && \varphi_n \sim Q\lambda^2\,, && \psi_s \sim Q\lambda^3\,, \\ &A_n^\mu \sim Q(\lambda^2,1,\lambda)\,, && A_s^\mu \sim Q(\lambda^2,\lambda^2,\lambda^2)\,. \end{aligned} \tag{1.33}$$

With all these considerations at hand, we can get the leading-order SCET Lagrangian after making the substitutions given in Eq. (1.24) in the QCD action and grouping together all λ^0 operators:[7]

$$\begin{aligned} \mathcal{L}^0_{\text{SCET}} &\equiv \mathcal{L}_{n\xi} + \mathcal{L}_{ng} + \mathcal{L}_s\,, \\ \mathcal{L}_{n\xi} &= e^{-ix\cdot\mathcal{P}}\overline{\xi}_n\left(in\cdot D + i\not{D}_{n\perp}\frac{1}{i\overline{n}\cdot D_n}i\not{D}_{n\perp}\right)\frac{\not{\overline{n}}}{2}\xi_n\,, \\ \mathcal{L}_{ng} &= \frac{1}{2g^2}\text{Tr}\left\{\left([i\mathcal{D}^\mu, i\mathcal{D}^\nu]\right)^2\right\}, \\ \mathcal{L}_s &= \overline{\psi}_s i\not{D}_s\psi_s - \frac{1}{2}\text{Tr}\left\{\left(\frac{i}{g}[D_s^\mu, D_s^\nu]\right)^2\right\}, \end{aligned} \tag{1.34}$$

where:

$$\begin{aligned} D &= \partial - i\mathcal{P} - igA_n - igA_s\,, \\ D_n &\equiv -i\mathcal{P} - igA_n\,, \\ \mathcal{D} &\equiv -i\overline{n}\cdot(\mathcal{P} + gA_n)\frac{n}{2} - in\cdot(i\partial + gA_n + gA_s)\frac{\overline{n}}{2} - i\left(\mathcal{P}_\perp + gA_{n\perp}\right), \\ D_s &\equiv \partial - igA_s\,. \end{aligned} \tag{1.35}$$

To obtain the EFT Lagrangian we have integrated out the power-suppressed field φ_n using its equation of motion:

$$\frac{\delta\mathcal{L}}{\delta\varphi_n} = 0 \quad \longrightarrow \quad \varphi_n = \frac{1}{\overline{n}\cdot D_n}\not{D}_{n\perp}\frac{\not{\overline{n}}}{2}\xi_n\,, \tag{1.36}$$

since it is sub-leading with respect to ξ_n [see Eq. (1.33)] and therefore can be considered as pure background at this order.

[7] To see these operators make the action $\mathcal{O}(\lambda^0)$ one must include the corresponding d^4x scaling.

Finally, the modifications one has to account for when considering a non-vanishing quark mass depend on its scaling with respect to the SCET power counting parameter. In the case of a jet initiated by a massive quark, the collinear quark modes become massive and one has to consider $m \sim Q\lambda$ in order to maintain a homogeneous virtuality. Therefore, the $\mathcal{L}_{n\xi}$ Lagrangian becomes:[8]

$$\mathcal{L}_{n\xi} = e^{-ix\cdot\mathcal{P}}\bar{\xi}_n \left[in\cdot D + \left(i\not{D}_{n\perp} - m\right)\frac{1}{i\bar{n}\cdot D_n}\left(i\not{D}_{n\perp} + m\right)\right]\frac{\not{\bar{n}}}{2}\xi_n \,. \tag{1.37}$$

Nevertheless, it is possible to establish a framework to include quark masses with a variable scaling with respect to λ. We will discuss this possibility later, within the factorization theorem setup.

Wilson lines and mode separation

Collinear Wilson lines W_n account for the full-theory interactions between collinear particles belonging to different sectors. They arise naturally in SCET when matching to QCD operators, are crucial to factorize the cross section, and are needed to preserve collinear gauge invariance. For primary quarks, in position space they can be written as:

$$\begin{aligned} W_n(x) &= \overline{P}\exp\left(-ig\int_0^\infty \mathrm{d}s\,\bar{n}\cdot A_n(\bar{n}s+x)\right), \\ W_{\bar{n}}^\dagger(x) &= P\exp\left(ig\int_0^\infty \mathrm{d}s\,n\cdot A_{\bar{n}}(ns+x)\right), \end{aligned} \tag{1.38}$$

being $P, \overline{P}$ the path and anti-path ordering operators respectively, necessary due to the non-abelian nature of QCD. Moreover, they also appear in the SCET Lagrangian through the leading order relation:

$$i\bar{n}\cdot D_n W_n = W_n \bar{n}\cdot\mathcal{P}\,, \tag{1.39}$$

in such a way that $\mathcal{L}_{n\xi}$ is manifestly non-local at the high energy scale, but remains local at low energies:

$$\mathcal{L}_{n\xi} = e^{-ix\cdot\mathcal{P}}\bar{\xi}_n\left(in\cdot D + i\not{D}_{n\perp}W_n^\dagger\frac{1}{\bar{n}\cdot\mathcal{P}}W_n i\not{D}_{n\perp}\right)\frac{\not{\bar{n}}}{2}\xi_n\,. \tag{1.40}$$

Next we consider (quark) soft Wilson lines along the two collinear directions [5, 10]:

$$\begin{aligned} Y_n(x) &= \overline{P}\exp\left(-ig\int_0^\infty \mathrm{d}s\,n\cdot A_s(ns+x)\right), \\ Y_{\bar{n}}^\dagger(x) &= P\exp\left(ig\int_0^\infty \mathrm{d}s\,\bar{n}\cdot A_s(\bar{n}s+x)\right). \end{aligned} \tag{1.41}$$

The emission/absorption of soft gluons from/to collinear particles leads to eikonal propagators that can be summed up and expressed globally in terms of the previous objects (or analogous ones depending on whether it is a quark or an anti-quark, and if it is incoming or outgoing). Implementing the so-called BPS field redefinition:[5]

$$\xi_n \to Y_n\xi_n^{(0)}\,, \qquad A_n \to Y_n A_n^{(0)} Y_n^\dagger\,, \tag{1.42}$$

we see how collinear and soft sectors decouple in the leading-power Lagrangian when expressed in terms of the new soft-gauge-invariant fields $\xi_n^{(0)}$ and $A_n^{(0)}$. Soft interactions will be confined to the soft Wilson lines now showing up in the QCD currents giving rise to the jets, factorizing collinear and soft scales.

The Feynman rules obtained from the expansion of the Wilson lines at $\mathcal{O}(g)$ (one gluon attachment) are provided in appendix A.3.

[8] The respective Feynman rules will be given in appendix A.1.

Massless Factorization Theorem

The quark current operator represented in terms of SCET fields after BPS field redefinition is given by:

$$J^\mu_{C,n_1n_2}(x;p_1,p_2) = e^{i(p_1-p_2)\cdot x}\overline{\chi}^{(0)}_{n_1,p_1}(x)Y^\dagger_{n_1}(x)\Gamma^\mu_C Y_{n_2}(x)\chi^{(0)}_{n_2,p_2}(x) \tag{1.43}$$
$$= e^{-ix\cdot\mathcal{P}}\overline{\chi}^{(0)}_{n_1}(x)\delta_{p_1,\mathcal{P}^\dagger}\, Y^\dagger_{n_1}(x)\Gamma^\mu_C Y_{n_2}(x)\,\delta_{p_2,\mathcal{P}}\chi^{(0)}_{n_2}(x)\,,$$

where $\mathcal{P}^\dagger$ is the label momentum operator acting to the left and where we have introduced the jet fields:

$$\chi^{(0)}_n(x) \equiv W^{(0)\dagger}_n(x)\,\xi^{(0)}_n(x)\,, \tag{1.44}$$
$$\chi^{(0)}_{n,p}(x) \equiv \left(\hat{W}^{(0)\dagger}_n(x)\,\hat{\xi}^{(0)}_n(x)\right)_{n,p}(x) = \delta_{p,\mathcal{P}}\chi^{(0)}_n(x)\,,$$

referring the first line to the unhatted (sum of labeled) fields and the second to the labeled part [see Eq. (1.28)].

In order to compute an event-shape e distribution in SCET we just need to introduce the corresponding measurement delta $\delta(e-e(X))$ in Eq. (1.11) and match the QCD current onto the SCET renormalized operator[9]

$$\mathcal{J}^\mu_C(x) = \sum_{\vec{n}_1\vec{n}_2}\sum_{p_1\,p_2} C_{n_1n_2}(p_1,p_2;\mu)\,J^{\mu,\mathrm{ren}}_{C,n_1n_2}(x;p_1,p_2)\,. \tag{1.46}$$

This is the most general form of the matching between operators, depending on the two arbitrary collinear directions $\vec{n}_1$ and $\vec{n}_2$, but in the center of mass frame they are constrained to be back-to-back such that we can write:

$$\mathcal{J}^\mu_C(x) = \sum_{\vec{n}}\sum_{p_n\,p_{\overline{n}}} C_{n\overline{n}}(p_n,p_{\overline{n}};\mu)\,J^{\mu,\mathrm{ren}}_{C,n\overline{n}}(x;p_n,p_{\overline{n}})\,. \tag{1.47}$$

After several manipulations described in Ref. [23] one ends up with the following factorized formula for the event-shape differential cross-section at leading order in SCET:

$$\frac{1}{\sigma^C_0}\frac{\mathrm{d}\sigma^C_{\mathrm{SCET}}}{\mathrm{d}e} = H(Q,\mu)\int \mathrm{d}e'\,J(e-e',\mu)\,S(e',\mu)\,, \tag{1.48}$$

being $\sigma_0^{C=V,A}$ the total massless tree-level (Born) cross section which serves as a normalization. The different matrix elements entering the factorization are the hard function $H(Q,\mu)$, defined as the modulus square of the matching coefficient (which does not depend on the direction $\vec{n}$):

$$H(Q,\mu) \equiv |C_{n\overline{n}}(Q,-Q;\mu)|^2 \equiv |C(Q;\mu)|^2\ ; \tag{1.49}$$

the jet function $J(e,\mu)$, resulting from the convolution of the n and $\overline{n}$ hemisphere jet functions[10]

$$J(e,\mu) \equiv \int \mathrm{d}e'\,J_n(e-e',\mu)\,J_{\overline{n}}(e',\mu)\,, \tag{1.50}$$
$$J_n(e,\mu) = \frac{1}{4N_c}\int\frac{\mathrm{d}\ell^+}{2\pi}\,\mathrm{Tr}\int \mathrm{d}^dx\,e^{i\ell\cdot x}\,\langle 0|\,\overline{\not{n}}\chi_n(x)\,\delta(e-\hat{e}_n)\,\delta_{Q,\mathcal{P}^-}\,\overline{\chi}_n(0)|0\rangle^{\mathrm{ren}}\ ,$$
$$J_{\overline{n}}(e,\mu) = \frac{1}{4N_c}\int\frac{\mathrm{d}\ell^-}{2\pi}\,\mathrm{Tr}\int \mathrm{d}^dx\,e^{i\ell\cdot x}\,\langle 0|\,\overline{\chi}_{\overline{n}}(x)\not{n}\,\delta(e-\hat{e}_{\overline{n}})\,\delta_{-Q,\mathcal{P}^+}\,\chi_{\overline{n}}(0)|0\rangle^{\mathrm{ren}}\ ,$$

[9] Unlike the QCD current, the SCET operator is UV divergent. Therefore, one can consider that either the matching coefficient ($C = Z_C C^{\mathrm{bare}}$) or the SCET current ($J^{\mathrm{bare}} = Z_J J^{\mathrm{ren}}$) need multiplicative renormalization. Either way, the renormalization factor will remove the divergences from the computation, and one can derive the following relation:

$$\mathcal{J}_{QCD} = Z_C C J^{\mathrm{bare}} = Z_C C Z_J J^{\mathrm{ren}} = C J^{\mathrm{ren}}\,, \tag{1.45}$$

with $Z_C = Z_J^{-1}$. This relation leads to consistency conditions for the different running setups.

[10] From now on we omit the superscript $^{(0)}$ for BPS-redefined fields unless in cases when it can lead to confusion.

and the soft function:

$$S(e,\mu) = \frac{1}{N_c}\int \frac{\mathrm{d}^d r}{(2\pi)^d}\mathrm{Tr}\int \mathrm{d}^d x\, e^{ir\cdot x}\,\langle 0|\,\overline{Y}^\dagger_{\overline{n}}(x)Y^\dagger_n(x)\delta(e-\hat{e}_s)Y_n(0)\overline{Y}_{\overline{n}}(0)\,|0\rangle^{\mathrm{ren}}\ . \tag{1.51}$$

In the previous two equations, the trace is taken over spin and color indices, N_c is the number of colors, $\hat{e}_{n,\overline{n},s}$ pulls out the $n,\overline{n},s$ contribution to the event-shape from the final state: $\hat{e}_{n,\overline{n},s}|X\rangle = e_{n,\overline{n},s}(X)|X\rangle$ [see Eq. (1.13)] and $\overline{Y}_{\overline{n}}$ is the corresponding soft Wilson line involving soft gluon fields in the anti-adjoint representation:

$$\begin{aligned}\overline{Y}_{\overline{n}}(x) &= P\exp\left(ig\int_0^\infty \mathrm{d}s\,\overline{n}\cdot\overline{A}_s(\overline{n}s+x)\right)\ , \\ \overline{A}_s &\equiv A_{s,a}\overline{T}^a = -A_{s,a}\,(T^a)^* = -A_{s,a}\,(T^a)^T\ ,\end{aligned} \tag{1.52}$$

with $T^a = (T^a)^\dagger$ the SU(3) generators in the fundamental representation.

All matrix elements are evaluated at the same renormalization scale μ in the factorization theorem[11]

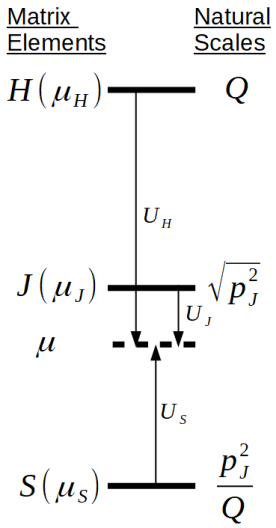

Figure 1.5: Renormalization group evolution for matrix elements in SCET massless factorization theorems. The U_i operators are the evolution kernels, μ_i stand for the renormalization scales, and the associated natural scales are shown on the right side, with p_J the jet momentum.

even though they have different typical scales: the natural scale for the hard function is the COM energy Q, for the jet function is the square root of the jet invariant mass[12] and for the soft function is the fraction of the jet off-shellness over the center of mass energy. Therefore, we need to use RGE in order to avoid the appearance of large logarithms, reproducing the running setup sketched in Fig. 1.5. Since the μ-dependence cancels in the factorization theorem (this is nothing less than the cancellation of the various renormalization factors), we can derive the following consistency condition for the running

[11] Formally, one can also consider all matrix elements unrenormalized (bare). Otherwise, they must be renormalized in the same scheme, typically $\overline{\mathrm{MS}}$, such that all renormalization factors cancel out.

[12] The jet constituents are the massless initialization quark (satisfying $p_q^2 = 0$) and other particles radiated from it such that, if they were exactly collinear, the jet momentum would become light-like: $p_J^2 = 0$.

kernels by setting different values for the final scale:

$$U_H(\mu_i \to \mu_f)\, U_J(\mu_i \to \mu_f) = U_S^{-1}(\mu_i \to \mu_f)\,. \tag{1.53}$$

This condition can be rephrased in terms of the cusp and non-cusp anomalous dimensions, that must add up to zero.

Massive quarks

Next we discuss the modifications of the factorization theorem when working with a non-vanishing quark mass. These depend on the massive quark being primary —that is the quark that produces the jet (in this case, always collinear)— or secondary, coming from gluon splitting (soft or collinear).

Beginning with the secondary quark mass case, the contribution starts at two loops from massive quark bubbles in the gluon propagators or real radiation from gluon splitting. This case was studied in Ref. [56], where a framework was established to include these corrections in the SCET factorization theorem under the name of Variable Flavor Number Scheme (VFNS for short), with the relevant computations for thrust also carried out.

There are four scenarios that account for the different scaling of the mass with respect to the hard, jet, and soft scales, represented in Fig. 1.6. Let's consider $\mathbb{M}^{n_\ell+n_h}_{n_\ell,n_h}(\mu_{\mathbb{M}})$, a generic matrix element with

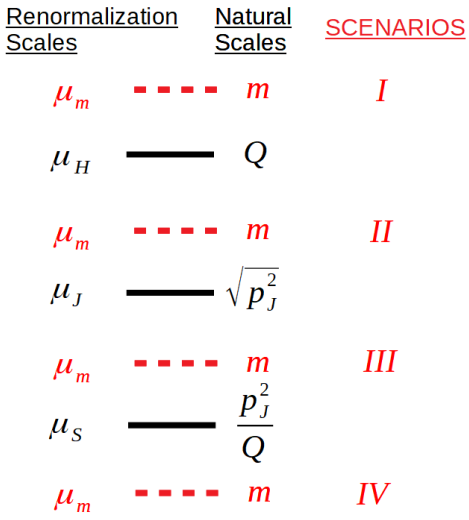

Figure 1.6: Scenarios taking into account the different scaling of the mass with respect to the hard, jet, and soft scales. The renormalization scales μ_i must be taken of the order of the corresponding natural scale to avoid the appearance of large logarithms in the fixed-order matrix elements.

contributions from n_h massive (heavy) quarks, and n_ℓ massless (light) quarks, expressed as a power series in α_s renormalized in $\overline{\text{MS}}$ with $n_\ell + n_h$ active flavors. We will also simplify the notation writing the renormalization and matchings as multiplicative in any case [even for jet and soft functions for which a convolution is actually required as can be seen in the factorization formula Eq. (1.48)].

- $\mu_{\mathbb{M}} > \mu_m$:

If the renormalization scale of the matrix element is above the mass scale, all massive quark effects must be taken into account. Furthermore, the heavy quark is an active flavor in the corresponding kernel and in the strong coupling. Finally, the $\overline{\rm MS}$ renormalized matrix element satisfies the massless limit.

$$\begin{aligned} \mathbb{M}^{n_\ell+1}_{n_\ell,1}(\mu_{\mathbb{M}} > \mu_m) &\equiv \mathbb{M}^{n_\ell+1}_{n_\ell,0} + \Delta\mathbb{M}_m \,, \\ \lim_{m\to 0} \mathbb{M}^{n_\ell+1}_{n_\ell,1}(\mu_{\mathbb{M}} > \mu_m) &= \mathbb{M}^{n_\ell+1}_{n_\ell+1,0} \,. \end{aligned} \tag{1.54}$$

- $\underline{\mu_{\mathbb{M}} < \mu_m}$:

  For a renormalization scale smaller than the mass scale, the heavy quark cannot be an active flavor any more, and has to be integrated out, leading to a matching coefficient $\mathcal{M}$:

$$\mu_{\mathbb{M}} \to \mu_m \implies \mathcal{M}^n \mathbb{M}^n_{n_\ell,1}(\mu_{\mathbb{M}} > \mu_m) = \mathbb{M}^n_{n_\ell,1}(\mu_{\mathbb{M}} < \mu_m) \,. \tag{1.55}$$

  The natural scale for the matching coefficient $\mathcal{M}^n$ is $\mu_m \sim m$, and can be expressed as a series in powers of α_s with n active flavors. There are two equivalent choices: $n = n_\ell$ and $n = n_\ell + 1$. Furthermore, the massive quark contribution must vanish when the value of the mass tends to infinity (decoupling limit) but nevertheless we can still retain these effects that disappear in this limit in order to impose a smooth transition between the different scenarios:

$$\mathbb{M}^{n_\ell}_{n_\ell,1}(\mu_{\mathbb{M}} < \mu_m) \equiv \mathbb{M}^{n_\ell}_{n_\ell,0} + (\Delta\mathbb{M}_m - \Delta\mathbb{M}_{m\to\infty}) \,. \tag{1.56}$$

Eq. (1.56) can be seen as an on-shell renormalization prescription for the bare matrix element:

$$\mathbb{M}^{\text{bare},n_\ell}_{n_\ell,1} = Z^{n_\ell}_{\text{OS}\,n_\ell,1}\, \mathbb{M}^{n_\ell}_{n_\ell,1}(\mu_{\mathbb{M}} < \mu_m) \,, \tag{1.57}$$

and the μ-dependence of this renormalization constant can be shown to be the same as for the $\overline{\rm MS}$ renormalization for massless quarks, that is:[13]

$$\begin{aligned} \mu\frac{\mathrm{d}Z^{n_\ell}_{\text{OS}\,n_\ell,1}}{\mathrm{d}\mu} &= \mu\frac{\mathrm{d}Z^{n_\ell}_{\overline{\text{MS}}\,n_\ell,0}}{\mathrm{d}\mu} \,, \\ \mathbb{M}^{\text{bare},n_\ell}_{n_\ell,0} &= Z^{n_\ell}_{\overline{\text{MS}}\,n_\ell,0}\mathbb{M}^{n_\ell}_{n_\ell,0} \,, \end{aligned} \tag{1.58}$$

so, indeed, $\mathbb{M}^{n_\ell}_{n_\ell,1}(\mu_{\mathbb{M}} < \mu_m)$ evolves as if it were $\overline{\rm MS}$ renormalized with n_ℓ active flavors. In addition, the matching $\mathcal{M}$ can also be obtained from the ratio of the renormalization constants in both schemes:

$$\mathcal{M}^n = \frac{Z^n_{\overline{\text{MS}}\,n_\ell,1}}{Z^n_{\text{OS}\,n_\ell,1}} \,, \qquad n = n_\ell,\, n_\ell + 1 \,, \tag{1.59}$$

where we have used $\mathbb{M}^{\text{bare},n_\ell+1}_{n_\ell,1} = Z^{n_\ell+1}_{\overline{\text{MS}}\,n_\ell,1}\, \mathbb{M}^{n_\ell+1}_{n_\ell,1}(\mu_{\mathbb{M}} > \mu_m)$ and Eqs. (1.55) and (1.57).

With the modifications introduced above, the setup for the evolution of the matrix elements in the factorization theorem will depend on the scenario and the value of the final μ. But, since the result is independent of this scale, we will have consistency conditions between the different matching coefficients $\mathcal{M}$. For instance, the two situations giving rise to such relation in scenario III are depicted in Fig. 1.7.

[13] Since $Z_{\overline{\text{MS}}}$ does not depend on the mass we have that all $Z_{\overline{\text{MS}}\,n_\ell,n_h}$ with the same value of $n_\ell + n_h$ are equivalent.

In the case of a massive primary quark, we also have massive collinear degrees of freedom in addition to the corrections due to massive bubbles discussed above, leading in scenarios III and IV to a massive jet function [now computed using the Lagrangian Eq. (1.37)] with $(p_J^2 - m^2)/m$ as its natural scale.

In this case, scenario II is given by the condition $m^2 \gg p_J^2 - m^2$ that leads to large logarithms in the jet function and therefore calls for another EFT known as boosted Heavy Quark Effective Theory (bHQET for short). As a remark, scenario I is not realizable for a primary quark since there is enough energy to produce the massive primary quarks.

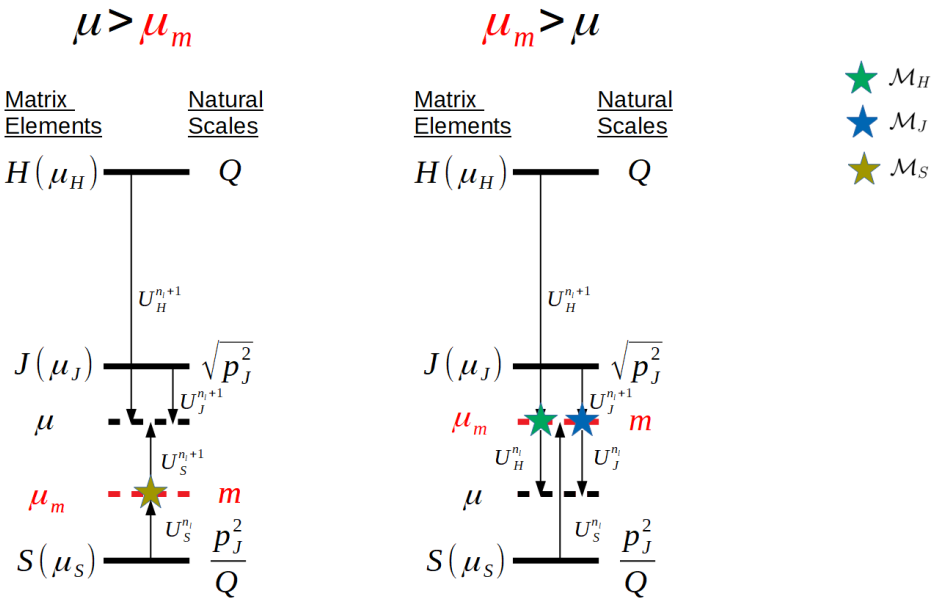

Figure 1.7: Running setups in scenario III leading to the consistency relation for the matching coefficients: $\mathcal{M}_H\,\mathcal{M}_J = \mathcal{M}_S^{-1}$

1.4.2 bHQET

bHQET accounts for fluctuations very close to the mass-shell of the primary quarks. It is built integrating out the mass of the primary quarks in their respective rest frames, which leads to two copies of Heavy Quark Effective Theory (HQET for short). Boosting them back to the COM frame and matching them onto SCET for the global soft radiation yields the bHQET Lagrangian.

HQET Lagrangian

In order to study the soft degrees of freedom around the heavy quark mass it is convenient to parametrize the heavy quark momentum as: $p = mv + k$ where $k \sim \Gamma(1,1,1)$ being Γ the decay width of the massive quark (let's say, the top quark) and $v = (1,1,0)$ the quark's velocity in the rest frame.
From the Dirac equation we obtain:

$$\not{p}\psi = m\psi \Longrightarrow (1 - \not{v})\psi \sim 0\,, \tag{1.60}$$

hence we can split the QCD Dirac spinor into large and small components:

$$\psi = \frac{1+\not{v}}{2}\psi + \frac{1-\not{v}}{2}\psi \equiv \psi_v + \overline{\psi}_v \,. \tag{1.61}$$

Finally, setting the small component $\overline{\psi}_v$ to zero and factoring out the mass contribution to the momentum:[14]

$$\psi_v \equiv e^{-imv\cdot x} h_v \,, \tag{1.62}$$

we get the leading order HQET Lagrangian:

$$\mathcal{L}_{\text{HQET}} = \overline{h}_v \, iv\cdot D \, \frac{1+\not{v}}{2} h_v \,. \tag{1.63}$$

Feynman rules for bHQET can be found in Appendix A.2.

Degrees of freedom (DOF for short) in bHQET

The scaling for the different degrees of freedom within bHQET and the corresponding HQET copies is summarized in Tab. 1.1. The soft fluctuations around the quark mass in HQET become ultra-collinear after the boost[15] and we have cross-talk between jets through soft radiation in the center of mass frame.

	REST FRAMES		bHQET	
	DOF	Scaling	DOF	Scaling
HQET_q	quark: $p = mv + k$	$v = (1,1,0)$	quark: $p = mv_+ + k_+$	$v_+ = \left(\frac{m}{Q}, \frac{Q}{m}, 0\right)$
	soft: k	$k \sim \Gamma\,(1,1,1)$	n-ucollinear: k_+	$k_+ \sim \Gamma\left(\frac{m}{Q}, \frac{Q}{m}, 1\right)$
$\text{HQET}_{\overline{q}}$	anti-quark: $p = mv + k$	$v = (1,1,0)$	anti-quark: $p = mv_- + k_-$	$v_- = \left(\frac{Q}{m}, \frac{m}{Q}, 0\right)$
	soft: k	$k \sim \Gamma\,(1,1,1)$	$\overline{n}$-ucollinear: k_-	$k_- \sim \Gamma\left(\frac{Q}{m}, \frac{m}{Q}, 1\right)$
			soft: q_s	$q_s \sim \frac{\Gamma m}{Q}\,(1,1,1)$

Table 1.1: Degrees of freedom involved in the construction of bHQET.

Factorization Theorem

The quark current takes the following form within bHQET:

$$J^\mu_{C\,\text{bHQET}} = \left(\overline{h}_{v_+} W_n\right) Y_n^\dagger \, \Gamma^\mu_C \, Y_{\overline{n}} \left(W_{\overline{n}}^\dagger h_{v_-}\right) , \tag{1.64}$$

where the soft Wilson lines remain as in SCET but collinear Wilson lines are now made of ultra-collinear gluons:

$$\begin{aligned} W_n(x) &= \overline{P} \exp\left(-ig\int_0^\infty \mathrm{d}s\, \overline{n}\cdot A_+(\overline{n}s + x)\right) , \\ W_{\overline{n}}^\dagger(x) &= P \exp\left(ig\int_0^\infty \mathrm{d}s\, n\cdot A_-(ns + x)\right) . \end{aligned} \tag{1.65}$$

[14] For now we assume the mass being factored is the pole mass.

[15] If only two back-to-back quarks are produced, their velocity equals $\beta = \sqrt{1-4\hat{m}^2} \simeq 1 - 2\hat{m}^2$, and therefore the boost factor reads $\gamma = 1/(2\hat{m})$. When boosting momenta in light-cone coordinates the plus/minus components get multiplied/divided by $\gamma(1-\beta) \simeq 1/\hat{m}$.

After matching the bHQET current onto its SCET counterpart:

$$J^{\mu}_{C\,\mathrm{SCET}} = C_m\, J^{\mu}_{C\,\mathrm{bHQET}}\,, \tag{1.66}$$

we obtain the differential cross-section in bHQET at leading power:

$$\frac{1}{\sigma_0^C}\frac{\mathrm{d}\sigma^C_{\mathrm{bHQET}}}{\mathrm{d}e} = H(Q,\mu_m)\, H_m\left(m,\frac{Q}{m},\mu_m,\mu\right)\int \mathrm{d}e'\, B\left(e-e',\mu\right)\, S(e',\mu)\,, \tag{1.67}$$

with $H(Q,\mu_m)$ and $S(e,\mu)$ the SCET hard and soft functions, respectively. Additionally, new bHQET hard and jet functions appear:

$$\begin{aligned} H_m &= |C_m|^2\,, \\ B(e,\mu) &\equiv \int \mathrm{d}e'\, B_n(e-e',\mu)\, B_{\overline{n}}(e',\mu)\,, \\ B_n(e,\mu) &= \frac{(2\pi)^{d-1}Q}{2mN_c}\mathrm{Tr}\,\langle 0|\, W_n^{\dagger}(0)\, h_{v_+}(0)\,\delta\left(e-\hat{e}_n\right)\,\delta^{(d-2)}(\vec{\mathcal{K}}^{\perp})\,\delta(\mathcal{K}^-)\,\overline{h}_{v_+}(0)\, W_n(0)\,|0\rangle^{\mathrm{ren}}\,. \end{aligned} \tag{1.68}$$

The corresponding running setup is represented in Fig. 1.8. Notice that since the (primary) quark mass

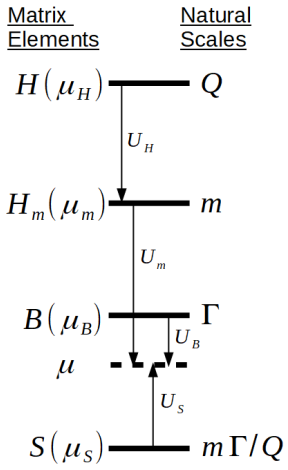

Figure 1.8: Renormalization group evolution for matrix elements in the bHQET factorization theorem. The U_i operators are the evolution kernels, μ_i are the renormalization scales. The associated natural scales are on the right side.

has been integrated out there is no contribution from massive (primary) quark bubbles to the bHQET jet and soft functions. All the (primary) quark mass dependence is located in the bHQET Hard function.

1.5 Mellin-Barnes representation

In the last section of this introductory Chapter we review the basics of the Mellin-Barnes representation, which is a useful tool employed in multi-loop computations that it will appear several times throughout this thesis although applied in a different way and for different purposes than, as far as we know, it has been done so far in the literature.

Given a function $f(x)$, its Mellin transform is defined as:

$$\hat{f}(h) \equiv [\,\mathcal{M}f\,](h) \equiv \int_0^\infty \mathrm{d}x\, x^{h-1}\, f(x)\,, \tag{1.69}$$

such that $\hat{f}(h)$ is convergent for $a < \mathrm{Re}(h) < b$. Then, the initial function can be recovered through the inverse Mellin transform:

$$[\,\mathcal{M}^{-1}\hat{f}\,](x) \equiv \frac{1}{2\pi i}\int_{c-i\infty}^{c+i\infty} \mathrm{d}h\, x^{-h}\, \hat{f}(h) = f(x)\,, \tag{1.70}$$

with $c \in (a,b)$. We also introduce the following identity:

$$\frac{1}{(1+x)^\nu} = \frac{1}{2\pi i}\int_{c-i\infty}^{c+i\infty} \mathrm{d}h\, x^{-h}\, \frac{\Gamma(h)\Gamma(\nu-h)}{\Gamma(\nu)}\,, \tag{1.71}$$

with $c \in (0,\nu)$, typically used to solve loop integrals and to obtain expansions in the different regimes given by the hierarchies between their scales [25]. The procedure to get the power series from the Mellin plane (converse mapping theorem) is based integrating by residues. The situation is similar to that depicted in Fig. 1.9, with the poles of the Mellin transform $\hat{f}(h)$ sitting at points $h = \xi$ along the real axis, and where the path of the inverse integral is also shown.

- **l.h.s:** if the Mellin transform satisfies $\lim_{h\to-\infty} h\, x^{-h}\, \hat{f}(h) = 0$, by Jordan's lemma we can close the contour to the left and use the residue theorem, leading to the small x expansion:

$$f(x) = \sum_{\xi,k} \frac{(-1)^k}{k!}\, a_{\xi,k}\, x^\xi \log^k(x)\,, \tag{1.72}$$

  where the logarithms are given by the poles with order higher than one.

- **r.h.s:** on the other hand, if $\lim_{h\to\infty} h\, x^{-h}\, \hat{f}(h) = 0$, the large x expansion is obtained closing the contour to the right:

$$f(x) = \sum_{\xi,k} \frac{(-1)^{k+1}}{k!}\, a_{\xi,k}\, x^{-\xi} \log^k(x)\,. \tag{1.73}$$

In the previous equations, the coefficients $a_{\xi,k}$ are the residues at the corresponding poles with multiplicity k, $\hat{f}(h) \sim \sum_k \frac{a_{\xi,k}}{(h-\xi)^{k+1}}$. Finally, it is also worth noting that the vanishing condition at infinity provides the convergence radius of the series.

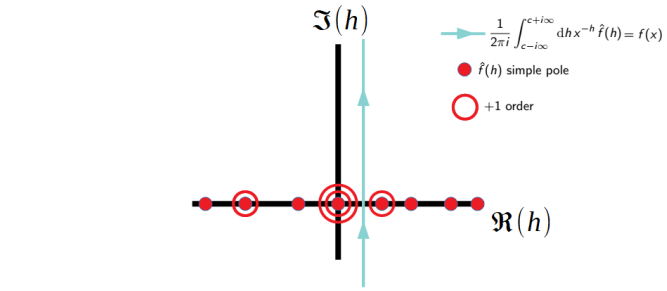

(a) Initial configuration

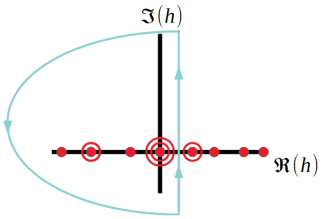

(b) Small x expansion

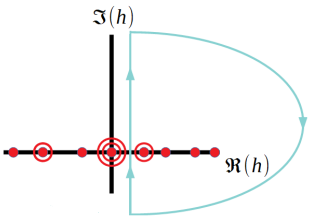

(c) Large x expansion

Figure 1.9: Converse mapping theorem.

Chapter 2

Event-shape schemes (Massive event-shape distributions at $\mathrm{N^2LL}$)

This Chapter is dedicated to study how the mass sensitivity of an event-shape distribution changes for different choices of the schemes used to treat the heavy quark mass in the corresponding event-shape definition. Firstly, we will show the equivalence of two of the schemes in the collinear limit, result that shall be used to compute the missing pieces to achieve $\mathrm{N^2LL} + \mathcal{O}(\alpha_s)$ accuracy in SCET and bHQET differential and cumulative cross-sections. The calculation will be carried out for thrust, heavy jet mass and C-parameter but it can be easily generalized to angularities and other event-shapes. We will also obtain analytical and fast-convergent expansion series for the resummation of the non-distributional parts, which otherwise would require a numerical integration, slowing down significantly the numerical code use to obtain the distributions. Finally, a numerical analysis for the thrust full distribution using our computations, based on SCET with resummation but also including power corrections and matching onto fixed-order QCD will be presented.

Let us begin, before introducing the schemes, by working out the decomposition Eq. (1.13) for the event-shapes we will be dealing with. Whereas this task is trivial for thrust, since it is already defined as single sum of final-state particle momenta [see Eq. (1.14)], if there are correlations among the various components one has to show this explicitly as it was done for C-parameter [see Eq. (1.15)] in Ref. [38]. This is also the case of heavy jet mass, defined as the largest hemisphere invariant mass normalized to the center of mass energy: $\rho \equiv s_+/Q^2$. For this shape variable we have:

$$Q^2\rho = \sum_{i\in+} p_i^+ \sum_{j\in+} p_j^- - \left(\sum_{i\in+} p_i^\perp\right)^2 = \sum_{i\in+} p_i^+ \sum_{j\in+} p_j^-, \tag{2.1}$$

where we assumed the thrust axis in the z-direction and used that the component of the total hemisphere momenta normal to the thrust axis is identically zero. We can take the negative direction of z-axis pointing towards the plus hemisphere so that it does not contain $\overline{n}$-collinear particles (with $p_z > 0$). Hence, in dijet limit we will have the following contributions:

Soft-Collinear: it has the following form at leading order $\mathcal{O}(\lambda^2)$:

$$Q^2\rho_s = \left(\sum_{j\in n} p_j^-\right)\left(\sum_{i\in s_+} p_i^+\right) \simeq 2\left(\sum_{j\in n} E_j\right)\left(\sum_{i\in s_+} p_i^+\right) \simeq Q\sum_{i\in s_+} p_i^+ = QP_{s_+}^+, \tag{2.2}$$

where s_+ denotes the soft particles in the plus hemisphere and we made use of the leading order approximations: $p_{j\in n}^- \simeq 2E_j$ and $\sum_{j\in n} E_j \simeq Q$.

Collinear-Collinear: analogously to the previous case, we have for the leading order $\mathcal{O}(\lambda^2)$:

$$Q\rho_n \simeq \sum_{i\in n} p_i^+ = P_n^+ \,. \tag{2.3}$$

Soft-Soft: from Eq. (2.1) and the power counting of soft particles we see that if particles i and j are soft the result is power suppressed $\mathcal{O}(\lambda^4)$.

All in all, the dijet limit of heavy jet mass is the total plus momentum in the hemisphere:

$$Q\overline{\rho} = Q\rho_n + Q\rho_s = P_n^+ + P_{s_+}^+ \,. \tag{2.4}$$

2.1 Massive schemes

If the final state contains only massless particles, one can interchange the energy and magnitude of its momentum, but whenever there are masses into play, this is no longer true. In this context, massive schemes are a generalization introduced in the event-shape definition for massive particles. They were initially considered to study the hadron mass effects on (soft) hadronization power corrections [59, 52] but, since only light quarks were included, they had no consequences for the partonic cross-section. The computation of the cross section at NLO in fixed-order was carried out in Ref. [48]. In this part of the thesis, we aim to complete the analysis by incorporating the resummation of the large logarithms that appear in the peak and tail regions.

Different ways of treating the energy E_p and momentum magnitude $|\vec{p}|$ of a massive particle lead to the three different massive schemes:

- **E-scheme:** is defined by the substitution of the momentum magnitude by the energy:

$$p = \left(p^0, \vec{p}\right) \to p_E = p^0 \left(1, \frac{\vec{p}}{|\vec{p}|}\right) . \tag{2.5}$$

  In this way, the scalar product becomes:

$$p_E \cdot q_E = p^0 q^0 \left(1 - \frac{\vec{p}\cdot\vec{q}}{|\vec{p}||\vec{q}|}\right) , \tag{2.6}$$

  and the E-scheme momentum square will vanish for massless as well as massive particles: $p_E^2 = 0$.

- **P-scheme:** the replacement is in this case the other way around, that is:

$$p = \left(p^0, \vec{p}\right) \to p_P = |\vec{p}| \left(1, \frac{\vec{p}}{|\vec{p}|}\right) , \tag{2.7}$$

  giving the following form for the scalar product:

$$p_P \cdot q_P = |\vec{p}||\vec{q}| - \vec{p}\cdot\vec{q} \tag{2.8}$$

  which again implies that the square is always zero: $p_P^2 = 0$.

- **M-scheme:** refers to definitions that contain both energy and momentum magnitude. It is the most sensitive to the mass because entails working with the actual four-momentum, which satisfies (for massive particles): $p^2 = m^2$.

	τ	C	ρ
E	$\frac{1}{Q}\min_{\hat{t}} \sum_i \frac{p_i^0}{\lvert\vec{p}_i\rvert}(\lvert\vec{p}_i\rvert - \lvert\hat{t}\cdot\vec{p}_i\rvert)$	$\frac{3}{2}\left[1 - \frac{1}{Q^2}\sum_{i,j}\frac{p_i^0 p_j^0 (\vec{p}_i\cdot\vec{p}_j)^2}{\lvert\vec{p}_i\rvert^2\lvert\vec{p}_j\rvert^2}\right]$	$\frac{1}{Q^2}\sum_{i,j\in \mathrm{h}}\frac{p_i^0 p_j^0(\lvert\vec{p}_i\rvert\lvert\vec{p}_j\rvert - \vec{p}_i\cdot\vec{p}_j)}{\lvert\vec{p}_i\rvert\lvert\vec{p}_j\rvert}$
P	$\frac{1}{Q_P}\min_{\hat{t}} \sum_i (\lvert\vec{p}_i\rvert - \lvert\hat{t}\cdot\vec{p}_i\rvert)$	$\frac{3}{2}\left[1 - \frac{1}{Q_P^2}\sum_{i,j}\frac{(\vec{p}_i\cdot\vec{p}_j)^2}{\lvert\vec{p}_i\rvert\lvert\vec{p}_j\rvert}\right]$	$\frac{1}{Q_P^2}\sum_{i,j\in \mathrm{h}}(\lvert\vec{p}_i\rvert\lvert\vec{p}_j\rvert - \vec{p}_i\cdot\vec{p}_j)$
M	$\frac{1}{Q}\min_{\hat{t}} \sum_i (p_i^0 - \lvert\hat{t}\cdot\vec{p}_i\rvert)$	$\frac{3}{2}\left[2 - \frac{1}{Q^2}\sum_{i\neq j}\frac{(p_i\cdot p_j)^2}{p_i^0 p_j^0}\right]$	$\frac{1}{Q^2}\left(\sum_{i\in h} p_i\right)^2$

Table 2.1: Thrust, C-parameter and hemisphere jet mass in the three massive schemes. We show in green the original definitions. The P-scheme normalization is $Q_P \equiv \sum_i |\vec{p}_i|$, and h is the heaviest hemisphere of the ones of delimited by the plane normal to the thrust axis $\hat{t}$

It is worth mentioning that, since the energy and momentum are frame dependent, the cases described above refer to quantities defined in the COM frame which is usually chosen for most event-shapes definitions. As a final remark, the light-cone decomposition in Eq. (1.17) applies and the collinear and soft scaling remain the same for any of the schemes. The original definitions, along with the generalizations for thrust, Heavy Jet Mass and C-parameter, are given in Tab. 2.1. For other event-shapes see Appendix D of Ref. [48].

2.1.1 Mass Sensitivity

When studying the sensitivity of event shapes at parton level[1] the leading order contribution for e^+e^- annihilation comes from the production of a heavy quark-antiquark pair without additional radiation. In this case, the thrust axis is parallel to the three-momenta of the quarks, which makes trivial to calculate the event-shape value for two particles in the final state with equal mass m. Moreover, this simple computation sets the minimum value even if additional gluons and (massless) quarks are radiated.

	τ	C	ρ
M-scheme	$1-\beta$	$12\hat{m}^2(1-\hat{m}^2)$	$\hat{m}^2$
P- and E- schemes	0	0	0

Table 2.2: Minimum value for the considered event shapes in the case of primary production of a stable quark-antiquark pair in different massive schemes. Here $\beta = \sqrt{1-4\hat{m}^2}$ stands for the velocity of the quarks at this limit in natural units and $\hat{m} \equiv m/Q$ the reduced mass.

The results in Tab. 2.2 show that for events in which a massive stable quark-antiquark pair is produced (*primary production*) only the M-scheme is sensitive to the quark mass while P- and E-schemes are not. In most of the events there will be some extra radiation present which will modify the former dijet into two fatter jets or an even more isotropic momentum distributions. For the observables we study, such processes will mainly contribute for event-shape values away from the lower limit adding subleading mass sensitivity (i.e. suppressed by a factor of α_s) even in the P- and E-schemes, but will not substantially change the leading sensitivity of the M-scheme definition since it comes from the tree-level peak position. From this we can conclude that the M-scheme is preferred if the aim is a mass-sensitive

[1] We consider for now partonic final states, assuming stable massive quarks.

observable (e.g. for quark mass determinations), but in case that one seeks a mass-insensitive observable, the P- and E-schemes are a better choice.[2]

2.1.2 Massive Schemes in the Collinear Limit

At N^{2}LL order, the only modification of the SCET factorization theorem caused by massive primary quarks is confined to the jet function. Therefore, in this Chapter we compute the jet function at $\mathcal{O}(\alpha_s)$. The first step is then working out the collinear measurement for the event-shapes under consideration but let us first analyze the differences between schemes at this limit. Recalling the scalings[3]:

$$p, p_E, p_P \sim p_n \sim (\lambda^2, 1, \lambda)\,, \qquad m \sim \lambda\,. \tag{2.9}$$

One can show that the large components p^-, $p^\perp$ are equivalent at leading order in the three schemes since swapping energy and momentum magnitude causes only a power suppressed effect, that is:

$$\left.\begin{aligned} p^0 &= (p^+ + p^-)/2 \simeq p^-/2 + \mathcal{O}(\lambda^2) \\ |\vec{p}| &= \sqrt{(p^0)^2 - m^2} \simeq p^-/2 + \mathcal{O}(\lambda^2) \end{aligned}\right\} \Longrightarrow p^0 = |\vec{p}| + \mathcal{O}(\lambda^2) \overset{\text{LO}}{\Longrightarrow} \boxed{\begin{aligned} p^- &= p_E^- = p_P^- \\ p^\perp &= p_E^\perp = p_P^\perp \end{aligned}}\,.$$

From the previous statement we can also see that the E-scheme ($Q = \sum_i p_i^0$) and P-scheme ($Q_p \equiv \sum_i |\vec{p}_i|$) normalizations will take the same value in the collinear limit. Therefore, differences among the three schemes can only be caused by the small components p^+, p_E^+, p_P^+ which take the following form (for n-collinear particles the z component of momenta is negative):

$$\left.\begin{aligned} p^+ &= p^0 + p_z = p^0 - \sqrt{|\vec{p}|^2 - |\vec{p}_\perp|^2} \simeq \frac{p_\perp^2 + m^2}{2p^0} + \mathcal{O}(\lambda^4) \\ p_P^+ &= |\vec{p}| + p_z = |\vec{p}| - \sqrt{|\vec{p}|^2 - |\vec{p}_\perp|^2} \simeq \frac{|\vec{p}_\perp|^2}{2p^0} + \mathcal{O}(\lambda^4) \\ p_E^+ &= p^0 + \frac{p^0}{|\vec{p}|}\, p_z = \frac{p^0}{|\vec{p}|}\, p_P^+ \simeq p_P^+ + \mathcal{O}(\lambda^4) \end{aligned}\right\} \overset{\text{LO}}{\Longrightarrow} \boxed{p_P^+ = p_E^+ = p^+ - \tfrac{m^2}{p^-}}\,.$$

It is important to notice that in general $p_P^+ \neq p^+$ because $m^2/(p^+p^-) \simeq \mathcal{O}(1)$. Moreover, this mass term (and in any other that appears in an event-shape measurement function) comes from kinematic on-shell considerations and us such it corresponds to the pole scheme.

Since from the previous discussion we obtained for collinear particles (in any direction) $p_P^\mu = p_E^\mu$ at leading power, we can safely conclude that at this order the collinear measurements for all event shapes take the same form in the P- and E-schemes, but is in general different from the M-scheme. We will use this result to determine the explicit expressions for thrust, heavy jet mass and C-parameter:

Thrust

The original thrust definition is already in the P-scheme as showed in Tab. 2.1. For n-collinear particles one has $|\hat{t}\cdot\vec{p}_i| = -p_z$ and therefore up to power corrections we have:

$$Q\tau_c^P = Q\tau_c^E = \sum_{i\in+} p_{P,i}^+ = \sum_{i\in+}\left(p_i^+ - \frac{m_i^2}{p_i^-}\right), \tag{2.10}$$

[2] If the massive partons enter the final state via gluon splitting in a massive quark-antiquark pair (that is, through secondary production) the sensitivity to the quark mass will again be subleading (now suppressed by a factor of α_s^2).

[3] We omit in this section the overall factor of Q in the scaling for clarity.

where we already indicate that the collinear measurement is the same in the E-scheme. On the other hand, the collinear limit of the M-scheme generalization of thrust, also known as 2-jettiness, is the total plus momentum flowing into the plus hemisphere:

$$Q\tau_c^J = \sum_{i\in+} p_i^+ \,. \tag{2.11}$$

Since the measurement is completely inclusive, the computation of the jet function can be carried out as the discontinuity of a forward-scattering matrix element. This is not the case for the E- and P-schemes if quark masses are non-vanishing.

Heavy Jet Mass

We already worked out the collinear measurement for heavy jet mass in Eq. (2.3), and getting the P-scheme measurement is equally simple since Eq. (2.1) still applies with minimal modifications:

$$Q^2\rho^P = \left(\sum_{i\in+}|\vec{p}_i|\right)^2 - \left(\sum_{i\in+}p_i^z\right)^2 = \left[\sum_{i\in+}(|\vec{p}_i| + p_i^z)\right]\left[\sum_{j\in+}(|\vec{p}_j| - p_j^z)\right] = \sum_{i\in+}p_{P,i}^+\sum_{j\in+}p_{P,j}^- \,, \tag{2.12}$$

where we once again had use that the total perpendicular momentum vanishes and the identity $a^2 - b^2 = (a+b)(a-b)$. With this result we can trivially obtain the collinear measurement using that $p_{P,j}^- = 2p_j^0 + \mathcal{O}(\lambda^2)$:

$$Q\rho_c^P = Q\rho_c^E = \sum_{i\in+}\left(p_i^+ - \frac{m_i^2}{p_i^-}\right), \tag{2.13}$$

that matches the P-scheme thrust result. The total perpendicular momentum does not vanish in the E-scheme, since there is not such thing as E-scheme three-momentum conservation (in the same way, P-scheme energy is not conserved either). However, in the dijet limit the perpendicular components are already $\mathcal{O}(\lambda)$ and therefore $p_E^\perp = p^\perp + \mathcal{O}(\lambda^3)$, making $\sum_{i\in+}p_{E,i}^\perp \propto \mathcal{O}(\lambda^3)$, thence power suppressed, such that the result in Eq. (2.13) is also valid for the E-scheme.

C-parameter

From the C-parameter original definition in the P-scheme, as shown in Tab. 2.1, we get:

$$\begin{aligned} C^P &= \frac{3}{2Q_P^2}\sum_{i,j}|\vec{p}_i||\vec{p}_j|\sin^2(\theta_{ij}) = \frac{3}{2Q_P^2}\sum_{i,j}|\vec{p}_i||\vec{p}_j|[1+\cos(\theta_{ij})][1-\cos(\theta_{ij})] \\ &= \frac{3}{2Q_P^2}\sum_{i,j}\frac{(|\vec{p}_i||\vec{p}_j| + \vec{p}_i\cdot\vec{p}_j)(|\vec{p}_i||\vec{p}_j| - \vec{p}_i\cdot\vec{p}_j)}{|\vec{p}_i||\vec{p}_j|}\,, \end{aligned} \tag{2.14}$$

where we simply use $\sin^2(\theta_{ij}) = 1 - \cos^2(\theta_{ij}) = [1+\cos(\theta_{ij})][1-\cos(\theta_{ij})]$ and the definition of the euclidean scalar product to get to the final form. Next one can express the result in terms of P-scheme light-cone coordinates using Eq.s (2.8) and (1.17) as follows:

$$\begin{aligned} C^P &= \frac{3}{2Q_P^2}\sum_{i,j}\frac{(2|\vec{p}_i||\vec{p}_j| - p_{P,i}\cdot p_{P,j})\,p_{P,i}\cdot p_{P,j}}{|\vec{p}_i||\vec{p}_j|} \\ &= \frac{3}{2Q_P^2}\sum_{i,j}\frac{(p_{P,i}^+p_{P,j}^+ + p_{P,i}^-p_{P,j}^- + 2\vec{p}_{\perp,i}\cdot\vec{p}_{\perp,j})(p_{P,i}^+p_{P,j}^- + p_{P,i}^-p_{P,j}^+ - 2\vec{p}_{\perp,i}\cdot\vec{p}_{\perp,j})}{(p_{P,i}^+ + p_{P,i}^-)(p_{P,j}^+ + p_{P,j}^-)}\,, \end{aligned} \tag{2.15}$$

with a similar result in the E-scheme. We first consider that both i and j are n-collinear such that the SCET scaling implies

$$C_{nn}^P = \frac{3}{Q^2}\left[\left(\sum_{i\in n} p_{P,i}^+\right)\left(\sum_{j\in n} p_{P,j}^-\right) - \left(\sum_{i\in n} \vec{p}_{\perp,i}\right)\cdot\left(\sum_{j\in n} \vec{p}_{\perp,j}\right)\right] = \frac{3}{Q}\sum_{i\in n} p_{P,i}^+ + \mathcal{O}(\lambda^3)\,, \tag{2.16}$$

where once again we use that the total collinear perpendicular momenta flowing into the plus hemisphere is zero up to power corrections. For $C_{\bar{n}\bar{n}}^P$ one gets analogously:

$$C_{\bar{n}\bar{n}}^P = \frac{3}{Q}\sum_{i\in \bar{n}} p_{P,i}^+ + \mathcal{O}(\lambda^3)\,, \tag{2.17}$$

while if i is n-collinear and j is $\bar{n}$-collinear we get (we already include a factor of 2 to account for the case in which i is $\bar{n}$-collinear and j is n-collinear)

$$\begin{aligned} C_{n\bar{n}}^P &= \frac{3}{Q^2}\left[\left(\sum_{i\in n} p_{P,i}^+\right)\left(\sum_{j\in \bar{n}} p_{P,i}^+\right) + \left(\sum_{i\in n} p_{P,i}^-\right)\left(\sum_{j\in \bar{n}} p_{P,i}^-\right) + 2\left(\sum_{i\in n} \vec{p}_{\perp,i}\right)\cdot\left(\sum_{j\in \bar{n}} \vec{p}_{\perp,j}\right)\right] \\ &= \frac{3}{Q}\left(\sum_{i\in n} p_{P,i}^+ + \sum_{i\in \bar{n}} p_{P,i}^-\right) + \mathcal{O}(\lambda^3)\,. \end{aligned} \tag{2.18}$$

Summing up the contributions in Eqs. (2.16) and (2.18) we obtain the collinear and anti-collinear measurements in the P-scheme:

$$C_{nn}^P + C_{\bar{n}\bar{n}}^P + C_{n\bar{n}}^P = \frac{6}{Q}\left(\sum_{i\in n} p_{P,i}^+ + \sum_{i\in \bar{n}} p_{P,i}^-\right) \equiv C_c^P + C_{\bar{c}}^P\,, \tag{2.19}$$

and hence the result is identical to that of thrust or the hemisphere masses up to a factor of 6:

$$QC_c^P = QC_c^E = 6\sum_{i\in +} p_{P,i}^+ = 6\sum_{i\in +}\left(p_i^+ - \frac{m_i^2}{p_i^-}\right). \tag{2.20}$$

For the M-scheme, also called C-jettiness, the procedure is similar. From the definition in Tab. 2.1 we can write:

$$\begin{aligned} C^J &= \frac{3}{2Q^2}\left[2Q^2 - \sum_{i\neq j}\frac{(p_i\cdot p_j)^2}{p_i^0 p_j^0}\right] = \frac{3}{2Q^2}\sum_{i,j}\frac{1}{p_i^0 p_j^0}\left[2(p_i\cdot p_j)p_i^0 p_j^0 - (p_i\cdot p_j)^2(1-\delta_{ij})\right] \\ &= \frac{3}{2Q^2}\sum_{i,j}\frac{1}{p_i^0 p_j^0}\left[(p_i\cdot p_j)(2p_i^0 p_j^0 - p_i\cdot p_j) + \delta_{ij} m_i^4\right]\,, \end{aligned} \tag{2.21}$$

where we used $Q^2 = \left(\sum_i p_i\right)^2 = \sum_{i,j} p_i\cdot p_j$. Switching to light-cone coordinates and neglecting the mass term since it is $\mathcal{O}(\lambda^4)$ we get the same result as in the second line of Eq. (2.15) but with actual four-momenta. Applying the corresponding power counting leads to:

$$QC_c^J = 6\sum_{i\in +} p_i^+\,. \tag{2.22}$$

Therefore, for the reduced C-parameter variable $\widetilde{C} \equiv C/6$ the collinear measurement for the three event shapes we consider coincide in every massive scheme.

2.2 Factorization Theorems

In this section we will take a deeper look at the already introduced factorization theorems. The discussion will be carried out considering the case of thrust (in either massive scheme) but it can be easily adapted to C-parameter (changing the soft function and taking into account factors of 6 in the measurement function) or heavy jet mass (using the hemisphere jet and soft functions, and including two convolutions, one per hemisphere).

It is worth mentioning that the factorization formulas already given in Secs. 1.4.1 and 1.4.2, and those that shall be discussed next, stand for the leading order partonic distribution in the corresponding EFT. Nevertheless, the leading hadronization corrections (which are soft) can also be factorized as an extra convolution with the so-called shape function, which will be included in the numerical analysis. Additionally, we will include kinematic and mass power corrections in the final analysis, but their discussion is postponed until Sec. 2.7.

2.2.1 SCET

Even though the heavy quark mass is a parameter with a fixed value, the jet and soft scales depend on the event-shape value and therefore they change along the spectrum, such that several scenarios might occur in a given distribution. For simplicity, we assume the quark mass is always smaller than the soft scale, such that we stay in scenario IV even in the peak of the distribution.[4] In this way, we avoid having to deal with integrating out the heavy quark mass and the partonic factorization formula reads:[5].

$$\frac{1}{\sigma_0}\frac{\mathrm{d}\hat{\sigma}_{\mathrm{SCET}}}{\mathrm{d}\tau} = Q^2 H(Q,\mu)\int_0^{Q(\tau-\tau_{\min})} \mathrm{d}\ell\, J_\tau(Q^2\tau - Q\ell,\mu) S_\tau(\ell,\mu)\,, \tag{2.23}$$

with the thrust jet function being the convolution of two single-hemisphere jet functions:

$$J_\tau(s,\mu) \equiv \int_{s_{\min}}^{s-s_{\min}} \mathrm{d}s' J_n(s-s',\mu) J_n(s',\mu)\,. \tag{2.24}$$

The M-scheme hemisphere jet function has support for $s > s_{\min} = m^2$, that sets the integration limits in Eq. (2.24). Accordingly, the thrust jet function has support for $s > 2s_{\min}$, implying that the minimal value for 2-jettiness is $\tau^J_{\min} = 2\hat{m}^2$. We shall present the computation of the missing piece of the factorization theorem, which is the P-scheme jet function, in Sec. 2.3 where we also will carry out the calculation for the known M-scheme result as a benchmark and sanity check.

The factorization formula takes a simpler form in Fourier space:

$$\frac{1}{\sigma_0}\frac{\mathrm{d}\hat{\sigma}_{\mathrm{SCET}}}{\mathrm{d}\tau} = \frac{Q}{2\pi} H(Q,\mu)\int \mathrm{d}x\, e^{ixp}\tilde{J}_\tau\left(\frac{x}{Q},\mu\right)\tilde{S}_\tau(x,\mu)\,, \tag{2.25}$$

with $p = Q(\tau-\tau_{\min})$ and $\tilde{J}_\tau$ and $\tilde{S}$ the Fourier transforms of the jet and soft functions, respectively. The thrust jet function in position space is the square of its hemisphere counterpart, and can be computed as follows

$$\tilde{J}_\tau(y,\mu) = \int_0^\infty \mathrm{d}\bar{s}\, e^{-i\bar{s}y} J_\tau(\bar{s}+2s_{\min},\mu) = \tilde{J}_n(y,\mu)^2\,. \tag{2.26}$$

[4] Strictly speaking, the SCET counting $m \sim Q\lambda$ only applies in Scenarios II and III: in Scenario I no massive collinear particle can be produced while in IV the mass can be power-counted away. In practice the $m \to 0$ limit is smooth and using the counting $m \lesssim Q\lambda$ in Scenario IV captures some power corrections that make the transition between Scenarios III and IV smooth.

[5] We have rearranged the Q factors with respect to Eq. (1.48) in order to match the units of the arguments of the soft and jet functions in the original articles, Refs. [23, 24].

The form and solution of the renormalization group equations is also simpler in position space. Using those and changing variables to $y = px$ one arrives at

$$\frac{1}{\sigma_0}\frac{\mathrm{d}\hat{\sigma}_{\mathrm{SCET}}}{\mathrm{d}\tau} = \frac{H(Q,\mu_H)}{p}\left(\frac{e^{\gamma_E}\mu_S}{p}\right)^{\tilde{\omega}} R(Q,\mu_i)\int\frac{\mathrm{d}y}{2\pi}\, e^{iy}(iy)^{\tilde{\omega}}\tilde{J}_\tau\Big(\frac{y}{Qp},\mu_J\Big)\tilde{S}_\tau\Big(\frac{y}{p},\mu_S\Big)\,, \tag{2.27}$$

where μ_i denotes collectively all renormalization scales (including the common μ) which now satisfy $\mu_H \sim Q$, $\mu_J \sim Q\sqrt{\tau}$ and $\mu_S \sim Q\tau$, such that for small τ there is a strict hierarchy among those: $\mu_H > \mu_J > \mu_S$ and the SCET scaling parameter takes the value $\lambda \sim \sqrt{\tau}$. These are the same scaling as in Fig. 1.5 but expressed in terms of the event shape thrust.[6] We also used the following compact notation

$$\begin{aligned}
R(Q,\mu_i) &= Q\left(\frac{\mu_H}{Q}\right)^{-2\tilde{\omega}_H} e^{\tilde{k}}\left(\frac{\mu_J^2}{Q\mu_S}\right)^{\tilde{\omega}_J}\,, \\
\tilde{k} &= \tilde{k}_H + \tilde{k}_J + \tilde{k}_S\,, & \tilde{\omega} &= \tilde{\omega}_J - 2\tilde{\omega}_S\,, \\
\tilde{\omega}_S &= \tilde{\omega}_{\Gamma_c}(\mu_S,\mu), & \tilde{\omega}_J &= \tilde{\omega}_{\Gamma_c}(\mu_J,\mu), \\
\tilde{\omega}_H &= \tilde{\omega}_{\Gamma_c}(\mu_H,\mu)\,, & \tilde{k}_S &= \tilde{\omega}_{\gamma_S}(\mu_S,\mu) - 2\tilde{k}_{\Gamma_c}(\mu_S,\mu)\,, \\
\tilde{k}_H &= \tilde{\omega}_{\gamma_H}(\mu_H,\mu) - 2\tilde{k}_{\Gamma_c}(\mu_H,\mu)\,, & \tilde{k}_J &= \tilde{\omega}_J(\mu_J,\mu) + 4\tilde{k}_{\Gamma_c}(\mu_J,\mu)\,,
\end{aligned} \tag{2.28}$$

with $\tilde{\omega}$ and $\tilde{k}$ the exponential running kernels defined in terms of integrals over the SCET and QCD anomalous dimensions as follows

$$\begin{aligned}
\tilde{\omega}_\gamma(\mu_0,\mu) &= 2\int_{\alpha_0}^{\alpha_\mu}\mathrm{d}\alpha\,\frac{\gamma(\alpha)}{\beta_{\mathrm{QCD}}(\alpha)}\,, \\
\tilde{k}_\gamma(\mu_0,\mu) &= 2\int_{\alpha_0}^{\alpha_\mu}\mathrm{d}\alpha\,\frac{\gamma(\alpha)}{\beta_{\mathrm{QCD}}(\alpha)}\int_{\alpha_0}^{\alpha}\mathrm{d}\alpha'\frac{1}{\beta_{\mathrm{QCD}}(\alpha')}\,.
\end{aligned} \tag{2.29}$$

Here γ can refer to cusp or non-cusp anomalous dimensions, and their dependence on α is in the form of perturbative series that define their respective coefficients

$$\beta_{\mathrm{QCD}}(\alpha) = -2\,\alpha_s\sum_{n=1}\beta_{n-1}\Big(\frac{\alpha}{4\pi}\Big)^n, \quad \Gamma_{\mathrm{cusp}}(\alpha) = \sum_{n=1}\Gamma_n\Big(\frac{\alpha}{4\pi}\Big)^n, \quad \gamma(\alpha) = \sum_{n=1}\gamma_n\Big(\frac{\alpha}{4\pi}\Big)^n. \tag{2.30}$$

The integrals in Eq. (2.29) can be solved analytically in terms of the anomalous-dimension coefficients if an expansion in α_s is carried out and their explicit form up to N^{3}LL can be found e.g. in Ref. [1].

The jet function of a massive quark contains terms which are distributions, and hence easy to Fourier transform, plus others which are regular functions. Up to one loop, the momentum-space hemisphere jet function can be decomposed in the following form:

$$\begin{aligned}
J_n(\bar{s}+s_{\min},\mu) &= \delta(\bar{s}) + \frac{\alpha_s(\mu)}{4\pi}C_F\Big[J_{\mathrm{dist}}(\bar{s},\mu) + \frac{1}{m^2}J_{\mathrm{nd}}\Big(\frac{\bar{s}}{m^2}\Big)\Big] + \mathcal{O}(\alpha_s^2)\,, \\
J_{\mathrm{dist}}(\bar{s},\mu) &= \frac{1}{\mu^2}J_{m=0}\Big(\frac{\bar{s}}{\mu^2}\Big) + \frac{1}{m^2}J_m\Big(\frac{\bar{s}}{m^2}\Big)\,,
\end{aligned} \tag{2.31}$$

where the massive corrections, either with distributions J_m or fully non-distributional J_{nd}, are μ-independent dimensionless functions with support for positive values of their (dimensionless) arguments. The μ dependence of J_{dist} is entirely determined from the jet and QCD anomalous dimensions, does not depend

[6] Notice that the hemisphere jet mass s is the square of the jet momentum p_J^2 and in the dijet region it satisfies $s_c \simeq Q^2\tau_c$.

on the quark mass, and therefore can be fully accounted for in the massless jet function of Eq. (2.31).

The integral in Eq. (2.27) can be easily solved for all terms involving only distributions and for the non-distributional piece of the jet function we carry out resummation in momentum space. At one loop it is multiplied by the hard and soft functions at tree-level only so using Eq. (2.26) in (2.27) and carrying out the y integration, the non-distributional part of the 1-loop partonic cross section reads

$$\begin{aligned}\frac{1}{\sigma_0}\frac{\mathrm{d}\hat{\sigma}_{\rm nd}}{\mathrm{d}\tau} &= \frac{C_F\alpha_s(\mu_J)}{2\pi}\frac{R(Q,\mu_i)}{Q\hat{m}^2\Gamma(-\tilde{\omega})}(Qe^{\gamma_E}\mu_S)^{\tilde{\omega}}\int_{2s_{\rm min}}^{Q^2\tau}\mathrm{d}s\, J_{\rm nd}\Big(\frac{s-2s_{\rm min}}{m^2}\Big)(Q^2\tau-s)^{-1-\tilde{\omega}} \\ &= \frac{C_F\alpha_s(\mu_J)}{2\pi}\frac{R(Q,\mu_i)}{Q\hat{m}^2}\left[\frac{\mu_S e^{\gamma_E}}{Q(\tau-\tau_{\rm min})}\right]^{\tilde{\omega}} I_{\rm nd}\Big(\tilde{\omega},\frac{\tau-\tau_{\rm min}}{\hat{m}^2}\Big)\,, \\ I_{\rm nd}(\tilde{\omega},y) &= \frac{y^{\tilde{\omega}}}{\Gamma(-\tilde{\omega})}\int_0^y \mathrm{d}x\,(y-x)^{-1-\tilde{\omega}}J_{\rm nd}(x) = \frac{1}{\Gamma(-\tilde{\omega})}\int_0^1 \mathrm{d}z\,(1-z)^{-1-\tilde{\omega}}J_{\rm nd}(zy)\,.\end{aligned} \tag{2.32}$$

The lower limit of integration in the first line has been moved to $2s_{\rm min}$ since below that value the jet function has no support. In the E- and P-schemes $s_{\rm min}=0$ so we have not lost any generality. To get to the second line we have switched variables in the integral to $s=xm^2+2s_{\rm min}$, and to obtain the second expression for $I_{\rm nd}(\tilde{\omega},y)$ we switch variables to $x=zy$. For the partonic cumulative distribution one gets instead

$$\begin{aligned}\hat{\Sigma}_{\rm nd}(\tau_c) &\equiv \frac{1}{\sigma_0}\int_0^{\tau_c}\mathrm{d}\tau\,\frac{\mathrm{d}\sigma_{\rm nd}}{\mathrm{d}\tau} \\ &= \frac{C_F\alpha_s(\mu_J)}{2\pi}\frac{R(Q,\mu_i)}{\hat{m}^2}\frac{\mu_S e^{\gamma_E}}{Q}\left[\frac{\mu_S e^{\gamma_E}}{Q(\tau_c-\tau_{\rm min})}\right]^{\tilde{\omega}-1} I_{\rm nd}\Big(\tilde{\omega}-1,\frac{\tau_c-\tau_{\rm min}}{\hat{m}^2}\Big).\end{aligned} \tag{2.33}$$

To make the function $I(\tilde{\omega},y)$ smooth in the no resummation limit, achieved when $\tilde{\omega}\to 0$, one can integrate by parts to obtain

$$I_{\rm nd}(\tilde{\omega},y) = \frac{1}{\Gamma(1-\tilde{\omega})}\left[y\int_0^1 \mathrm{d}z(1-z)^{-\tilde{\omega}}J'_{\rm nd}(zy)+J_{\rm nd}(0)\right], \tag{2.34}$$

with $J'_{\rm nd}$ the derivative of the $J_{\rm nd}$ function. This form is particularly useful if the integration has to be carried out numerically, making it more convergent and defining its analytic continuation to values $0<\tilde{\omega}<1$. Further integration by parts can be implemented to define the integral for even larger values of $\tilde{\omega}$. Nevertheless, this procedure is unnecessary if a closed analytical form is found.

The discussion in this section has been carried out assuming the pole mass for the heavy quark, but we can express the result as a function of a short-distance mass by introducing the power series in α_s for the difference of both schemes. In the scenarios in which SCET applies, the $\overline{\rm MS}$ scheme is perfectly adequate. In scenario II it is more convenient to employ low-scale short-distance schemes such as the MSR mass [36, 37].

2.2.2 bHQET

The need for using this effective theory in Scenario II for massive primary quarks can be seen in a practical way by looking at the structure of the one-loop jet function in Eq. (2.31). Since the non-distributional terms are power suppressed when $s\to s_{\rm min}$, it is enough to focus on the terms with

distributions,[7] which generically read

$$\frac{1}{\mu^2}J_{m=0}\Big(\frac{\bar{s}}{\mu^2}\Big) = A\,\delta(\bar{s}) + \frac{B}{\mu^2}\left[\frac{\mu^2}{\bar{s}}\right]_+ + \frac{C}{\mu^2}\left[\frac{\mu^2\log(\bar{s}/\mu^2)}{\bar{s}}\right]_+,$$
$$\frac{1}{m^2}J_{m}\Big(\frac{\bar{s}}{m^2}\Big) = A_m\,\delta(\bar{s}) + \frac{B_m}{m^2}\left[\frac{m^2}{\bar{s}}\right]_+ + \frac{C_m}{m^2}\left[\frac{m^2\log(\bar{s}/m^2)}{\bar{s}}\right]_+, \tag{2.37}$$

where the coefficients A, B and C (with or without subindex m) depend neither on μ nor on m. In scenarios III and IV one has $\bar{s} \lesssim m^2$ and therefore the choice $\mu^2 \sim \bar{s}$ makes sure there are no large logarithms in neither term (the massless limit is smooth since $J_m + J_{\rm nd} \to 0$ when $m \to 0$ and no new class of large logarithms emerges). On the other hand, if $\bar{s} \ll m^2$ the choice $\mu^2 \sim \bar{s}$ cannot prevent the logarithms in J_m from becoming large in such a way that the physics at the scale $\overline{s}/m = Q^2\overline{\tau}/m$, which in the case of an unstable top quark will be of the order of its decay width Γ, has to be separated from that at the mass scale, as the bHQET framework allows.

The factorization theorem for thrust reads:[8]

$$\frac{1}{\sigma_0}\frac{\mathrm{d}\hat{\sigma}_{\rm bHQET}}{\mathrm{d}\tau} = Q^2 H(Q,\mu_m) H_m\Big(m,\frac{Q}{m},\mu_m,\mu\Big)\int\mathrm{d}\ell\, B_\tau\Big(\frac{Q^2(\tau-\tau_{\rm min})-Q\ell}{m},\mu\Big) S_\tau(\ell,\mu), \tag{2.38}$$

with:

$$B_\tau(\hat{s},\mu) = m\int_0^{\hat{s}}\mathrm{d}\hat{s}' B_n(\hat{s}-\hat{s}',\mu) B_n(\hat{s}',\mu)\,. \tag{2.39}$$

The H_m matching coefficient and bHQET jet function satisfy $J_\tau(s+s_{\rm min}) = H_m B_\tau(s/m)[1+\mathcal{O}(s/m^2)]$, such that both factorization theorems smoothly join.

The resummation is done analogously to the SCET case, making use of the Fourier transform, but with the corresponding anomalous dimensions. The procedure is explained, including explicit expressions up to N^{3}LL + $\mathcal{O}(\alpha_s^2)$ order in Ref. [3] and we will apply it in Chapter 5, whereas in this Chapter we limit our numerical analysis to situations in which it is sufficient to use SCET with masses.

2.3 SCET Jet Function Computation

The jet function accounts for the dynamics of collinear particles within the same hemisphere. Since the collinear measurement function in the P- and E-schemes is not the total plus momentum, it cannot be computed as the discontinuity of a forward-scattering amplitude. Instead, one has to use the definition given in Eq. (1.50) which, after a small modification to match the form of our factorization theorem for

[7] We recall here the definition of the plus distribution. For arbitrary exponent ω we have:

$$\left[\frac{\theta(x)}{x^{1+\omega}}\right]_+ = \lim_{\beta\to 0}\left[\frac{\theta(x-\beta)}{x^{1+\omega}} - \delta(x-\beta)\frac{\beta^{-\omega}}{\omega}\right], \tag{2.35}$$

but it can also be obtained through the analytical continuation of the corresponding integration result to any value of ω. Expanding for small ω value leads to

$$\left[\frac{\theta(x)\log^n(x)}{x}\right]_+ = \lim_{\beta\to 0}\left[\frac{\theta(x-\beta)\log^n(x)}{x} + \delta(x-\beta)\frac{\log^{n+1}(\beta)}{n+1}\right], \tag{2.36}$$

with $n \geq 0$, which will appear several times throughout this work.

[8] We have rearranged again the factors of Q and also m with respect to Eq. (1.67) to match the units with those for hemisphere jet mass.

thrust in Eq. (2.23), can be cast into the form:

$$J_n(s,\mu) = \int \frac{\mathrm{d}\ell^+}{2\pi}\, \mathcal{J}_n(s,\ell^+)\,, \tag{2.40}$$
$$\mathcal{J}_n(s,\ell^+) = \frac{1}{4N_c}\mathrm{Tr}\int \mathrm{d}^d x\, e^{i\ell x}\, \langle 0|\, \frac{\overline{n}\!\!\!/}{2}\chi_n(x)\, \delta(s-Q^2\hat{e}_n)\, \overline{\chi}_{n,Q}(0)|0\rangle\ ,$$

with $\chi_{n,Q}$ the jet field with total minus momentum equal to Q. To simplify the expression in the second line of Eq. (2.40) we insert the identity $I = \sum_X |X\rangle\langle X|$ after the delta function and shift the field $\chi_{n,Q}(x)$ to $x = 0$ employing the momentum operator. Using the label operators for the large components of the momenta, the sum over X can be carried out and we obtain the following convenient expression:

$$J_n(s,\mu) = \frac{(2\pi)^{d-1}}{N_C}\mathrm{Tr}\left[\frac{\overline{n}\!\!\!/}{2}\langle 0|\chi_n(0)\delta(s-Q\hat{e}_n)\delta^{(d-2)}(\vec{\mathcal{P}}_X^{\perp})\delta(\bar{\mathcal{P}}-Q)\overline{\chi}_n(0)|0\rangle\right]. \tag{2.41}$$

For practical computations one inserts a complete set of states after $\delta(\bar{\mathcal{P}}-Q)$

$$\sum_X |X\rangle\langle X| \equiv \sum_{n=1}\sum_{\text{spin}}\int\prod_{i=1}^{n}\frac{\mathrm{d}^{d-1}\vec{p}_i}{(2\pi)^{d-1}(2E_i)}|X_n\rangle\langle X_n|\,, \tag{2.42}$$

where we exclude the vacuum from the sum because it does not contribute to the jet function. Each term in the sum over n can include several contributions, accounting for various particle species (heavy or light quarks and gluons), and the sum over polarizations affects all particles in the final state. The perturbative expansion of the jet function in powers of α_s is obtained by adding more particles to the sum as well as more virtual (loop) contributions to the matrix elements that appear after inserting the identity, which in compact form can be written as

$$J_n(s,\mu) = \frac{(2\pi)^{d-1}}{N_C}\sum_X \delta^{(d-2)}(\vec{p}_X^{\perp})\delta(p_X^- - Q)\delta[s-Q^2 e_n(X)]\mathrm{Tr}\left[\gamma^0\frac{\overline{n}\!\!\!/}{2}\,|\langle\, 0\,|\chi_n(0)|\, X\,\rangle|^2\right]. \tag{2.43}$$

In the following, we carry out the computation of the jet function using Eq. (2.41) for both 2-jettiness and P-scheme thrust. Although the result is already known for the former, it is instructive to repeat its computation to highlight the differences between the two approaches. In a way, the computation that uses Eq. (2.41) can be obtained applying Cutkosky rules to directly obtain the imaginary part of the forward-scattering matrix element.

It is important to remember that χ_n in Eq. (2.41) is composed of bare SCET (quark and gluon) fields, and that it is convenient to carry out our computations using perturbation theory "around" those (that is, we will not use the so-called renormalized perturbation theory). For the jettiness computation through the discontinuity of the forward matrix element, this entails that the wave-function renormalization factor

$$Z_\xi = 1 + \frac{\alpha_s C_F}{4\pi}\left[-\frac{3}{\varepsilon} + 6\log\left(\frac{m}{\mu}\right) - 4\right] + \mathcal{O}(\alpha_s^2)\,, \tag{2.44}$$

computed with the diagrams shown in Fig. 2.1 (the soft-gluon contribution vanishes), never appears directly. The mass in Eq. (2.44) should be understood as the pole scheme.

When using Eq. (2.41) one needs to account for $Z_\xi^{1/2}$ since this factor is precisely the overlap between the quantum (bare) collinear field ξ_n and the physical collinear state $|q_n\rangle$: $\langle 0|\,\xi_n\,|q_n(\vec{p},s)\rangle = Z_\xi^{1/2}u_s(\vec{p})$,

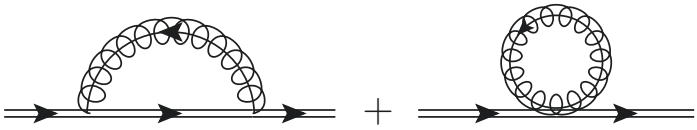

Figure 2.1: One-loop diagrams contributing to the wave-function renormalization at $\mathcal{O}(\alpha_s)$.

with u a particle spinor in the collinear limit, and s, $\vec{p}$ the spin and 3-momentum of the on-shell collinear quark. On the other hand, when using Eq. (2.41) self-energy diagrams on external legs are not included, since their effect is already accounted for in the $Z_\xi^{1/2}$ factor, and it is in this way that one has a one-to-one correspondence with the computation through the imaginary part of the forward matrix element.

The computation at leading order is simple enough that can be carried out for the two massive schemes simultaneously. The corresponding tree-level diagram is shown in Fig. 2.2, where the double line represents a heavy quark and the dashed line marks which particles are on-shell. To compute the phase-space integration it is convenient to use the following parametrization

$$\begin{aligned} \frac{\mathrm{d}^{d-1}\vec{p}}{2E_p} &= \frac{\mathrm{d}p^-}{2p^-}\,\theta(p^-)\,\mathrm{d}^{d-2}\vec{p}_\perp\,, \\ \int \mathrm{d}^{d-2}\vec{p}_\perp &= \frac{2\pi^{1-\varepsilon}}{\Gamma(1-\varepsilon)}|\vec{p}_\perp|^{1-2\varepsilon}\int \mathrm{d}|\vec{p}_\perp|\,, \end{aligned} \tag{2.45}$$

which implies that p^+ has to be expressed in terms of the minus and perpendicular components through

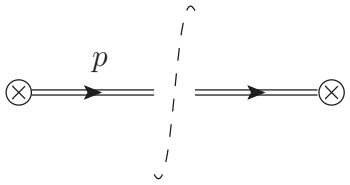

Figure 2.2: Lowest order diagram for the jet function.

the on-shell condition $p^+ = (m^2 + |\vec{p}_\perp|^2)/p^-$, and since the mass appears through on-shell kinematic relations it corresponds always to the pole scheme. In the second line we have carried out the angular integrals for the perpendicular momentum, assuming that matrix elements depend only on its magnitude. We then obtain

$$J_n^{\mathrm{tree}}(s) = \int \frac{\mathrm{d}p^-}{2p^-}\mathrm{d}^{d-2}\vec{p}_\perp\,\delta^{(d-2)}(\vec{p}_\perp)\,\delta(p^- - Q)\,\delta[s - Q^2 e_n(X)]\sum_s \mathrm{Tr}\left[\frac{\overline{n}\!\!\!/}{2}u_s(p)\overline{u}_s(p)\right] = \delta(s - s_{\mathrm{min}}), \tag{2.46}$$

where we have used that the trace of the polarization sum equals $2p^-$ and have integrated all delta functions except the one with the measurement. The color trace cancels the $1/N_c$ prefactor, and the on-shell condition implies $p^+ = m^2/Q$, such that for the 2-particle collinear measurement we get

$$e_J(X) = \frac{p^+}{Q} = \frac{m^2}{Q^2}\,, \qquad e_\tau(X) = \frac{p^+}{Q} - \frac{m^2}{p^-} = 0\,, \tag{2.47}$$

which correspond to e_{min}. To include the wave-function renormalization at $\mathcal{O}(\alpha_s)$ one only needs to multiply this result by Z_ξ.

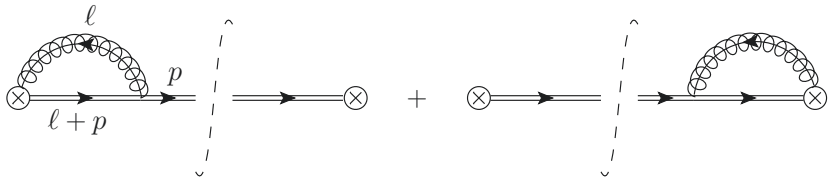

Figure 2.3: Virtual diagrams contributing to the jet function at $\mathcal{O}(\alpha_s)$.

2.3.1 Virtual Radiation

The contribution from virtual gluons can be carried out for the two massive schemes simultaneously since the phase-space integration is identical to the tree-level computation. There are two diagrams contributing, as shown in Fig. 2.3, which yield the same result, so we will compute only one of them which will be multiplied by a factor of 2. Pulling out a collinear gluon field from the Wilson line and using the Feynman rules for massive collinear quarks we obtain the following integral for the leftmost diagram:

$$J_1^{\text{virt}} = -2iC_F g_s^2 \tilde{\mu}^{2\varepsilon} \int \frac{\mathrm{d}^d \ell}{(2\pi)^d} \frac{\bar{n}(p+\ell)}{(\bar{n}\ell)\ell^2[(p+\ell)^2 - m^2]} \equiv -2iC_F g_s^2 (I_1 + p^- I_2)\,, \tag{2.48}$$

where $\tilde{\mu}^2 = \mu^2 e^{\gamma_E}/(4\pi)$, the factor of 2 comes from the product $\bar{n}n$ and the Casimir C_F from the color trace with two Gell-Mann matrices. We are left with two master integrals I_1 and I_2 that can be solved using Feynman parameters for the former

$$I_1 = \int_0^1 \mathrm{d}x \int \frac{\mathrm{d}^d \ell}{(2\pi)^d} \frac{\tilde{\mu}^{2\varepsilon}}{(\ell^2 - x^2 m^2)^2} = \frac{i\,\Gamma(\varepsilon) e^{\varepsilon\gamma_E}}{4\pi} \int_0^1 \mathrm{d}x \left(\frac{xm}{\mu}\right)^{-2\varepsilon} = \frac{i}{(4\pi)^2} \frac{\Gamma(\varepsilon) e^{\varepsilon\gamma_E}}{(1-2\varepsilon)} \left(\frac{m}{\mu}\right)^{-2\varepsilon}, \tag{2.49}$$

and with a combination of Feynman and Georgi parameters for the latter

$$\begin{aligned} I_2 &= 2\int_0^\infty \mathrm{d}\lambda \int_0^1 \mathrm{d}x \int \frac{\mathrm{d}^d \ell}{(2\pi)^d} \frac{(1-x)\tilde{\mu}^{2\varepsilon}}{[\ell^2 - x^2 m^2 - x(1-x)\lambda]^3} \\ &= -\frac{i\,\mu^{2\varepsilon} e^{\gamma_E}}{(4\pi)^2}\,\Gamma(1+\varepsilon) \int_0^1 \mathrm{d}x\, x^{-1-\varepsilon} \int_0^\infty \mathrm{d}\lambda \left\{ x(1-x)p^- \left[\lambda + \frac{m^2 x}{(1-x)p^-}\right]\right\}^{-1-\varepsilon} \\ &= -\frac{i}{(4\pi)^2} \frac{\Gamma(\varepsilon) e^{\gamma_E}}{p^-} \left(\frac{m}{\mu}\right)^{-2\varepsilon} \int_0^1 \mathrm{d}x\, x^{-1-2\varepsilon} = \frac{i}{(4\pi)^2} \frac{\Gamma(\varepsilon)}{2\varepsilon p^-} \left(\frac{m}{\mu}\right)^{-2\varepsilon}. \end{aligned} \tag{2.50}$$

Adding those two results we find a closed expression for J_1^{virt}:

$$\begin{aligned} J_1^{\text{virt}} &= \frac{\alpha_s C_F}{4\pi} \frac{e^{\varepsilon\gamma_E}\Gamma(1+\varepsilon)}{\varepsilon^2(1-2\varepsilon)} \left(\frac{m}{\mu}\right)^{-2\varepsilon} \\ &= \frac{\alpha_s C_F}{4\pi} \left\{ \frac{1}{\varepsilon^2} + \frac{2}{\varepsilon}\left[1 - \log\left(\frac{m}{\mu}\right)\right] + 4 + \frac{\pi^2}{12} - 4\log\left(\frac{m}{\mu}\right) + 2\log^2\left(\frac{m}{\mu}\right)\right\}. \end{aligned} \tag{2.51}$$

Interestingly, this result is zero in the massless limit (which has to be taken before expanding in ε). Therefore, using dimensional regularization, only real-radiation diagrams contribute. The m appearing in Eq. (2.51) is strictly speaking bare, but since we limit our computation to $\mathcal{O}(\alpha_s)$ we can safely take it as the pole mass, as the difference between these two is a higher order correction. Implementing this result into the jet function computation and integrating the real momentum results in adding a factor

of $\delta(e_n - e_{\min})$. Multiplying by 2, expanding in ε and adding the wave-function renormalization, which is obviously a virtual contribution, we obtain

$$J_n^{\rm virt}(s,\mu) = \frac{\alpha_s C_F}{4\pi}\,\delta(s-s_{\min})\bigg[\frac{2}{\varepsilon^2}+\frac{1}{\varepsilon}-\frac{4}{\varepsilon}\log\Big(\frac{m}{\mu}\Big)+4+\frac{\pi^2}{6}-2\log\Big(\frac{m}{\mu}\Big)+4\log^2\Big(\frac{m}{\mu}\Big)\bigg], \tag{2.52}$$

which is the final result of this section.

2.3.2 Real Radiation

Since the phase-space integrals with two particles do not fully collapse with the Dirac delta functions, the real radiation contributions differ depending on the collinear measurement. The diagrams that

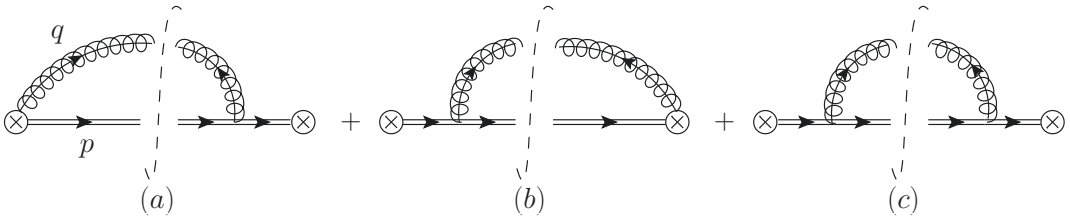

Figure 2.4: Real-radiation diagrams contributing to the jet function at $\mathcal{O}(\alpha_s)$.

contribute at $\mathcal{O}(\alpha_s)$ are shown in Fig. 2.4, where we have omitted the term in which both gluons are radiated from the Wilson line since it vanishes. Diagrams (a) and (b) give identical contributions and therefore we will compute one of them which will be multiplied by a factor of 2. For all the real contributions label-momentum conservation implies $\vec{q}_\perp = -\vec{p}_\perp$ and $q^- = Q - p^-$, which together with the Heaviside function in Eq. (2.45) sets the integration limits for p^- between 0 and Q.

For the first diagram, after integrating the gluon momenta with the delta functions and carrying out the angular perpendicular integration one gets

$$J_a^{\rm real}(s,\mu) = \frac{4\alpha_s C_F\, Q\tilde{\mu}^{2\varepsilon}}{(4\pi)^{1-\varepsilon}\Gamma(1-\varepsilon)}\int_0^Q \mathrm{d}p^-\,\frac{p^-}{Q-p^-}\,\frac{|\vec{p}_\perp|^{1-2\varepsilon}\mathrm{d}|\vec{p}_\perp|}{m^2(Q-p^-)^2+Q^2|\vec{p}_\perp|^2}\,\delta(s-Q^2e_n)\,. \tag{2.53}$$

whereas the third (symmetric) diagram result, which does not need a factor of two, reads

$$\begin{aligned} J_c^{\rm real}(s,\mu) = \frac{\alpha_s C_F\, Q^2 e^{\varepsilon\gamma_E}\mu^{2\varepsilon}}{(2\pi)\Gamma(1-\varepsilon)}\int_0^Q \mathrm{d}p^-\delta(s-Q^2e_n)\,\frac{(Q-p^-)(p^-)^2|\vec{p}_\perp|^{1-2\varepsilon}\mathrm{d}|\vec{p}_\perp|}{m^2(Q-p^-)^2+Q^2|\vec{p}_\perp|^2} \\ \times\bigg[\frac{2(1-\varepsilon)(|\vec{p}_\perp|^2+m^2)}{(p^-)^2}-2(1-\varepsilon)\frac{m^2}{Q^2}+\frac{4(2-\varepsilon)m^2}{Qp^-}\bigg]. \end{aligned} \tag{2.54}$$

P-scheme Thrust

To solve the integrals in the previous section, the thrust measurement must be expressed in terms of p^- and $|\vec{p}_\perp|$. Since the gluon is massless and the quark has mass m we have

$$Q^2\tau = Q\bigg(p^+ + q^+ - \frac{m^2}{p^-}\bigg) = Q\,|\vec{p}_\perp|^2\bigg(\frac{1}{p^-}+\frac{1}{Q-p^-}\bigg) = \frac{Q^2|\vec{p}_\perp|^2}{(Q-p^-)p^-}\,, \tag{2.55}$$

which is mass independent. With this result we can use the measurement delta function to integrate $|\vec{p}_\perp|$

$$\delta(s - Q^2\tau) = \frac{(Q-p^-)p^-}{2|\vec{p}_\perp|Q^2}\,\delta\!\left(|\vec{p}_\perp| - \frac{\sqrt{(Q-p^-)s\,p^-}}{Q}\right). \tag{2.56}$$

Switching variables to $p^- = Qx$ we find the following 1-dimensional integral for J_a:

$$J^{\text{real}}_{a,P}(s,\mu) = \frac{C_F\alpha_s\, e^{\varepsilon\gamma_E}}{2\pi m^2\Gamma(1-\varepsilon)}\left(\frac{s}{\mu^2}\right)^{-\varepsilon}\!\int_0^1 \mathrm{d}x\,\frac{x^{2-\varepsilon}(1-x)^{-1-\varepsilon}}{1-x\big(1-\frac{s}{m^2}\big)}\,. \tag{2.57}$$

The complication arises because the integral diverges as $1/\varepsilon^2$ and contains distributions. The divergence comes from the $(1-x)^{-1-\varepsilon}$ factor, but the subtraction around $x=1$ behaves as $1/s$, which combined with the $s^{-\varepsilon}$ prefactor implies a new divergence and invalidates the subtraction.

This pathological behavior is usual in two-loop computations involving double integrals, and the standard way of solving it is using sector decomposition [6]. To do so, one needs to get rid of distributions by considering the cumulative jet function, which converts Eq. (2.57) into a double integral. In Appendix B.1 we show how to use this general method to solve the integral, and follow in this section an easier, albeit less general, procedure.

Before that, we solve the integral for the massless case, which is not affected by the problem just described, and is valid for 2-jettiness and thrust:

$$\begin{aligned} J^{\text{real}}_{a,m=0}(s,\mu) &= -\frac{C_F\alpha_s e^{\gamma_E}}{(2\pi)\mu^2}\left(\frac{s}{\mu^2}\right)^{-1-\varepsilon}\frac{\Gamma(2-\varepsilon)}{\varepsilon\Gamma(2-2\varepsilon)} \\ &= \frac{C_F\alpha_s}{(2\pi)}\left[\left(\frac{1}{\varepsilon^2}+\frac{1}{\varepsilon}+2-\frac{\pi^2}{4}\right)\delta(s) - \frac{1}{\mu^2}\left(\frac{\mu^2}{s}\right)_+\left(\frac{1}{\varepsilon}+1\right)+\frac{1}{\mu^2}\left(\frac{\mu^2\log(s/\mu^2)}{s}\right)_+\right]. \end{aligned} \tag{2.58}$$

In the second line we have expanded the result around $\varepsilon = 0$ to obtain distributions using the identity

$$x^{-1+\varepsilon} = \frac{1}{\varepsilon}\delta(x) + \sum_{n=0}\frac{\varepsilon^n}{n!}\left[\frac{\log^n(x)}{x}\right]_+. \tag{2.59}$$

For the $m > 0$ case we can transform the integral using hypergeometric function identities. Since these special functions will appear also in Sec. (2.6), we remind here its integral definition (the hypergeometric function is symmetric with respect to its first two arguments):

$$\begin{aligned} {}_2F_1(a,b,c,z) &= \frac{\Gamma(c)}{\Gamma(b)\Gamma(c-b)}\int_0^1 \mathrm{d}x\, x^{b-1}(1-x)^{c-b-1}(1-zx)^{-a} \\ &= (1-z)^{c-b-a}\,{}_2F_1(c-a,c-b,c,z)\,, \end{aligned} \tag{2.60}$$

where the second line is the so called Euler transformation.[9] The integral in Eq. (2.57) is already in this canonical form and therefore we can write

$$
\begin{aligned}
J^{\rm real}_{a,P}(s,\mu) &= -\frac{\Gamma(3-\varepsilon)\,C_F\alpha_s}{(2\pi)m^2\varepsilon\Gamma(3-2\varepsilon)}\left(\frac{s}{\mu^2}\right)^{-\varepsilon}{}_2F_1\left(1,3-\varepsilon,3-2\varepsilon,1-\frac{s}{m^2}\right) \\
&= -\frac{\Gamma(3-\varepsilon)\,C_F\alpha_s}{(2\pi)m^2\varepsilon\Gamma(3-2\varepsilon)}\left(\frac{s}{m^2}\right)^{-1-2\varepsilon}\left(\frac{\mu^2}{m^2}\right)^{\varepsilon}{}_2F_1\left(2-2\varepsilon,-\varepsilon,3-2\varepsilon,1-\frac{s}{m^2}\right) \\
&= \frac{C_F\alpha_s}{(2\pi)m^2\Gamma(1-\varepsilon)}\left(\frac{s}{m^2}\right)^{-1-2\varepsilon}\left(\frac{\mu^2}{m^2}\right)^{\varepsilon}\int_0^1 {\rm d}x(1-x)^{2-\varepsilon}x^{-1-\varepsilon}\left[1-x\left(1-\frac{s}{m^2}\right)\right]^{-2+2\varepsilon},
\end{aligned}
\tag{2.62}
$$

where in the second step we have used Euler's identity and in the third we write the hypergeometric function back as an integral. The integration in the last term can be easily expanded in ε using Eq. (2.59), and defining $\tilde{s}\equiv s/m^2$ we have [10]

$$
\begin{aligned}
&I_3(\tilde{s}) \equiv \int_0^1 {\rm d}x\,(1-x)^{2-\varepsilon}x^{-1-\varepsilon}[1-x(1-\tilde{s})]^{-2+2\varepsilon} = -\frac{1}{\varepsilon}-\tilde{s}\int_0^1 {\rm d}x\,\frac{[2-(2-\tilde{s})x]}{[1-(1-\tilde{s})x]^2} \\
&+\varepsilon\int_0^1 {\rm d}x\frac{2(1-x)^2\log[1-x(1-\tilde{s})]+\tilde{s}x[2-(2-\tilde{s})x+2]\log(x)-(1-x)^2\log(1-x)}{x[1-(1-\tilde{s})x]^2} \\
&= -\frac{1}{\varepsilon}+\frac{\tilde{s}\,[1-\tilde{s}+(2-\tilde{s})\log(\tilde{s})]}{(1-\tilde{s})^2}+\varepsilon f_1(\tilde{s}) \equiv -\frac{1}{\varepsilon}+\tilde{s}\,f_0(\tilde{s})+\varepsilon f_1(\tilde{s})+\mathcal{O}(\varepsilon^2)\,,
\end{aligned}
\tag{2.63}
$$

with $f_1(s)$ a function involving a dilogarithm. This result can be reexpanded in ε together with the prefactor $\tilde{s}^{\,-1-2\varepsilon}$, responsible for the appearance of distributions, finding then

$$
\tilde{s}^{\,-1-2\varepsilon}I_3(\tilde{s}) = \frac{2}{\varepsilon^2}\,\delta(\hat{s})-\frac{1}{\varepsilon}\left(\frac{1}{\hat{s}}\right)_+ +2\left(\frac{\log(\hat{s})}{\hat{s}}\right)_+ -\frac{1}{2}f_1(0)\,\delta(\hat{s})+f_0(\hat{s})+\mathcal{O}(\varepsilon)\,. \tag{2.64}
$$

Therefore one only needs $f_1(0)$, which takes a simple form

$$
f(0) = \int_0^1 {\rm d}x\,\frac{\log(1-x)}{x} = -\frac{\pi^2}{6}\,. \tag{2.65}
$$

Gathering all partial results and expanding in ε we get the following expression

$$
\begin{aligned}
J^{\rm real}_{a,P}(s,\mu) = \frac{C_F\alpha_s}{2\pi}\Bigg\{&\delta(s)\left[\frac{1}{2\varepsilon^2}+\frac{1}{\varepsilon}\log\left(\frac{m}{\mu}\right)+\log^2\left(\frac{m}{\mu}\right)+\frac{\pi^2}{24}\right]+\frac{2}{\mu^2}\left[\frac{\mu^2\log(s/\mu^2)}{s}\right]_+ \\
&-\left[\frac{1}{\varepsilon}+2\log\left(\frac{m}{\mu}\right)\right]\frac{1}{\mu^2}\left(\frac{\mu^2}{s}\right)_+ -\frac{1}{s-m^2}-\frac{s-2m^2}{(s-m^2)^2}\log\left(\frac{s}{m^2}\right)\Bigg\}.
\end{aligned}
\tag{2.66}
$$

The result is divergent for $s\to m^2$, although at that kinematic point there is no physical phenomenon that implies a singularity. We therefore expect that the singularity will cancel when adding together all real-radiation diagrams.

[9] This property can be easily shown as follows: switching variables $x\to 1-x$ and rearranging terms one finds

$$
{}_2F_1(a,b,c,z) = (1-z)^{-a}{}_2F_1\Big(a,c-b,c,\frac{z}{z-1}\Big) = (1-z)^{-b}{}_2F_1\Big(c-a,b,c,\frac{z}{z-1}\Big), \tag{2.61}
$$

where the second term is obtained using the symmetry $a\leftrightarrow b$ on the first equality. Using the first relation followed from the second one arrives to the second line of Eq. (2.60).

[10] Alternatively one can use the Mathematica package HypExp [41] to expand directly the hypergeometric function.

For the cut self-energy diagram in Fig. 2.4 (c), performing the same change of variable as in Eq. (2.57) we arrive at

$$J^{\rm real}_{c,P}(s,\mu) = \frac{C_F\alpha_s\, e^{\varepsilon\gamma_E}}{(2\pi)\Gamma(1-\varepsilon)}\left(\frac{s}{\mu^2}\right)^{-\varepsilon} \times \int_0^1 {\rm d}x\, \frac{x^{-\varepsilon}(1-x)^{1-\varepsilon}}{[s(1-x)+xm^2]^2}\{(1-\varepsilon)(1-x)xs - m^2[2(1-x)-(1-\varepsilon)x^2]\}\,. \tag{2.67}$$

To see how the $1/\varepsilon$ divergence occurs, we compute first the massless limit of $J^{\rm real}_c$, for which we get

$$\begin{aligned} J^{\rm real}_{c,m=0}(s,\mu) &= \frac{C_F\alpha_s\,(1-\varepsilon)\, e^{\varepsilon\gamma_E}}{2\pi\mu^2\Gamma(1-\varepsilon)}\left(\frac{s}{\mu^2}\right)^{-1-\varepsilon}\int_0^1 {\rm d}x\, x^{1-\varepsilon}(1-x)^{-\varepsilon} \\ &= \frac{C_F\alpha_s\, e^{\varepsilon\gamma_E}\Gamma(2-\varepsilon)}{4\pi\mu^2\Gamma(2-2\varepsilon)}\left(\frac{s}{\mu^2}\right)^{-1-\varepsilon} = \frac{C_F\alpha_s}{4\pi}\left[\frac{1}{\mu^2}\left(\frac{\mu^2}{s}\right)_+ - \left(\frac{1}{\varepsilon}+1\right)\delta(s)\right]. \end{aligned} \tag{2.68}$$

At the light of this result one can realize that switching variables to $x = ys/m^2$ exposes the divergence, factoring it out front the integral:

$$\begin{aligned} J^{\rm real}_{c,P}(s,\mu) &= \frac{C_F\alpha_s}{2\pi\Gamma(1-\varepsilon)\mu^2}\left(\frac{m\, e^{\gamma_E}}{\mu}\right)^{2\varepsilon}\left(\frac{s}{\mu^2}\right)^{-1-2\varepsilon}\int_0^{\frac{m^2}{s}} {\rm d}y\, \frac{y^{-\varepsilon}\big(1-\frac{s}{m^2}\big)^{1-\varepsilon}}{\big[1+y\big(1-\frac{s}{m^2}\big)\big]^2} \\ &\quad\times\left[(1-\varepsilon)y(1+y)\frac{s^2}{m^4} - (1-\varepsilon)y^2\frac{s^3}{m^6} + \frac{2sy}{m^2} - 2\right] \\ &= \frac{C_F\alpha_s}{2\pi}\left\{\frac{\delta(s)}{\varepsilon\Gamma(1-\varepsilon)}\left(\frac{m\, e^{\gamma_E}}{\mu}\right)^{2\varepsilon}\int_0^{\infty} {\rm d}y\, \frac{y^{-\varepsilon}}{(1+y)^2} + \frac{1}{\mu^2}\left(\frac{\mu^2}{s}\right)_+\right. \\ &\quad\left.\times\int_0^{\frac{m^2}{s}} {\rm d}y\, \frac{1-\frac{s}{m^2}}{\big[1+y\big(1-\frac{s}{m^2}\big)\big]^2}\left[y(1+y)\frac{s^2}{m^4} - y^2\frac{s^3}{m^6} + \frac{2sy}{m^2} - 2\right]\right\} \\ &= \frac{C_F\alpha_s}{2\pi}\left\{\left[\frac{1}{\varepsilon} - 2\log\Big(\frac{m}{\mu}\Big)\right]\delta(s) - \frac{2}{\mu^2}\left(\frac{\mu^2}{s}\right)_+\right. \\ &\quad\left. + \frac{1}{2(s-m^2)^3}\left[5s^2 - 16m^2s + 11m^4 - 2m^2(s-4m^2)\log\Big(\frac{s}{m^2}\Big)\right]\right\}. \end{aligned} \tag{2.69}$$

In the one-to-last step we have used Eq. (2.59) to partially expand in ε and in the last step the following relation is used:

$$f(x)\left[\frac{1}{x}\right]_+ = f(0)\left[\frac{1}{x}\right]_+ + \frac{f(x)-f(0)}{x}\,. \tag{2.70}$$

The Dirac delta function $\delta(s)$ sets the upper integration limit to infinity and $s = 0$ in the integrand. This makes the integral so simple that no further expansion in ε is necessary for this term. For the contribution proportional to the plus distribution we can set $\varepsilon = 0$ right away, and solve the integral with standard methods. In the last step we have consistently expanded in ε the full result. The expression is again divergent as $s \to m^2$, but as anticipated, the full real-radiation contribution is regular in this

limit:

$$J_P^{\text{real}}(s,\mu) = \frac{C_F\alpha_s}{2\pi}\bigg\{\bigg[\frac{1}{\varepsilon^2}+\frac{1}{\varepsilon}+\frac{2}{\varepsilon}\log\Big(\frac{m}{\mu}\Big)+\frac{\pi^2}{12}-2\log\Big(\frac{m}{\mu}\Big)+2\log^2\Big(\frac{m}{\mu}\Big)\bigg]\delta(s) \\ -\bigg[\frac{1}{\varepsilon}+1+2\log\Big(\frac{m}{\mu}\Big)\bigg]\frac{1}{\mu^2}\bigg(\frac{\mu^2}{s}\bigg)_+ + \frac{4}{\mu^2}\bigg[\frac{\mu^2\log(s/\mu^2)}{s}\bigg]_+ \\ +\frac{s-7m^2}{2(s-m^2)^2}-\frac{s(2s-5m^2)}{(s-m^2)^3}\log\Big(\frac{s}{m^2}\Big)\bigg\}. \tag{2.71}$$

For completeness, we also provide the real-radiation contribution for the massless case, which coincides with the full jet function. Adding the tree-level order we recover the known result

$$\begin{aligned} J_{m=0} &= \delta(s) - \frac{C_F\alpha_s e^{\gamma_E}}{4\pi\mu^2}\bigg(\frac{s}{\mu^2}\bigg)^{-1-\varepsilon}\frac{(4-\varepsilon)\Gamma(2-\varepsilon)}{\varepsilon\Gamma(2-2\varepsilon)} \\ &= \delta(s) + \frac{C_F\alpha_s}{4\pi}\bigg\{\delta(s)\bigg(\frac{4}{\varepsilon^2}+\frac{3}{\varepsilon}+7-\pi^2\bigg) - \frac{3+\frac{4}{\varepsilon}}{\mu^2}\bigg(\frac{\mu^2}{s}\bigg)_+ + \frac{4}{\mu^2}\bigg[\frac{\mu^2\log(s/\mu^2)}{s}\bigg]_+\bigg\}. \end{aligned} \tag{2.72}$$

Jettiness

Let us express the jettiness measurement in terms of minus and perpendicular components:

$$Q^2\tau = Q(p^+ + q^+) = Q\bigg(\frac{|\vec{p}_\perp|^2+m^2}{p^-}+\frac{|\vec{p}_\perp|^2}{Q-p^-}\bigg) = \frac{Q^2|\vec{p}_\perp|^2+m^2Q(Q-p^-)}{(Q-p^-)p^-}\,, \tag{2.73}$$

which can be used to solve the measurement delta function for the magnitude of the perpendicular momentum

$$\delta(s-Q^2\tau_J) = \frac{(Q-p^-)p^-}{2|\vec{p}_\perp|Q^2}\,\delta\bigg(|\vec{p}_\perp| - \frac{\sqrt{(Q-p^-)(sp^- - Qm^2)}}{Q}\bigg). \tag{2.74}$$

The argument of this delta function can be zero only if $sp^- > Qm^2$, what sets the lower limit of integration. Therefore, changing variables to $p^- = Q(1-x)$ we obtain for the diagram in which the gluons are radiated from the Wilson line and the quark particle the following result

$$\begin{aligned} J_{a,J}^{\text{real}}(s,\mu) &= \frac{C_F\alpha_s}{2\pi\Gamma(1-\varepsilon)}\frac{\mu^{2\varepsilon}e^{\varepsilon\gamma_E}}{s-m^2}\int_0^{1-\frac{m^2}{s}}\mathrm{d}x\,(1-x)x^{-1-\varepsilon}[(1-x)s-m^2]^{-\varepsilon} \\ &= \frac{C_F\alpha_s}{2\pi\Gamma(1-\varepsilon)}\frac{s^\varepsilon\mu^{2\varepsilon}e^{\varepsilon\gamma_E}}{(s-m^2)^{1+2\varepsilon}}\int_0^1\mathrm{d}y\,(1-y)^{-\varepsilon}\bigg(y^{-1-\varepsilon}-y^{-2\varepsilon}\frac{s-m^2}{s}\bigg) \\ &= -\frac{C_F\alpha_s e^{\varepsilon\gamma_E}}{2\pi\mu^2}\frac{\Gamma(1-\varepsilon)}{\varepsilon\,\Gamma(2-2\varepsilon)}\bigg(\frac{s}{\mu^2}\bigg)^{-1+\varepsilon}\bigg(\frac{s-m^2}{\mu^2}\bigg)^{-1-2\varepsilon}[\,s(1-\varepsilon)-\varepsilon\,m^2\,] \\ &= \frac{C_F\alpha_s}{2\pi}\bigg\{\delta(s-m^2)\bigg[\frac{1}{2\varepsilon^2}+\frac{1}{\varepsilon}\log\Big(\frac{m}{\mu}\Big)+\log^2\Big(\frac{m}{\mu}\Big)-\frac{\pi^2}{8}\bigg]-\frac{1}{s}-\frac{\log\big(\frac{s}{m^2}\big)}{s-m^2} \\ &\quad -\bigg[\frac{1}{\varepsilon}+2\log\Big(\frac{m}{\mu}\Big)\bigg]\frac{1}{\mu^2}\bigg(\frac{\mu^2}{s-m^2}\bigg)_+ + \frac{2}{\mu^2}\bigg[\frac{\mu^2\log[(s-m^2)/\mu^2]}{s-m^2}\bigg]_+\bigg\}, \end{aligned} \tag{2.75}$$

where in the second line we have switched variables to $x = y(1 - m^2/s)$. Performing the same change of variables in the diagram in which the gluons are radiated from both quark lines one gets

$$\begin{aligned}
J_{c,J}^{\rm real}(s,\mu) &= \frac{C_F\alpha_s}{2\pi\Gamma(1-\varepsilon)}\frac{\mu^{2\varepsilon}e^{\varepsilon\gamma_E}}{(s-m^2)^2}\int_0^{1-\frac{m^2}{s}}\mathrm{d}x\,x^{-\varepsilon}[(1-x)s-m^2]^{-\varepsilon} \\
&\quad \big\{(1-\varepsilon)\big[xs+(2-x)m^2\big]-(2-\varepsilon)m^2\big\} \\
&= \frac{C_F\alpha_s}{2\pi}\frac{(s-m^2)^{-1-2\varepsilon}}{s^2\Gamma(1-\varepsilon)}\left(\frac{s\,e^{\gamma_E}}{\mu^2}\right)^{\varepsilon}\int_0^1\mathrm{d}y\,y^{-\varepsilon}(1-y)^{-\varepsilon}\big[(s-m^2)^2y(1-\varepsilon)-2m^2s\big] \\
&= \frac{C_F\alpha_s}{4\pi}\frac{(s-m^2)^{-1-2\varepsilon}}{s^2}\left(\frac{s\,e^{\gamma_E}}{\mu^2}\right)^{\varepsilon}\frac{\Gamma(1-\varepsilon)}{\Gamma(2-2\varepsilon)}[(1-\varepsilon)(s-m^2)^2-4m^2s] \\
&= \frac{C_F\alpha_s}{2\pi}\left\{\left[\frac{1}{\varepsilon}+2+2\log\Big(\frac{m}{\mu}\Big)\right]\delta(s-m^2)-\frac{2}{\mu^2}\left(\frac{\mu^2}{s-m^2}\right)_+ + \frac{5s-m^2}{2s^2}\right\},
\end{aligned} \tag{2.76}$$

where we have carried out the same manipulations as in Eq. (2.75). Adding the two results we obtain the total contribution for 2-jettiness:

$$\begin{aligned}
J_J^{\rm real}(s,\mu) = \frac{C_F\alpha_s}{2\pi}\Bigg\{&\left[\frac{1}{\varepsilon^2}+\frac{1}{\varepsilon}+\frac{2}{\varepsilon}\log\Big(\frac{m}{\mu}\Big)+2-\frac{\pi^2}{4}+2\log\Big(\frac{m}{\mu}\Big)+2\log^2\Big(\frac{m}{\mu}\Big)\right]\delta(s) \\
&-\left[\frac{1}{\varepsilon}+1+2\log\Big(\frac{m}{\mu}\Big)\right]\frac{1}{\mu^2}\left(\frac{\mu^2}{s}\right)_+ + \frac{4}{\mu^2}\left[\frac{\mu^2\log(s/\mu^2)}{s}\right]_+ \\
&+\frac{s-m^2}{2s^2}-\frac{2}{s-m^2}\log\Big(\frac{s}{m^2}\Big)\Bigg\}.
\end{aligned} \tag{2.77}$$

2.3.3 Final Result for the Jet Function

Adding together the contributions from real and virtual corrections one obtains the complete jet function. The divergences are now entirely of UV origin and can be renormalized multiplicatively (with a convolution). Since in either massive scheme these are the same as for massless quarks, the renormalization factor is identical, along with the anomalous dimension. Therefore we quote directly the result for the renormalized jet functions [$\alpha_s \equiv \alpha_s(\mu)$]:

$$\begin{aligned}
J_n^P(s,\mu) &= \delta(s)+\frac{\alpha_s C_F}{4\pi}\Bigg\{\left[2\log\Big(\frac{m}{\mu}\Big)+8\log^2\Big(\frac{m}{\mu}\Big)+4+\frac{\pi^2}{3}\right]\delta(s)+\frac{8}{\mu^2}\left[\frac{\log(s/\mu^2)}{s/\mu^2}\right]_+ \\
&\quad -\frac{4}{\mu^2}\left[1+2\log\Big(\frac{m}{\mu}\Big)\right]\left(\frac{\mu^2}{s}\right)_+ + \frac{s-7m^2}{(s-m^2)^2}-\frac{2s(2s-5m^2)}{(s-m^2)^3}\log\Big(\frac{s}{m^2}\Big)\Bigg\}, \\
J_n^J(s+m^2,\mu) &= \delta(s)+\frac{\alpha_s C_F}{4\pi}\Bigg\{\left[2\log\Big(\frac{m}{\mu}\Big)+8\log^2\Big(\frac{m}{\mu}\Big)+8-\frac{\pi^2}{3}\right]\delta(s)+\frac{8}{\mu^2}\left[\frac{\log(s/\mu^2)}{s/\mu^2}\right]_+ \\
&\quad -\frac{4}{\mu^2}\left[1+2\log\Big(\frac{m}{\mu}\Big)\right]\left(\frac{\mu^2}{s}\right)_+ + \frac{s}{(m^2+s)^2}-\frac{4}{s}\log\Big(1+\frac{s}{m^2}\Big)\Bigg\}.
\end{aligned} \tag{2.78}$$

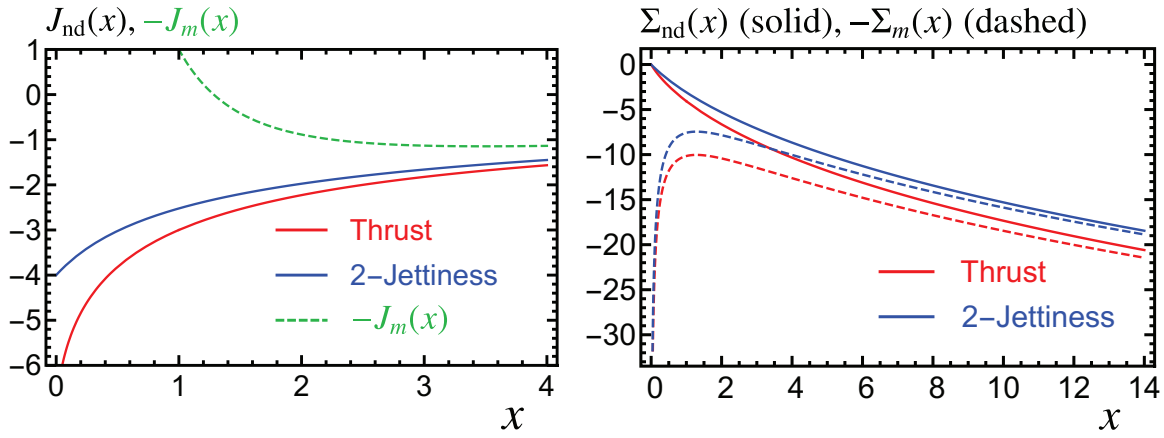

(a) (b)

Figure 2.5: Massive corrections to the jet function. Panels (a) and (b) show the differential and cumulative jet functions, respectively. We show with solid lines the non-distributional functions $J_{\rm nd}$ and $\Sigma_{\rm nd}$ for P- (red) and M- (blue) schemes. The differential J_m function is shown multiplied -1 as a green dashed line in panel (a) (for $x > 0$ it is common to both schemes), while $-\Sigma_m$ is shown in panel (b) with red and blue dashed lines for P- and M-schemes, respectively.

From these equations one can easily read out the functional form of $J_{\rm nd}(x)$ defined in Eq. (2.31). With some manipulations one can also figure out expressions for $J_m(x)$ defined in the same equation:

$$
\begin{aligned}
J_m(x) &= A_S\,\delta(x) - \left(\frac{1}{x}\right)_+ + 4\left[\frac{\log(x)}{x}\right]_+ , \\
J^J_{\rm nd}(x) &= \frac{x}{(x+1)^2} - \frac{4}{x}\log(1+x)\,, \\
J^P_{\rm nd}(x) &= \frac{x-7}{(x-1)^2} - \frac{2x(2x-5)}{(x-1)^3}\log(x)\,,
\end{aligned}
\tag{2.79}
$$

with $A_J = 2\pi^2/3 + 1$ and $A_P = 4\pi^2/3 - 3$. We shall see that $J_{\rm nd}(x \to \infty) = -J_m(x)$ for both schemes, and show this behavior graphically in Fig. 2.5(a). This is expected since it corresponds to taking the massless limit, and therefore mass corrections should vanish such that the jet function becomes equal to the (renormalized) massless result of Eq. (2.72). Since $J_{\rm nd}$ contains distributions in this limit, it is advantageous to work with the cumulative jet function

$$
\Sigma_n(s_c) \equiv \int_0^{s_c} {\rm d}s\, J_n(s)\,, \tag{2.80}
$$

which is a regular function. Likewise, one can define the cumulative functions for $J_{\rm nd}$ and J_m, which are also shown in Fig. 2.5(b). The result can be obtained easily and involves polylogarithms:

$$\begin{aligned}\Sigma_n^J(s+m^2,\mu) =& 1+\frac{\alpha_s C_F}{4\pi}\bigg\{2\log\Big(\frac{m}{\mu}\Big)+8\log^2\Big(\frac{m}{\mu}\Big)+8-\frac{\pi^2}{3}+\log\Big(1+\frac{s}{m^2}\Big)-\frac{s}{s+m^2}\\ &+4\log^2\Big(\frac{s}{\mu^2}\Big)-4\bigg[1+2\log\Big(\frac{m}{\mu}\Big)\bigg]\log\Big(\frac{s}{\mu^2}\Big)+4\,\mathrm{Li}_2\Big(-\frac{s}{m^2}\Big)\bigg\},\\ \Sigma_n^P(s,\mu) =& 1+\frac{\alpha_s C_F}{4\pi}\bigg\{2\log\Big(\frac{m}{\mu}\Big)+8\log^2\Big(\frac{m}{\mu}\Big)+4+\frac{\pi^2}{3}-4\bigg[1+2\log\Big(\frac{m}{\mu}\Big)\bigg]\log\Big(\frac{s}{\mu^2}\Big)\\ &+4\log^2\Big(\frac{s}{\mu^2}\Big)+4\,\mathrm{Li}_2\Big(1-\frac{s}{m^2}\Big)+\frac{3s}{s-m^2}+\frac{(s-4m^2)s}{(s-m^2)^2}\log\Big(\frac{s}{m^2}\Big)\bigg\}.\end{aligned} \tag{2.81}$$

As expected, in the $m\to 0$ limit both results reduce to the (same) massless cumulative jet function

$$\Sigma_n^{m=0}(s,\mu) = 1+\frac{\alpha_s(\mu) C_F}{4\pi}\bigg[7-\pi^2-3\log\Big(\frac{s}{\mu^2}\Big)+2\log^2\Big(\frac{s}{\mu^2}\Big)\bigg]. \tag{2.82}$$

To take the derivative one needs to recall that the jet function has support only for positive s, such that it is effectively proportional to an (implicit) Heaviside function $\theta(s)$. Using the following relations:

$$\frac{\mathrm{d}\theta(x)}{\mathrm{d}x}=\delta(x)\,,\qquad \frac{\mathrm{d}}{\mathrm{d}x}[\theta(x)\log^n(x)] = n\bigg[\frac{\log^{n-1}(x)}{x}\bigg]_+, \tag{2.83}$$

one readily arrives at Eq. (2.72). For $s>0$ one can expand around $m=0$ to find the following compact series

$$\begin{aligned}J_n^P(s>0,\mu) &= \frac{\alpha_s C_F}{4\pi}\frac{1}{s}\bigg\{4\log\Big(\frac{s}{\mu^2}\Big)-3+\sum_{i=1}\bigg[1-6i-(4+i-3i^2)\log\Big(\frac{s}{m^2}\Big)\bigg]\Big(\frac{m^2}{s}\Big)^i\bigg\},\\ J_n^J(s>0,\mu) &= \frac{\alpha_s C_F}{4\pi}\frac{1}{s}\bigg\{4\log\Big(\frac{s}{\mu^2}\Big)-3+\sum_{i=1}(-1)^i\Big(i+1+\frac{4}{i}\Big)\Big(\frac{m^2}{s}\Big)^i\bigg\},\end{aligned} \tag{2.84}$$

with similar results for the cumulative jet functions. Since individual pieces of the P-scheme thrust jet function have divergences at $s=m^2$ it is convenient to compute the expansion of $J_{\rm nd}^P(x)$ around $x=1$, which can be cast as

$$J_{\rm nd}^P(x) = -2\sum_{i=0}(1-x)^i\frac{9+5i}{(i+1)(i+2)(i+3)}\,. \tag{2.85}$$

2.4 Fixed-order Prediction in SCET

Inserting our result for the jet function into the SCET factorization theorem of Eq. (2.23), setting all renormalization scales equal and using the known results for the hard and soft function at one loop

$$\begin{aligned}H(Q,\mu) =& 1+\frac{\alpha_s(\mu) C_F}{4\pi}\bigg[\frac{7\pi^2}{3}-16+12\log\Big(\frac{Q}{\mu}\Big)-8\log^2\Big(\frac{Q}{\mu}\Big)\bigg],\\ S(\ell,\mu) =& \delta(\ell)+\frac{\alpha_s(\mu) C_F}{4\pi}\bigg\{\frac{\pi^2}{3}\delta(\ell)-\frac{16}{\mu}\bigg[\frac{\mu\log(\ell/\mu)}{\ell}\bigg]_+\bigg\},\end{aligned} \tag{2.86}$$

one arrives at the fixed-order prediction for the partonic singular terms of the P-scheme thrust differential cross section: [11]

$$\frac{1}{\sigma_0}\frac{\mathrm{d}\hat{\sigma}_{\mathrm{FO}}^{\mathrm{SCET}}}{\mathrm{d}\tau} = \delta(\tau) + \frac{\alpha_s(\mu)C_F}{4\pi}F_1^{\mathrm{SCET}}(\tau,\hat{m}) + \mathcal{O}(\alpha_s^2) \tag{2.87}$$

$$\begin{aligned} F_1^{\mathrm{SCET}}(\tau,\hat{m}) &= \delta(\tau)\bigg[\frac{10\pi^2}{3} - 8 + 4\log(\hat{m}) + 16\log^2(\hat{m})\bigg] - 8[1+2\log(\hat{m})]\bigg(\frac{1}{\tau}\bigg)_+ \\ &\quad + \frac{2(\tau-7\hat{m}^2)}{(\tau-\hat{m}^2)^2} - \frac{4\tau(2\tau-5\hat{m}^2)}{(\tau-\hat{m}^2)^3}\log\Big(\frac{\tau}{\hat{m}^2}\Big) \\ &\equiv A^{\mathrm{SCET}}(\hat{m})\delta(\tau) + B_{\mathrm{plus}}^{\mathrm{SCET}}(\hat{m})\bigg(\frac{1}{\tau}\bigg)_+ + F_{\mathrm{NS}}^{\mathrm{SCET}}(\tau,\hat{m})\,. \end{aligned}$$

In the same way, one can get a similar expression for the cumulative distribution Σ_P^{SCET}, which is, among other things, useful to take the $m \to 0$ limit. The differential cross section has a similar structure in full QCD, although it is different for vector and axial-vector currents as discussed in Ref. [48], and for P-scheme thrust takes the following form [12]

$$\frac{1}{\sigma_0^C}\frac{\mathrm{d}\hat{\sigma}_{\mathrm{FO}}^{C}}{\mathrm{d}\tau} = R_0^C(\hat{m})\,\delta(\tau) + C_F\frac{\alpha_s}{\pi}F_C^{\mathrm{QCD}}(\tau,\hat{m}) + \mathcal{O}(\alpha_s^2)\,, \tag{2.88}$$

$$F_C^{\mathrm{QCD}}(\tau,\hat{m}) = A^C(\hat{m})\delta(\tau) + B_{\mathrm{plus}}^C(\hat{m})\bigg(\frac{1}{\tau}\bigg)_+ + F_{\mathrm{NS}}^C(\tau,\hat{m})\,,$$

where $C = V, A$ labels the type of current and with R_0^C the tree-level massive R-ratio. Analytic results for A^C and B_C^{plus} can be found in Ref. [48] and we quote here the universal value for the latter:

$$B_{\mathrm{plus}}^C(\hat{m}) = \begin{pmatrix} 3-\beta^2 \\ 2\beta^2 \end{pmatrix}\bigg[(1+\beta^2)\log\bigg(\frac{1+\beta}{2\hat{m}}\bigg) - \beta\bigg], \tag{2.89}$$

with $\beta = \sqrt{1-4\hat{m}^2}$, and where the first and second line of the expression in big parentheses correspond to the vector and axial-vector currents, respectively. One recovers the SCET result for small masses, $A^C(\hat{m}\to 0) = A^{\mathrm{SCET}}(\hat{m})$ and $B_{\mathrm{plus}}^C(\hat{m}\to 0) = B_{\mathrm{plus}}^{\mathrm{SCET}}(\hat{m})$, and also

$$\lim_{\tau\to 0} F_{\mathrm{NS}}^C\Big(\tau, \hat{m} = \alpha\sqrt{\tau}\,\Big) \to F_{\mathrm{NS}}^{\mathrm{SCET}}\Big(\tau, \hat{m} = \alpha\sqrt{\tau}\,\Big), \tag{2.90}$$

with $\alpha \sim \mathcal{O}(1)$. Since for thrust F_{NS}^C is only known numerically, in Fig. 2.6 we show a comparison of QCD and SCET results for the NLO corrections scaling the mass as indicated in Eq. (2.90). Excellent numerical agreement is found as $\tau \to 0$ for various values of α between 1.2 and 15. We show only the vector current as for small values of τ it is indistinguishable from the axial-vector one.

2.5 bHQET Jet Function Computation

The computation of the bHQET jet function is significantly simpler than for its SCET counterpart since in this EFT the mass is no longer a dynamical scale and we are left with tadpole-like integrals. As an immediate consequence of that, much as it happened for the massless SCET jet function, all virtual graphs are automatically zero in dimensional regularization since they are scaleless (this includes the

[11] The partonic fixed-order bHQET cross section is identical to the SCET one dropping $F_{\mathrm{NS}}^{\mathrm{SCET}}$.

[12] In the $\tau_P \to \tau_P^{\mathrm{min}} = 0$ limit one gets the same result as in full QCD dropping $F_{\mathrm{NS}}^C(\tau,\hat{m})$, which is a power correction.

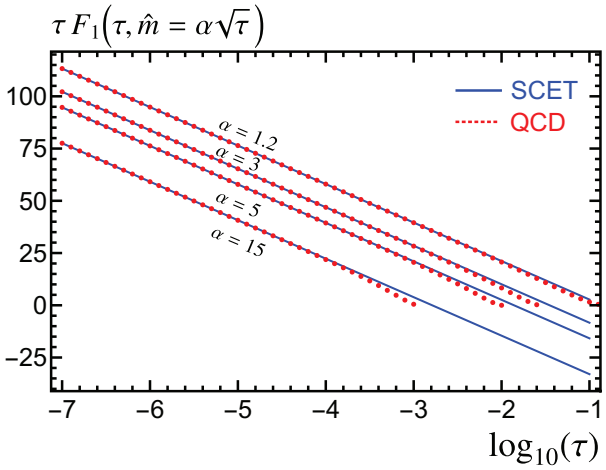

Figure 2.6: Comparison of the $\mathcal{O}(\alpha_s)$ correction to the differential cross sections in QCD $[\,F_V^{\rm QCD}(\tau,\hat{m})\,]$ and SCET $[\,F_1^{\rm SCET}(\tau,\hat{m})\,]$. We enforce the SCET power counting by scaling the reduced mass as $\hat{m} = \alpha\sqrt{\tau}$, with $\alpha = \mathcal{O}(1)$. Solid blue lines show SCET analytic results, while red dots correspond to QCD numerical predictions obtained from the computations in Ref. [48]. The numerical values of α are shown in the figure.

wave-function renormalization factor). We are then left with the tree-level, which is common for both massive schemes, and real-radiation diagrams. The collinear event-shape measurements are the same in SCET and bHQET, although the contribution of massive particles needs to be power expanded, such that using $p = mv + k$ we obtain for thrust and 2-jettiness the following results[13]

$$\begin{aligned} Q(\tau_n^J - \hat{m}^2) &= p^+ - \frac{m^2}{Q} = mv_+ - \frac{m^2}{Q} + k^+ = k^+\,, \\ Q\tau_n^P &= p^+ - \frac{m^2}{p^-} = k^+ + \frac{m^2}{Q} - \frac{m^2}{Q + k^-} = k^+ + \hat{m}^2 k^- = 0\,, \end{aligned} \tag{2.91}$$

where to get to the third equality of the second line we have used $Q \gg k^-$ (as can be seen in Tab. 1.1), and to obtain $\tau_n^P = 0$ we use the on-shell condition for heavy quarks $v \cdot k = 0$, to be discussed later in this section.

The adaptation of the field-theoretical definition for the bHQET jet function Eq. (1.68) to the thrust factorization formula in Eq. (2.38) can be written as

$$B_n(\hat{s}) = \frac{(2\pi)^{d-1}Q}{2m^2 N_C}\mathrm{Tr}\langle 0|W_n^\dagger(0)h_{v_+}(0)\delta\Big[\hat{s} - \frac{Q^2}{m}(\hat{e}_n - e_{\rm min})\Big]\delta^{(d-2)}(\vec{\mathcal{K}}^\perp)\delta(\mathcal{K}^-)\overline{h}_{v_+}(0)W_n(0)|0\rangle. \tag{2.92}$$

where $\vec{\mathcal{K}}$ is an operator that pulls out the residual momenta of the heavy quarks and the (full) momenta of ultra-collinear particles.

The bHQET phase-space integration involving a heavy quark gets also simplified, and using again

[13] We will omit subscripts $_{+,-}$ for clarity where it does not lead to confusion. Since in this section we describe the computation for the n-collinear hemisphere jet function (recall that the $\overline{n}$-collinear case is symmetric and gives the same result) we will be actually using $p = mv_+ + k_+$

$p = mv + k$ one has that

$$\begin{aligned}\frac{\mathrm{d}^d p}{(2\pi)^{d-1}}\,\delta(p^2-m^2)\theta(p^0) &= \frac{\mathrm{d}p^+\mathrm{d}p^-\mathrm{d}^{d-2}\vec{p}_\perp}{2(2\pi)^{d-1}}\,\delta\big[p^-p^+-|\vec{p}_\perp|^2-m^2\big]\theta(p^-+p^+) \\ &= \frac{\mathrm{d}k^+\mathrm{d}k^-\mathrm{d}^{d-2}\vec{k}_\perp}{2(2\pi)^{d-1}}\,\delta\Big(Qk^+ + \frac{m^2}{Q}k^- + k^2\Big)\theta\Big(Q + k^- + \frac{m^2}{Q} + k^+\Big) \\ &= \frac{\mathrm{d}k^+\mathrm{d}k^-\mathrm{d}^{d-2}\vec{k}_\perp}{2(2\pi)^{d-1}}\,\delta\Big(Qk^+ + \frac{m^2}{Q}k^-\Big)\theta(Q) = \frac{\mathrm{d}k^-\mathrm{d}^{d-2}\vec{k}_\perp}{2Q(2\pi)^{d-1}}\,,\end{aligned} \tag{2.93}$$

where in the second line we have used the scaling shown in Tab. 1.1 and in the third we power-count away the k^2 in the delta function argument along with all terms but Q inside the Heaviside function. The on-shell condition for heavy quarks written in light-cone coordinates implies $v^-k^+ + k^-v^+ = 0$, in agreement with the argument of the delta function. When comparing to Eq. (2.45) we observe that the p^- in the denominator got replaced by Q and that the p^- integration is not limited to positive values only. The phase-space integration for ultracollinear particles stays the same as in SCET.

Feynman diagrams look exactly the same in SCET and bHQET, with the replacement $p \to k$ for the heavy quark momenta. Let us compute the tree-level contribution as given in Fig. 2.2, which is analogous to the corresponding SCET calculation:

$$mB_n^{\mathrm{tree}}(s) = \int\frac{\mathrm{d}k^-}{4m}\mathrm{d}^{d-2}\vec{k}_\perp\delta^{(d-2)}(\vec{k}_\perp)\delta(k^-)\delta\Big[\hat{s}-\frac{Q^2}{m}(\hat{e}_n - e_{\min})\Big]\sum_s \mathrm{Tr}\big[u_s(p)\overline{u}_s(p)\big] = \delta(\hat{s})\,, \tag{2.94}$$

where we have used that the trace of the polarization sum equals $4m$ and have integrated all delta functions except the one with the measurement. The condition $k^- = 0$ imposed by the Dirac delta function makes both (shifted) measurements coincide at tree-level, see Eq. (2.91).

There are some generic features to be learned from this diagram: since there is no Dirac structure in the diagram, the trace of the polarization sum will be always $4m$ at any loop order, and since there is always one heavy quark which brings an inverse power of Q through its phase space one has the following combination:

$$\frac{Q}{2m}\frac{1}{2Q}\mathrm{Tr}\big[u_s(p)\overline{u}_s(p)\big] = 1\,, \tag{2.95}$$

which eliminates the spurious dependence on m and Q, ultraviolet scales that should not appear in EFT computations. To make this non-dependence explicit at higher orders one can rescale the minus component of ultracollinear real particles as $q_i^- = (Q/m)\ell_i$, as we shall do in the rest of the section.

We turn our attention now to real-radiation contributions, for which we can simplify the heavy-quark propagator using $v \cdot k = 0$. We start with diagram (a) of Fig. 2.4, that after applying the bHQET Feynman rules becomes

$$mB_a^{\mathrm{real}}(\hat{s},\mu) = \frac{2\alpha_s C_F(\mu^2 e^{\gamma_E})^\varepsilon}{\pi\Gamma(1-\varepsilon)}\int\frac{\mathrm{d}\ell^-}{(\ell^-)^2}\frac{|\vec{q}_\perp|^{1-2\varepsilon}\mathrm{d}|\vec{q}_\perp|}{v\cdot q}\theta(\ell^-)\delta\Big[\hat{s}-\frac{Q^2}{m}(\hat{e}_n - e_{\min})\Big]. \tag{2.96}$$

The on-shell condition on the ultra-collinear gluon momenta implies in light-cone coordinates: $2\,v\cdot q = |\vec{q}_\perp|^2 Q/(mq^-) + mq^-/Q = [\,|\vec{q}_\perp|^2 + (\ell^-)^2\,]/\ell^-$. For diagram (c) we get instead

$$mB_c^{\mathrm{real}}(\hat{s},\mu) = -\frac{\alpha_s C_F(\mu^2 e^{\gamma_E})^\varepsilon}{2\pi\Gamma(1-\varepsilon)}\int\frac{\mathrm{d}\ell^-}{\ell^-}\frac{|\vec{q}_\perp|^{1-2\varepsilon}\mathrm{d}|\vec{k}_\perp|}{(v\cdot q)^2}\theta(\ell^-)\delta\Big[\hat{s}-\frac{Q^2}{m}(\hat{e}_n - e_{\min})\Big]. \tag{2.97}$$

Let us work out the measurements for thrust and 2-jettiness

$$\frac{Q^2}{m}(\tau_n^J - \hat{m}^2) = \frac{Q}{m}(q^+ + k^+) = \frac{Q}{m}\frac{|\vec{q}_\perp|^2}{q^-} + \frac{m}{Q}q^- = \frac{|\vec{q}_\perp|^2}{\ell^-} + \ell^-\,, \tag{2.98}$$
$$\frac{Q^2}{m}\tau_n^P = \frac{Q}{m}q^+ = \frac{Q}{m}\frac{|\vec{q}_\perp|^2}{q^-} = \frac{|\vec{q}_\perp|^2}{\ell^-}\,,$$

where we have used Eq. (2.91), the on-shell condition for heavy quarks and ultra-collinear massless gluons, and the fact that label momentum conservation implies $k^- = -q^-$. With this result it is very simple to solve the measurement delta function in terms of the perpendicular gluon momenta

$$\delta\Big[\hat{s} - \frac{Q^2}{m}(\tau_n^J - \hat{m}^2)\Big] = \frac{\ell^-}{2|\vec{q}_\perp|}\,\delta\Big[|\vec{q}_\perp| - \sqrt{\hat{s}\,\ell^- - (\ell^-)^2}\,\Big], \tag{2.99}$$
$$\delta\Big(\hat{s} - \frac{Q^2}{m}\tau_n^P\Big) = \frac{\ell^-}{2|\vec{q}_\perp|}\,\delta\Big(|\vec{q}_\perp| - \sqrt{\hat{s}\,\ell^-}\,\Big),$$

and we will use these results to compute the jet functions in the next two sub-sections.

2.5.1 Thrust

We start with the diagram in which the gluon is radiated from the Wilson line. Switching variables to $\ell^- = \hat{s}x$ we arrive at

$$mB_{a,P}^{\rm real}(\hat{s},\mu) = \frac{\alpha_s(\mu^2 e^{\gamma_E})^\varepsilon C_F}{2\pi}\frac{\hat{s}^{\,-1-2\varepsilon}}{\Gamma(1-\varepsilon)}\int_0^\infty \mathrm{d}x\,\frac{x^{-1-\varepsilon}}{1+x} = -\frac{\alpha_s\Gamma(1+\varepsilon)C_F\,e^{\varepsilon\gamma_E}}{2\pi\mu\varepsilon}\left(\frac{\hat{s}}{\mu}\right)^{-1-2\varepsilon} \tag{2.100}$$
$$= \frac{\alpha_s C_F}{4\pi}\left[\left(\frac{1}{\varepsilon^2} + \frac{\pi^2}{12}\right)\delta(\hat{s}) - \frac{2}{\varepsilon\mu}\left(\frac{\mu}{\hat{s}}\right)_+ + \frac{4}{\mu}\left(\frac{\mu\log(\hat{s}/\mu)}{\hat{s}}\right)_+\right].$$

With an identical change of variables we arrive at the following result for diagram (c):

$$mB_{c,P}^{\rm real}(\hat{s},\mu) = -\frac{\alpha_s(\mu^2 e^{\gamma_E})^\varepsilon C_F}{\pi}\frac{\hat{s}^{\,-1-2\varepsilon}}{\Gamma(1-\varepsilon)}\int_0^\infty \mathrm{d}x\,\frac{x^{-\varepsilon}}{(1+x)^2} \tag{2.101}$$
$$= -\frac{\alpha_s\Gamma(1+\varepsilon)C_F\,e^{\varepsilon\gamma_E}}{\pi\mu}\left(\frac{\hat{s}}{\mu}\right)^{-1-2\varepsilon} = \frac{\alpha_s C_F}{4\pi}\left[\frac{2}{\varepsilon}\,\delta(\hat{s}) - \frac{4}{\mu}\left(\frac{\mu}{\hat{s}}\right)_+\right].$$

Adding both diagrams with the appropriate factors we obtain the final expression for the P-scheme hemisphere jet function:

$$mB_n^P(\hat{s},\mu) = -\frac{\alpha_s\Gamma(2+\varepsilon)C_F\,e^{\varepsilon\gamma_E}}{\pi\mu\varepsilon}\left(\frac{\hat{s}}{\mu}\right)^{-1-2\varepsilon} \tag{2.102}$$
$$= \frac{\alpha_s C_F}{4\pi}\left[\left(\frac{2}{\varepsilon^2} + \frac{2}{\varepsilon} + \frac{\pi^2}{6}\right)\delta(\hat{s}) - \frac{4}{\mu}\left(\frac{1}{\varepsilon}+1\right)\left(\frac{\mu}{\hat{s}}\right)_+ + \frac{8}{\mu}\left(\frac{\mu\log(\hat{s}/\mu)}{\hat{s}}\right)_+\right].$$

2.5.2 Jettiness

The Dirac delta function in Eq. (2.99) implies that there is a solution for $|\vec{q}_\perp|$ only if $\ell^- < \hat{s}$, which can be implemented through a Heaviside function and bounds the upper integration limit for ℓ^-. With

the change of variables implemented in the previous section the integration limits are mapped to the interval $(0,1)$ and we get the following result for diagram (a):

$$\begin{aligned} mB^{\rm real}_{a,J}(\hat{s},\mu) &= \frac{\alpha_s(\mu^2 e^{\gamma_E})^\varepsilon C_F}{2\pi}\frac{\hat{s}^{\,-1-2\varepsilon}}{\Gamma(1-\varepsilon)}\int_0^1 \mathrm{d}x\, x^{-1-\varepsilon}(1-x)^{-\varepsilon} \\ &= -\frac{\alpha_s\Gamma(1-\varepsilon)C_F e^{\varepsilon\gamma_E}}{2\pi\mu\varepsilon\Gamma(1-2\varepsilon)}\left(\frac{\hat{s}}{\mu}\right)^{-1-2\varepsilon} \\ &= \frac{\alpha_s C_F}{4\pi}\left[\left(\frac{1}{\varepsilon^2}-\frac{\pi^2}{4}\right)\delta(\hat{s}) - \frac{2}{\varepsilon\mu}\left(\frac{\mu}{\hat{s}}\right)_+ + \frac{4}{\mu}\left(\frac{\mu\log(\hat{s}/\mu)}{\hat{s}}\right)_+\right], \end{aligned} \tag{2.103}$$

that, as expected, differs from the expression in Eq. (2.100) only in the non-divergent term of the delta-function coefficient. Similarly, we obtain for diagram (c)

$$\begin{aligned} mB^{\rm real}_{c,J}(\hat{s},\mu) &= -\frac{\alpha_s(\mu^2 e^{\gamma_E})^\varepsilon C_F}{\pi}\frac{\hat{s}^{\,-1-2\varepsilon}}{\Gamma(1-\varepsilon)}\int_0^1 \mathrm{d}x\,[x(1-x)]^{-\varepsilon} \\ &= -\frac{\alpha_s\Gamma(1-\varepsilon)C_F\, e^{\varepsilon\gamma_E}}{\pi\mu\Gamma(2-2\varepsilon)}\left(\frac{\hat{s}}{\mu}\right)^{-1-2\varepsilon} = \frac{\alpha_s C_F}{4\pi}\left[2\left(\frac{1}{\varepsilon}+2\right)\delta(\hat{s}) - \frac{4}{\mu}\left(\frac{\mu}{\hat{s}}\right)_+\right], \end{aligned} \tag{2.104}$$

again almost identical to the corresponding P-scheme computation. Adding twice the first diagram plus the second we recover the known result for the 2-jettiness bHQET jet function:

$$\begin{aligned} mB^J_n(\hat{s},\mu) &= -\frac{\alpha_s\Gamma(2-\varepsilon)C_F\, e^{\varepsilon\gamma_E}}{\pi\mu\varepsilon\Gamma(2-2\varepsilon)}\left(\frac{\hat{s}}{\mu}\right)^{-1-2\varepsilon} \\ &= \frac{\alpha_s C_F}{4\pi}\left[\left(\frac{2}{\varepsilon^2}+\frac{2}{\varepsilon}+4-\frac{\pi^2}{2}\right)\delta(\hat{s}) - \frac{4}{\mu}\left(\frac{1}{\varepsilon}+1\right)\left(\frac{\mu}{\hat{s}}\right)_+ + \frac{8}{\mu}\left(\frac{\mu\log(\hat{s}/\mu)}{\hat{s}}\right)_+\right]. \end{aligned} \tag{2.105}$$

Both schemes have the same divergent structure and hence their anomalous dimension, as expected, are identical. Furthermore, the difference between the respective delta coefficients is the same as that in the SCET jet functions. This result was also expected since both EFTs should smoothly match in the bHQET limit.

2.6 RG Evolution of the SCET Jet Function

In this section we solve the renormalization group equation for the non-distributional part of the jet function for thrust and 2-jettiness. This amounts to finding an analytic expression for the function $I_{\rm nd}$ defined in the last line of Eq. (2.32).

Even though the result for $I^J_{\rm nd}$ has been already worked out in Ref. [24], we present here the main steps to find the solution as they are illustrative. Using the rightmost integral expression of the bottom line in Eq. (2.32) we find

$$I^J_{\rm nd}(\tilde{\omega},y) = \frac{1}{\Gamma(-\tilde{\omega})}\int_0^1 \mathrm{d}z\,(1-z)^{-1-\tilde{\omega}}\left[\frac{zy}{(1+zy)^2} - \frac{4\log(1+zy)}{zy}\right]. \tag{2.106}$$

While the first term on the right-hand side of Eq. (2.106) is already in a canonical form such that Eq. (2.60) can be directly applied, the second contains a logarithm. Expressing it as an integral

$$\frac{\log(1+zy)}{zy} = \int_0^1 \mathrm{d}x\,\frac{1}{1+xzy}\,, \tag{2.107}$$

brings the second term also into a canonical form that we can easily integrate, finding

$$\int_0^1 \mathrm{d}z(1-z)^{-1-\tilde{\omega}}\,\frac{\log(1+zy)}{zy} = \int_0^1 \mathrm{d}x \int_0^1 \mathrm{d}z(1-z)^{-1-\tilde{\omega}}\frac{1}{1+xzy} \tag{2.108}$$
$$= -\frac{1}{\tilde{\omega}}\int_0^1 \mathrm{d}x\, {}_2F_1(1,1,1-\tilde{\omega},-xy) = -\frac{1}{\tilde{\omega}}\,{}_3F_2(1,1,1,2,1-\tilde{\omega},-y)\,,$$

where in the last step we have used the integral representation of the ${}_3F_2$ function:

$${}_3F_2(a_1,a_2,a_3,b_1,b_2,z) = \frac{\Gamma(b_2)}{\Gamma(a_3)\Gamma(b_2-a_3)}\int_0^1 \mathrm{d}t\, t^{a_3-1}(1-t)^{b_2-1-a_3}\,{}_2F_1(a_1,a_2,b_1,tz)\,, \tag{2.109}$$

with $a_1 = a_2 = a_3 = 1$, $b_1 = 1-\tilde{\omega}$ and $b_2 = 2$. After adding the result for the first term we find an expression slightly simpler than that quoted in Ref. [24], although fully equivalent:

$$I^J_{\mathrm{nd}}(\tilde{\omega},y) = \frac{1}{\Gamma(2-\tilde{\omega})}\left[y\,{}_2F_1(2,2,2-\tilde{\omega},-y) - (1-\tilde{\omega})\,{}_3F_2(1,1,1,2,1-\tilde{\omega},-y)\right], \tag{2.110}$$

which has a smooth $\tilde{\omega}\to 0$ limit.

For P-scheme thrust we can write the logarithm as a derivative to bring all terms into a canonical form:

$$I^P_{\mathrm{nd}}(\tilde{\omega},y) = \frac{1}{\Gamma(-\tilde{\omega})}\int_0^1 \mathrm{d}z(1-z)^{-1-\tilde{\omega}}\left[\frac{zy-7}{(1-yz)^2} + \frac{2zy(2zy-5)}{(1-yz)^3}\log(zy)\right] \tag{2.111}$$
$$\frac{1}{\Gamma(-\tilde{\omega})}\int_0^1 \mathrm{d}z\,(1-z)^{-1-\tilde{\omega}}\left\{\frac{zy-7}{(1-yz)^2} + \frac{2yz(2zy-5)}{(1-yz)^3}\left[\log(y) + \frac{\mathrm{d}}{\mathrm{d}\varepsilon}z^{\varepsilon}\right]\right\}_{\varepsilon\to 0}.$$

For $y>1$ each one of the terms in the integral diverges when $z = 1/y$. We can regularize the divergence adding a small imaginary part $y\to y+i\epsilon$. This makes each integral complex, although the sum is real when $\epsilon\to 0$. To express our result in terms of a minimal set of hypergeometric functions, we use the following identity:

$$(c-b){}_2F_1(a,b-1,c,z) + (c-1)(z-1){}_2F_1(a,b,c-1,z) \tag{2.112}$$
$$+\,[z(a-c+1)+b-1]{}_2F_1(a,b,c,z) = 0.$$

Furthermore, one can use an additional identity to make the final result manifestly real also for the case $y>1$

$${}_2F_1(a,b;c;z) = \frac{\Gamma(c)(1-z)^{c-a-b}\Gamma(a+b-c)\,{}_2F_1(c-a,c-b,1+c-a-b,1-z)}{\Gamma(a)\Gamma(b)} \tag{2.113}$$
$$+\,\frac{\Gamma(c)\Gamma(c-a-b)\,{}_2F_1(a,b,a+b-c+1,1-z)}{\Gamma(c-a)\Gamma(c-b)}.$$

After solving all integrals, recursively applying Eq. (2.112) and transforming the hypergeometric functions using Eq. (2.113), one arrives at:[14]

$$I^P_{\rm nd}(\tilde\omega,y) = \frac{4y^2-2(\tilde\omega+5)y-\tilde\omega(3\,\tilde\omega+7)}{(1-y)^2(1+\tilde\omega)\Gamma(1-\tilde\omega)}\Bigg\{\tilde\omega\frac{\rm d}{{\rm d}\varepsilon}\,{}_2F_1(1,1+\varepsilon,2+\tilde\omega,1-y) \\ +\left(\tilde\omega\log(y)-\tilde\omega H_{1-\tilde\omega}-\frac{1-2\tilde\omega}{1-\tilde\omega}\right){}_2F_1(1,1,2+\tilde\omega,1-y)\Bigg\}_{\varepsilon\to0} \\ -\frac{(1-\tilde\omega)\tilde\omega(3\,\tilde\omega-y+7)[H_{1-\tilde\omega}-\log(y)]-\tilde\omega[3\,\tilde\omega(y+1)-5y+14]-y+7}{\Gamma(2-\tilde\omega)(1-y)^2}\,, \tag{2.115}$$

with H_a the harmonic number, which for non-integer values of a can be expressed in terms of the digamma function: $H_a=\psi^{(0)}(1+a)+\gamma_E$.

Equation (2.115) has been cast in a way in which the no-resummation limit $\tilde\omega\to0$ is smooth. The singularities that appear in individual terms of $J^P_{\rm nd}$ for $x=1$ manifest themselves now as a double pole in $I^P_{\rm nd}$ at $y=1$, which is however fictitious, as the result is indeed smooth at this value. To solve this problem in numerical implementations we provide in Sec. 2.6.2 an expansion of this result around $y=1$ at an arbitrarily high order.

The result in Eq. (2.115) is adequate for a numerical implementation since the derivative with respect to ε can be taken numerically through finite differences. It can be also performed analytically, using Eq. (2.113) in ${}_2F_1(1,1+\varepsilon,2+\tilde\omega,1-y)$ and the following identity

$$\frac{\rm d}{{\rm d}\varepsilon}{}_2F_1(1,1+\varepsilon,1-\tilde\omega+\varepsilon,y)\Big|_{\varepsilon\to0} = -\frac{\tilde\omega\,y(1-y)^{-1-\tilde\omega}}{(1-\tilde\omega)^2}{}_3F_2(1-\tilde\omega,1-\tilde\omega,1-\tilde\omega,2-\tilde\omega,2-\tilde\omega,y), \tag{2.116}$$

to arrive at the equivalent expression:

$$I^P_{\rm nd}(\tilde\omega,y) = \\ \frac{\tilde\omega\,y(1-y)^{-3-\tilde\omega}[\,2\,y\,(\tilde\omega+5)+\tilde\omega(3\tilde\omega+7)-4y^2\,]\,{}_3F_2(1-\tilde\omega,1-\tilde\omega,1-\tilde\omega,2-\tilde\omega,2-\tilde\omega,y)}{\Gamma(2-\tilde\omega)(1-\tilde\omega)} \\ -\frac{(1-\tilde\omega)\,\tilde\omega\,(3\,\tilde\omega-y+7)[\,H_{1-\tilde\omega}-\log(y)\,]-\tilde\omega\,[\,3\,\tilde\omega\,(y+1)-5\,y+14\,]-y+7}{\Gamma(2-\tilde\omega)(1-y)^2} \\ +\frac{[\,2\,y\,(\tilde\omega+5)+\tilde\omega\,(3\,\tilde\omega+7)-4y^2\,]\{(1-\tilde\omega)[\,H_{1-\tilde\omega}-\log(y)\,]-1\}{}_2F_1(1,1,1-\tilde\omega,y)}{\Gamma(2-\tilde\omega)(1-y)^2}. \tag{2.117}$$

The $(1-y)^{-3-\tilde\omega}$ factor and both hypergeometric functions are complex for $y>1$ but the combination is real. To have all terms explicitly real for $y>1$ one can use the following relation

$$\frac{\rm d}{{\rm d}\varepsilon}{}_2F_1(1,1+\varepsilon,2+\tilde\omega,1-y)\Big|_{\varepsilon\to0} = \frac{1-y}{y^2(2+\tilde\omega)^2}\,{}_3F_2\left(2,2+\tilde\omega,2+\tilde\omega,3+\tilde\omega,3+\tilde\omega,1-\frac{1}{y}\right) \\ +y^{\tilde\omega}(1-y)\frac{1+\tilde\omega}{(2+\tilde\omega)^2}\,{}_3F_2(2+\tilde\omega,2+\tilde\omega,2+\tilde\omega,3+\tilde\omega,3+\tilde\omega,1-y)\,, \tag{2.118}$$

[14] The result as given in this equation is very convenient for a numerical implementation, since one only needs to evaluate two hypergeometric functions (which might be numerically expensive) using the following approximations:

$$\frac{\rm d}{{\rm d}\varepsilon}\,{}_2F_1(1,1+\varepsilon,2+\tilde\omega,1-y)\Big|_{\varepsilon=0} \simeq \frac{1}{2\varepsilon}[{}_2F_1(1,1+\varepsilon,2+\tilde\omega,1-y)-{}_2F_1(1,1-\varepsilon,2+\tilde\omega,1-y)]\,, \tag{2.114}$$
$${}_2F_1(1,1,2+\tilde\omega,1-y) \simeq \frac{1}{2}[{}_2F_1(1,1+\varepsilon,2+\tilde\omega,1-y)+{}_2F_1(1,1-\varepsilon,2+\tilde\omega,1-y)]\,,$$

with a value of ε which can be safely taken as small as 10^{-6}.

which does not rely on numerical derivatives, is manifestly real for all positive values of y but is numerically unstable if $y \to 0$. This poses no problem in practice, since for $y < 1$ one can simply switch to Eq. (2.117). To derive the result in Eq. (2.118) we proceed as follows:

$$\begin{aligned}
\frac{\mathrm{d}}{\mathrm{d}\varepsilon}{}_2F_1(1,1+\varepsilon,2+\tilde{\omega},1-y)\Big|_{\varepsilon\to 0} &= -\frac{1}{y}\frac{\mathrm{d}}{\mathrm{d}b}{}_2F_1\left(1,b,2+\tilde{\omega},1-\frac{1}{y}\right)\Big|_{b\to 1+\tilde{\omega}} \\
&= \frac{1}{y}\frac{\mathrm{d}}{\mathrm{d}b}\left[{}_2F_1\left(1,1+\tilde{\omega},b+1,1-\frac{1}{y}\right) - {}_2F_1\left(1,b,b+1,1-\frac{1}{y}\right)\right]_{b\to 1+\tilde{\omega}} \\
&= \frac{1}{y}\frac{\mathrm{d}}{\mathrm{d}b}\left[y^{1+\tilde{\omega}}{}_2F_1(b,1+\tilde{\omega},b+1,1-y) - {}_2F_1\left(1,b,b+1,1-\frac{1}{y}\right)\right]_{b\to 1+\tilde{\omega}}
\end{aligned} \tag{2.119}$$

where in the first step we have used Eq. (2.61), in the second we apply the chain rule on derivatives, and in the third line we use again Eq. (2.61) on the first term. Using the identity

$$\frac{\mathrm{d}}{\mathrm{d}a}\,{}_2F_1(a,b,a+1,z) = \frac{bz}{(a+1)^2}\,{}_3F_2(a+1,a+1,b+1,a+2,a+2,z)\,, \tag{2.120}$$

in the two terms of the last line in Eq. (2.119) we arrive at the result quoted in Eq. (2.118).

In Appendix B.2 we present an alternative (although more complicated) expression for I^P_{nd} which does not involve numerical derivatives and with every term manifestly real for $y > 1$. We use this result as an additional cross-check of our analytic derivations. In any case, we shall see that for implementations in computer codes, one never needs to use expressions involving hypergeometric functions.

2.6.1 Expansion around $s = 0$

For numerical implementation purposes, it might be convenient to obtain an analytic expansion of $I_{\mathrm{nd}}(\tilde{\omega}, y)$ around $y = 0$ since otherwise the evaluation of the non-distributional jet function running might lead to a performance bottleneck. One can do so by using the known expansions for the hypergeometric functions, e.g.

$${}_2F_1(a,b,c,z) = \frac{\Gamma(c)}{\Gamma(a)\Gamma(b)}\sum_{i=0}^{\infty}\frac{\Gamma(a+i)\Gamma(b+i)}{\Gamma(c+i)\Gamma(i+1)}\,z^i\,, \tag{2.121}$$

but in order to have a relation valid at arbitrarily high orders it is simpler to use the expansion of $J_{\mathrm{nd}}(x)$ around $x = 0$

$$\begin{aligned}
J^P_{\mathrm{nd}}(x) &= -\sum_{i=0}[\,6\,i+7+i(7+3i)\log(x)\,]\,x^i\,, \\
J^J_{\mathrm{nd}}(x) &= -\sum_{i=0}\left(i+\frac{4}{i+1}\right)(-x)^i\,,
\end{aligned} \tag{2.122}$$

on the leftmost expression of the bottom line in Eq. (2.32) and integrate analytically term by term. It turns out that one can sum up the corresponding series using Eq. (2.121) to recover an expression analytically equivalent to Eq. (2.117). The master integrals that we will need are

$$\begin{aligned}
\frac{y^{\tilde{\omega}}}{\Gamma(-\tilde{\omega})}\int_0^y \mathrm{d}x\,(y-x)^{-1-\tilde{\omega}}x^i &= y^i\frac{\Gamma(1+i)}{\Gamma(1+i-\tilde{\omega})}\,, \\
\frac{y^{\tilde{\omega}}}{\Gamma(-\tilde{\omega})}\int_0^y \mathrm{d}x\,(y-x)^{-1-\tilde{\omega}}x^i\log(x) &= y^i\frac{\Gamma(1+i)}{\Gamma(1+i-\tilde{\omega})}[H_i - H_{i-\tilde{\omega}} + \log(y)]\,,
\end{aligned} \tag{2.123}$$

where the bottom line can be obtained from the top one acting with a derivative with respect to i. We then arrive at

$$I^P_{\rm nd}(\tilde\omega,y) = -\frac{1}{\Gamma(1-\tilde\omega)}\sum_{i=0}\frac{i!}{(1-\tilde\omega)_i}\{(6i+7)+i(7+3i)[H_i - H_{i-\tilde\omega}+\log(y)]\}\,y^i\,, \tag{2.124}$$
$$I^J_{\rm nd}(\tilde\omega,y) = -\frac{1}{\Gamma(1-\tilde\omega)}\sum_{i=0}\left(i+\frac{4}{i+1}\right)\frac{i!}{(1-\tilde\omega)_i}(-y)^i\,,$$

where we have used the Pochhammer symbol $(a)_n \equiv \Gamma(a+n)/\Gamma(a)$. Both series converge well for $|y|<1$, and therefore apply mainly in the peak of the distribution. For 2-jettiness the series can be easily summed up using Eq. (2.121) and the series expansion for the ${}_3F_2$ hypergeometric function:

$${}_3F_2(a,b,c,d,e,z) = \frac{\Gamma(c)}{\Gamma(a)\Gamma(b)}\sum_{i=0}^{\infty}\frac{\Gamma(a+i)\Gamma(b+i)\Gamma(c+i)}{\Gamma(d+i)\Gamma(e+i)\Gamma(i+1)}\,z^i\,. \tag{2.125}$$

For P-scheme thrust one can convert the term involving harmonic numbers into the derivative of ratios of gamma functions to use Eq. (2.121) and recover the result we already obtained with a direct integration.

2.6.2 Expansion around $s = m^2$

The results obtained in Eqs. (2.115) and (2.117) are not useful for a numerical implementation in the vicinity of $y=1$. When y is sufficiently close to unity one can switch to a series expansion to arbitrary high power using the change of variables $z \to 1-z$ in the rightmost expression at the bottom of Eq. (2.32) and the following expansion:

$$\begin{aligned}
J^P_{\rm nd}[(1-z)(1+y)] &= -\left[\frac{2(1-z)(3+2z)}{z^3}\log(1-z)+\frac{z+6}{z^2}\right] - y(1-z)\left[2\frac{9-2z-2z^2}{z^4}\right. \\
&\left.\times\log(1-z)+\frac{5z+18}{z^3}\right] - y^2(1-z)\left\{\frac{2(1-z)(18-3z-2z^2)}{z^5}\log(1-z)\right. \\
&\left.+\frac{36-24z-7z^2}{z^4}\right\} - \log(1-z)\sum_{i=3}y^i\frac{(1-z)^i}{z^{i+3}}[3(i+1)(i+2)-2(i+1)z-4z^2] \\
&-\frac{1}{2}\sum_{i=3}y^i\frac{(1-z)^{i-1}}{z^{2+i}}\{6(i+1)(i+2)-(i+1)(3i+10)z-2[1-(i-5)i]z^2\} \\
&+\sum_{i=3}y^i\sum_{k=0}^{i-3}(-1)^{k+i}\frac{(1-z)^{k+1}}{z^{k+3}}\frac{(k+1)(k+2)(6-5i+5k+4z)}{(i-k-2)(i-k-1)(i-k)}.
\end{aligned} \tag{2.126}$$

Terms have been combined such that the coefficient of each power in y has a well-defined $z\to 0$ limit and therefore we can integrate coefficient by coefficient. In practice, one can integrate each piece assuming a non-integer value of i and subsequently convert the gamma functions that would become divergent if $\tilde\omega = 0$ using the identity

$$\frac{\Gamma(\varepsilon-n)}{\Gamma(1+\varepsilon)} = \frac{(-1)^{n-1}\Gamma(-\varepsilon)}{\Gamma(n+1-\varepsilon)}. \tag{2.127}$$

As expected, there are large cancellations among the various terms for a given power of y, but when adding all contributions one gets the following nicely convergent series:

$$
\begin{aligned}
I^P_{\rm nd}(\tilde\omega,y) = &-\frac{2(5\,\tilde\omega+9)\tilde\omega H_{-\tilde\omega}+7\,\tilde\omega^3+19\,\tilde\omega^2+22\,\tilde\omega+18}{(\tilde\omega+1)(\tilde\omega+2)(\tilde\omega+3)\Gamma(1-\tilde\omega)} \\
&-\frac{\tilde\omega\,\Gamma(1+\tilde\omega)}{\Gamma(1-\tilde\omega)}\sum_{i=3}(1-y)^i\sum_{k=0}^{i-3}\frac{(k+1)(k+2)![(k+2)(5\,\tilde\omega+9)-5i(\tilde\omega+1)]}{(i-k-2)(i-k-1)(i-k)\Gamma(k+\tilde\omega+4)} \\
&+\frac{\Gamma(1+\tilde\omega)}{2\,\Gamma(1-\tilde\omega)}\sum_{i=1}\frac{i!(1-y)^i}{\Gamma(i+\tilde\omega+4)}\big\{\tilde\omega(i+\tilde\omega+1)[2i^3+i^2(\tilde\omega-3)+i(\tilde\omega(5\,\tilde\omega-8)-39) \\
&-(\tilde\omega+6)(5\,\tilde\omega+9)]+[20i-2\,i\,\tilde\omega(i(3\,\tilde\omega+7)+7\,\tilde\omega+9)+4(5\,\tilde\omega+9)] \\
&\times[\tilde\omega\,\psi^{(0)}(i+1)-\tilde\omega\,\psi^{(0)}(1-\tilde\omega)-1]\big\},
\end{aligned}
\tag{2.128}
$$

where again special care has been taken to write the expression in a manner in which one can set $\tilde\omega = 0$ without any worries. The series converges well for $|1-y|<1$, and therefore, combined with the expansion worked out in the previous section, for P-scheme thrust one can use expansions if $y<2$.

2.6.3 Expansion around $s=\infty$

Since the numerical evaluation of hypergeometric functions is slow, it is convenient to figure out another series expression (in this case, of asymptotic type) around $s=\infty$, which is of course tantamount to $m=0$. This limit is very relevant, since it can be applied in the tail of the distribution and almost everywhere if the heavy quark mass is much smaller than the center-of-mass energy, as is the case for bottom quarks at LEP.

Even though one could, in principle, use known results for the asymptotic expansions of ${}_2F_1$ and ${}_3F_2$ hypergeometric functions, it is in practice simpler and more efficient to compute the series directly in its integral form. This is complicated since, as we shall see, the expansions involve powers of $\log(y)$, and so one cannot simply expand the integrand and integrate term by term, as we did in Secs. 2.6.1 and 2.6.2.

We found out that the Mellin-Barnes representation in Eq. (1.71) is optimal to achieve our goal.[15] As we saw in Sec. 1.5, after applying Eq. (1.71), the expansion around $x\gg 1$ is obtained integrating by residues the poles that appear on the real axis for the Mellin plane variable[16] $t>\nu$ (the poles for $t\le 0$ correspond to the expansion $x\ll 1$).

Mellin-Barnes will be further exploited in Chapter 4 for the development of an easier way to compute massive bubbles contributions, whereas in the rest of this section we just apply it to work out the corresponding asymptotic expansions for thrust and 2-jettiness in the regime we are now studying.

We note that this expansion is well convergent if $1/y<1$, which for P-scheme thrust means that in numerical evaluations one can always use one of the three expansions presented in this section and never

[15] This representation can also be used to solve the RG equation exactly. Applying a Mellin transformation to the first line of Eq. (2.111) in the y-variable, solving the z-integral and transforming back one gets a closed (and rather short) analytic expression for $I^P_{\rm nd}$ in terms of MeijerG functions,

$$
I^P_{\rm nd}(\tilde\omega,y) = 3\,G^{2,3}_{3,3}\left(y\left|\begin{matrix}0,0,0\\1,1,\tilde\omega\end{matrix}\right.\right) - 7\,G^{2,3}_{3,3}\left(y\left|\begin{matrix}0,0,0\\0,1,\tilde\omega\end{matrix}\right.\right),
\tag{2.129}
$$

which are not very convenient for a direct numerical evaluation, but can be related to hypergeometric functions.

[16] In this Chapter we will use t instead of h.

needs to evaluate hypergeometric functions with dedicated routines. For jettiness the same statement is almost true, except in a small vicinity of $y = 1$ in which no expansion was found but, unlike for P-scheme, the analytical results already provided are numerically stable since there are no large cancellations.

2-Jettiness

We start from the integral form given in Eq. (2.106). The only complication in this case is that we have to deal with a logarithm, which does not have the form in Eq. (1.71). However, it can be brought to the standard form using Eq. (2.107)

$$\begin{aligned}\frac{1}{yz}\log(1+zy) &= \frac{1}{2\pi i}\int_0^1 \mathrm{d}x \int_{d-i\infty}^{d+i\infty} \mathrm{d}t\,(xyz)^{-t}\Gamma(t)\Gamma(1-t) \\ &= \frac{1}{2\pi i}\int_{d-i\infty}^{d+i\infty} \mathrm{d}t\,(zy)^{-t}\frac{\Gamma(t)\Gamma(1-t)}{1-t},\end{aligned} \tag{2.130}$$

with $0 < d < 1$. Since the denominator of the first term in Eq. (2.106) is squared, when applying the Mellin-Barnes representation (1.71) the first pole appears at $t = 2$. This is accompanied by an extra power of y, such that we can nicely map the poles of the first term into those of the second by shifting the integration variable $t \to t + 1$ in the former. After integrating over z we obtain

$$I^J_{\mathrm{nd}}(\tilde{\omega}, y) = \frac{1}{2\pi i}\int_{c-i\infty}^{c+i\infty} \mathrm{d}t\, y^{-t}\frac{\Gamma(1-t)^2\Gamma(t)}{\Gamma(1-t-\tilde{\omega})}\frac{t^2-t+4}{t-1}\,, \tag{2.131}$$

with $0 < c < 1$. The integrand has a triple pole at $t = 1$ and double poles at natural values of t larger than 1. We compute the triple pole by itself and treat the rest generically using

$$\Gamma(\varepsilon - n)^2 = \frac{1}{(n!)^2}\left[\frac{1}{\varepsilon^2} + \frac{2(H_n - \gamma_E)}{\varepsilon}\right] + \mathcal{O}(\varepsilon^0)\,. \tag{2.132}$$

With this result we obtain the following asymptotic expansion:

$$\begin{aligned} I^J_{\mathrm{nd}}(\tilde{\omega}, y) &= \frac{1}{\Gamma(1-\tilde{\omega})}\sum_{n=1}(-y)^{-n}c_n[\tilde{\omega}, \log(y)]\,, \\ c_1(\tilde{\omega}, L) &= -1 - 2\tilde{\omega}[H_{-\tilde{\omega}} - L]^2 - (4+\tilde{\omega})[H_{-\tilde{\omega}} - L] - [1 + \pi^2 - 2\psi^{(1)}(1-\tilde{\omega})]\tilde{\omega}\,, \\ c_{n>1}(\tilde{\omega}, L) &= \frac{(1+\tilde{\omega})_{n-1}}{(n-1)^2(n-1)!}\{(n-1)[(n-2)(n+1)+6][\tilde{\omega}(H_{n-1} - H_{n+\tilde{\omega}-1} + L) \\ &\quad - \cos(\pi\tilde{\omega})\Gamma(1-\tilde{\omega})\Gamma(1+\tilde{\omega})] - (n-3)(n+1)\,\tilde{\omega}\}\,, \end{aligned} \tag{2.133}$$

using again the Pochhammer symbol. We have written each coefficient in a form such that the $\tilde{\omega} \to 0$ limit, relevant in the far tail of the distribution, is smooth.

P-scheme thrust

Applying the Mellin-Barnes representation in Eq. (1.71) to the first line of Eq. (2.111) and integrating over z we arrive at an expression that involves different powers of y with poles shifted accordingly. Therefore, using the same strategy as in the previous section, we can shift the integration variable by one or two units such that poles and powers of y in each term exactly match. This is very important, since the expansion in $1/y$ must be carried out consistently given the large cancellations that take

place among the various terms due to the divergence at $x = 1$ of individual terms in $J^P_{\rm nd}$ (exactly as it happened for the expansion around $s = m^2$). After some work we arrive at the following expression:

$$I^P_{\rm nd}(\tilde{\omega}, y) = \frac{1}{2\pi i}\int_{c-i\infty}^{c+i\infty} {\rm d}t\, y^{-t}\frac{\cos(\pi t)\Gamma(1-t)^2\Gamma(t)}{\Gamma(1-t-\tilde{\omega})} \times \{(7-3t)t[H_{-t} - H_{-t-\tilde{\omega}} + \log(y)] + 6t - 7\}\,. \tag{2.134}$$

We have already implemented a few simplifications because we assume the result is real, and therefore discarded the imaginary parts that would arise from $(-y)^{-t}$. We have checked that indeed this is the case as long as one expands strictly in y without mixing any powers. Harmonic numbers are caused by the term in $J^P_{\rm nd}$ proportional to $\log(z)$.

The integrand has now double and triple poles, located at natural values of t, the latter arising precisely because of the harmonic numbers. There are no poles arising from $H_{-t-\tilde{\omega}}$ because the corresponding gamma function in the denominator has poles at the same values, making the ratio regular. To compute the residues of the poles we need, on top of Eq. (2.132), the following expansion

$$H_{\varepsilon-n}\Gamma(\varepsilon-n)^2 = \frac{1}{(n!)^2}\left\{-\frac{1}{\varepsilon^3} + \frac{1}{\varepsilon^2}[\psi^{(0)}(n) - 2H_n + 3\gamma_E] + \frac{2\gamma_E n + 2(n\gamma_E - 1)n\psi^{(0)}(n) - 3}{n^2\varepsilon}\right\} + \mathcal{O}(\varepsilon^0)\,, \tag{2.135}$$

which can be obtained from the relation between harmonic numbers and the digamma function and a bit of algebra. Using these results we arrive at the following expression, in which again special care has been taken to make the $\tilde{\omega} \to 0$ limit smooth:

$$I^P_{\rm nd}(\tilde{\omega}, y) = \frac{1}{\Gamma(1-\tilde{\omega})}\sum_{n=1}\frac{c_n[\tilde{\omega}, \log(y)]}{y^n}\,, \tag{2.136}$$

$$\begin{aligned} c_n(\tilde{\omega}, L) = {}& \frac{(1+\tilde{\omega})_{n-1}}{2(n-1)!}\left\{\frac{2}{n+\tilde{\omega}}[L(3n-7)n(n+\tilde{\omega}) - 3n^2 - 6n\tilde{\omega} + 7\tilde{\omega}]\right. \\ & \times [\cos(\pi\tilde{\omega})\Gamma(1-\tilde{\omega})\Gamma(1+\tilde{\omega}) - \tilde{\omega}(\psi^{(0)}(n) - \psi^{(0)}(n+\tilde{\omega}+1))] \\ & + \frac{\tilde{\omega}}{n(n+\tilde{\omega})}[2Ln(3n(n+2\tilde{\omega}) - 7\tilde{\omega}) - 3n(\tilde{\omega} - 3n + 7) - 7\tilde{\omega}] \\ & - (7-3n)n\left[\tilde{\omega}\,\psi^{(1)}(n+1) - \tilde{\omega}\psi^{(1)}(n+\tilde{\omega}) - \tilde{\omega}L^2 - \frac{\tilde{\omega}}{(n+\tilde{\omega})^2}\right. \\ & + [\psi^{(0)}(n) - \psi^{(0)}(n+\tilde{\omega}+1)][\tilde{\omega}(\psi^{(0)}(1+n+\tilde{\omega}) - \psi^{(0)}(n)) \\ & \left.\left. + 2\cos(\pi\tilde{\omega})\Gamma(1-\tilde{\omega})\Gamma(\tilde{\omega}+1)]\right]\right\}. \end{aligned}$$

2.7 Power corrections

Once we have all the ingredients in the factorization theorems we can carry out the implementation of the partonic cross-section at leading order in the corresponding EFT. As discussed before, when considering a massive primary quark, the bHQET and SCET frameworks will be suitable to describe the peak and tail regions respectively. Nevertheless in this section we present a procedure to complete the EFT setup by adding the missing power corrections to extend the regime of validity.

Since the numerical analysis will be for the SCET results we will also consider this case for the discussion below but an analogous process can be applied in bHQET.

2.7.1 Mass and kinematic

For massless quarks, there are only kinematic power corrections and SCET reproduces entirely the singular terms[17] (which are the leading order part) of QCD. Therefore to include the fair-tail region in the analysis by matching to the full-theory description one can just add the non-singular part of the corresponding fixed-order massless QCD cross-section to the massless resummed SCET result

$$\frac{1}{\sigma_0}\frac{\mathrm{d}\hat{\sigma}^{\mathrm{m=0}}}{\mathrm{d}\tau}=\frac{1}{\sigma_0}\frac{\mathrm{d}\hat{\sigma}^{\mathrm{SCET,m=0}}}{\mathrm{d}\tau}+\frac{1}{\sigma_0}\frac{\mathrm{d}\hat{\sigma}_{\mathrm{NS}}^{\mathrm{QCD,m=0}}}{\mathrm{d}\tau}\,, \tag{2.137}$$

On the other hand, a non-vanishing primary quark mass is power counted in SCET as the square root of the kinematic variable $\hat{m}\sim\sqrt{\tau}\sim\lambda$ in such a way that in the factorization theorem only the leading order mass terms of the singular and the limit $\lambda\to 0$ of the non-singular QCD distribution [see Eq. (2.90)] are considered:

$$\frac{1}{\sigma_0}\frac{\mathrm{d}\hat{\sigma}_{\mathrm{FO}}^{\mathrm{SCET}}}{\mathrm{d}\tau}=\frac{1}{\sigma_0}\frac{\mathrm{d}\hat{\sigma}_{\mathrm{sing}}^{\mathrm{QCD}}}{\mathrm{d}\tau}(\tau,\hat{m}=0)+\lim_{\lambda\to 0}\frac{1}{\sigma_0}\frac{\mathrm{d}\hat{\sigma}_{\mathrm{NS}}^{\mathrm{QCD}}}{\mathrm{d}\tau}(\tau\sim\lambda^2,\hat{m}\sim\lambda)\,. \tag{2.138}$$

Then, to account for the power corrections we will follow the same approach as in Refs. [1, 2, 8], where the corresponding singular structures are implemented within the SCET factorization theorem in order to apply the resummation on them as well. This is achieved by modifying the matrix elements in the following way:

$$H^C(Q,\hat{m},\mu)=R_0^C(\hat{m})\left\{1+\frac{\alpha_s(\mu)C_F}{4\pi}\left[\frac{7\pi^2}{3}-16+h_m^C(\hat{m})+12\log\left(\frac{Q}{\mu}\right)-8\log^2\left(\frac{Q}{\mu}\right)\right]\right\}, \tag{2.139}$$

$$J_m^C(x,\hat{m})=[\,j_m^C(\hat{m})+A_P\,]\delta(x)+4\left[\frac{\log(x)}{x}\right]_+-[\,1-y_m^C(\hat{m})\,]\left(\frac{1}{x}\right)_+,$$

and carrying out the rescaling due to the tree level mass corrections $R_0^C(\hat{m})$ accordingly when combining them together. Notice that the soft function cannot have mass contributions at one loop so it remains unchanged. Imposing that the modified factorization theorem to reproduces full-QCD at fixed order, one arrives at

$$y_m^C(\hat{m})=\frac{1}{2R_0^C(\hat{m})}\{[1-R_0^C(\hat{m})]B_S(\hat{m})+B_{\mathrm{NS}}^C(\hat{m})\}\,, \tag{2.140}$$

$$\begin{aligned}R_0^C(\hat{m})\,[\,h_m^C(\hat{m})+2j_m^C(\hat{m})\,]&=2\,\{B_S(\hat{m})[1-R_0^C(\hat{m})]+B_{\mathrm{NS}}^C(\hat{m})\}\log(\hat{m})\\&\quad+[1-R_0^C(\hat{m})]A_S(\hat{m})+A_{\mathrm{NS}}^C(\hat{m})\equiv H_{\mathrm{corr}}^C(\hat{m})\,,\end{aligned}$$

where we defined $A^C(\hat{m})=A^{\mathrm{SCET}}(\hat{m})+A_C^{\mathrm{NS}}(\hat{m})$ and $B_{\mathrm{plus}}^C(\hat{m})=B^{\mathrm{SCET}}(\hat{m})+B_{\mathrm{NS}}^C(\hat{m})$. The system of equations is undetermined but we can distribute the corrections according to a parameter ξ and vary it in the numerical analysis (between 0 and 1) to account for this uncertainty:

$$h_m^C(\hat{m})=\frac{1-\xi}{R_0^C(\hat{m})}H_{\mathrm{corr}}^C(\hat{m})\,,\qquad j_m^C(\hat{m})=\frac{\xi}{2R_0^C(\hat{m})}H_{\mathrm{corr}}^C(\hat{m})\,. \tag{2.141}$$

[17] By singular terms we mean in practice those terms that contain distributions. There may be other terms with divergences in the dijet limit but they are of logarithmic nature and therefore integrable singularities. This happens for the event shapes whose minimum value is zero such as any in P- or E-schemes.

The final partonic cross-section is then given by adding the non-singular corrections to the resummed SCET factorization theorem with modified matrix elements denoted by $\frac{\mathrm{d}\tilde{\sigma}^C_{\mathrm{SCET}}}{\mathrm{d}\tau}$, that is:

$$\begin{aligned}\frac{\mathrm{d}\hat{\sigma}^C}{\mathrm{d}\tau} &= \frac{\mathrm{d}\tilde{\sigma}^C_{\mathrm{SCET}}}{\mathrm{d}\tau} + \frac{\mathrm{d}\hat{\sigma}^C_{\mathrm{NS}}}{\mathrm{d}\tau}\,, \\ \frac{1}{\sigma_0^C}\frac{\mathrm{d}\hat{\sigma}^C_{\mathrm{NS}}}{\mathrm{d}\tau} &= \frac{\alpha_s(\mu)C_F}{4\pi}[F^C_{\mathrm{NS}}(\tau,\hat{m}) - F^{\mathrm{SCET}}_{\mathrm{NS}}(\tau,\hat{m})]\,.\end{aligned} \tag{2.142}$$

2.7.2 Hadronization

Despite the fact that in the fair tail of the distribution hadronization effects can be taken into account through an OPE leading to a shift towards the right at leading power, to account for them in the whole range one needs to convolve the partonic result with a hadronic shape function:

$$\frac{\mathrm{d}\sigma^C(\tau)}{\mathrm{d}\tau} = \int_0^{Q\tau}\mathrm{d}p\,\frac{\mathrm{d}\hat{\sigma}^C}{\mathrm{d}\tau}\left(\tau - \frac{p}{Q}\right)F(p)\,. \tag{2.143}$$

The shape function properties are the following: it must be different form zero only for positive values of p, should be normalized to unity $\int_0^\infty \mathrm{d}pF(p) = 1$, has to peak at $p \sim \Lambda_{\mathrm{QCD}}$ and its moments shall be well defined such that they can be matched to the OPE results. In particular, even though the code we have developed allows the convolution with any function, for the numerical analysis we will work with:

$$F(p) = \frac{128\,p^3\,e^{-\frac{4p}{\lambda}}}{3\lambda^4}\,, \tag{2.144}$$

that comes from the basis proposed on Ref. [49], taking $\lambda = 0.5\,\mathrm{GeV}$.

2.8 Numerical analysis

In this section we present an analysis based on the numerical results obtained for the P-scheme thrust distribution at N^{2}LL+$\mathcal{O}(\alpha_s)$ in SCET including power corrections for a (massive) primary bottom quark, but first we shall discuss a last couple of details necessary to obtain the final expression.

The natural scales of the matrix elements are dynamical (different on each point of the distribution) therefore, to properly implement the resummation, a different value for the renormalization scales on each point is also needed. This is achieved through so-called profile functions, that is, function that depend on the value of the event-shape. Here we use the ones introduced for the massless case in Ref. [38] because we will consider physical situations in which the mass effects are still small (scenario IV) and, in principle, there is no need of mass-dependent profile functions.

Additionally, the fixed-order QCD distribution, necessary to extend the validity of the analysis to the far tail as explained in the previous section, is only known numerically (but with arbitrary precision) from the algorithms described in Ref. [48]. To incorporate this contribution in our code, we parametrize the function obtained after the known singular behavior is subtracted, combining a fit (for the lower values) and an interpolation, smoothly joined.

Having added all pieces to our code, we show some cross sections as a number of plots in the rest of this section for which we use α_s running at 4-loops with five active flavors (four light quarks plus the heavy bottom) and the reference value $\alpha_s^{(n_f=5)}(m_Z) = 0.1181$. We also employ the 4-loop $\overline{\mathrm{MS}}$ mass

scheme with, unless otherwise stated, the following reference value: $\overline{m}_b(\overline{m}_b) = 4.2\,\text{GeV}$.

Fig. 2.7 represents the contribution from the different pieces (each of them convolved with the shape function) in the following cross-section decomposition:

$$\begin{aligned}\frac{\mathrm{d}\sigma}{\mathrm{d}\tau} &= \frac{\mathrm{d}\sigma_{\text{SCET}}}{\mathrm{d}\tau} + \frac{\mathrm{d}\sigma_{\text{NS}}}{\mathrm{d}\tau} \equiv \frac{\mathrm{d}\sigma_{\text{sing}}}{\mathrm{d}\tau} + \frac{\mathrm{d}\sigma_{\text{nd}}}{\mathrm{d}\tau} + \frac{\mathrm{d}\sigma_{\text{NS}}}{\mathrm{d}\tau} \\ &\equiv \frac{\mathrm{d}\sigma^{\text{sing}}_{m=0}}{\mathrm{d}\tau} + \frac{\mathrm{d}\sigma^{\text{sing}}_{m}}{\mathrm{d}\tau} + \frac{\mathrm{d}\sigma_{\text{nd}}}{\mathrm{d}\tau} + \frac{\mathrm{d}\sigma_{\text{NS}}}{\mathrm{d}\tau} \equiv \frac{\mathrm{d}\sigma^{\text{sing}}_{m=0}}{\mathrm{d}\tau} + \frac{\mathrm{d}\sigma^{\text{SCET}}_{m}}{\mathrm{d}\tau} + \frac{\mathrm{d}\sigma_{\text{NS}}}{\mathrm{d}\tau}\,,\end{aligned} \tag{2.145}$$

where the current superscript C is omitted to alleviate the notation. The SCET part, given by the modified factorization theorem [see Eq. (2.142)], is split first into terms with non-distributional origin and those coming from singular ones, which then are further divided into massless and mass corrections. In the last equality all kind of mass corrections, singular and non-distributional, are grouped together. It is worth noting the large cancellation between the singular mass corrections and the non-distributional terms that, together with the fact that the non-singular corrections are almost negligible, leads to the

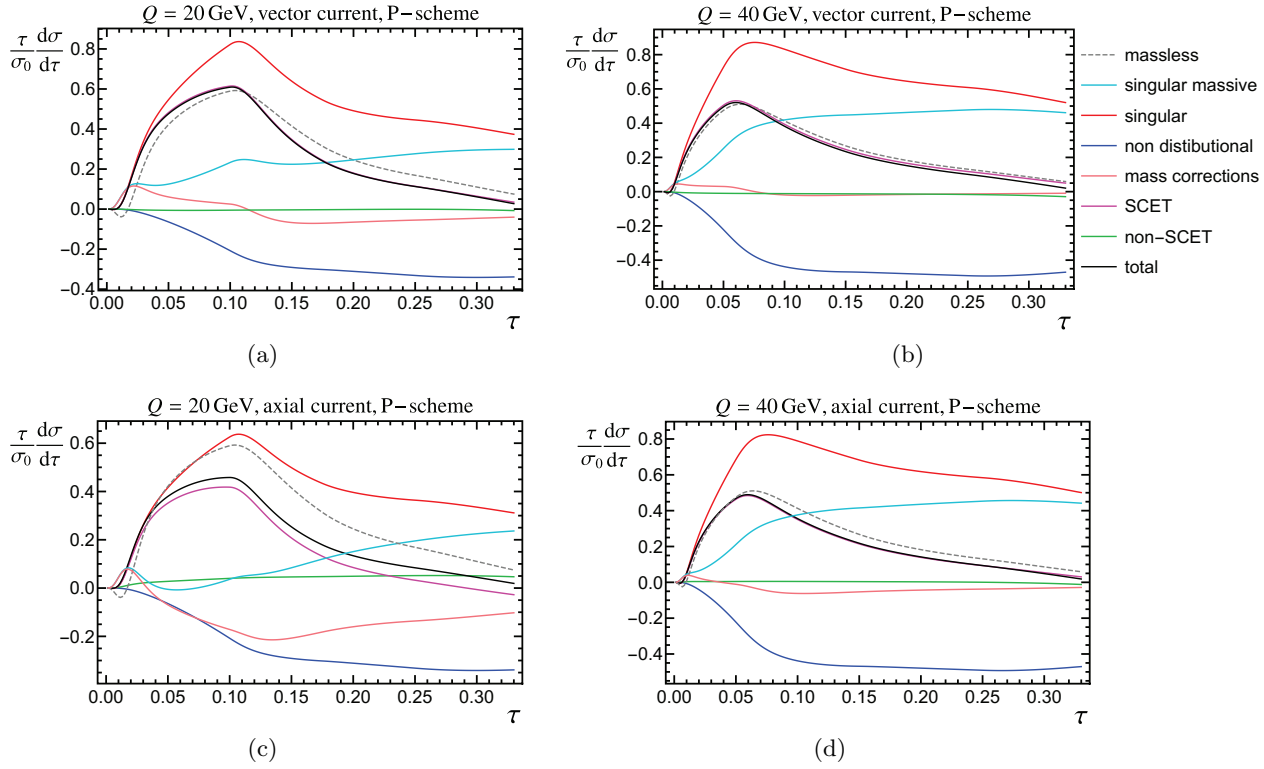

Figure 2.7: Decomposition of the differential cross section at $Q = 20\,\text{GeV}$ (left panels) and $40\,\text{GeV}$ (right panels) in various components for the vector (upper plots) and axial-vector (lower plots) currents. Red and blue correspond to the singular and non-distributional terms, respectively, while their sum defines the SCET cross section, shown in magenta. The massless approximation is shown as a dashed gray line, while massive singular corrections are depicted in cyan. The massive corrections to the SCET cross section (massive singular plus non-distributional) are shown in pink. Finally, the black solid line is the sum of all contributions.

expected low mass sensitivity of the distribution, in such a way that the sum of all contributions is very similar to just the massless result, specially for the vector current.

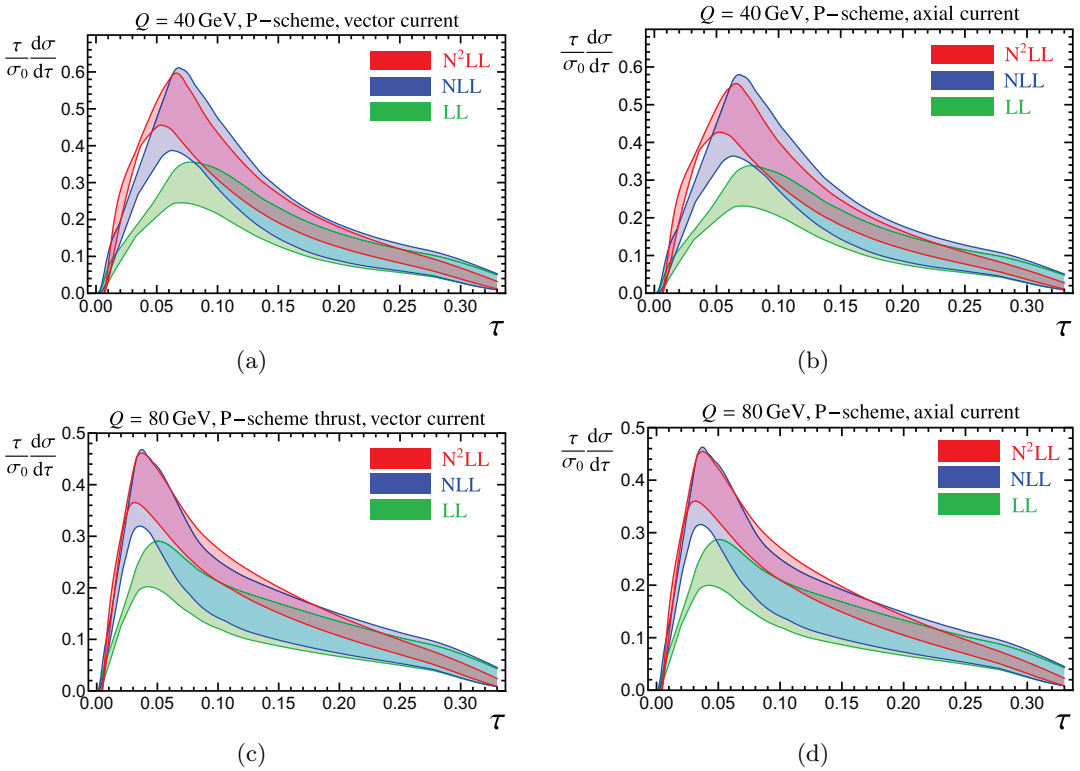

Figure 2.8: Uncertainty bands for LL (green), NLL (blue) and N^{2}LL (red) for P-scheme thrust cross sections at 40 GeV (figures on top) and 80 GeV (figures at the bottom), for vector (left figures) and axial-vector (right figures) currents. The bands are obtained with 500 profiles generated randomly selecting values for the parameters that define them.

The quantities in Fig. 2.7 were obtained with the default values for the profile-function parameters and $\xi = 0.5$ but we varied them within given intervals to estimate the uncertainty in each perturbative order of resummation. The profiles ranges are those specified in Ref. [38] and we also considered:

$$\mu_{\rm ns} = \frac{1}{2}[(2+n_s)\mu_H - \mu_J]\,, \qquad n_s \in [-1,1]\,, \qquad \xi \in [0,1]\,. \tag{2.146}$$

As a result, we ended up with the error bands in Fig. 2.8 where we can see a good convergence in the tail region since the higher-order bands are contained within the lower-order ones. This is however not happening in the peak with the LL band being far below the other ones, which could be a sign of the need of wider intervals for the variation of the parameters setting that part of the profile functions. On the other hand LL and NLL orders lead to very similar relative uncertainties, increasing with the value of τ: at $Q = 40\,[80]$ GeV they change from 36 [45]% at $\tau = 0.07$ to 84 [80]% at $\tau = 0.28$. At N^{2}LL the relative uncertainty is completely flat between $0.07 \leq \tau \leq 0.3$, and smaller than the two lower orders: 36 [30]% for $Q = 40\,[80]$ GeV. We observe the same relative uncertainties for vector and axial-vector currents.

In Fig. 2.9 we plot the difference between the vector and axial-vector currents normalized to their average. To make the figure clearer, we use a logarithmic scale on the y axis. We observe, as expected, that for larger energies the difference becomes smaller, since both currents approach the (current-independent) massless result.

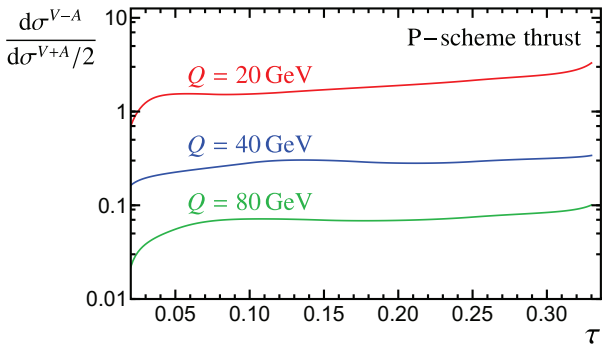

Figure 2.9: Difference between the vector and axial-vector differential cross sections normalized to the average of the two currents. We show results for $Q = 20\,\text{GeV}$ (red), $Q = 40\,\text{GeV}$ (blue) and $Q = 80\,\text{GeV}$ (green).

Finally, we carried out a comparison between schemes. Fig. 2.10 shows the P-scheme result together with the 2-jettiness and massless distributions. The 2-jettiness pothole is caused by large logarithms signaling the necessity of bHQET to correctly describe that region, as explained in Sec. 2.2.2. As expected, the three cross-sections become similar for large energies but the P-scheme is always closer to the massless case whereas 2-jettiness' peak is higher and shifted to the right.

This behavior of the peak is better appreciated in Fig. 2.11 where its position and height are represented for different values of the $\overline{\text{MS}}$ mass reference value at a fixed center of mass energy. Indeed, we can see how both P-scheme plots are almost constants while the 2-jettiness ones increase. In the case of the position the growth is basically quadratic, coming mainly from the tree level dependence: $\tau^J_{\text{min}} = 1 - \sqrt{1 - 4\hat{m}^2} \simeq 2\hat{m}^2$. In fact, we performed a fit of the form: $\tau_{\text{max}} \simeq 0.0255 + 1.75\hat{m}^2$ which closely reproduces the curve.

2.9 Summary

In this Chapter we have studied the mass sensitivity of event-shape cross-sections when considering variations of their massive scheme. First, we examined the collinear limit of the 4-momentum and found the same expression both in the P- an E-schemes, which leads to equivalent jet functions in both cases.

We have computed for thrust, heavy jet mass and C-parameter the remaining matrix element in the SCET and bHQET factorization theorems at $\text{N}^2\text{LL} + \mathcal{O}(\alpha_s)$ precision, namely the NLO jet function. Since the P-scheme measurement is non-inclusive, the calculation has been done through cut Feynman diagrams which therefore involve phase space and loop integrals. Nevertheless, we provided an optimized and compact form for the jet function definition in each EFT, written in terms of quantum and kinematic operators, that facilitates its computation and applied it also for M-scheme as a comparison with the previously employed method, that is, through the discontinuity of a forward-scattering amplitude.

The results contain singular terms and a non-distributional part whose RG evolution represents the

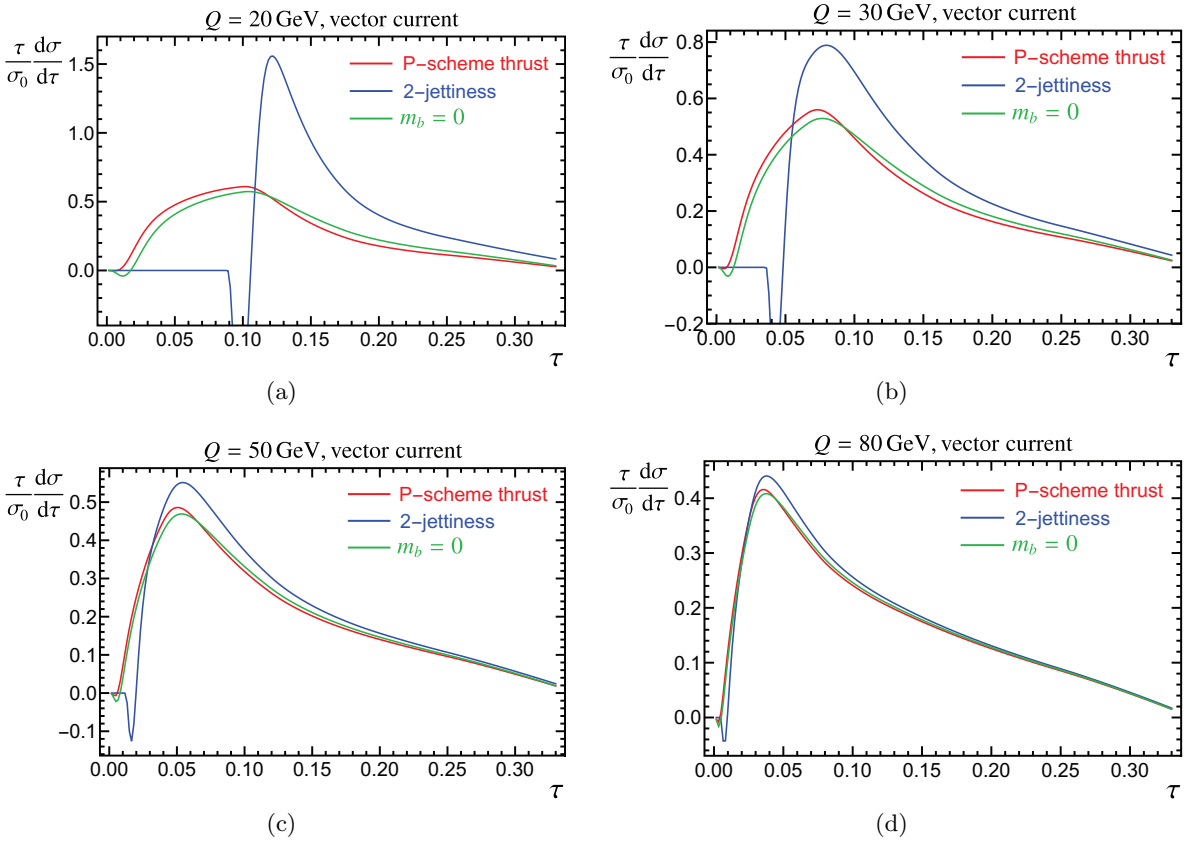

Figure 2.10: Differential cross section for massless quarks (green lines), 2-jettiness (blue lines) and P-scheme thrust (red lines) produced through the vector current. Panels (a), (b), (c) and (d) correspond to center-of-mass energies of 20, 30, 50 and 80 GeV, respectively.

most severe source of computational resources in the code for the final cross-section. As a consequence, we tried to get the most optimized expression for the implementation of its corresponding convolution with the running kernel and ended up with several analytical solutions as well as fast converging expansion series for each regime, that overlap, so the whole range can be covered.

Before carrying out a numerical analysis, we discussed how to complete the EFT description, extending its validity region by incorporating full-theory power-suppressed information. Having a non-vanishing mass leads to singular power corrections, which can however be absorbed in the factorization theorem by modifying the matrix elements in order to have resummation over these divergent terms. We can also account for soft hadronization effects through a shape model function. All these theoretical refiniments have been included into a numerical code.

Finally, several plots for the final SCET P-scheme thrust distribution were shown making important remarks, among which we count: the cancellation between singular mass corrections and the non-distributional part, the convergence of the resummed perturbative series and the low mass sensitivity, which makes this scheme more suitable for α_s determinations.

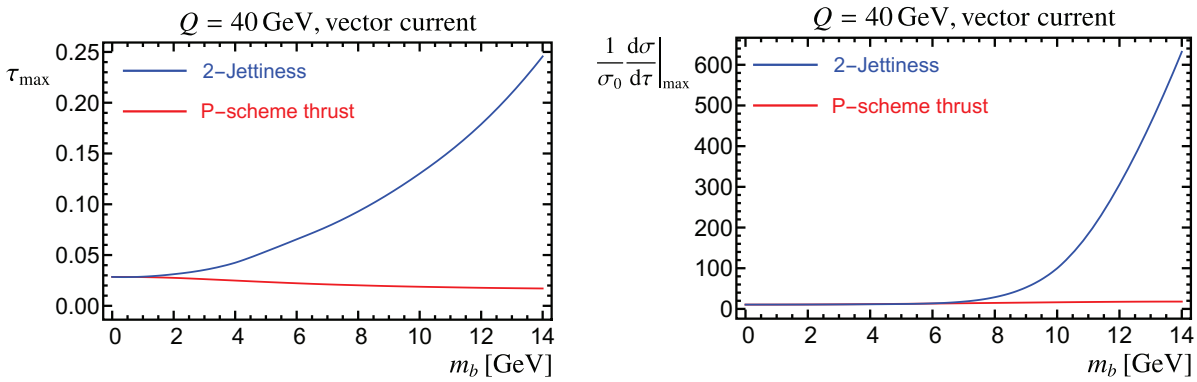

(a) (b)

Figure 2.11: Peak position (a) and peak height (b) for 2-jettiness (blue) and P-scheme thrust (red) massive cross section. Results correspond to default profiles, vector current and a center-of-mass energy of 40 GeV, and with $m_b \equiv \overline{m}_b(\overline{m}_b)$. We vary the bottom mass between 0 and 14 GeV, such that SCET still applies.

Chapter 3

Oriented event-shapes (NLO Oriented Event-Shape Distributions for Massive Quarks)

In this Chapter we will be concerned not only with the geometric properties of the event (so to say, the value of the event shape variable itself) but also with its orientation with respect to the beam direction, that is we will consider double (event-shape and angular) differential cross-sections. An infrared- and collinear-safe way of determining this orientation is by employing the axis that appear in the thrust determination of Eq. (1.14). The final-state configuration studied in this part of the work is represented in Fig. 3.1.

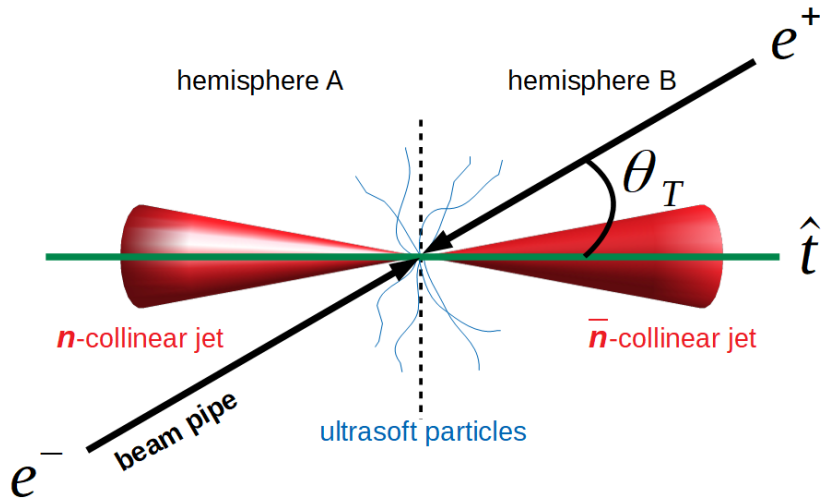

Figure 3.1: Schematic representation for the measurement of the event orientation through the thrust axis

In Ref. [51] it was shown that, if the QCD-electroweak factorization shown in Eq. (1.5) holds, the oriented distributions in the final state for massive or massless particles, parton or hadron, can be decomposed

in two different structures at all orders in perturbation theory:

$$\frac{1}{\sigma_0}\frac{\mathrm{d}\sigma}{\mathrm{dcos}(\theta_T)\mathrm{d}e} = \frac{3}{8}[1+\cos^2(\theta_T)]\frac{1}{\sigma_0}\frac{\mathrm{d}\sigma}{\mathrm{d}e} + [1-3\cos^2(\theta_T)]\frac{1}{\sigma_0}\frac{\mathrm{d}\sigma_{\mathrm{ang}}}{\mathrm{d}e}\,, \tag{3.1}$$

$$\frac{1}{\sigma_0}\frac{\mathrm{d}\sigma}{\mathrm{d}e} = \int_{-1}^{1}\mathrm{dcos}(\theta_T)\frac{1}{\sigma_0}\frac{\mathrm{d}\sigma}{\mathrm{dcos}(\theta_T)\mathrm{d}e}\,,$$

$$\frac{1}{\sigma_0}\frac{\mathrm{d}\sigma_{\mathrm{ang}}}{\mathrm{d}e} = \frac{3}{8}\int_{-1}^{1}\mathrm{dcos}(\theta_T)[2-5\cos^2(\theta_T)]\frac{1}{\sigma_0}\frac{\mathrm{d}\sigma}{\mathrm{dcos}(\theta_T)\mathrm{d}e}\,,$$

and the specific computations were carried out at parton level for massless quarks, analytically at $\mathcal{O}(\alpha_s)$ and through a Monte Carlo generator at $\mathcal{O}(\alpha_s^2)$. From these differential distribution one can also define the total oriented cross-section:

$$R_{\mathrm{ang}} = \int \mathrm{d}e\frac{1}{\sigma_0}\frac{\mathrm{d}\sigma_{\mathrm{ang}}}{\mathrm{d}e}\,, \tag{3.2}$$

which is in fact a suitable observable for α_s determinations since it is proportional to the strong coupling but is less affected by hadronization effects that event-shape differential distributions.

In this Chapter we aim to obtain these analytical fixed-order results at NLO for massive quarks. We will see that, unlike for the massless case, the leading order $\mathcal{O}(\alpha_s^0)$ contribution for the vector current channel is different from zero due to the primary quark mass, leading also to singular terms at one-loop with infrared divergences in the virtual and real contributions that will cancel each other when added up to yield the final result, making necessary to keep $d = 4-2\varepsilon$ in the phase space integrals if dimensional regularization is chosen to make such IR divergences manifest.

The form of the angular event-shape distribution is the same as in Ref. [48] for the unoriented case:[1]

$$\begin{aligned}\frac{1}{\sigma_0^C}\frac{\mathrm{d}\sigma_{\mathrm{ang}}^C}{\mathrm{d}e} =& R_{\mathrm{ang}}^{0,C}(\hat{m})\,\delta[e-e_{\min}(\hat{m})] + C_F\frac{\alpha_s(\mu)}{\pi}A_e^{\mathrm{ang},C}(\hat{m})\delta[e-e_{\min}(\hat{m})] \\ &+ C_F\frac{\alpha_s(\mu)}{\pi}B_{\mathrm{plus}}^{\mathrm{ang},C}(\hat{m})\left[\frac{1}{e-e_{\min}(\hat{m})}\right]_+ + C_F\frac{\alpha_s(\mu)}{\pi}F_{C,e}^{\mathrm{ang}}(e,\hat{m}) + \mathcal{O}(\alpha_s^2)\,,\end{aligned} \tag{3.3}$$

with the non-singular terms contained in $F_{C,e}^{\mathrm{ang}}$. For the axial-vector current one has $R_{\mathrm{ang}}^{0,A} = A_e^{\mathrm{ang},A} = B_{\mathrm{plus}}^{\mathrm{ang},A} = 0$ in Eq. (3.3). Therefore, for simplicity we adopt the convention $R_{\mathrm{ang}}^0 \equiv R_{\mathrm{ang}}^{0,V}$, $A_e^{\mathrm{ang}} \equiv A_e^{\mathrm{ang},V}$ and $B_{\mathrm{plus}}^{\mathrm{ang}} = B_{\mathrm{plus}}^{\mathrm{ang},V}$, and do not refer to the axial-current coefficients anymore.

3.1 Procedure and Notation

The strategy we follow is projecting out the angular part from the beginning of the computation through the application of the third line in Eq. (3.1). However, one could also carry out the calculation of the whole double differential cross-section and group the coefficients for the structures together at the end, checking that indeed no other angular structures emerge. We have followed both paths and found agreement, but present here only the direct strategy.

Since we are sensitive to the orientation, the starting point in this case is Eq. (1.3), to which we have to insert the measurement delta and the oriented projector to get the angular part of the event-shape

[1] See also Eq. (2.88) for the specific case of unoriented P-scheme thrust.

distribution.
Writing the hadronic vector as:

$$\langle X|\mathcal{J}^{C,\mu}_{n\lambda}|0\rangle = \left[\frac{\alpha_s(\mu)}{\pi}\right]^{\frac{n-2}{2}} \sum_{i=0}^{\infty}\left[\frac{\alpha_s(\mu)}{\pi}\right]^i h^{C,\mu}_{ni\lambda}\,, \tag{3.4}$$

where renormalization has already taken into account, the hadronic tensor takes the following form:

$$\langle 0|\mathcal{J}^{\mu\dagger}_C|X\rangle\langle X|\mathcal{J}^{\nu}_C|0\rangle = \left[\frac{\alpha_s(\mu)}{\pi}\right]^{n-2} H^{C,\mu\nu}_n\,, \tag{3.5}$$

$$H^{C,\mu\nu}_n = \sum_{i=0}^{\infty}\left[\frac{\alpha_s(\mu)}{\pi}\right]^i H^{C,\mu\nu}_{ni}, \qquad H^{C,\mu\nu}_{ni} = \sum_{j=0}^{i}\sum_{\lambda} h^{C,\mu}_{nj\lambda}\big[h^{C,\nu}_{n,i-j,\lambda}\big]^\dagger\,,$$

where in the previous two equations the subscripts p and λ stand for the polarization of the initial- and final-state particles, respectively, n for the number of external partons, and we have also factored out some powers of the coupling constant such that i represents the number of loops. All in all, the expression for the angular cross-section is:[2]

$$\frac{1}{\sigma^C_0}\frac{\mathrm{d}\sigma^C_{\rm ang}}{\mathrm{d}e} = \sum_{n=0}^{\infty}\left[\frac{\alpha_s(\mu)}{\pi}\right]^n f^{{\rm ang},C}_{e,n}\left(\hat{m}, e, \frac{\mu}{Q}\right), \qquad R^C_{\rm ang} = \sum_{n=0}^{\infty}\left[\frac{\alpha_s(\mu)}{\pi}\right]^n R^{{\rm ang},C}_n\left(\hat{m}, \frac{\mu}{Q}\right), \tag{3.6}$$

$$f^{{\rm ang},C}_{e,n}\left(\hat{m}, e, \frac{\mu}{Q}\right) = \frac{3L_{\mu\nu}}{16Q^2}\sum_{i=0}^{n}\int \mathrm{d}\Phi_{n-i+2} H^{C,\mu\nu}_{n+2-i,i}\delta[e-e(\Phi_n)][2-5\cos^2\theta_T(\Phi_n)]\,,$$

$$R^{{\rm ang},C}_n\left(\hat{m}, \frac{\mu}{Q}\right) = \int \mathrm{d}e\, f^{{\rm ang},C}_{e,n}\left(e, \hat{m}, \frac{\mu}{Q}\right),$$

being $\mathrm{d}\Phi_n$ the Lorentz-invariant n-particle phase space. Here $e(\Phi_n)$ and $\theta_T(\Phi_n)$ return respectively the value of the event shape e and angle θ_T at the phase space point Φ_n. For $n = 2$ one has that $e(\Phi_2) = e_{\rm min}$, the lowest possible value of the event shape and $\theta_T(\Phi_2) = \theta$ is the angle formed by the massive quark and the beam. In the remainder of this Chapter we compute the first two perturbative orders:

$$H^C_0 \equiv L_{\mu\nu}\int \mathrm{d}\Phi_2 H^{C,\mu\nu}_{20}, \qquad H^C_1 \equiv L_{\mu\nu}\left[\int \mathrm{d}\Phi_2 H^{C,\mu\nu}_{21} + \int \mathrm{d}\Phi_3 H^{C,\mu\nu}_{30}\right], \tag{3.7}$$

with $H^{C,\mu\nu}_{21} = 2\mathrm{Re}\{\sum_\lambda h^{C,\mu}_{20\lambda}\big[h^{C,\nu}_{21\lambda}\big]^\dagger\}$ and $H^{C,\mu\nu}_{30} = \sum_\lambda h^{C,\mu}_{30\lambda}\big[h^{C,\nu}_{30\lambda}\big]^\dagger$. Finally, $h^{C,\mu}_{30\lambda}$ has contributions from two different Feynman diagrams.

3.2 d-dimensional phase space

Since virtual and real contributions are individually IR divergent (collinear divergences are regulated by the primary quark mass) we need to regulate the phase space integrals. We choose dimensional regularization $\mathrm{d} = 4 - 2\varepsilon$ because it does not introduce an additional scale that would make computations much harder, and moreover also preserves gauge invariance.

The final state containing the lowest possible number of particles consists of a massive quark-antiquark

[2] In practice, to compute $R^{{\rm ang},C}_n$ one can simply use the integral formula for $f^C_{e,n}$ dropping the measurement delta function $\delta[e - e(Q_n)]$.

pair which are back-to-back (we consider the computation in the center of mass frame). Therefore, setting the z axis on the beam direction, the factor necessary for the tree-level and virtual-radiation contributions is:

$$\frac{1}{2Q^2}\frac{\mathrm{d}\Phi_2}{\mathrm{dcos}(\theta)} = \frac{\beta^{1-2\varepsilon}\sin^{-2\varepsilon}(\theta)}{2^{5-4\varepsilon}Q^{2+2\varepsilon}\Gamma(1-\varepsilon)\pi^{1-\varepsilon}}\,, \tag{3.8}$$

with m and $\beta \equiv \sqrt{1-4\hat{m}^2}$ the primary quark mass and velocity, respectively, and θ the angle formed by the quark's 3-momentum and the beam direction that corresponds to the fist polar angle θ_1 in the construction of the $(3-2\varepsilon)$-dimensional spherical coordinate system. Carrying out the integration over θ one recovers the known result for the 2-body phase space:

$$\Phi_2 = \frac{\beta^{1-2\varepsilon}\Gamma(1-\varepsilon)}{2Q^{2\varepsilon}(4\pi)^{1-\varepsilon}\Gamma(2-2\varepsilon)}\,. \tag{3.9}$$

At NLO the real-radiation part is given by two particles with the equal mass m (the quark-antiquark pair), labeled as 1 and 2, and a gluon labeled as 3 in the final-state. We introduce the dimensionless variables $x_i \equiv 2E_i/Q$ with E_i the energy of the i-th particle and $i = 1, 2, 3$. Conservation of 3-momentum in the beam direction (z axis) and energy conservation implies:

$$\beta_1\cos(\theta_1) + \beta_2\cos(\theta_2) + x_3\cos(\theta_3) = 0\,, \qquad\qquad x_1 + x_2 + x_3 = 2\,, \tag{3.10}$$

where we have defined $\beta_i \equiv 2|\vec{p}_i|/Q = \sqrt{x_i^2 - 4\hat{m}_i^2}$ —not to be confused with the particle's velocity β— with $\hat{m}_1 = \hat{m}_2 = \hat{m}$ and $\hat{m}_3 = 0$. One has that $x_i \geq 2\hat{m}$ within the phase space boundaries.

For simplicity, we define the x axis such that $\vec{p}_1$ has no y component and a positive projection on the x axis (that is, through the Gram-Schmidt process):

$$\hat{u}_x = \frac{\vec{p}_1 - (\vec{p}_1\cdot\hat{u}_z)\hat{u}_z}{\sqrt{|\vec{p}_1|^2 - (\vec{p}_1\cdot\hat{u}_z)^2}}\,. \tag{3.11}$$

Here $\hat{u}_i$ with $i = x, y, z$ are three unitary vectors pointing in the direction of the respective coordinate axes. To define the y axis we use once again the Gram-Schmidt procedure:

$$\hat{u}_y = \frac{\vec{p}_2 - (\vec{p}_2\cdot\hat{u}_z)\hat{u}_z - (\vec{p}_2\cdot\hat{u}_x)\hat{u}_x}{\sqrt{|\vec{p}_2|^2 - (\vec{p}_2\cdot\hat{u}_z)^2 - (\vec{p}_2\cdot\hat{u}_x)^2}}\,, \tag{3.12}$$

such that, by construction, $\hat{u}_y\cdot\vec{p}_2 > 0$, which is exactly what we need to define spherical coordinates in a coherent way in our $(3-2\varepsilon)$-dimensional euclidean vector space. This choice greatly simplifies the computations but, however, implies $\hat{u}_x \times \hat{u}_y = \mathrm{sign}[\hat{u}_z\cdot(\vec{p}_1\times\vec{p}_2)]\hat{u}_z$, so that the axes orientation is not always standard. Since there are no outer products in our matrix elements this fact is irrelevant. Moreover, the inner product $\vec{p}_1\cdot\vec{p}_2$ can take positive and negative values. In any case, to avoid this issue, whenever $\hat{u}_z\cdot(\vec{p}_1\times\vec{p}_2) < 0$ one can use $\vec{p}_2$ first to define the x axis followed by $\vec{p}_1$ that fixes the y axis. In Fig. 3.2 we illustrate this procedure for the $\varepsilon = 0$ case.

To compute oriented event shapes we need the phase space differential in the quark and anti-quark energies, as well as in the angles θ_i and θ_j defined by the 3-momenta of particles i and j, which do not have to be necessarily the quark and anti-quark (but of course we need $i \neq j$), and the beam. The angles $\tilde{\theta}_{ij}$ formed by the 3-momenta of any two different particles in the final state do not depend on θ_i or θ_j (ergo, do not depend on the orientation), and can be expressed in terms of masses and energies

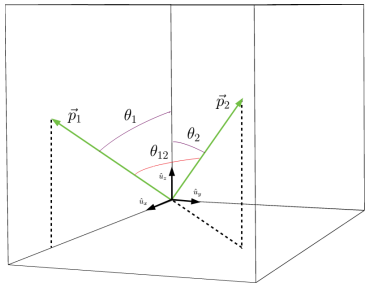

Figure 3.2: 3-dimensional coordinate system for the computation of the three particles phase space

as follows:

$$\sin^2(\tilde{\theta}_{ij}) = \frac{4[(1-x_1)(1-x_2)(x_1+x_2-1)-\hat{m}^2x_3^2]}{\beta_i^2\beta_j^2} \equiv \frac{4\xi(\hat{m},x_1,x_2)}{\beta_i^2\beta_j^2}\,, \tag{3.13}$$
$$\cos(\tilde{\theta}_{ij}) = \frac{x_ix_j-2(x_i+x_j-1)+4\hat{m}_i\hat{m}_j}{\beta_i\beta_j}\,.$$

The result on the first line shows that $\beta_i\beta_j\sin(\tilde{\theta}_{ij}) = \sqrt{4\xi(\hat{m},x_1,x_2)}$ is independent of i and j as long as $i \neq j$. Since $0 \leq \theta_{ij} \leq \pi$ one has that $\sin(\tilde{\theta}_{ij}) \geq 0$ anywhere in the phase space such that the square root can be computed unambiguously. Including the flux factor one finds the following result for the 3-particle phase space in $d = 4-2\varepsilon$ dimensions:

$$\frac{\mathrm{d}\Phi_3}{2Q^2} = \frac{4^\varepsilon Q^{-4\varepsilon}}{2(4\pi)^{4-2\varepsilon}\Gamma(1-2\varepsilon)}\int \mathrm{d}x_1\mathrm{d}x_2\mathrm{d}\cos(\theta_i)\mathrm{d}\cos(\theta_j)\frac{\beta_i^{-2\varepsilon}\beta_j^{-2\varepsilon}\theta(h_{ij})}{h_{ij}^{1/2+\varepsilon}}\,, \tag{3.14}$$
$$h_{ij} = \sin^2(\tilde{\theta}_{ij}) - \cos^2(\theta_i) - \cos^2(\theta_j) + 2\cos(\tilde{\theta}_{ij})\cos(\theta_i)\cos(\theta_j)\,,$$
$$\equiv [\cos(\theta_i) - \cos(\theta_{ij}^-)][\cos(\theta_{ij}^+) - \cos(\theta_i)]\,,$$
$$\cos(\theta_{ij}^\pm) = \cos(\tilde{\theta}_{ij})\cos(\theta_j) \pm \sin(\tilde{\theta}_{ij})\sin(\theta_j) = \cos(\tilde{\theta}_{ij} \mp \theta_j)\,.$$

As expected, the flux-normalized 3-particle phase space is dimensionless for $\varepsilon \to 0$. Here θ_i is identified with the first polar angle θ_i^1 in the $(3-2\varepsilon)$-dimensional spherical coordinates that specify the direction of the i-th particle's 3-momentum.

For simplicity, we carry out our discussion for the choice $i = 1$, $j = 2$, but the result is valid for any other pair of values, as shall be proven later. Our axes choice is such that, as far as particle 1 is concerned, there is no angular dependence except for $\theta_1^1 \equiv \theta_1$, therefore we can integrate $\theta_1^{n>1}$ getting simply a solid angle. There is, however, dependence on $\theta_2^1 \equiv \theta_2$, and θ_2^2, the two polar angles that specify the direction of $\vec{p}_2$. We stress that since $\hat{u}_y \cdot \vec{p}_2 > 0$ one has $0 \leq \theta_2^2 \leq \pi$, such that θ_2^2 is necessarily a polar angle, not azimuth. We therefore can integrate $\theta_2^{n>2}$ getting again a solid angle. We note that in $d-1$ dimensions there is a single azimuth angle $\phi \equiv \theta_{d-1}$ that is always integrated over in our computations. The dependence on θ_2^2 comes solely from the scalar product

$$\vec{p}_1 \cdot \vec{p}_2 = |\vec{p}_1||\vec{p}_2|\cos(\theta_{12}) = \frac{Q^2}{4}\beta_1\beta_2\left[\sin(\theta_1)\sin(\theta_2)\cos(\varphi_2) + \cos(\theta_1)\cos(\theta_2)\right], \tag{3.15}$$

that appears in the Dirac delta function enforcing energy conservation. We integrate θ_2^2 against this delta function to obtain the result in Eq. (3.14).[3]

[3] Enforcing 4-momentum conservation in Eq. (3.15) one obtains the result in the second line of Eq. (3.13).

Before going on, we pause and show that $\int \mathrm{dcos}(\theta_i)\mathrm{dcos}(\theta_j)\beta_i^{-2\varepsilon}\beta_j^{-2\varepsilon}/h_{ij}^{1/2+\varepsilon}$ does not depend on the values of i and j as long as $i \neq j$. To that end we need to use the following relations:

$$1+\frac{\beta_k^2}{\beta_\ell^2}-\frac{2\beta_k}{\beta_\ell}\cos(\tilde{\theta}_{12})=\frac{x_3^2}{\beta_\ell^2}\,,\qquad \frac{\beta_k}{\beta_\ell}+\cos(\tilde{\theta}_{12})=-\frac{x_3}{\beta_\ell}\cos(\tilde{\theta}_{13})\,, \tag{3.16}$$

with $k,\ell \leq 2$ and $k \neq \ell$. Using Eq. (3.10) to express $\cos(\theta_2)$ $[\cos(\theta_1)]$ as a linear combination of $\cos(\theta_1)$ $[\cos(\theta_2)]$ and $\cos(\theta_3)$, with the help of Eq. (3.16) it is trivial to show $h_{12}=(x_3/\beta_2)^2 h_{13}=(x_3/\beta_1)^2 h_{23}$ and $\mathrm{dcos}(\theta_1)\mathrm{dcos}(\theta_2)=(x_3/\beta_2)\mathrm{dcos}(\theta_1)\mathrm{dcos}(\theta_3)=(x_3/\beta_1)\mathrm{dcos}(\theta_2)\mathrm{dcos}(\theta_3)$. The first result implies that $\theta(h_{ij})$ does not depend on i or j, and together with the second it is immediate to check that

$$\int \mathrm{dcos}(\theta_1)\mathrm{dcos}(\theta_2)\frac{\beta_1^{-2\varepsilon}\beta_2^{-2\varepsilon}}{h_{12}^{1/2+\varepsilon}}=\int \mathrm{dcos}(\theta_1)\mathrm{dcos}(\theta_3)\frac{\beta_1^{-2\varepsilon}\beta_3^{-2\varepsilon}}{h_{13}^{1/2+\varepsilon}}=\int \mathrm{dcos}(\theta_2)\mathrm{dcos}(\theta_3)\frac{\beta_2^{-2\varepsilon}\beta_3^{-2\varepsilon}}{h_{23}^{1/2+\varepsilon}}\,. \tag{3.17}$$

The Heaviside function $\theta(h_{ij})$ makes that, for a fixed value of θ_j, the integration limits for θ_i coincide with $\theta_{ij}^{\pm}$ (note that $\theta_{ij}^{\pm} \neq \theta_{ji}^{\pm}$ even though $h_{ij}=h_{ji}$ and $\tilde{\theta}_{ij}=\tilde{\theta}_{ji}$). Let us provide some master integrals that will become necessary for projecting out the angular structure when dealing with real radiation [for simplicity the step function $\theta(h_{12})$ is over understood]:[4]

$$\begin{aligned}
\frac{4^\varepsilon}{\Gamma(1-2\varepsilon)}\int \frac{\mathrm{dcos}(\theta_1)\mathrm{dcos}(\theta_2)\cos^{2k}(\theta_j)}{\beta_1^{2\varepsilon}\beta_2^{2\varepsilon}h_{12}^{1/2+\varepsilon}} &= \frac{2\pi(2k)!\xi^{-\varepsilon}(\hat{m},x_1,x_2)}{4^k k!\left(\frac{3}{2}-\varepsilon\right)_k\Gamma(2-2\varepsilon)}\,, \\
\frac{4^\varepsilon}{\Gamma(1-2\varepsilon)}\int \frac{\mathrm{dcos}(\theta_1)\mathrm{dcos}(\theta_2)\cos(\theta_i)\cos^{2k+1}(\theta_j)}{\beta_1^{2\varepsilon}\beta_2^{2\varepsilon}h_{12}^{1/2+\varepsilon}} &= \frac{2\pi[2(k+1)!\cos(\tilde{\theta}_{ij})\xi^{-\varepsilon}(\hat{m},x_1,x_2)}{4^{k+1}(k+1)!\left(\frac{3}{2}-\varepsilon\right)_{k+1}\Gamma(2-2\varepsilon)}\,, \\
\frac{4^\varepsilon}{\Gamma(1-2\varepsilon)}\int \frac{\mathrm{dcos}(\theta_1)\mathrm{dcos}(\theta_2)\cos^2(\theta_i)\cos^{2k}(\theta_j)}{\beta_1^{2\varepsilon}\beta_2^{2\varepsilon}h_{12}^{1/2+\varepsilon}} &= \frac{\pi(2k)![1+2k\cos^2(\tilde{\theta}_{ij})]\xi^{-\varepsilon}(\hat{m},x_1,x_2)}{4^k k!(\frac{3}{2}-\varepsilon)_{k+1}\Gamma(2-2\varepsilon)}\,,
\end{aligned} \tag{3.19}$$

with k a non-negative integer number, $i,j=1,2,3$ and $(a)_n=\Gamma(a+n)/\Gamma(a)$ the Pochhammer symbol. Of course one has $\cos(\tilde{\theta}_{ii})=1$, and in that sense the first line is contained in the second and third if one sets $i=j$. Likewise, for $i=j$ the second and third lines become equal, as can be easily checked. Setting $k=0$ in the third line is identical to setting $k=1$ in the first. Finally, if the power of $\cos(\theta_j)$ on the upper or lower (middle) lines is set to an odd (even) number, the integral vanishes.

Using the first line of Eq. (3.19) with $k=0$ one can integrate θ_i and θ_j in Eq. (3.14) to recover the known result for the angular-integrated 3-particle phase space in d dimensions:

$$\frac{\mathrm{d}\Phi_3}{\mathrm{d}x_1\mathrm{d}x_2}=\frac{Q^{2-4\varepsilon}}{2(4\pi)^{3-2\varepsilon}}\frac{[(1-x_1)(1-x_2)(x_1+x_2-1)-\hat{m}^2(2-x_1-x_2)^2]^{-\varepsilon}}{\Gamma(2-2\varepsilon)}\,, \tag{3.20}$$

While the Dalitz region looks somewhat awkward when expressed in terms of the x_i variables, it takes a much simpler and more symmetric form if the following change of variables is implemented:

[4] To obtain these results we use the fact that $\int \mathrm{dcos}(\theta_i)\mathrm{dcos}(\theta_j)\beta_i^{-2\varepsilon}\beta_j^{-2\varepsilon}/h_{ij}^{1/2+\varepsilon}$ does not depend on the values of i and j as long as $i \neq j$ and the following integrals:

$$\frac{1}{\Gamma(1-2\varepsilon)}\int \frac{\mathrm{dcos}(\theta_i)\cos^n(\theta_i)}{\beta_i^{2\varepsilon}\beta_j^{2\varepsilon}h_{ij}^{1/2+\varepsilon}}=\frac{\pi\xi^{-\varepsilon}(\hat{m},x_1,x_2)\sin^{-2\varepsilon}(\theta_j)}{\Gamma(1-\varepsilon)^2}\times\begin{cases}1 & n=0\\ \cos(\tilde{\theta}_{ij})\cos(\theta_j) & n=1\\ \frac{\cos^2(\theta_2)[2(1-\varepsilon)-(3-2\varepsilon)\sin^2(\tilde{\theta}_{ij})]+\sin^2(\tilde{\theta}_{ij})}{2(1-\varepsilon)} & n=2\end{cases}\,,$$

$$\frac{4^\varepsilon}{\Gamma(1-\varepsilon)^2}\int_{-1}^{1}\mathrm{d}x(1-x^2)^{-\varepsilon}x^{2k}=\frac{2^{1-2k}(2k)!}{k!\Gamma(2-2\varepsilon)\left(\frac{3}{2}-\varepsilon\right)_k}\,. \tag{3.18}$$

$x_1 = 1-(1-z)y$, $x_2 = 1-zy$, making the soft limit $y \to 0$ apparent as $y = x_3$ is proportional to the gluon energy. The Dalitz region is now specified by the conditions $z_- \leq z \leq z_+$ and $0 \leq y \leq y_{\max}(\hat{m}, z)$, with $z_\pm$ and the symmetric function $y_{\max}(\hat{m}, z) = y_{\max}(\hat{m}, 1-z)$ defined as:

$$y_{\max}(\hat{m}, z) = 1 - \frac{\hat{m}^2}{z(1-z)}\,, \qquad z_\pm \equiv \frac{1 \pm \beta}{2}\,. \tag{3.21}$$

Since we aim to obtain a distribution differential in θ_T and the thrust axis coincides with the direction of the particle with largest 3-momentum magnitude, it is clear that $\theta_T = \theta_i$ if $\beta_i = \max\{\beta_1, \beta_2, \beta_3\}$. Hence we can design a function that will project out the correct value of θ_T depending on the phase-space point:

$$\begin{aligned}\delta_T^{(3)} =& \,\theta(2z-1)\theta[y_\tau(\hat{m}, 1-z) - y]\delta[\cos(\theta_T) - \cos(\theta_1)] \\ &+ \theta(1-2z)\theta[y_\tau(\hat{m}, z) - y]\delta[\cos(\theta_T) - \cos(\theta_2)] \\ &+ \theta[y - y_\tau(\hat{m}, z)]\theta[y - y_\tau(\hat{m}, 1-z)]\delta[\cos(\theta_T) - \cos(\theta_3)] \equiv \delta_T^{(1)} + \delta_T^{(2)} + \delta_T^{(3)},\end{aligned} \tag{3.22}$$

where we assume that $\delta_T^{(3)}$ acts only inside the Dalitz region. We have defined the function

$$y_\tau(\hat{m}, z) = \frac{\sqrt{1 - 4\hat{m}^2(1-z^2)} - z}{1-z^2}\,, \tag{3.23}$$

which, for $\hat{m} \leq z \leq 1/2$ sets the limit between the regions in which the thrust axis points into the anti-quark or gluon momenta. Likewise, $y_\tau(\hat{m}, 1-z)$ for $1/2 \leq z \leq 1-\hat{m}$ is the limit between the regions in which it points into the momenta of the quark and gluon. For completeness, the boundary between the regions in which it points in the same direction as the quark or anti-quark momenta is parametrized by $z = 1/2$ and $0 \leq y \leq 4(\sqrt{1-3\hat{m}^2} - 1/2)/3 \equiv y_{\text{middle}}(\hat{m})$. The Dalitz region, along with these borders, is depicted in Fig. 3.3.

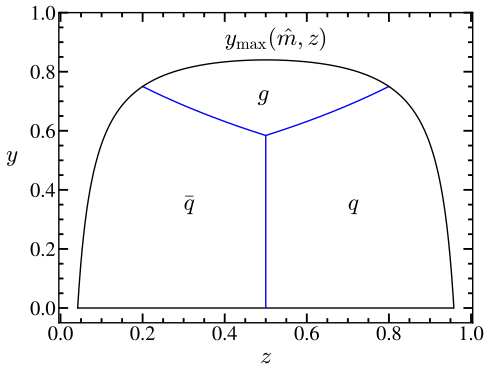

Figure 3.3: Dalitz region in (z, y) coordinates for two massive quarks and a gluon. In addition to the phase-space boundaries, in black, we show in blue the borders between the regions in which the thrust axis points into the direction of the quark, anti-quark or gluon 3-momentum. To generate the plot we use $m/Q = 0.2$.

Since in this Chapter we exclusively deal with the angular distribution, we can project out this term using Eq. (3.22) and the third line of Eq. (3.1) to obtain the following integration kernel for 3-particle

contributions:

$$K(\theta_i,y,z)=\frac{3}{8}\int_{-1}^{1}\mathrm{dcos}(\theta_T)[2-5\cos^2(\theta_T)]\delta_T^{(3)}=\frac{3}{8}\Big\{\theta(2z-1)\theta[y_\tau(\hat{m},1-z)-y][2-5\cos^2(\theta_1)] \quad (3.24)$$
$$+\theta(1-2z)\theta[y_\tau(\hat{m},z)-y][2-5\cos^2(\theta_2)]+\theta[y-y_\tau(\hat{m},z)]\theta[y-y_\tau(\hat{m},1-z)][2-5\cos^2(\theta_3)]\Big\}.$$

3.3 Lowest Order Result

At the lowest order in the strong coupling we have to compute the tree-level Feynman diagram shown in Fig. 3.4. Despite the results are known since long, we sketch the computation as it sets the basis for the more complex NLO case. Furthermore, the results presented in this section with the quark mass set to zero constitute the normalization of the cross section at any order. To make each step of the computation free from spurious logarithms with dimensionful arguments that would otherwise appear when expanding the results in ε —as an artifact of having d-dimensional phase space integrals—, we normalize the distributions with the d-dimensional Born cross-section.

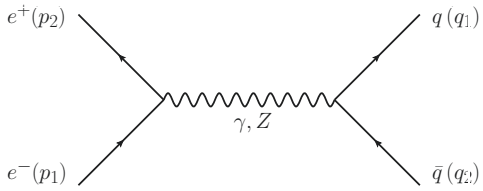

Figure 3.4: Lowest-order Feynman diagram contributing to oriented event shapes for massive quarks. The distribution is proportional to a Dirac delta function.

A standard computation yields the following result for the hadronic tensor

$$H_{2,0}^{C,\mu\nu}=4\Big\{q_2^\mu q_1^\nu+q_1^\mu q_2^\nu-\frac{1}{2}\big[s+2(1\mp1)m^2\big]g^{\mu\nu}\Big\}, \quad (3.25)$$

where in $\mp$ the upper (lower) part corresponds to the vector (axial-vector) current. Taking the massless limit, including the flux factor and integrating over the phase space one obtains the d-dimensional massless Born cross-section

$$\sigma_0^C=\frac{N_cQ^2}{4\pi}\frac{(1-\varepsilon)\Gamma(2-\varepsilon)}{(3-2\varepsilon)\Gamma(2-2\varepsilon)}\left(\frac{4\pi\mu^2e^{\gamma_E}}{Q^2}\right)^\varepsilon L^C\,, \quad (3.26)$$

with the factors L^C, containing the different leptonic couplings, given in Eq. (1.6) such that, neglecting the Z-boson contribution (that is, only the photon exchange is considered) the result, called point-like cross section reads:

$$\sigma_B=N_cQ_q^2\frac{(4\pi)^{1+\varepsilon}(1-\varepsilon)\Gamma(2-\varepsilon)\alpha_{\mathrm{em}}^2}{(3-2\varepsilon)\Gamma(2-2\varepsilon)Q^{2+2\varepsilon}}. \quad (3.27)$$

If quark masses are not neglected and the polar angle is left unintegrated one obtains the following result for the vector and axial-vector currents:

$$\frac{1}{\sigma_0^V}\frac{\mathrm{d}\sigma_{\mathrm{tree}}^V}{\mathrm{dcos}(\theta)}=\frac{(3-2\varepsilon)\Gamma(2-2\varepsilon)}{2^{3-2\varepsilon}\Gamma^2(2-\varepsilon)}\beta^{1-2\varepsilon}\sin^{-2\varepsilon}(\theta)[2(1-\varepsilon)-\beta^2\sin^2(\theta)]\,, \quad (3.28)$$
$$\frac{1}{\sigma_0^A}\frac{\mathrm{d}\sigma_{\mathrm{tree}}^A}{\mathrm{dcos}(\theta)}=\frac{(3-2\varepsilon)\Gamma(2-2\varepsilon)}{2^{3-2\varepsilon}\Gamma^2(2-\varepsilon)}\beta^{3-2\varepsilon}\sin^{-2\varepsilon}(\theta)[1-2\varepsilon+\cos^2(\theta)]\,.$$

Both results shown above coincide for $\beta = 1$. We can project out the total angular cross-section using the last line of Eq. (3.1) and the second line of Eq. (3.18), obtaining

$$\begin{aligned} R_0^{\text{ang},V} &= \frac{3\beta^{1-2\varepsilon}}{16(1-\varepsilon)} \frac{[5+8\varepsilon^2-22\varepsilon-\beta^2(5-4\varepsilon)]}{5-2\varepsilon} \xrightarrow[\varepsilon=0]{} \frac{3\hat{m}^2\beta}{4}\,, \\ R_0^{\text{ang},A} &= -\frac{3\beta^{3-2\varepsilon}}{8} \frac{\varepsilon(9-4\varepsilon)}{(1-\varepsilon)(5-2\varepsilon)} \xrightarrow[\varepsilon=0]{} 0\,, \end{aligned} \tag{3.29}$$

where, the tree-level Born-normalized differential distribution is simply $f_{e,0}^{\text{ang},C} = R_0^{\text{ang},C}\delta[e - e_{\min}(\hat{m})]$.

A graphical representation of $R_0^{\text{ang},V}$ is shown in Fig. 3.5, together with its massless and mass threshold expansions. For the axial-vector current we obtain a vanishing result, but the vector result only becomes zero in the $\hat{m} \to 0$ limit. As anticipated, this will significantly complicate the NLO computation.

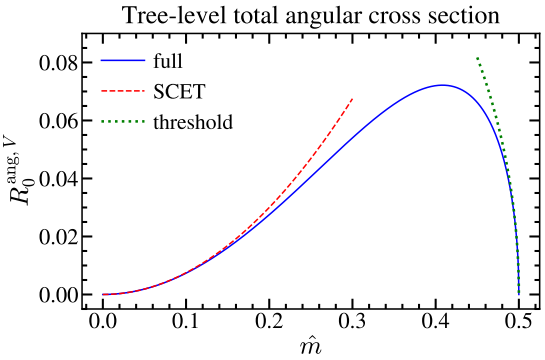

Figure 3.5: Total angular cross-section at $\mathcal{O}(\alpha_s^0)$ for the vector current $R_0^{\text{ang},V}(\hat{m})$ in solid blue, together with its SCET (dashed red) and mass threshold (dotted green) approximations. The $R_0^{\text{ang},V}(\hat{m})$ cross section vanishes in the massless limit $\hat{m} = 0$ and at threshold $\hat{m} = 1/2$.

3.4 Virtual Contribution

As long as IR singularities are handled in dimensional regularization, the computation of the virtual contribution is very similar to the lowest-order term outlined in Sec. 3.3. We take advantage of the well-known results for the so-called vector and axial-vector form factors for massive quarks shown in Fig 3.6, which, after accounting for the wave function renormalization Z_q^{OS}, are UV finite due to vector current conservation, making the present $1/\varepsilon$ pole of IR origin. The general form of the wave-function-corrected form factors up to one loop is as follows [5]

$$\begin{aligned} V^\mu &= \left[1 + C_F\frac{\alpha_s}{\pi}A(\hat{m})\right]\gamma^\mu + C_F\frac{\alpha_s}{\pi}\frac{B(\hat{m})}{2m}(q_1-q_2)^\mu\,, \\ A^\mu &= \left[1 + C_F\frac{\alpha_s}{\pi}C(\hat{m})\right]\gamma^\mu\gamma_5 + C_F\frac{\alpha_s}{\pi}\frac{D(\hat{m})}{2m}\gamma_5\, q^\mu\,, \end{aligned} \tag{3.30}$$

with $q = q_1 + q_2$ the photon or Z-boson momentum, and q_i with $i = 1, 2$ the quark and anti-quark momenta, respectively.

[5] Mass renormalization is carried out in the OS scheme such that, unless otherwise stated, all quark masses appearing in the various expressions are understood in the pole scheme.

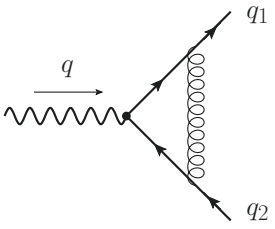

Figure 3.6: Feynman diagram representing the vector and axial-vector form factors for massive quarks.

Vector current conservation implies $q_\mu V^\mu = 0$ and also ensures (when applied on the leptonic current) that the term proportional to $D(\hat{m})$ from the axial-vector current will vanish when contracted with the leptonic tensor. For our purposes we only need the real part of the A, B and C coefficients that can be written as [44, 32]

$$\begin{aligned}
\mathrm{Re}[A(\hat{m})] &= \left(\frac{1+\beta^2}{2\beta}L_\beta - \frac{1}{2}\right)\left[\frac{1}{\varepsilon} - 2\log\left(\frac{m}{\mu}\right)\right] + A_{\mathrm{reg}}(\hat{m})\,, \\
A_{\mathrm{reg}}(\hat{m}) &= \frac{3}{2}\beta L_\beta - 1 + \frac{1+\beta^2}{4\beta}\left[\pi^2 - 2L_\beta^2 - 2\,\mathrm{Li}_2\left(\frac{2\beta}{1+\beta}\right)\right], \\
\mathrm{Re}[C(\hat{m})] &= \mathrm{Re}[A(\hat{m})] + \frac{4\hat{m}^2}{\beta}L_\beta\,,
\end{aligned} \tag{3.31}$$

where we have defined $L_\beta \equiv \log[(1+\beta)/(2\hat{m})]$. For the vector and axial-vector current, after taking the $\varepsilon \to 0$ limit we find

$$\begin{aligned}
R_{21}^{\mathrm{ang},V} =& \frac{3C_F\beta}{8}\left\{\left[1 - \frac{2}{\beta}(1-2\hat{m}^2)L_\beta\right]\left[2\hat{m}^2\log\left(\frac{m}{\mu}\right) - \frac{\hat{m}^2}{\varepsilon} + \frac{3}{10}(3-2\hat{m}^2) + 2\hat{m}^2\log(\beta)\right]\right. \\
&\left. + 2\hat{m}^2\mathrm{Re}[A_{\mathrm{reg}}(\hat{m})] - \hat{m}^2\beta L_\beta\right\}, \\
R_{21}^{\mathrm{ang},A} =& \frac{27C_F\beta^2}{20}\left[\frac{\beta}{2} - (1-2\hat{m}^2)L_\beta\right].
\end{aligned} \tag{3.32}$$

Since there are two particles in the final state, the contribution of the virtual radiation to the differential cross section is once again $f_{e,21}^{\mathrm{ang},C} = R_{21}^{\mathrm{ang},C}\delta[e - e_{\min}(\hat{m})]$. Surprisingly, we find a non-zero result for the axial-vector current. Likewise, the vector-current result does not vanish in the massless limit. These are artifacts of dimensional regularization, and once the real-radiation contribution is added, there will be no term proportional to $\delta(e - e_{\min})$ for the axial-vector current, and the coefficient of such delta will vanish as $\hat{m} \to 0$.

3.5 Real Radiation and Total Angular Cross Section

The last terms that contribute at $\mathcal{O}(\alpha_s)$ come from the two diagrams shown in Fig. 3.7 in which a real gluon is emitted. The complete contribution consists on the modulus squared of each diagram plus the interference of the two. We compute the relevant traces using `TRACER` [43], and organize the result in

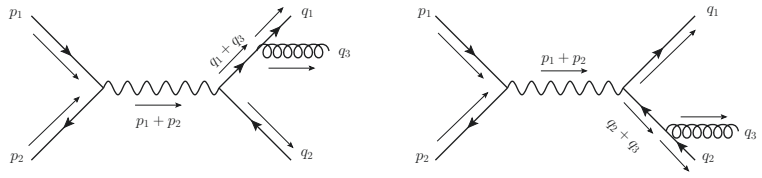

Figure 3.7: Feynman diagrams for the real-radiation contribution at NLO.

the following angular structures:

$$
\begin{aligned}
L_{\mu\nu}H_{30}^{C,\mu\nu} &= \frac{8\pi^2 C_F}{s}\left(\frac{\mu^2 e^{\gamma_E}}{4\pi}\right)^{\varepsilon}\left[A_0^C + A_1^C\beta_1^2\cos^2(\theta_1) + A_2^C\beta_2^2\cos^2(\theta_2) + A_{12}^C\beta_1\beta_2\cos(\theta_1)\cos(\theta_2)\right],\\
A_0^V(x_1,x_2) &= \frac{(1-2\varepsilon)(x_1^2+x_2^2-x_3^2\varepsilon)}{(1-x_1)(1-x_2)} - \frac{8\hat{m}^4x_3^2}{(1-x_1)^2(1-x_2)^2} - \frac{2\hat{m}^2}{(1-x_1)^2(1-x_2)^2}[8-2\varepsilon x_3^2\\
&\quad + 5(x_1^2+x_2^2) + 14x_1x_2 - 4(x_1+x_2)(3+x_1x_2)],\\
A_0^A(x_1,x_2) &= \frac{(1-2\varepsilon)(x_1^2+x_2^2-x_3^2\varepsilon)}{(1-x_1)(1-x_2)} - \frac{8\hat{m}^4x_3^2}{(1-x_1)^2(1-x_2)^2} - \frac{2\hat{m}^2}{(1-x_1)^2(1-x_2)^2}\{-8(1-\varepsilon)\\
&\quad +2(1-\varepsilon)[x_1^3(1-x_2)+x_2^3(1-x_1)] + x_1[20-13x_1-8(3-2x_1)\varepsilon] + x_2[20\\
&\quad -13x_2-8(3-2x_2)\varepsilon] + 2x_1x_2[-19+24\varepsilon+(9-11\varepsilon)(x_1+x_2)-2(1-\varepsilon)x_1x_2]\},\\
A_1^V(x_1,x_2) &= A_2^V(x_2,x_1) = \frac{1-\varepsilon}{(1-x_1)(1-x_2)} - \frac{2\hat{m}^2}{(1-x_1)^2},\\
A_1^A(x_1,x_2) &= A_2^A(x_2,x_1) = \frac{1-\varepsilon+4\hat{m}^2\varepsilon}{(1-x_1)(1-x_2)} + \frac{2\hat{m}^2(3-2x_1-x_2)}{(1-x_1)^2(1-x_2)},\\
A_{12}^V(x_1,x_2) &= \frac{2(2\hat{m}^2-\varepsilon)}{(1-x_1)(1-x_2)}, \qquad A_{12}^A(x_1,x_2) = -\frac{2[2\hat{m}^2+\varepsilon(1-4\hat{m}^2)]}{(1-x_1)(1-x_2)}.
\end{aligned}
\tag{3.33}
$$

Of course, both currents yield the same result if $\hat{m}=0$, the functions A_0^C and A_{12}^C are symmetric under the exchange of its two arguments, and, as expected, A_{12}^C vanishes for $d=4$ if the quark mass is set to zero. With this result we find for the 4-times differential distribution at $\mathcal{O}(\alpha_s)$ the following expression (for conciseness, in what follows we omit the arguments of the A_i^C functions)

$$
\begin{aligned}
\frac{1}{\sigma_0^C}\frac{\mathrm{d}^4\sigma_{\alpha_s}^C}{\mathrm{d}x_1\mathrm{d}x_2\mathrm{d}\cos(\theta_i)\mathrm{d}\cos(\theta_j)} &= \frac{4^{\varepsilon}\alpha_s C_F}{16\pi^2}\frac{(3-2\varepsilon)(1-2\varepsilon)}{(1-\varepsilon)\Gamma(2-\varepsilon)}\left(\frac{\mu^2e^{\gamma_E}}{Q^2}\right)^{\varepsilon}\frac{\beta_i^{-2\varepsilon}\beta_j^{-2\varepsilon}}{h_{ij}^{1/2+\varepsilon}}\\
&\quad\times\left[A_0^C + A_1^C\beta_1^2\cos^2(\theta_1) + A_2^C\beta_2^2\cos^2(\theta_2) + A_{12}^C\beta_1\beta_2\cos(\theta_1)\cos(\theta_1)\right].
\end{aligned}
\tag{3.34}
$$

As a cross-check, we can integrate the polar angles to obtain the unoriented cross section, differential in the dimensionless variables y and z already defined:[6]

$$
\begin{aligned}
\frac{1}{\sigma_0^C}\frac{\mathrm{d}^2\sigma_{\alpha_s}^C}{\mathrm{d}y\mathrm{d}z} &= \frac{\alpha_s C_F}{8\pi}\frac{y^{1-2\varepsilon}}{(1-\varepsilon)\Gamma(2-\varepsilon)}\left(\frac{\mu^2e^{\gamma_E}}{Q^2}\right)^{\varepsilon}[(1-y)(1-z)z\ -\hat{m}^2]^{-\varepsilon}\\
&\quad\times\{(3-2\varepsilon)A_0^C + \beta_1^2A_1^C + \beta_2^2A_2^C + A_{12}^C[y+y^2(1-z)z+4\hat{m}^2-1]\}.
\end{aligned}
\tag{3.35}
$$

If the A_i^C coefficients given in Eq. (3.33) are substituted in the previous expression, full agreement with Ref. [48] is found. On the other hand, projecting out the angular distribution differential in y and z

[6] Note that in these variables one has $\xi(\hat{m},x_1,x_2) = y^2[(1-y)(1-z)z\ -\hat{m}^2]$ and $\mathrm{d}x_1\mathrm{d}x_2 = y\,\mathrm{d}y\mathrm{d}z$.

through the integration kernel in Eq. (3.24) yields

$$\begin{aligned}\frac{1}{\sigma_0^C}\frac{\mathrm{d}^2\sigma_{\mathrm{ang}}^{\alpha_s,C}}{\mathrm{d}z\mathrm{d}y} &= \frac{1}{\sigma_0}\int \mathrm{dcos}(\theta_1)\mathrm{dcos}(\theta_2)K(\theta_i,y,z)\frac{\mathrm{d}^4\sigma_{\alpha_s}^C}{\mathrm{d}z\mathrm{d}y\mathrm{dcos}(\theta_1)\mathrm{dcos}(\theta_2)} \\ &= \frac{3\alpha_s C_F}{8\pi}\frac{y^{1-2\varepsilon}}{(1-\varepsilon)^2\Gamma(1-\varepsilon)}\left(\frac{\mu^2 e^{\gamma_E}}{Q^2}\right)^{\varepsilon}[(1-y)(1-z)z\ -\hat{m}^2]^{-\varepsilon} \\ &\quad\times\Bigg\{A_q^C(\hat{m},y,z)\theta\left(z-\frac{1}{2}\right)\theta[y_\tau(\hat{m},1-z)-y]+A_{\bar{q}}^C(\hat{m},y,z)\theta\left(\frac{1}{2}-z\right)\theta[y_\tau(\hat{m},z)-y] \\ &\quad+A_g^C(\hat{m},y,z)\theta[y-y_\tau(\hat{m},z)]\theta[y-y_\tau(\hat{m},1-z)]\Bigg\},\end{aligned} \tag{3.36}$$

with $A_g^C(\hat{m},y,z)=A_g^C(\hat{m},y,1-z)$ and $A_q^C(\hat{m},y,z)=A_{\bar{q}}^C(\hat{m},y,1-z)$. A tedious but straightforward computation yields

$$\begin{aligned}8A_q^C(\hat{m},y,z) &= (1-4\varepsilon)A_0^C-\frac{5+4\varepsilon}{5-2\varepsilon}\Big\{\big([1-y(1-z)]^2-4\hat{m}^2\big)A_1^C+\big[(1-yz)^2-4\hat{m}^2\big]A_2^C \\ &\quad+A_{12}^C\big[y+y^2(1-z)z+4\hat{m}^2-1\big]\Big\}+\frac{40A_2^C}{5-2\varepsilon}\frac{y^2[(1-y)(1-z)z-\hat{m}^2]}{[1-y(1-z)]^2-4\hat{m}^2}, \\ 8A_g^C(\hat{m},y,z) &= (1-4\varepsilon)A_0^C-\frac{5+4\varepsilon}{5-2\varepsilon}\Big\{\big([1-y(1-z)]^2-4\hat{m}^2\big)A_1^C+\big[(1-yz)^2-4\hat{m}^2\big]A_2^C\Big\} \\ &\quad+\frac{40[(1-y)z(1-z)-\hat{m}^2]}{5-2\varepsilon}(A_1^C+A_2^C+2A_{12}^C) \\ &\quad+\frac{A_{12}^C}{5-2\varepsilon}\{(5+4\varepsilon)[1-y-y^2z(1-z)]-120z(1-z)(1-y)+4(25-4\varepsilon)\hat{m}^2\}.\end{aligned} \tag{3.37}$$

Plugging the expressions for A_i^C in Eq. (3.33) and setting both $\hat{m}=\varepsilon=0$ one recovers the results displayed in Eq. (1.3) of Ref. [51].

3.5.1 Axial-vector current

Since in this case there are no IR singularities, neither in the virtual-radiation term (as long as one sets $d=4$ in the phase-space right away) nor in the real-radiation one, for conciseness we show results with $\varepsilon=0$ only:

$$\begin{aligned}A_q^A(\hat{m},y,z) &= \frac{(1-y)z^2-\hat{m}^2z\{2-y^2+z[2+y(y-2)]\}+2\hat{m}^4}{z^2\{[1-y(1-z)]^2-4\hat{m}^2\}}, \\ A_g^A(\hat{m},y,z) &= \frac{2(1-y)(1-z)^2z^2-\hat{m}^2(1-z)z(4-y^2-2y)+2\hat{m}^4}{y^2(1-z)^2z^2}.\end{aligned} \tag{3.38}$$

As anticipated, $A_q^A(\hat{m},y,z)$ is finite as $y\to 0$, therefore no soft singularity is present. On the other hand, $y\,A_g^A(\hat{m},y,z)$ diverges if $y=0$, but the Heaviside functions that multiply this term in Eq. (3.36) impose $y>y_{\mathrm{middle}}(\hat{m})$ which is a positive number in the physical range $0\le\hat{m}<1/2$, and therefore screens the soft singularity. This entails that for any event shape, the angular axial-vector distribution will have no singular structures at $\mathcal{O}(\alpha_s)$. Only a non-singular distribution will remain, that can be computed analytically or numerically depending on the event shape. We will explore this further in subsequent sections.

Since, as we just discussed, for the axial-vector current only the real radiation contributes, we can

already provide a closed form for the total angular cross section, simply integrating A_q^A, $A_{\bar{q}}^A$ and A_g^A in their respective patches within the phase space. Since there is a mirror symmetry with respect to the $z = 1/2$ vertical axis, it is enough to integrate between $z = z_-$ and $z = 1/2$ and double the result. Finally, the region in which the thrust axis points into the anti-quark direction has two distinct upper boundaries: $y_{\max}(\hat{m}, z)$ for $z_- < z < \hat{m}$ and $y_\tau(\hat{m}, z)$ for $\hat{m} < z < 1/2$, and we split the corresponding integral accordingly:

$$
\begin{aligned}
R_1^{\text{ang},A}(\hat{m}) = \frac{3C_F}{4}\Bigg\{ & \int_{z_-}^{\hat{m}} \mathrm{d}z \tilde{A}_{\bar{q}}^A[\hat{m}, y_{\max}(\hat{m}, z), z] + \int_{\hat{m}}^{\frac{1}{2}} \mathrm{d}z \tilde{A}_{\bar{q}}^A[\hat{m}, y_\tau(\hat{m}, z), z] \\
& + \int_{\hat{m}}^{1/2} \mathrm{d}z \tilde{A}_g^A[\hat{m}, y_{\max}(\hat{m}, z), y_\tau(\hat{m}, z), z] \Bigg\}, \qquad (3.39) \\
\tilde{A}_{\bar{q}}^A(\hat{m}, y, z) = \frac{1}{4\hat{m}(1-z)^2 z^3}\Bigg\{ & [1 - z - 2\hat{m}^2(2-z)] \Bigg[(1-2\hat{m})(1-z-\hat{m})^2 \log\left(1 - \frac{yz}{1-2\hat{m}}\right) \\
& - (1+2\hat{m})(1-z+\hat{m})^2 \log\left(1 - \frac{yz}{1+2\hat{m}}\right) \Bigg] \\
& - 2\hat{m} y (1-z) z \{2(1-z) - \hat{m}^2[8 - (4-y)z]\} \Bigg\}, \\
\tilde{A}_g^A(\hat{m}, y_1, y_2, z) = \frac{1}{2(1-z)^2 z^2}\Bigg\{ & 4[(1-z)z - \hat{m}^2]^2 \log\left(\frac{y_1}{y_2}\right) \\
& + (1-z)z(y_1 - y_2)[\hat{m}^2(y_1 + y_2 + 4) - 4(1-z)z] \Bigg\},
\end{aligned}
$$

where the functions $\tilde{A}_q^A$ and $\tilde{A}_g^A$ are defined as

$$
\tilde{A}_{\bar{q}}^A(\hat{m}, y, z) = \int_0^y \mathrm{d}h \, h A_{\bar{q}}^A(\hat{m}, h, z)\,, \qquad \tilde{A}_g^C(\hat{m}, y_1, y_2, z) = \int_{y_2}^{y_1} \mathrm{d}h \, h A_g^C(\hat{m}, h, z)\,. \qquad (3.40)
$$

Even though the definition of $\tilde{A}_g^C$ can be used both for vector and axial-vector currents, due to soft singularities we need to define $\tilde{A}_{\bar{q}}^A$ and $\tilde{A}_{\bar{q}}^V$ separately. While the integrals in y have been carried out analytically, we have not found simple expressions for the z integrations.[7] Instead, we carry out these (along with similar ones for the vector current or cumulative cross sections, to be discussed in Sec. 3.6) numerically.

3.5.2 Vector current

Due to the non-vanishing tree-level result, the vector-current matrix element diverges in the soft limit and the linear dependence on ε must be retained. However, we only need to keep track of this parameter in the terms of $A_{q,\bar{q}}^V$ which do diverge when $y \to 0$. Accordingly we define

$$
\begin{aligned}
V^{\text{div}}(\hat{m}, z, \varepsilon) &= \lim_{y\to 0} y^2 A_q^V(\hat{m}, y, z) = \lim_{y\to 0} y^2 A_{\bar{q}}^V(\hat{m}, y, z) = V^{\text{div}}(\hat{m}, z, 0) + V^\varepsilon(\hat{m}, z)\varepsilon + \mathcal{O}(\varepsilon^2)\,, \qquad (3.41) \\
V^{\text{div}}(\hat{m}, z, 0) &= -2\hat{m}^2 M_V^1(\hat{m}, z)\,, \qquad V^\varepsilon(\hat{m}, z) = \frac{9 + 14\hat{m}^2}{5} M_V^1(\hat{m}, z)\,, \\
M_V^1(\hat{m}, z) &= -\frac{(1-z)z - \hat{m}^2}{(1-z)^2 z^2}\,,
\end{aligned}
$$

[7] We found extremely lengthy analytical expressions in terms of polylogarithms and have not been able to simplify them to an amenable size. Therefore it is unpractical to code these and we instead opt for a numerical implementation.

where the function $M_V^1(\hat{m},z)$ is present also in the computation of the unoriented cross section, see Eq. (3.18) of Ref. [48]. We note $V^{\rm div}(\hat{m},z,\varepsilon)=V^{\rm div}(\hat{m},1-z,\varepsilon)$ and also that $V^{\rm div}(\hat{m},z,0)$ vanishes in the massless limit. The fact that $V^{\varepsilon}(0,z)\neq 0$ is an artifact of dimensional regularization that leaves no trace once the virtual-radiation contribution is added. Keeping only the necessary (linear) dependence on ε to carry out the computation we end up with the following expressions:

$$\begin{aligned}
A_q^V(\hat{m},y,z) &= \frac{V^{\rm div}(\hat{m},z,0)+V^{\varepsilon}(\hat{m},z)\varepsilon}{y^2}+V^{\rm fin}(y,z,\hat{m})\,, \\
A_g^V(\hat{m},y,z) &= \frac{2[(1-y)z(1-z)-\hat{m}^2]}{y^2(1-z)z}, \\
V^{\rm fin}(\hat{m},y,z) &= \frac{(1-y)y(1-z)z^2-\hat{m}^2z[2-y(1-2z^2)]+2\hat{m}^4[y(1-z)+4z]}{y(1-z)z^2\{[1-y(1-z)]^2-4\hat{m}^2\}}\,.
\end{aligned} \tag{3.42}$$

It is simple to see that y integrals with zero lower integration limit (such as the total cross section or any cumulative distribution) will produce a $1/\varepsilon$ pole.

As for the axial-vector current, we postpone the computation of the differential distribution to the next section and show now results for the total angular cross-section, discussing how the cancellation takes place. One has to integrate A_q^V between the lowest part of the phase space, $y=0$, and the upper boundary of the region in which the thrust axis points in the same direction as the anti-quark's 3-momentum. We define $A_{\rm sing}^R(\hat{m})$ as the contribution to the total angular cross-section coming from the terms inversely proportional to y^2 in A_q^V. As we discussed in the previous section, the z integration can be restricted to $z<1/2$ such that one can compactly write the y upper integration limit as $y_{\rm top}(\hat{m},z)\equiv\min[y_\tau(\hat{m},z),y_{\rm max}(\hat{m},z)]$. With this definition one can compute $A_{\rm sing}^R$ analytically as follows (we do not include the prefactor $3C_F/4$ that equals unity in QCD):

$$\begin{aligned}
A_{\rm sing}^R(\hat{m}) &= \frac{1}{(1-\varepsilon)\Gamma(2-\varepsilon)}\left(\frac{\mu^2e^{\gamma_E}}{Q^2}\right)^{\varepsilon}\int_{z_-}^{\frac{1}{2}}{\rm d}zV^{\rm div}(\hat{m},z,\varepsilon)[(1-z)z-\hat{m}^2]^{-\varepsilon}\int_0^{y_{\rm top}(\hat{m},z)}\frac{{\rm d}y}{y^{1+2\varepsilon}} \\
&= \int_{z_-}^{\frac{1}{2}}{\rm d}z\left\{\hat{m}^2\left[\frac{1}{\varepsilon}+2-\log\left(\frac{Q^2}{\mu^2}\right)-\log\big[(1-z)z-\hat{m}^2\big]\right]-\frac{9+14\hat{m}^2}{10}\right\}M_V^1(\hat{m},z) \\
&\quad -2\hat{m}^2\int_{z_-}^{\frac{1}{2}}{\rm d}z\log[y_{\rm top}(\hat{m},z)]M_V^1(\hat{m},z)+\mathcal{O}(\varepsilon)\,,
\end{aligned} \tag{3.43}$$

where in the first line we have already discarded a term that vanishes as $\varepsilon\to 0$, see discussion after Eq. (3.51). Expanding in ε one gets $\int_0^{y_{\rm top}}{\rm d}y\,y^{-1-2\varepsilon}=-1/(2\varepsilon)+\log(y_{\rm top})+\mathcal{O}(\varepsilon)$ for the y integral. The divergent term does not depend on the upper integration limit, simplifying the subsequent computations. The z integrals in the second line can be carried out analytically, and for that we shall only need the following two integrals:

$$\begin{aligned}
\int_{z_-}^{\frac{1}{2}}{\rm d}zM_V^1(\hat{m},z) &= \beta-2(1-2\hat{m}^2)L_\beta\,, \\
\int_{z_-}^{\frac{1}{2}}{\rm d}zM_V^1(\hat{m},z)\log\big[(1-z)z-\hat{m}^2\big] &= 2L_\beta-2\beta\log(\beta)+\frac{1+\beta^2}{2}\left[{\rm Li}_2\left(\frac{2\beta}{\beta-1}\right)\right. \\
&\quad \left.-2{\rm Li}_2\left(\frac{2\beta}{\beta+1}\right)+4\log(\beta)L_\beta\right].
\end{aligned} \tag{3.44}$$

The result in the first line of the previous equation shows that the $1/\varepsilon$ pole cancels against its virtual counterpart, along with the μ dependence and the term which does not vanish in the massless limit.

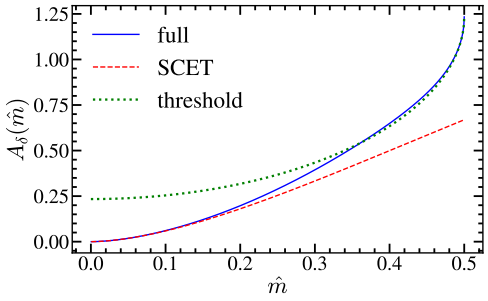

Figure 3.8: Coefficient A_δ (solid blue) and its SCET (dashed red) and threshold (dotted green) approximations.

We are now in position to show the final expression for the total angular cross-section at $\mathcal{O}(\alpha_s)$ for the vector current. We split the result in a term dubbed $A_\delta(\hat{m})$, which contains the virtual-radiation contribution from the second line of Eq. (2.52), and the analytical z integrals on the second line of Eq. (3.43) combined in an IR-free coefficient, plus terms in which the z integrals do not admit a simple analytical form and hence, in practice, are computed numerically:

$$
\begin{aligned}
R_1^{\mathrm{ang},V}(\hat{m}) &= \frac{3C_F}{4}\left\{A_\delta(\hat{m}) + \int_{z_-}^{1/2} \mathrm{d}z \tilde{A}_q^V[\hat{m}, y_{\mathrm{top}}(\hat{m},z), z] + \int_{\hat{m}}^{\frac{1}{2}} \mathrm{d}z \tilde{A}_g^V[\hat{m}, y_{\mathrm{max}}(\hat{m},z), y_\tau(\hat{m},z), z]\right\},\\
A_\delta(\hat{m}) &= \hat{m}^2\left\{2\beta[\log(\hat{m})-1] + \frac{1+\beta^2}{2}\left[\pi^2 - 2L_\beta^2 + \mathrm{Li}_2\left(\frac{2\beta}{\beta-1}\right) - 3\,\mathrm{Li}_2\left(\frac{2\beta}{\beta+1}\right)\right.\right.\\
&\qquad \left.\left. -4L_\beta[\log(\hat{m})-1]\right]\right\},\\
\tilde{A}_q^V(\hat{m},y,z) &= \tilde{V}^{\mathrm{fin}}(\hat{m},y,z) + \log(y)V^{\mathrm{div}}(\hat{m},z,0)\,,\\
\tilde{A}_g^V(\hat{m},y_{\mathrm{max}},y_\tau,z) &= 2\left[y_\tau - y_{\mathrm{max}} - M_V^1(z,\hat{m})\log\left(\frac{y_{\mathrm{max}}}{y_\tau}\right)\right],\\
\tilde{V}^{\mathrm{fin}}(\hat{m},y,z) &= \frac{1}{4\hat{m}(1-z)^2z^3}\left\{(1-z-2\hat{m}^2z)\left[(1-2\hat{m})(1-z-m)^2\log\left(1-\frac{yz}{1-2\hat{m}}\right)\right.\right.\\
&\qquad \left.\left. -(1+2\hat{m})(1-z+\hat{m})^2\log\left(1-\frac{yz}{1+2\hat{m}}\right)\right] - 4\hat{m}\,y(1-z)^2z\right\},
\end{aligned}
\tag{3.45}
$$

where the expression for $\tilde{A}_g^V$ can be found in Eq. (3.40) and $\tilde{V}^{\mathrm{fin}}$ is defined as

$$
\tilde{V}^{\mathrm{fin}}(\hat{m},y,z) = \int_0^y \mathrm{d}h h V^{\mathrm{fin}}(\hat{m},h,1-z)\,. \tag{3.46}
$$

The function A_δ can be expanded for small $\hat{m}$, and the leading term will be referred to as its SCET limit, and also around $\beta = 0$, whose leading approximation is the mass threshold limit:

$$
\begin{aligned}
A_\delta(\hat{m}) &= \frac{1}{3}\hat{m}^2[\pi^2 - 6\log(\hat{m}) - 6] + \mathcal{O}(\hat{m}^4)\,, \qquad (3.47)\\
A_\delta(\hat{m}) &= \frac{\pi^2}{8} - \beta + \mathcal{O}(\beta^2)\,.
\end{aligned}
$$

This coefficient, along with its expansions in the previous formula, are shown in Fig. 3.8, where an enhancement towards $\hat{m} = 1/2$ can be observed.

3.5.3 Total Angular Cross Section Results

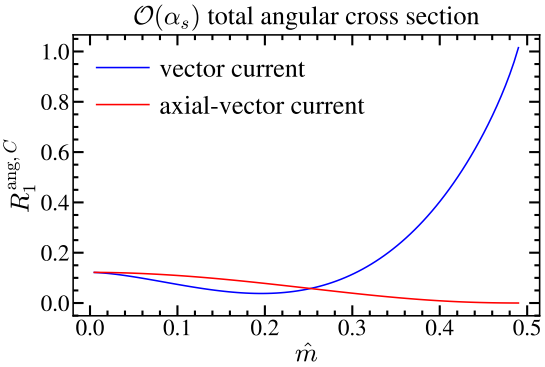

Figure 3.9: Total angular cross-section at $\mathcal{O}(\alpha_s)$ for vector (blue) and axial-vector (red) currents. While $R_1^{\mathrm{ang},A}(1/2) = 0$, one has that $R_1^{\mathrm{ang},C}(0)$ and $R_1^{\mathrm{ang},V}(1/2)$ are both non-zero.

In Fig. 3.9 the dependence of $R_1^{\mathrm{ang},C}$ on $\hat{m}$ is shown. One can observe that, whereas the $\mathcal{O}(\alpha_s)$ total angular cross-section vanishes at $\hat{m} = 1/2$ for the axial-vector current, the vector result does not vanish neither in the massless limit nor at threshold. Vector and axial-vector currents agree for $m = 0$ and reproduce the analytic result quoted in Ref. [51], that is $R_1^{\mathrm{ang},C}(\hat{m} = 0) = 3C_F/8[\log(3/2) - 3] \simeq 0.12186$. All terms in $R_1^{\mathrm{ang},V}$ except for A_δ tend to zero in the limit $\hat{m} \to 1/2$. Hence, we can provide an analytic result for the total angular cross section at threshold: $R_1^{\mathrm{ang},V}(1/2) = 3\pi^2 C_F/36 \approx 1.09662$. In fact, A_δ is responsible for the vector current cross section being larger than the axial-vector one over most of the spectrum. In particular, this non-vanishing result (which is also found for the total unoriented cross section) seems to point into a Sommerfeld enhancement at higher orders, which would imply the need for NRQCD resummation. This, a priory, indicates that R_{ang} might be an interesting viable observable to measure the top quark mass at a future linear collider through threshold scans.

Although all our results have been expressed in terms of the quark's pole mass, with a single simple modification we can obtain $\overline{\mathrm{MS}}$ results. At the order that we are working we only need the relation between these two mass schemes at leading order:

$$m_{\mathrm{pole}} = \overline{m}(\mu)\left\{1 + \left[\frac{\alpha_s(\mu)}{\pi}\right] C_F \left[1 - \frac{3}{2}\log\left(\frac{\overline{m}(\mu)}{\mu}\right)\right]\right\} + \mathcal{O}(\alpha_s^2)\,. \tag{3.48}$$

None of the results for the axial-vector current need any modification: one simply replaces the pole mass by $\overline{m}(\mu)$. For the vector current, one proceeds in the same way and corrects the $\mathcal{O}(\alpha_s)$ angular cross section. Defining $\tilde{m}_\mu \equiv \overline{m}(\mu)/Q$ and $\tilde{\beta}_\mu \equiv \sqrt{1 - 4\tilde{m}_\mu^2}$, and using the notation that quantities with a bar on top are expressed in the $\overline{\mathrm{MS}}$ scheme, one has:

$$\begin{aligned} \overline{R}_1^{\mathrm{ang},V}(\tilde{m}_\mu) &= R_1^{\mathrm{ang},V}(\tilde{m}_\mu) + \frac{3C_F}{4}\delta_{\mathrm{ang}}^{\overline{\mathrm{MS}}}\,, \\ \delta_{\mathrm{ang}}^{\overline{\mathrm{MS}}} &\equiv \frac{\tilde{m}_\mu^2}{\tilde{\beta}_\mu}\left\{2 - 3\log\left[\frac{\overline{m}(\mu)}{\mu}\right]\right\}. \end{aligned} \tag{3.49}$$

We close this section quantifying the size of the bottom quark mass corrections to the total angular cross section as a function of the center-of-mass energy Q. For this analysis we use the quark mass

in the $\overline{\text{MS}}$ scheme and set the renormalization scale to its canonical value $\mu = Q$. Finally, we use the canonical reference values $\overline{m}_b(\overline{m}_b) = 4.2\,\text{GeV}$ and $\alpha_s^{(n_f=5)}(m_Z) = 0.1181$, which are evolved to $\mu = Q$ using `REvolver` [39].

In our first analysis, we assume that one can experimentally 'tag' on bottom quarks and a given current and compute the ratio of the bottom correction over the massless result for both currents at leading and next-to-leading order for the vector current, and at the only available order for the axial-vector current —that is, $\mathcal{O}(\alpha_s)$. The vector current represents always a much bigger correction since it starts at $\mathcal{O}(\alpha_s^0)$ while the massless results and the axial-vector current have no tree-level contribution. As expected, the correction is significantly larger at smaller energies: for the NLO prediction, while at $Q = 30\,\text{GeV}$ the correction is 1.85 times larger than the massless approximation, at $Q = \{50, 100\}\,\text{GeV}$ it has already gone down to $\{64, 16\}\%$, as can be seen in Fig. 3.10. For the axial-vector current the correction is always negative and at the three energies just quoted amounts to 11%, 3.8% and 9 ‰, respectively.

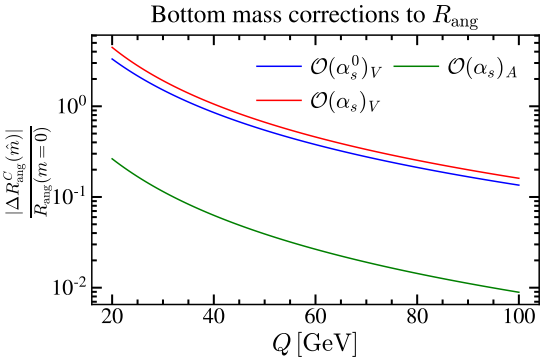

Figure 3.10: Bottom mass corrections to the total angular cross-section as a function of the center-of-mass energy Q for bottom- and current-tagged measurements. In blue and red we show the LO and NLO results for the vector cross section. The green line corresponds to the axial-vector current, which starts only at $\mathcal{O}(\alpha_s)$.

A more realistic comparison, presented in Fig. 3.11, considers the inclusive measurement of the cross section, that is, the incoherent sum of cross sections for all quarks lighter than the top and including the two currents. We again consider the ratio (mass correction)/(massless approximation), which

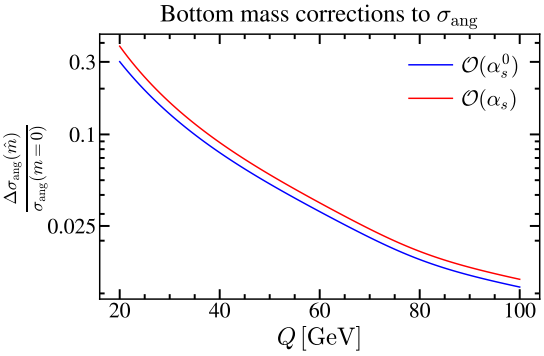

Figure 3.11: Bottom mass corrections to the total angular cross-section as a function of the center-of-mass energy Q for totally inclusive measurements. In blue and red we show the LO and NLO results.

is computed taking into account the electroweak factors L^C [see Eq. (1.6)] in the Born cross-section Eq. (3.26). We use the numerical values $m_Z = 91.1876\,\text{GeV}$, $\Gamma_Z = 2.4952\,\text{GeV}$ and $\sin(\theta_W) = 0.23119$. Here the correction is milder, but still sizable such that it has to be included in any precision analysis, in particular if it includes data at small or intermediate energies. For the NLO prediction the massive correction is 38%, 4.27% and 1.11% for $Q = 20, 50$ and $100\,\text{GeV}$, respectively.

3.6 Event-shape differential Distributions

In this section we combine the real- and virtual-radiation results and project out the differential distributions. For three particles in the final state, one has that the measurement for any event-shape is a function of the reduced mass and the kinematic variables y and z. Expanding the measurement function in the soft limit is useful to analytically obtain the plus and Dirac delta function coefficients:

$$\hat{e}(\hat{m}, y, z) = e_{\min}(\hat{m}) + y f_e(\hat{m}, z) + \mathcal{O}(y^2) \equiv \overline{e}(\hat{m}, y, z) + \mathcal{O}(y^2)\,. \tag{3.50}$$

This function has the property that $\hat{e}(\hat{m}, y, z) = e_{\min}(\hat{m})$ if and only if $y = 0$. We can use the measurement function to write down a formal integral expression for the angular-differential distribution which is valid for both currents:

$$\begin{aligned} f_{e,1}^{\text{ang},C}(\hat{m}, e) = \frac{3C_F}{4}\Bigg\{ & R_{21}^{\text{ang},C}\delta[e - e_{\min}(\hat{m})] + \int_{\hat{m}}^{\frac{1}{2}} \mathrm{d}z \int_{y_\tau(\hat{m},z)}^{y_{\max}(\hat{m},z)} \mathrm{d}y\, y A_g^C(\hat{m}, y, z)\delta[e - \hat{e}(\hat{m}, z, y)] \\ & + \frac{1}{(1-\varepsilon)\Gamma(2-\varepsilon)}\left(\frac{\mu^2 e^{\gamma_E}}{Q^2}\right)^{\varepsilon} \int_{z_-}^{\frac{1}{2}} \mathrm{d}z \int_0^{y_{\text{top}}(\hat{m},z)} \frac{\mathrm{d}y\, y^{1-2\varepsilon}}{[(1-z)z - \hat{m}^2]^{\varepsilon}} A_{\bar{q}}^C(\hat{m}, y, z)\delta[e - \hat{e}(\hat{m}, y, z)]\Bigg\}, \end{aligned} \tag{3.51}$$

where we have set $\varepsilon = 0$ already in the A_g^C integration as that term has no support in the soft part of the Dalitz region, and also $y = 0$ in $\xi(\hat{m}, x_1, x_2)/y^2$ since keeping a non-zero y yields the same result plus a term that vanishes in $d = 4$ dimensions.

3.6.1 Axial-vector current

For the axial-vector current, given that there are no soft singularities, one can use $\varepsilon = 0$ right away as long as $R_{21}^{\text{ang},A}$ is also set to zero. This implies that the ε-dependent factor out front the integral becomes 1 and also that $f_{e,1}^{\text{ang},A}(\hat{m}, e)$ is purely non-singular: it is an integrable function as $e \to e_{\min}(\hat{m})$.[8] The y and z integrals can be carried out analytically for some simple event shapes such as 2-jettiness or heavy jet mass (see next section for explicit expressions), and can be integrated numerically yielding unbinned distributions with machine precision in fractions of a second using the algorithm introduced in Ref. [48]. Finally, for completeness, we connect with the notation of Eq. (3.3): $C_F F_{A,e}^{\text{ang}}(\hat{m}, e) = f_{e,1}^{\text{ang},A}(\hat{m}, e)$.

3.6.2 Vector current

For the vector current one has to proceed with care, as there are soft singularities that need special treatment. To that end, following the same strategy as for the computation of the total angular cross-section, we single out the $A_{\bar{q}}^V$ terms inversely proportional to y^2 in the integral on the second line, as

[8] Recall that, as seen in the previous Chapter, this does not imply that $f_{e,1}^{\text{ang},A}[\hat{m}, e_{\min}(\hat{m})]$ is finite since it can have a logarithmic divergence in the dijet limit, which happens for those event shapes with $e_{\min}(\hat{m}) = 0$, including any observable in the E- or P-schemes.

those are the only ones, together with the virtual radiation, that can yield singular structures:

$$
\begin{aligned}
f_{\text{sing}}^{\text{real}} &= \frac{1}{(1-\varepsilon)\Gamma(2-\varepsilon)}\left(\frac{\mu^2 e^{\gamma_E}}{Q^2}\right)^{\varepsilon}\int_{z_-}^{\frac{1}{2}}\mathrm{d}z\,\frac{V^{\text{div}}(\hat{m},z,\varepsilon)}{[(1-z)z-\hat{m}^2]^{\varepsilon}}\int_0^{y_{\text{top}}(\hat{m},z)}\frac{\mathrm{d}y}{y^{1+2\varepsilon}}\delta[e-\hat{e}(\hat{m},y,z)] \qquad (3.52)\\
&= \delta[e-e_{\min}(\hat{m})]\int_{z_-}^{\frac{1}{2}}\mathrm{d}z\left\{\hat{m}^2\left[\frac{1}{\varepsilon}+2-\log[(1-z)z-\hat{m}^2]-\log\left(\frac{Q^2}{\mu^2}\right)\right]-\frac{9+14\hat{m}^2}{10}\right\}M_V^1(\hat{m},z)\\
&\quad-\hat{m}^2\int_{z_-}^{\frac{1}{2}}\mathrm{d}z M_V^1(\hat{m},z)\int_0^{y_{\text{top}}(\hat{m},z)}\mathrm{d}y\left[\frac{1}{y}\right]_+\delta[e-\overline{e}(\hat{m},y,z)]\\
&\quad-\hat{m}^2\int_{z_-}^{\frac{1}{2}}\mathrm{d}z M_V^1(\hat{m},z)\int_0^{y_{\text{top}}(\hat{m},z)}\frac{\mathrm{d}y}{y}\{\delta[e-\hat{e}(\hat{m},y,z)]-\delta[e-\overline{e}(\hat{m},y,z)]\}\,,
\end{aligned}
$$

where to get to the second line we have used the identity $y^{-1-2\varepsilon}=-1/(2\varepsilon)\delta(y)+[1/y]_+ + \mathcal{O}(\varepsilon)$ and expanded in ε. When one adds the virtual-radiation contribution to the first line, the IR singularity and μ dependence disappear and the coefficient A_δ defined in Eq. (3.45) is found. The term in the last line is regular when $y\to 0$ and does not yield any distribution. It is important to add and subtract $\delta[e-\overline{e}(\hat{m},y,z)]$ and not simply $\delta[e-e_{\min}(\hat{m})]$ since otherwise the subtracted term would still contain singular structures.

To fully disentangle the coefficient of the plus and Dirac delta functions we proceed as follows with the term in the third line:

$$
\begin{aligned}
&\int_{z_-}^{\frac{1}{2}}\mathrm{d}z\frac{M_V^1(\hat{m},z)}{f_e(\hat{m},z)}\int_0^1\mathrm{d}y\,\theta[y_{\text{top}}(\hat{m},z)-y]\left[\frac{1}{y}\right]_+\delta\left[y-\frac{e-e_{\min}(\hat{m})}{f_e(\hat{m},z)}\right] \qquad (3.53)\\
&=\int_{z_-}^{\frac{1}{2}}\mathrm{d}z\frac{M_V^1(\hat{m},z)}{f_e(\hat{m},z)}\left[\frac{f_e(\hat{m},z)}{e-e_{\min}(\hat{m})}\right]_+\theta[f_e(\hat{m},z)y_{\text{top}}(\hat{m},z)-e+e_{\min}(\hat{m})]\\
&=\int_{z_-}^{\frac{1}{2}}\mathrm{d}z M_V^1(\hat{m},z)\left\{\left[\frac{1}{e-e_{\min}(\hat{m})}\right]_+-\delta[e-e_{\min}(\hat{m})]\log[f_e(\hat{m},z)]\right.\\
&\qquad\qquad\left.-\frac{\theta[e-e_{\min}(\hat{m})-f_e(\hat{m},z)y_{\text{top}}(\hat{m},z])}{e-e_{\min}(\hat{m})}\right\},
\end{aligned}
$$

where we used the rescaling identity[9] and Eq. (2.70) for the plus distribution, and the completeness relation $\theta(x)+\theta(-x)=1$ for the Heaviside theta. We can now write down the analytic form for the Dirac delta and plus distribution coefficients defined in Eq. (3.3):

$$
\begin{aligned}
A_e^{\text{ang}}(\hat{m}) &= \frac{3}{4}[A_\delta(\hat{m})-2\hat{m}^2 I_e(\hat{m})]\,, \qquad B_{\text{plus}}^{\text{ang}}(\hat{m}) = \frac{3\hat{m}^2}{2}[2(1-2\hat{m}^2)L_\beta-\beta]\,, \qquad (3.55)\\
I_e(\hat{m}) &= -\int_{z_-}^{\frac{1}{2}}\mathrm{d}z M_V^1(\hat{m},z)\log[f_e(z)]\,,
\end{aligned}
$$

where both coefficients vanish in the massless limit and the event-shape-dependent function I_e was already defined in Ref. [48], and analytically computed for a large number of event shapes in various schemes.

[9] That is

$$
\left[\frac{\log^n(ax)}{ax}\right]_+ = \frac{1}{a}\left\{\frac{\log^{n+1}(a)}{n+1}\delta(x)+\sum_{i=0}^{n}\binom{n}{i}\log^{n-i}(a)\left[\frac{\log^n(x)}{x}\right]_+\right\}. \qquad (3.54)
$$

Additionally, we provide the leading term of the plus function coefficient when expanded around the massless limit, $B^{\rm ang}_{\rm plus}(\hat{m}) \approx -3\hat{m}^2[1+2\log(\hat{m})]/2$, which we again call the SCET approximation, and around $\beta = 0$ (threshold approximation), $B^{\rm ang}_{\rm plus}(\hat{m}) \approx \beta^3/2$. Therefore, $B^{\rm ang}_{\rm plus}$ vanishes both in the massless limit and at threshold. We have already argued that such behavior is expected for $\hat{m} = 0$: for massless quarks the distribution is purely non-singular. At threshold there is not enough energy to emit an extra particle and therefore there is no radiative tail, causing a null value for $B^{\rm ang}_{\rm plus}$ (one can however have a non-zero coefficient for the delta function). In Fig. 3.12 $B^{\rm ang}_{\rm plus}$, $A^{\rm ang}_{\tau_J}(\hat{m})$, $A^{\rm ang}_{\rho}(\hat{m})$ and their approximations are shown.

We close this section writing down an expression for the non-singular distribution

$$\begin{aligned} F^{\rm ang}_{V,e}(e,\hat{m}) = \frac{3}{4}\Bigg[\int_{\hat{m}}^{\frac{1}{2}} \mathrm{d}z \int_{y_\tau(\hat{m},z)}^{y_{\max}(\hat{m},z)} \mathrm{d}y\, y A^C_g(\hat{m},y,z) + \int_{z_-}^{\frac{1}{2}} \mathrm{d}z \int_0^{y_{\rm top}(\hat{m},z)} \mathrm{d}y\, y V^{\rm fin}(\hat{m},y,1-z)\Bigg]\delta[e-\hat{e}(\hat{m},z,y)] \\ -\frac{3\hat{m}^2}{4}\int_{z_-}^{\frac{1}{2}} \mathrm{d}z M^1_V(\hat{m},z) \int_0^{y_{\rm top}(\hat{m},z)} \frac{\mathrm{d}y}{y}\{\delta[e-\hat{e}(\hat{m},y,z)] - \delta[e-\overline{e}(\hat{m},y,z)]\} \\ +\frac{3\hat{m}^2}{4}\int_{z_-}^{\frac{1}{2}} \mathrm{d}z M^1_V(\hat{m},z) \frac{\theta[e-e_{\min}(\hat{m}) - f_e(\hat{m},z) y_{\rm top}(\hat{m},z])}{e-e_{\min}(\hat{m})}\,. \end{aligned} \tag{3.56}$$

Even though we have a formal expression for the non-singular terms, in practice it is simpler to compute (numerically or analytically, depending on the event shape) the complete distribution (singular plus non-singular) for $e > e_{\min}$ such that one can drop the plus prescription from $1/[e-e_{\min}(\hat{m})]_+$ and the delta function is simply zero. Furthermore, one can set $\varepsilon = 0$ and work only with the real-radiation contribution in $d = 4$ dimensions. Since the coefficient of the plus distribution has been computed analytically, the non-singular distribution is then obtained by simply subtracting the radiative tail:

$$C_F F^{\rm ang}_{V,e}(e,\hat{m}) = f^{{\rm ang},V}_{e,1}[\hat{m}, e > e_{\min}(\hat{m})]|_{\varepsilon=0} - C_F B^{\rm ang}_{\rm plus}(\hat{m})\left[\frac{1}{e-e_{\min}(\hat{m})}\right]. \tag{3.57}$$

As for the total angular cross section, in order to express the vector current result in the $\overline{\rm MS}$ scheme, one needs to account for the following modification:

$$\bar{A}^{\rm ang}_e(\tilde{m}_\mu) = A^{\rm ang}_e(\tilde{m}_\mu) + \delta^{\overline{\rm MS}}_{\rm ang}\,. \tag{3.58}$$

Eqs. (3.58) and (3.49) can be encompassed in the following single substitution: $A_\delta \to A_\delta + (4/3)\delta^{\overline{\rm MS}}_{\rm ang}$.

3.7 Thrust and Heavy Jet Mass Distributions

In this section we compute and discuss the differential and cumulative angular cross sections for 2-jettiness (M-scheme thrust) and heavy jet mass (see Tab. 2.1 for the corresponding definitions). While we are capable of obtaining fully analytical results for the differential distribution, for the cumulative versions we are left with a one-dimensional numerical integral.

For three partons, one of them massless, it can be shown that the 2-jettiness measurement function can be expressed as a minimum condition:

$$\tau_J = \min\{1-y, 1-\ \mathrm{mod}(\hat{m},y,1-z), 1-\ \mathrm{mod}(\hat{m},y,z)\}\,, \tag{3.59}$$

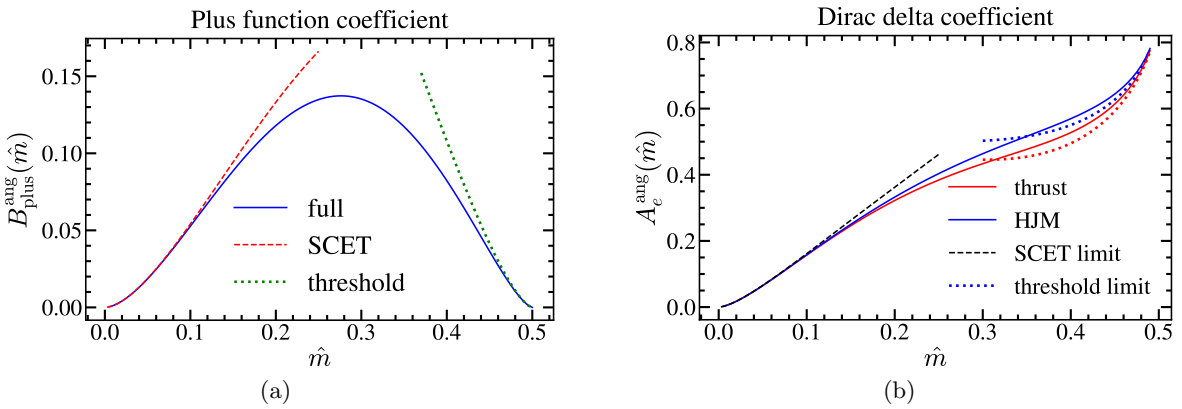

Figure 3.12: Panel (a): Plus function coefficient $B^{\rm ang}_{\rm plus}(\hat{m})$ (solid blue) and its leading SCET (dashed red) and threshold (dotted green) approximations. Panel (b): Dirac delta function coefficient $A^{\rm ang}_{e}(\hat{m})$ for 2-jettiness $e = \tau_J$ (blue) and heavy jet mass $e = \rho$ (red) as solid lines for the full result, dotted lines for the respective threshold expansions, and as a black dashed line for the common SCET expansion.

with $\mathrm{mod}(\hat{m}, y, z) \equiv \sqrt{(1-yz)^2 - 4\hat{m}^2}$. The three values in the list correspond to the thrust axis parallel to the 3-momentum of the gluon, quark and anti-quark, respectively.

On the other hand, for the configuration just described, the heavy jet mass measurement is best written as a piece-wise function:

$$\begin{aligned}
&z_- \leqslant z \leqslant \frac{1}{2}\,, && 0 \leqslant y \leqslant y_{\rm top}(\hat{m}, z)\,, && \rho = \hat{m}^2 + yz\,, \\
&\frac{1}{2} \leqslant z \leqslant z_+\,, && 0 \leqslant y \leqslant y_{\rm top}(\hat{m}, 1-z)\,, && \rho = \hat{m}^2 + y(1-z)\,, \\
&\hat{m} \leqslant z \leqslant 1-\hat{m}\,, && y_{\rm low}(\hat{m}, z) \leqslant y \leqslant y_{\rm max}(\hat{m}, z)\,, && \rho = 1-y\,,
\end{aligned} \tag{3.60}$$

where we have defined $y_{\rm low}(\hat{m}, z) = \max[y_\tau(\hat{m}, z), y_\tau(\hat{m}, 1-z)]$. Again, the three regions correspond to the thrust axis pointing into the anti-quark, quark and gluon 3-momentum directions, respectively. It is therefore trivial to see that in the massless limit heavy jet mass and 2-jettiness, with either two or three partons, are identical.

3.7.1 Thrust

Even though we have provided a very compact expression for the τ_J measurement in Eq. (3.59), for an analytic computation it is more practical to use the regions displayed in Eq. (3.60). The Dalitz region mirror symmetry simplifies the discussion, since it restricts the integration to $z < 1/2$ such that it is enough to consider the anti-quark and gluon regions only, for which the corresponding measurement delta functions read

$$\delta^{\tau_J}_{\bar{q}} = \frac{t(\tau_J)}{z\xi(\tau_J)}\delta\left[y - \frac{1-\xi(\tau_J)}{z}\right], \qquad \delta^{\tau_J}_{g} = \delta[y - t(\tau_J)]\,, \tag{3.61}$$

where we have defined $t(\tau_J) = 1 - \tau_J$ and $\xi(\hat{m}, \tau_J) = \sqrt{t(\tau_J)^2 + 4\hat{m}^2}$. Since the highest possible value of y in the Dalitz region is $y_{\rm max}(1/2) = \beta^2$ (in the gluon region), the contour line of constant τ_J lives only in the anti-quark region for $\tau_J < 4\hat{m}^2$, where it meets the phase space boundary at

$z_1(\hat{m},\tau_J) = [1+\tau_J - \xi(\hat{m},\tau_J)]/2$. From the limiting condition $z_1(\hat{m},\tau_J^{\min}) = z_-(\hat{m})$ one obtains the minimal value of 2-jettiness: $\tau_J^{\min}(\hat{m}) = 1-\sqrt{1-4\hat{m}^2}$. From the condition $z_1(\hat{m},\tau_J^{\rm mid}) = \hat{m}$ (that is, the contour line hits the point at which the phase-space boundary meets the line that separates the anti-quark and gluon regions) one can see that for $4\hat{m}^2 < \tau_J < \hat{m}/(1-\hat{m}) \equiv \tau_J^{\rm mid}(\hat{m})$ the contour line also has a patch in the gluon region, which cuts the phase space boundary at $z_2(\hat{m},\tau_J) = [1-\sqrt{1-4\hat{m}^2/\tau_J}]/2$ [one can imagine that the contour line "leaves" the Dalitz region (anti-quark patch) through z_1 and re-enters it in z_2 (gluon patch)]. One can easily check that $z_2(\hat{m},\tau_J^{\rm mid}) = \hat{m}$. Finally, if $\tau_J > \tau_J^{\rm mid}(\hat{m})$ the contour line becomes continuous (although not smooth), lives both in the anti-quark and gluon regions, never exits the Dalitz region but meets the thrust axis boundary at $z_3(\hat{m},\tau_J) = [1-\xi(\hat{m},\tau_J)]/t(\tau_J)$. From the limiting condition $z_3(\hat{m},\tau_J^{\max}) = 1/2$ one obtains the maximum value of 2-jettiness: $\tau_J^{\max}(\hat{m}) = (5-4\sqrt{1-3\hat{m}^2})/3$. One can easily see that for physical values of $\hat{m}$ the hierarchy $\tau_J^{\min}(\hat{m}) \leqslant 4\hat{m}^2 \leqslant \tau_J^{\rm mid}(\hat{m}) \leqslant \tau_J^{\max}(\hat{m})$ holds, as can be checked graphically in Fig. 3.13.

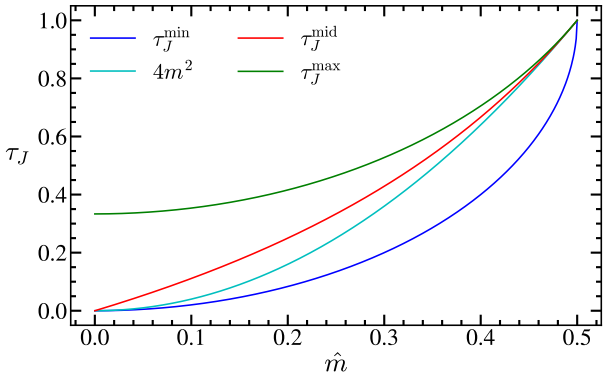

Figure 3.13: Values of 2-jettiness for which the contour lines of constant event shape reach a limiting value: either they take their maximum or minimal values or transition from hitting the phase space boundary to enter the Dalitz region.

Defining $z_{ij}(\hat{m},\tau_J) = \max[z_i(\hat{m},\tau_J), z_j(\hat{m},\tau_J)]$ we obtain

$$\frac{1}{\sigma_0}\frac{{\rm d}\sigma_{\rm ang}^C}{{\rm d}\tau_J} = \frac{3\alpha_s C_F}{4\pi} g_{\tau_J}^{{\rm ang},C}(\hat{m},\tau_J)\,, \tag{3.62}$$

$$\begin{aligned} g_{\tau_J}^{{\rm ang},C}(\hat{m},\tau) &= \frac{[1-\xi(\hat{m},\tau)]t(\tau)}{\xi(\hat{m},\tau)}\int_{z_{13}(\hat{m},\tau)}^{\frac{1}{2}} \frac{{\rm d}z}{z^2} A_{\bar{q}}^C\left[\hat{m},\frac{1-\xi(\hat{m},\tau)}{z},z\right] + t(\tau)\theta(\tau-4\hat{m}^2)\int_{z_{23}(\hat{m},\tau)}^{\frac{1}{2}} {\rm d}z A_g^C[\hat{m},t(\tau),z] \\ &= \frac{t(\tau)}{\xi(\hat{m},\tau)} g_{\bar{q}}^C[\hat{m},z_{13}(\hat{m},\tau),1-\xi(\hat{m},\tau)] + \theta(\tau-4\hat{m}^2) g_g^C[\hat{m},z_{23}(\hat{m},\tau),\tau]\,, \end{aligned}$$

where the functions $g^C_{g,\bar{q}}$ can be computed analytically:

$$
\begin{aligned}
g^V_{\bar{q}}(\hat{m},z,\xi) &= \frac{1}{2\xi[(1-\xi)^2-4\hat{m}^2]}\bigg[2\hat{m}^2\big[2+3(\xi-2)\xi+4\hat{m}^2(4\xi-3)+16\hat{m}^4\big]\log\left(\frac{1}{z}-1\right) \\
&\quad -\frac{1-2z}{(1-z)^2 z}\big\{\xi^2(1-z)[\xi-2(1-\xi)z]+\hat{m}^2\xi(1-z)[4(1-\xi)z+\xi] \\
&\quad +4\hat{m}^4 z(1-6\xi+4\xi z)-16\hat{m}^6 z\big\}\bigg], \\
g^A_{\bar{q}}(\hat{m},z,\xi) &= \frac{\xi}{2z_e^2(1-z)[(1-\xi)^2-4\hat{m}^2]}\bigg[-2\hat{m}^2 z^2(1-z)(2-4\hat{m}^2-\xi^2)\log\left(\frac{1}{z}-1\right) \\
&\quad -(1-2z)\{\xi(1-2\hat{m}^2)(1-z)(1+2z)-2z[1-z+2\hat{m}^2(\hat{m}^2+2z-2)]\} \\
&\quad -\hat{m}^2\xi^2(1-z)(1+4z)\bigg], \\
g^V_g(\hat{m},z,\tau_J) &= \frac{1}{1-\tau_J}\left[\tau_J(1-2z)-2\hat{m}^2\log\left(\frac{1}{z}-1\right)\right], \\
g^A_g(\hat{m},z,\tau_J) &= \frac{1}{1-\tau_J}\left\{(1-2z)\left[\tau_J+\frac{2\hat{m}^4}{(1-z)z}\right]+\hat{m}^2(\tau_J^2-4\tau_J-\beta^2)\log\left(\frac{1}{z}-1\right)\right\}.
\end{aligned}
\tag{3.63}
$$

A graphical representation of the 2-jettiness angular differential distribution at $\mathcal{O}(\alpha_s)$ is to be found in Fig. 3.14. For both currents, implementing the SCET counting $\tau \propto \mathcal{O}(\lambda^2)$ and $m \propto \mathcal{O}(\lambda)$ one finds:

$$
\begin{aligned}
g^V_{\tau_J}(\hat{m},\tau_J) &\simeq \frac{8\hat{m}^4-8\hat{m}^2\tau+\tau^2-4\hat{m}^2(\tau-\hat{m}^2)\log(\tau-\hat{m}^2)}{2(\tau-\hat{m}^2)(\tau-2\hat{m}^2)}+\mathcal{O}(\lambda)\,, \\
g^A_{\tau_J}(\hat{m},\tau_J) &\simeq \frac{\tau(\tau-2\hat{m}^2)}{2(\tau-\hat{m}^2)^2}+\mathcal{O}(\lambda)\,,
\end{aligned}
\tag{3.64}
$$

which is significantly different to the case of the unoriented cross section, for which both currents coincide at leading order in the SCET power counting.

One can also compute the oriented cumulative distribution, which is defined as

$$
\Sigma^{\text{ang},C}_e(\hat{m},e_c) = \frac{1}{\sigma_0^C}\int_{e_{\min}}^{e_c}\mathrm{d}e\frac{\mathrm{d}\sigma^C_{\text{ang}}}{\mathrm{d}e} \equiv R_0^{\text{ang},C}(\hat{m})\theta[e_c-e_{\min}(\hat{m})]+\sum_{n=1}\left[\frac{\alpha_s(\mu)}{\pi}\right]^n\Sigma^{\text{ang},C}_{e,n}(\hat{m},\mu,e_c)\,. \tag{3.65}
$$

Since $\Sigma^{\text{ang},C}_e$ obeys an homogeneous renormalization group equation, there is no μ dependence in $\Sigma^{\text{ang},C}_{e,1}$. At $\mathcal{O}(\alpha_s)$ one ends up in the following compact result:

$$
\begin{aligned}
\Sigma^{\text{ang},C}_{\tau_J,1}(\hat{m},\tau_c) &= R_1^{\text{ang},C}(\hat{m})-\frac{3C_F}{4}\int_{z_{13}(\hat{m},\tau_c)}^{\frac{1}{2}}\mathrm{d}z\left\{\tilde{A}^C_{\bar{q}}[\hat{m},y_{\text{top}}(\hat{m},z),z]-\tilde{A}^C_{\bar{q}}\left[\hat{m},\frac{1-\xi(\hat{m},\tau_c)}{z},z\right]\right\} \\
&\quad -\frac{3C_F}{4}\int_{\max[\hat{m},z^3(\hat{m},\tau_c)]}^{\frac{1}{2}}\mathrm{d}z\,\tilde{A}^C_g[\hat{m},\min[y_{\max}(\hat{m},z),1-\tau_c],y_\tau(\hat{m},z),z]\,,
\end{aligned}
\tag{3.66}
$$

where the analytic expressions for $\tilde{A}^C_{\bar{q},g}$ have been already given in Eqs. (3.39) and (3.45) for the axial-vector and vector currents, respectively. The z integrals are in practice computed numerically with high accuracy even for values very close to $\tau_J^{\min}(\hat{m})$. In Fig. 3.14 we show the NLO pieces for the 2-jettiness differential and cumulative cross sections for two values of $\hat{m}$. For $\hat{m}=0.32$ one can observe small kinks in $\tau=4\hat{m}^2$ and $\tau=\tau_J^{\text{mid}}$. Finally, we observe a negative cumulative cross section for the vector current and $\hat{m}=0.2$, indicating the necessity of Sudakov log resummation.

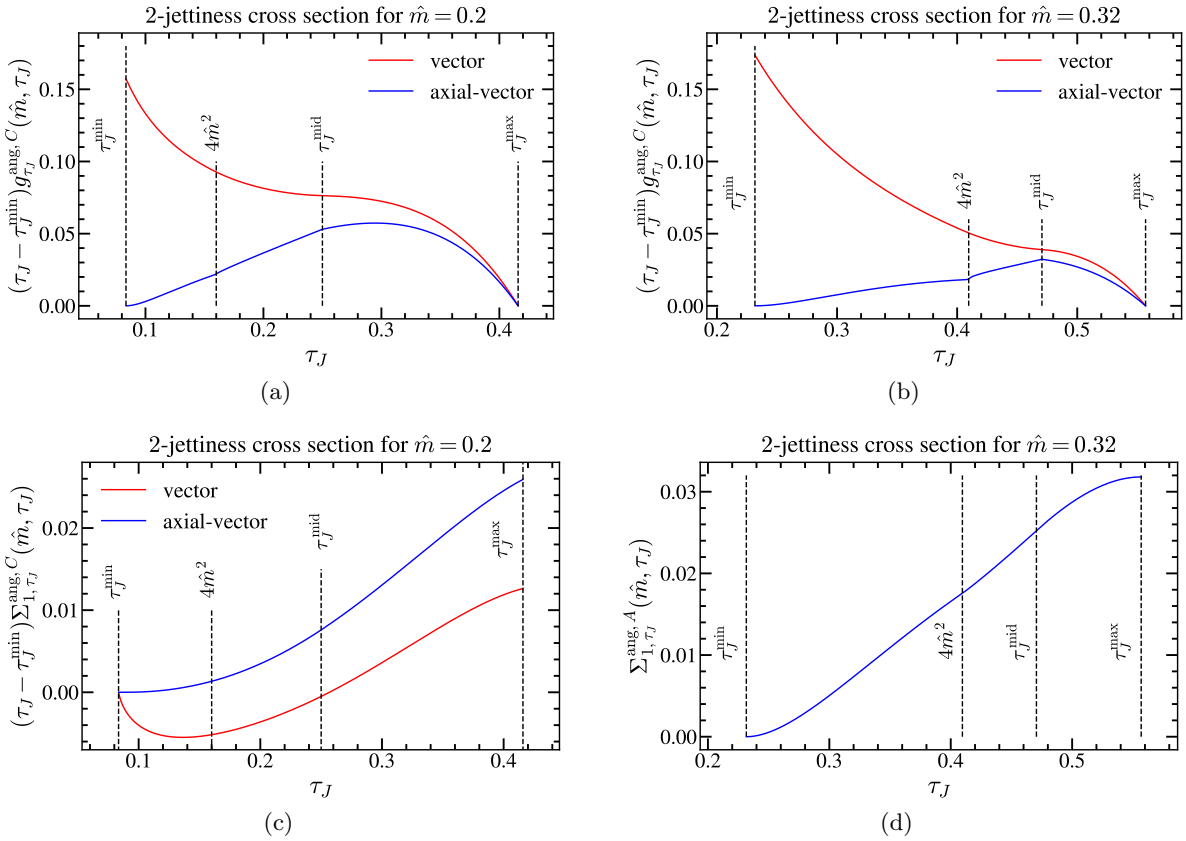

Figure 3.14: Differential (upper panels) and cumulative (lower panels) 2-jettiness distribution for $\hat{m} = 0.2$ (left panels) and $\hat{m} = 0.32$ (right panels) for the vector (red) and axial-vector (blue) currents. In panels (a) to (c) we multiply the cross section by $\tau_J - \tau_J^{\min}$ to achieve a finite result across the whole spectrum. In panel (d) we show only the axial-vector current and do not multiply by $\tau_J - \tau_J^{\min}$. Vertical dashed black lines signal the limiting values of τ shown in Fig. 3.13, where one can observe either cusps or discontinuities in the cross sections.

3.7.2 Heavy Jet Mass

The differential and cumulative cross sections for heavy jet mass can be expressed in terms of functions already computed. In fact, for the region in which the thrust axis is collinear to the gluon momentum, heavy jet mass and 2-jettiness are identical. For the region of $\hat{n}$ pointing into the same direction as $\vec{p}_{\bar{q}}$ the measurement delta function reads:

$$\delta^{\rho}_{\bar{q}} = \frac{1}{z}\delta\left(y - \frac{\rho - \hat{m}^2}{z}\right). \tag{3.67}$$

It is useful to define $r(\hat{m}, \rho) = 1 + \rho - \hat{m}^2$ and $\chi(\hat{m}, \rho) = \sqrt{r(\hat{m}, \rho)^2 - 4\rho}$. Since the patch of the contour line in the gluon region has been discussed at length in the previous subsection, we now focus on the $\bar{q}$ region exclusively. We anticipate that there is no value of ρ for which the full contour line becomes continuous. For $\hat{m}^2 < \rho < \hat{m}(1 - \hat{m} - \hat{m}^2)/(1 - \hat{m}) \equiv \rho_{\text{int}}(\hat{m})$ it hits the phase space boundary at $z_4(\hat{m}, \rho) = [r(\hat{m}, \rho) - \chi(\hat{m}, \rho)]/2$ in the $\bar{q}$ region. From the limiting condition $z_4(\hat{m}, \rho_{\min}) = z_-(\hat{m})$

we obtain the minimal value of heavy jet mass $\rho_{\min}(\hat{m}) = \hat{m}^2$. The value $\rho_{\rm int}(\hat{m})$ is obtained from the condition $z_4(\hat{m}, \rho_{\rm int}) = \hat{m}$. For $\rho_{\rm int}(\hat{m}) < \rho < \hat{m}^2 + 2\sqrt{1-3\hat{m}^2}/3 - 1/3 \equiv \rho_{\rm mid}(\hat{m})$ the contour line hits the boundary of the g and $\bar{q}$ regions at $z_5(\hat{m}, \rho) = [r(\hat{m}, \rho) - 1]/\sqrt{(1-\rho)^2 - 2\hat{m}^2(1+\rho) + \hat{m}^4} \neq z_3(\hat{m}, \rho)$. The expression for $\rho_{\rm mid}(\hat{m})$ is obtained from the condition $z_5(\hat{m}, \rho_{\rm mid}) = 1/2$. Finally, for $\rho_{\rm mid}(\hat{m}) < \rho < \tau_J^{\max}(\hat{m})$ the contour line exists only in the gluon region. Therefore the maximum value of heavy jet mass is $\rho_{\max}(\hat{m}) = \tau_J^{\max}(\hat{m})$. One can easily see that for $0 \leqslant \hat{m} \leqslant 1/2$ one has $\rho_{\min}(\hat{m}) \leqslant \rho_{\rm int}(\hat{m}) \leqslant \{\tau_J^{\rm mid}(\hat{m}), \rho_{\rm mid}(\hat{m})\} \leqslant \rho_{\max}(\hat{m})$ as can be checked graphically in Fig. 3.15.

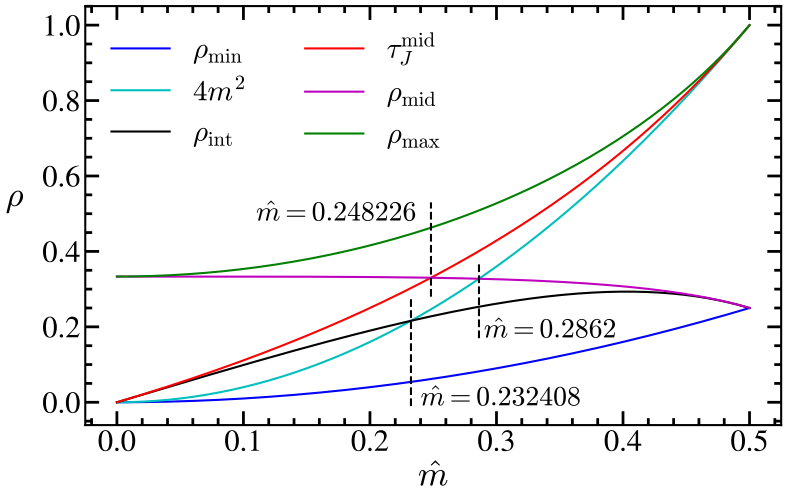

Figure 3.15: Values of heavy jet mass for which the contour lines of constant event shape reach a limiting value: either they take their maximum or minimal values or transition from hitting the phase space boundary to enter the Dalitz region.

For $\hat{m} \leqslant 0.248226$ one has $\rho_{\rm mid}(\hat{m}) \geqslant \tau_J^{\rm mid}(\hat{m})$, while $\hat{m} \leqslant (5-\sqrt{13})/6 \approx 0.232408$ implies $4\hat{m}^2 \leqslant \rho_{\rm int}(\hat{m})$, although these have no implications. On the other hand, if $\hat{m} \leqslant \sqrt{(2\sqrt{13}-5)/27} \approx 0.286169$ one has $4\hat{m}^2 \leqslant \rho_{\rm mid}(\hat{m})$, and this entails the cross section is zero for $\rho_{\rm mid}(\hat{m}) < \rho < 4\hat{m}^2$ as can be seen in Figs. 3.16(a) and 3.16(b).

A simple computation yields the following result for the differential cross section

$$\frac{1}{\sigma_0}\frac{\mathrm{d}\sigma_{\rm ang}^C}{\mathrm{d}\rho} = \frac{3\alpha_s C_F}{4\pi} g_{\tau_J}^{{\rm ang},C}(\hat{m}, \rho)\,, \tag{3.68}$$

$$\begin{aligned} g_\rho^{{\rm ang},C}(\hat{m}, \rho) &= \theta[\rho_{\rm mid}(\hat{m}) - \rho] \int_{z_{45}(\hat{m},\rho)}^{\frac{1}{2}} \frac{\mathrm{d}z}{z^2} A_{\bar{q}}^C\left[\hat{m}, \frac{\rho - \hat{m}^2}{z}, z\right] + t(\rho)\theta(\rho - 4\hat{m}^2) \int_{z_{23}(\hat{m},\rho)}^{\frac{1}{2}} \mathrm{d}z A_g^C[\hat{m}, t(\rho), z] \\ &= \theta[\rho_{\rm mid}(\hat{m}) - \rho] g_{\bar{q}}^C[\hat{m}, z_{45}(\hat{m}, \rho), \rho - \hat{m}^2] + \theta(\rho - 4\hat{m}^2) g_g^C[\hat{m}, z_{23}(\hat{m}, \rho), \rho]\,, \end{aligned}$$

where the analytic form of $g_{g,\bar{q}}^C$ for both currents has been given already in Eq. (3.63). Implementing the SCET counting $\rho \propto \mathcal{O}(\lambda^2)$ and $m \propto \mathcal{O}(\lambda)$ one finds:

$$\begin{aligned} f_\rho^V(\hat{m}, \rho) &= \frac{\hat{m}^4 - 6\hat{m}^2\rho - 4\hat{m}^2\rho\log(\rho) + \rho^2}{2\rho(\rho - \hat{m}^2)} + \mathcal{O}(\lambda)\,, \\ f_\rho^A(\hat{m}, \rho) &= \frac{\rho^2 - \hat{m}^4}{2\rho^2} + \mathcal{O}(\lambda)\,, \end{aligned} \tag{3.69}$$

where again we find different limits for vector and axial-vector currents. Finally, for $\hat{m} = 0$ the limits of both currents coincide.

For the cumulative distribution we have

$$\Sigma_{\rho,1}^{\text{ang},C}(\hat{m},\rho_c) = R_1^{\text{ang},C}(\hat{m}) - \frac{3C_F}{4}\left\{\int_{\max[\hat{m},z_3(\hat{m},\rho_c)]}^{\frac{1}{2}} \mathrm{d}z \tilde{A}_g^C[\hat{m},\min[y_{\max}(\hat{m},z),1-\rho_c],y_\tau(\hat{m},z)]\right. \quad (3.70)$$
$$\left. - \theta[\rho_{\text{mid}}(\hat{m})-\rho_c]\int_{z_{45}(\hat{m},\rho_c)}^{\frac{1}{2}} \mathrm{d}z\left[\tilde{A}_{\bar{q}}^C[\hat{m},y_{\text{top}}(\hat{m},z),z] - \tilde{A}_{\bar{q}}^C\left(\hat{m},\frac{\rho_c-\hat{m}^2}{z},z\right)\right]\right\},$$

where again all pieces are known and we compute the z integration numerically. In Figs. 3.16(c) and 3.16(d) we show $\Sigma_{\rho,1}^{\text{ang},C}$ for two values of $\hat{m}$. In general we find that cusps for cumulative cross sections are less pronounced than for their differential counterparts. In particular, for $\hat{m} = 0.32$ one can see that for $\rho_{\text{mid}} < \rho < 4\hat{m}^2$ the cumulative cross section is constant, since the differential cross section is zero in that patch.

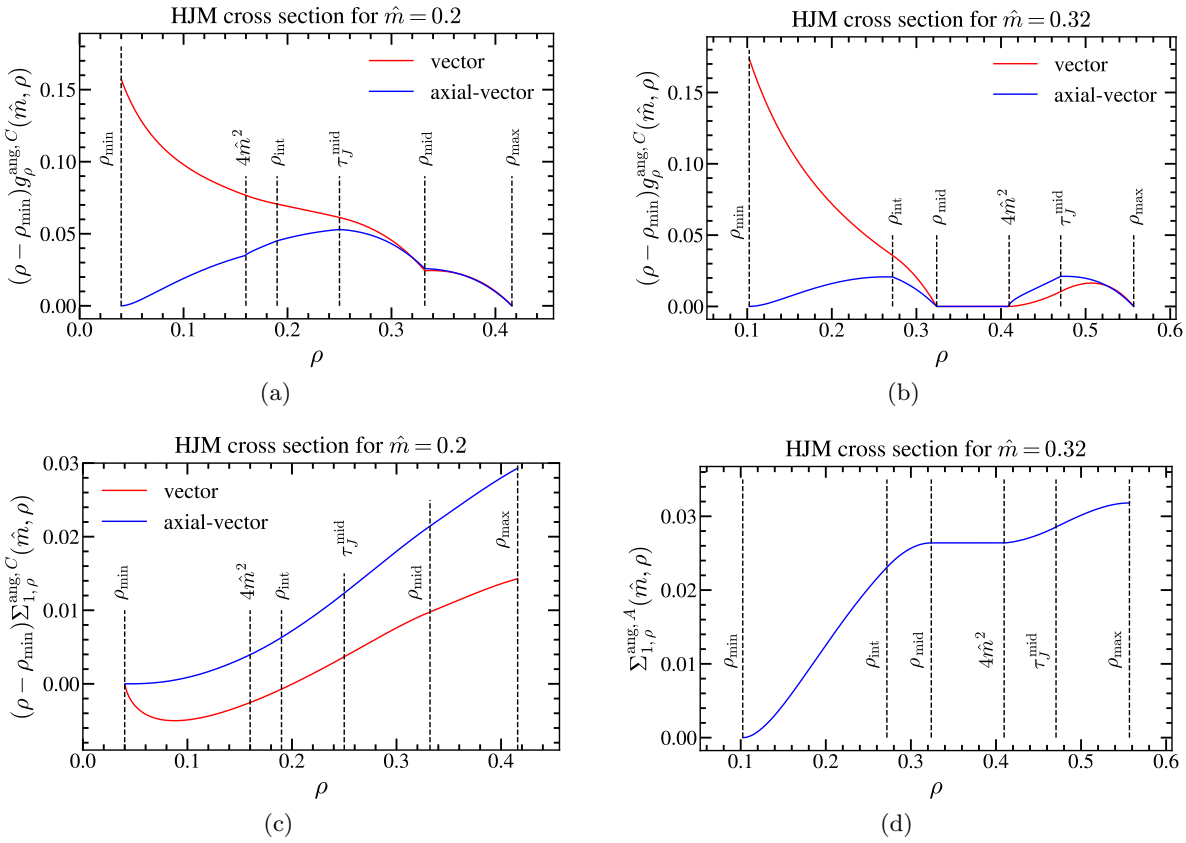

Figure 3.16: Same as Fig. 3.14 for heavy jet mass. Panel (d) shows only the results for the axial-vector current to highlight the region of constant cumulative cross section.

3.7.3 Cross-checks

One can perform a number of tests on the numerical and analytic computations carried out in this section. First, we have checked that both for 2-jettiness and heavy jet mass, taking a numerical derivative of the cumulative distribution accurately reproduces the differential one, including the kinks.

Second, the differential cross section for the vector current must verify the following condition (the equivalent statement for the axial-vector current is that the limit is simply zero)

$$\lim_{e\to e_{\min}(\hat{m})}[e-e_{\min}(\hat{m})]g_e^{\text{ang},V}(\hat{m},e)=\frac{4}{3}B_{\text{plus}}^{\text{ang}}(\hat{m})\,. \tag{3.71}$$

A graphical verification of this requirement can be found in Fig. 3.17(a) for the vector current.

Third, integrating the differential cross section must yield the total cross section. For the vector current this implies a constraint between the radiative tail of the differential cross section and the coefficients of the singular distributions, while for the axial-vector current it is simply an integral condition:

$$\begin{aligned}
R_1^{\text{ang},V}(\hat{m}) &= C_F\left\{\int_{e_{\min}}^{e_{\max}}\mathrm{d}e\left[\frac{3}{4}g_e^{\text{ang},V}(\hat{m},e)-\frac{B_{\text{plus}}^{\text{ang}}(\hat{m})}{e-e_{\min}}\right]+B_{\text{plus}}^{\text{ang}}(\hat{m})\log(e_{\max}-e_{\min})+A_e^{\text{ang}}(\hat{m})\right\},\\
R_1^{\text{ang},A}(\hat{m}) &= \frac{3C_F}{4}\int_{e_{\min}}^{e_{\max}}\mathrm{d}e\,g_e^{\text{ang},A}(\hat{m},e)\,.
\end{aligned} \tag{3.72}$$

An equivalent test on the cumulative cross section can be derived. To that end we note that $\Sigma_{e,1}^{\text{ang},V}$ can also be decomposed into singular and non-singular terms:

$$\Sigma_{e,1}^{\text{ang},V}(\hat{m},e)=C_F A_e^{\text{ang}}(\hat{m})\theta(e-e_{\min})+C_F B_{\text{plus}}^{\text{ang}}(\hat{m})\log(e-e_{\min})+\Sigma_{e,\text{NS},1}^{\text{ang},V}(\hat{m},e)\,, \tag{3.73}$$

while for the axial-vector current one has only the non-singular term. For the cumulative non-singular cross section (which is nothing more than the cumulative of the non-singular differential cross section) implies $\Sigma_{e,\text{NS},1}^{\text{ang},C}(\hat{m},e_{\min})=0$ (again, this is trivial to see because the non-singular differential distribution is by definition integrable and therefore vanishes if the lower and upper integration limits coincide). This can be translated into the following constraints:

$$\begin{aligned}
C_F A_e^{\text{ang}}(\hat{m}) &= \lim_{e\to e_{\min}}\left[\Sigma_{e,1}^{\text{ang},V}(\hat{m},e)-C_F B_{\text{plus}}^{\text{ang}}(\hat{m})\log(e-e_{\min})\right],\\
0 &= \lim_{e\to e_{\min}}\Sigma_{e,1}^{\text{ang},A}(\hat{m},e)\,.
\end{aligned} \tag{3.74}$$

These conditions have been checked graphically, as can be seen for the axial-vector current in Fig. 3.17(b) (both for 2-jettiness and heavy jet mass), and for the vector current in Figs. 3.17(c) and 3.17(d) for 2-jettiness and heavy jet mass, respectively.

3.8 Results for other event shapes

For cases other than 2-jettiness and heavy jet mass, in which analytical expressions were obtained for their differential distributions, we have adapted the formalism described in Ref. [48] to project out the event-shape distribution from the double differential cross-section in the variables y and z by replacing the unoriented result with the one for the angular part in Eq. (3.36).

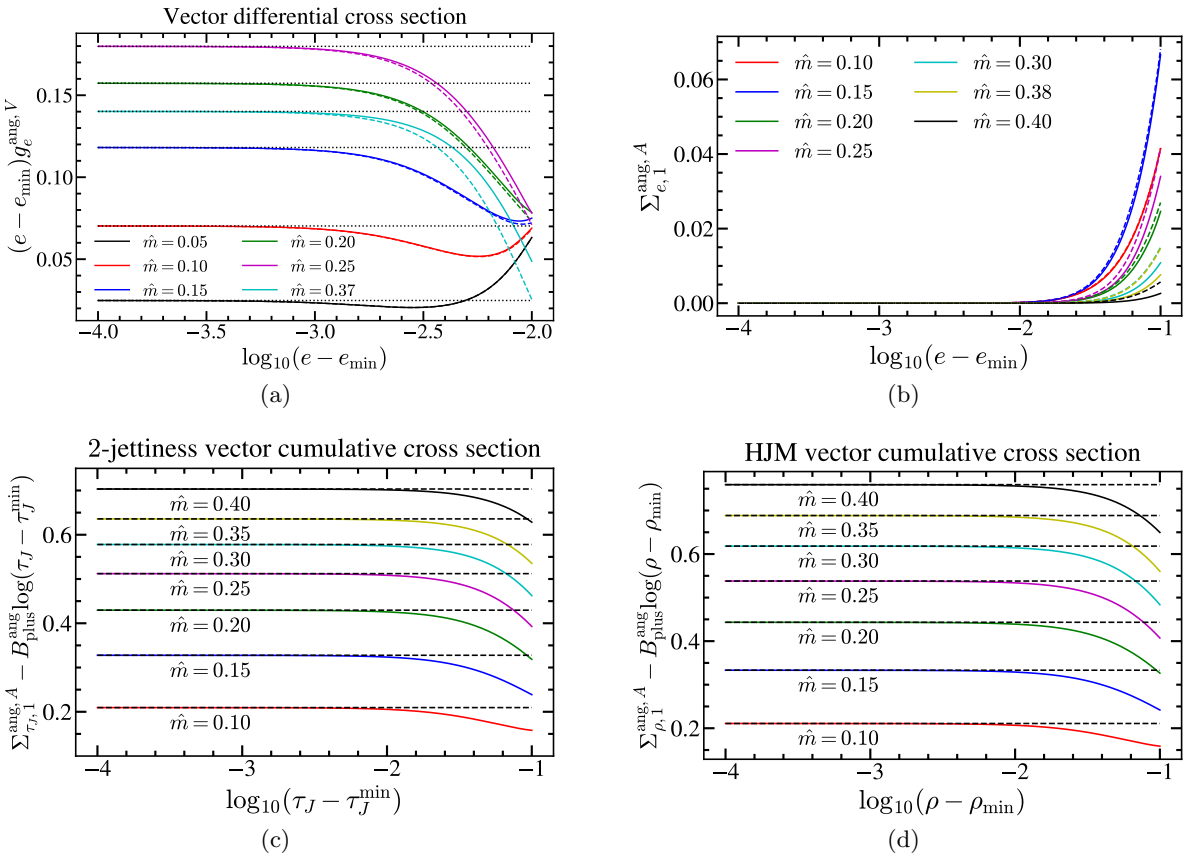

Figure 3.17: Panel (a): Limit of the differential cross section as taken in Eq. (3.71) for the vector current, for 2-jettiness (solid lines) and heavy jet mass (dashed lines), for various values of the reduced mass $\hat{m}$. The dotted lines indicate the analytic value of $(4/3)B_{\text{plus}}^{\text{ang}}$. Panel (b): Limit of the axial-vector cumulative distribution as taken in the second line of Eq. (3.74) for 2-jettiness (solid lines) and heavy jet mass (dashed lines), for a number of reduced masses $\hat{m}$. Lower panels: Limit of the vector current cumulative cross section as taken in the first line of Eq. (3.74) for 2-jettines [panel(c)] and heavy jet mass [panel (d)] for various values of $\hat{m}$. Dashed horizontal lines indicate the analytic values of $C_F A_e(\hat{m})$.

The algorithm computes the radiative tail of the distribution, that is, the contribution for $e > e_{\min}$, which consists in the plus and non-singular terms:

$$f_{e,1}[\hat{m}, e > e_{\min}(\hat{m})] = \frac{C_F B_{\text{plus}}^{\text{ang}}(\hat{m})}{e - e_{\min}(\hat{m})} + C_F F_e(e, \hat{m})\,, \tag{3.75}$$

through a one-dimensional numerical integral in the z variable. Since the coefficients of the plus and delta can be obtained analytically we know the contributions from each different term [see Eq. (3.57)].

The measurement delta is solved for the variable y as a function of z and the event shape value e and the Brent algorithm [7] is used to determine the boundaries of the integration depending on the form of the contour lines with constant event-shape value. For continuous convex curves with no intersections

with the phase space boundaries, the radiative tail can be written as:

$$\frac{\alpha_s}{\pi} f_{e,1}[\hat{m}, e > e_{\min}(\hat{m})] = \int \mathrm{d}z\mathrm{d}y \frac{1}{\sigma_0} \frac{\mathrm{d}^2\sigma^{\alpha_s}}{\mathrm{d}z\mathrm{d}y} \delta[e - \hat{e}(\hat{m}, y, z)] \Big|_{e>e_{\min}(\hat{m})} \tag{3.76}$$
$$= 2 \int_{z_{\min}(e)}^{1/2} \mathrm{d}z \sum_{y=y_\pm(e,z)} \frac{1}{\left|\frac{\mathrm{d}\hat{e}(\hat{m},y,z)}{\mathrm{d}y}\right|} \frac{1}{\sigma_0} \frac{\mathrm{d}^2\sigma^{\alpha_s}}{\mathrm{d}z\mathrm{d}y} ,$$

where $y_\pm(e,z)$ are the two zeros of the Dirac delta argument, $z_{\min}(e)$ is the minimum value of the variable z for the line with constant event-shape value e and the upper limit of the integral is $1/2$ since the phase space symmetry was taken into account with the factor 2.

For discontinuous contour lines, the intersection with the curves delimiting the thrust axis (see Fig. 3.3) is needed and computed also through the Brent algorithm, and a different event-shape function $\hat{e}(\hat{m}, y, z)$ is defined for each of the three regions.

Finally, for the cases having intersections with the phase space boundaries, which are the mass sensitive ones such as M-scheme thrust, C-parameter and heavy jet mass, an individual analysis of the contour lines is carried out to get the integral limits similar to the one in the analytic computation of the previous section.

The output for the angular distributions of several event shapes[10] in the P- and E-schemes is represented in Fig. 3.18 considering the vector current and different values of the reduced mass $\hat{m}$. We multiply the results by the event shape value e in order to have a finite result at $e = 0$. Recall that both schemes have a small sensitivity to the quark mass since $e_{\min}^{E,P} = 0$. The E-scheme heavy-jet-mass distribution for large values of the reduced mass presents kinks and discontinuities, while the rest of schemes, masses and event shapes are quite smooth.

As a comparison, the angular differential cross sections for thrust and heavy jet mass in their original (mass-sensitive) schemes are provided in the same way as for P- and E-schemes in Fig. 3.19.

Furthermore, we also checked that the results given through this procedure agree with those analytical in the previous section.

3.9 Summary

This Chapter was dedicated to the computation of event-shape distributions for massive primary quarks at NLO when considering the angle between the beam and the thrust axis θ_T . As was already demonstrated in Ref. [51], only two structures involving θ_T contribute, the one multiplied by the known unoriented cross section and the angular part. Here we presented the direct computation of the later

[10] The corresponding definitions are in Tab. 2.1 except for jet broadening, which reads:

$$B_P = \frac{1}{2Q_P} \sum_i \left(|\vec{p}_i| - |\hat{t}\cdot\vec{p}_i|\right)^{1/2} \left(|\vec{p}_i| + |\hat{t}\cdot\vec{p}_i|\right)^{1/2} , \tag{3.77}$$
$$B_E = \frac{1}{2Q} \sum_i \frac{p_i^0}{|\vec{p}_i|} \left(|\vec{p}_i| - |\hat{t}\cdot\vec{p}_i|\right)^{1/2} \left(|\vec{p}_i| + |\hat{t}\cdot\vec{p}_i|\right)^{1/2} ,$$
$$B_Q = \frac{1}{2Q} \sum_i \left(p_i^0 - |\hat{t}\cdot\vec{p}_i|\right)^{1/2} \left(p_i^0 + |\hat{t}\cdot\vec{p}_i|\right)^{1/2} .$$

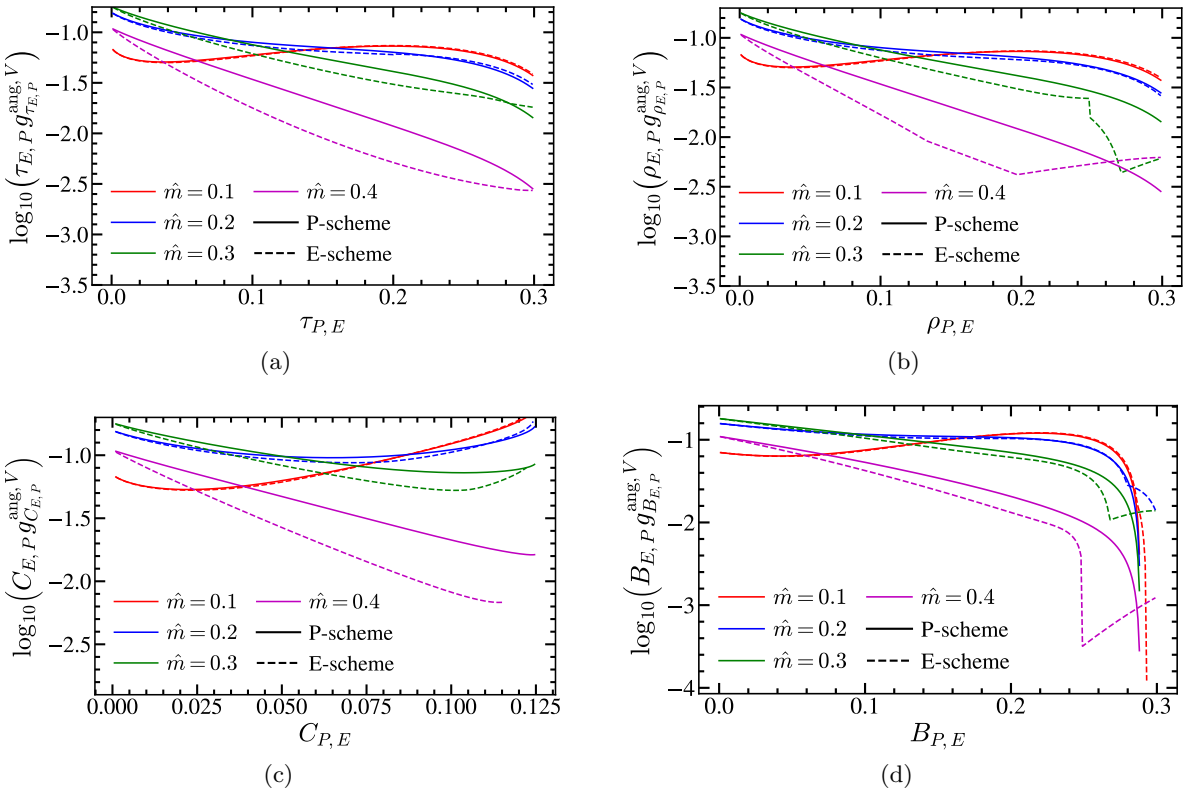

Figure 3.18: Differential cross sections for the vector current in the P- (solid lines) and E-scheme (dashed lines) for $\hat{m} = 0.1, 0.2, 0.3$ and 0.4 in red, blue, green and magenta, respectively. Panels (a), (b), (c) and (d) correspond to thrust, heavy-jet-mass, C-parameter and jet broadening, respectively.

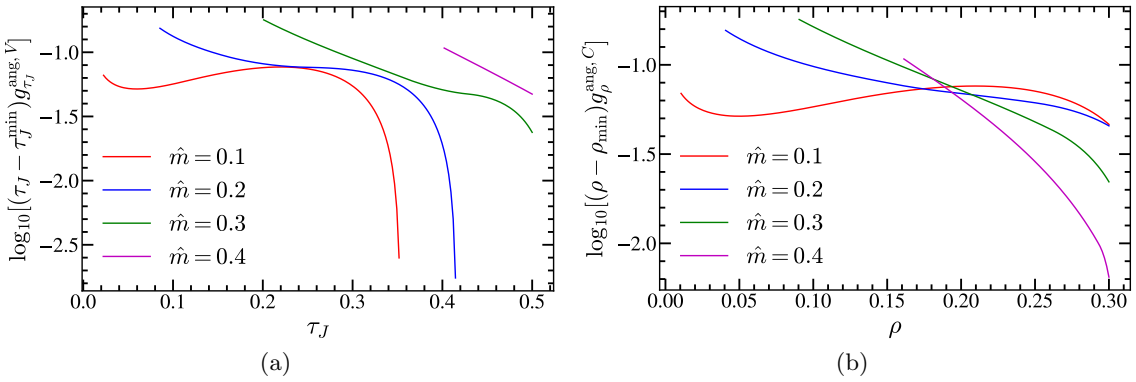

Figure 3.19: Same as Fig. 3.18 in the original massive scheme for 2-jettiness and heavy jet mass.

by introducing the corresponding projector.

The vector-current contribution begins at tree level, leading also to a non-vanishing virtual part at

one loop, which is IR divergent. These infinite terms cancel out when the real emission is added to the virtual one, but it forces us to keep $d = 4 - 2\varepsilon$ in the phase space integrals in order to regulate them.

Therefore, we first worked out the d-dimensional phase space integrals for two and three particles in the final state and next we carried out the calculation of the virtual and real matrix elements. Putting both pieces together, a result for the total angular cross section has been obtained, and the corrections due to the primary bottom mass have been analyzed. The small hadronization effects afflicting this observable and its high sensitivity to the strong coupling (it is proportional to α_s for massless quarks) makes it a suitable candidate for accurate determinations of this parameter. It also turned out to be a plausible choice to measure the value of the top quark mass through threshold scans, due to the enhancement our result shows in the limit of top quarks produced with small velocity.

Since the axial-vector part is purely non-singular, once the soft singularities of the vector-current contribution have been isolated, we were able to obtain a closed expression for the plus coefficient, which is universal, and for the factor multiplying the Dirac delta (as an integral depending on the event-shape) in the oriented event-shape differential cross-sections.

Finally, we studied the cross sections for two of the most recurrent observables in the literature: thrust and heavy jet mass, finding analytical results for the differential distributions while, for other event shapes, we modified the algorithm described in Ref. [48] in order to numerical obtain the oriented cross sections.

Chapter 4

Massive secondary quark corrections to bHQET cross-section (Secondary massive quark corrections to boosted-top cross sections)

As we saw in Chapter 2, the minimal value of an event shape in the M-scheme depends on the mass of the primary quark, see Tab. 2.2 for several examples. Since the peak position of the distribution is in the vicinity of this lower limit, it is very sensitive to the primary quark mass (denoted as M in this Chapter) and can be used for determining this parameter through comparisons with experimental data or to calibrate parton shower Monte Carlo generators.[1] Nevertheless, energy fluctuations around the minimal value in the peak region are in general very small. For instance, in the case of hemisphere jet masses one has:

$$\frac{s - s_{\min}}{M} = \frac{s - M^2}{M} \ll M \,, \tag{4.1}$$

and therefore, accounting for (perturbative) low-energy effects is of utmost importance to get a precise position for the peak.

We also argued in previous Chapters of this thesis that this regime is conveniently described within bHQET, and the corresponding 2-jettines distribution has been implemented and analyzed at $\mathrm{N^3LL} + \mathcal{O}(\alpha_s^2)$ precision in Ref. [3]. In this Chapter we aim to include the corrections due to a non-vanishing secondary (lighter) quark mass (the bottom quark), which remain the last missing piece at this order.

Regarding the matrix elements of the factorization theorem [see Eq. (2.38)], the mass of the massive lighter quark will be always smaller than the primary quark mass, therefore it will be an infrared scale of SCET, having no effect on the QCD to SCET matching coefficient (that is, on the SCET hard function).[2] We will discuss about the different possibilities for the secondary mass scaling below in

[1] Trying to measure the top quark mass by a determination of the endpoint is pointless since the top is unstable and the minimal value of any dijet event shape is effectively zero, no matter what the value of m_t is.

[2] For massless primary quarks, one can choose not take the (secondary) massless limit ($m/Q \equiv \hat{m} \to 0$) to compute the (strict) QCD-SCET matching coefficient, that is, keeping the effects of the secondary mass corrections. This implies accounting for all power-suppressed terms of the form $\hat{m}^n$ in the matching condition. Keeping such subleading terms makes the transition between scenarios smooth. This does not work when there are massive primary quarks involved. A

Sec. 4.5. Finally, the soft function is the same as in SCET and the corresponding contribution was already computed in Ref. [30].

All in all, we just need to consider the corrections to the bHQET hard and jet functions which, due to the fact that the latter can be cast as the imaginary part of a forward scattering matrix element (as we will see in Sec. 4.3), come solely from a virtual massive quark bubble in the gluon propagators, leading to the possibility of using the dispersive integral method.

4.1 Dispersive integral method

Computations beyond the 1-loop level are in general hard, but if they include more than one scale, the difficulty is severely increased. The special class of bubble diagrams for massless quarks can be computed to all orders at once using a modified propagator. If the quarks running in the bubble are massive there is also a standard trick to simplify the 2-loop computation. The idea is to write the insertion of the massive quark bubble in the gluon self-energy as an integral over the mass of an effective massive gluon propagator. In this way, to get the 2-loop result we only need to perform the calculation at one loop with the massive gluon on top of which we carry out the dispersive integration. For a graphical representation see Fig. 4.1.

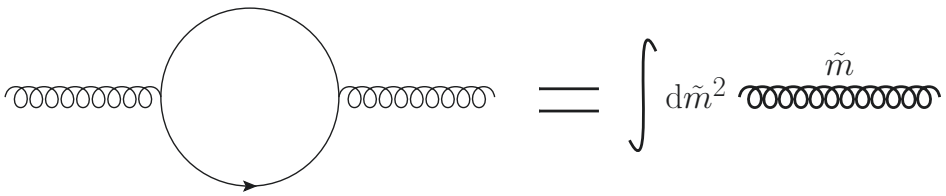

Figure 4.1: Dispersive integral method. The bold gluon propagator in the Feynman diagrams of this Chapter will represent the massive gluon (we will omit the label of the effective mass $\tilde{m}$).

Let us start by writing the massive bubble insertion to the gluon propagator (left hand side of Fig. 4.1) in a closed form. Applying Feynman rules and after some algebraic manipulations we obtain:

$$\frac{-i}{p^2}g^{\mu\alpha}\underbrace{i\Pi(p^2,m^2)(p^2 g_{\alpha\beta}-p_\alpha p_\beta)}_{\text{Massive Bubble}}\frac{-i}{p^2}g^{\beta\nu}=-\frac{i}{p^2}\left(g^{\mu\nu}-\frac{p^\mu p^\nu}{p^2}\right)\Pi(p^2,m^2)\,, \tag{4.2}$$

with:

$$\begin{aligned}\Pi(p^2,m^2)=\frac{4in_f T_F g^2}{3-2\varepsilon}\Bigg[&\left(1-\varepsilon+\frac{2m^2}{p^2}\right)\int\frac{\mathrm{d}^d\ell}{(2\pi)^d}\frac{1}{(\ell^2-m^2)[(\ell+p)^2-m^2]}\\&-\frac{2(1-\varepsilon)}{p^2}\int\frac{\mathrm{d}^d\ell}{(2\pi)^d}\frac{1}{\ell^2-m^2}\Bigg]\,,\end{aligned} \tag{4.3}$$

and solving the 1-loop scalar master integrals leads to:

$$\Pi(p^2,m^2)=-\frac{4n_f T_F g^2}{3-2\varepsilon}\frac{\Gamma(\varepsilon)}{(4\pi)^2}\left(\frac{4\pi\tilde{\mu}^2}{m^2}\right)^{\varepsilon}\left[\left(1-\varepsilon+\frac{2m^2}{p^2}\right){}_2F_1\left(1,\varepsilon;\frac{3}{2};\frac{p^2}{4m^2}\right)-\frac{2m^2}{p^2}\right]. \tag{4.4}$$

similar procedure can be carried out for the matching between SCET and bHQET.

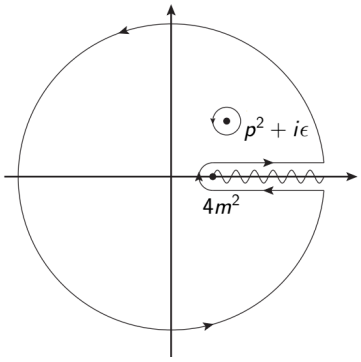

Figure 4.2: Contours in the complex λ plane that give rise to the dispersive representation.

In order to have an on-shell renormalized result we need to consider the subtraction of the zero-momentum vacuum polarization function, that is:

$$\begin{aligned}
\Pi(p^2,m^2) &\overset{\text{on-shell}}{\longrightarrow} \Pi(p^2,m^2) - \Pi(0,m^2) \equiv \Pi^{\rm OS}(p^2,m,\mu)\,, \\
\Pi(0,m^2) \equiv \Pi_0(m^2) &= -\frac{n_f T_F g^2 \Gamma(\varepsilon)}{12\pi^2}\left(\frac{4\pi\tilde{\mu}^2}{m^2}\right)^{\varepsilon}\,, \\
\Pi_0^{\overline{\rm MS}}(m^2) &\equiv -\frac{n_f T_F g^2}{12\pi^2}\left[\Gamma(\varepsilon)\left(\frac{4\pi\tilde{\mu}^2}{m^2}\right)^{\varepsilon} - \frac{1}{\varepsilon}\right]\,.
\end{aligned} \tag{4.5}$$

The original derivation of the dispersive integral expression was based on the unitarity and analyticity properties of the bubble, accounting for the fact that it develops an imaginary part for $p^2 > 4m^2$. The derivation starts choosing as contour a small circle around the point p^2 in the λ complex plane, such that through Cauchy's residue theorem one gets:

$$\Pi(p^2,m^2) = \frac{1}{2\pi i}\oint \mathrm{d}\lambda\,\frac{\Pi(\lambda,m^2)}{\lambda - p^2} \longrightarrow \Pi_0(m^2) = \frac{1}{2\pi i}\oint \mathrm{d}\lambda\,\frac{\Pi(\lambda,m^2)}{\lambda}\,. \tag{4.6}$$

The circle can be deformed to the contour drawn in Fig. 4.2 and provided the function vanishes at infinity, the on-shell renormalized bubble takes the following form:

$$\frac{\Pi^{\rm OS}(p^2,m,\mu)}{p^2} = \frac{1}{2\pi i}\oint \mathrm{d}\lambda \frac{\Pi(\lambda,m^2)}{\lambda(\lambda-p^2)} = \frac{1}{\pi}\int_{4m^2}^{\infty}\mathrm{d}\lambda \frac{\mathrm{Im}[\Pi(\lambda+i\epsilon,m^2)]}{\lambda(\lambda-p^2)}\,. \tag{4.7}$$

Finally, plugging in the imaginary part of the massive vacuum polarization function in d dimensions (that can be computed e.g. using Cutkosky rules or using properties of the hypergeometric function) gives the dispersive representation:

$$\begin{aligned}
\frac{\Pi^{\rm OS}(p^2,m,\mu)}{p^2} &= \frac{n_f T_F g^2}{2\pi^2}\frac{\Gamma(2-\varepsilon)}{\Gamma(4-2\varepsilon)}\int_{4m^2}^{\infty}\frac{\mathrm{d}\lambda}{\lambda}\left(1-\varepsilon+\frac{2m^2}{\lambda}\right)\left(\frac{4\pi\tilde{\mu}^2}{\lambda}\right)^{\varepsilon}\frac{\left(1-\frac{4m^2}{\lambda}\right)^{\frac{1}{2}-\varepsilon}}{p^2-\lambda+i\epsilon} \\
&\equiv T_F\frac{\alpha_s}{4\pi}\int_{4m^2}^{\infty}\mathrm{d}\tilde{m}^2\frac{\mathcal{V}^{(d=4-2\varepsilon)}(\tilde{m},\tilde{\mu})}{p^2-\tilde{m}^2+i\epsilon}\,,
\end{aligned} \tag{4.8}$$

where we represent the gluon mass by $\tilde{m}$, here and in the remaining computations of this Chapter.

There is however no need to follow the path explained above to achieve the previous result. Here we present an alternative derivation that will be the starting point of the method developed in the next Chapter. Starting from the integral form of the hypergeometric function in Eq. (4.4)

$$\frac{2m^2}{p^2}\,{}_2F_1\left(1,\varepsilon;\frac{3}{2};\frac{p^2}{4m^2}\right)=-\frac{m^2}{\Gamma(\varepsilon)}\frac{4^{1-\varepsilon}\Gamma(1-\varepsilon)}{\Gamma(2-2\varepsilon)}\int_0^1 \mathrm{d}x\,\frac{2m^2}{p^2}\frac{x^{-2+\varepsilon}(1-x)^{\frac{1}{2}-\varepsilon}}{p^2-\frac{4m^2}{x}}\,, \tag{4.9}$$

one can apply partial fractioning in the following way:

$$\frac{2m^2}{p^2}\frac{1}{p^2-\frac{4m^2}{x}}=\frac{x}{2}\left(\frac{1}{p^2-\frac{4m^2}{x}}-\frac{1}{p^2}\right)\,, \tag{4.10}$$

to recover Eq. (4.8) from the relation

$$\frac{\Pi^{\mathrm{OS}}(p^2,m,\mu)}{p^2}=\frac{n_f T_F g^2}{2\pi^2}\left(\frac{\pi\tilde{\mu}^2}{m^2}\right)^{\varepsilon}\frac{\Gamma(2-\varepsilon)}{\Gamma(4-2\varepsilon)}\int_0^1 \mathrm{d}x\left(1-\varepsilon+\frac{x}{2}\right)\frac{x^{-1+\varepsilon}(1-x)^{\frac{1}{2}-\varepsilon}}{p^2-\frac{4m^2}{x}}\,, \tag{4.11}$$

after performing the change of variables $x\to\lambda=4m^2/x$.

4.2 HQET Lagrangian with massive gluons

Before getting into the main calculation, let us discuss a modification in the HQET Lagrangian one needs to introduce compared to Eq. (1.63) when an additional infrared scale such as the gluon mass is present in the theory. It has been discussed that in HQET the pole mass of the heavy quark is integrated out and its off-shellness is proportional to $v\cdot k$ with v the heavy quark velocity parameter and k the residual momentum describing the fluctuations around the mass. On the other hand, if we denote the one-particle-irreducible diagrams by $i\Sigma(v\cdot k,\Lambda,\mu)$, where Λ represents a generic IR scale, and carry out the infinite sum for the contribution to the dressed propagator, using the geometric series one finds:

$$\mathrm{Prop}_\Sigma=\frac{i}{v\cdot k+\Sigma(v\cdot k,\Lambda,\mu)}\,. \tag{4.12}$$

By dimensional analysis we can infer from the previous expression that if $\Lambda=0$ the propagator has a pole when the primary quark is on-shell. However, in general $\Sigma(0,\Lambda,\mu)$ may be different from zero, such that we need to include a counterterm in the HQET self energy such that the 2-point Green functions in full QCD and the EFT agree with one another. This is achieved adding a quark bilinear term in the Lagrangian — which is allowed by symmetry — that cancels the $\Sigma(0,\Lambda,\mu)$ contribution and which will be dubbed ΔM, leading to the following primary quark part of the HQET Lagrangian:

$$\begin{aligned}\mathcal{L}^{\Lambda}_{\mathrm{HQET}}&=\overline{h}_v\,iv\cdot D\,h_v+\overline{h}_v\,\Delta M\,h_v\,,\\ \Delta M&\equiv-\Sigma(0,\Lambda,\mu)\,.\end{aligned} \tag{4.13}$$

Next, we focus on the 1-loop determination of this shift when having massive gluons. The Feynman diagram we need to consider is shown in Fig. 4.3 and this self-energy term reads

$$i\Sigma^{\tilde{m}}_{\mathrm{HQET}}=-4\pi\alpha_s C_F\tilde{\mu}^{2\varepsilon}\int\frac{\mathrm{d}^dl}{(2\pi)^d}\frac{1}{[l^2-\tilde{m}^2+i0]\,[v\cdot(k-l)+i0]}\equiv-4\pi\alpha_s C_F\tilde{\mu}^{2\varepsilon}I^{\Sigma^{\tilde{m}}_{\mathrm{HQET}}}\,. \tag{4.14}$$

To solve the integral we use Georgi parameters and after the loop integration one finds

$$I^{\Sigma^{\tilde{m}}_{\mathrm{HQET}}}=\frac{2i\Gamma(\varepsilon)}{(4\pi)^{2-\varepsilon}}\int_0^\infty \mathrm{d}\lambda\,[\lambda^2-2v\cdot k\lambda+\tilde{m}^2]^{-\varepsilon}\,. \tag{4.15}$$

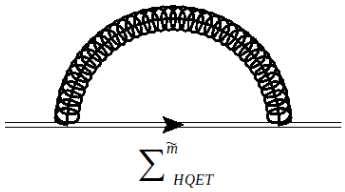

Figure 4.3: One loop massive gluon contribution to HQET quark self-energy.

We assume $v \cdot k < 0$ in order to simplify the computation. The general case can be recovered using analyticity and the $i\varepsilon$ prescription. Hence, implementing the change of variables $z = \frac{\lambda}{-v\cdot k} + 1$ in order to complete the square, followed by $x = 1/z$ leads to the expression:

$$I^{\Sigma^{\tilde{m}}_{\rm HQET}} = \frac{i\Gamma(\varepsilon)4^{\varepsilon}}{(4\pi)^{2-\varepsilon}}(-2v\cdot k)^{1-2\varepsilon}\int_0^1 \mathrm{d}x\,\frac{1}{x^2}\Big[\frac{1}{x^2} - 1 + \frac{4\tilde{m}^2}{(-2v\cdot k)^2}\Big]^{-\varepsilon}, \tag{4.16}$$

which can be easily integrated

$$I^{\Sigma^{\tilde{m}}_{\rm HQET}} = \frac{i}{2^{4-2\varepsilon}\pi^{2-\varepsilon}}\frac{\Gamma(\varepsilon)}{2\varepsilon-1}\,(-v\cdot k)^{1-2\varepsilon}\;{}_2F_1\left(\varepsilon-\frac{1}{2},\varepsilon;\varepsilon+\frac{1}{2};1-\frac{\tilde{m}^2}{(-v\cdot k)^2}\right). \tag{4.17}$$

With this result we find a closed form for $\Sigma^{\tilde{m}}_{\rm HQET}$ in d dimensions

$$i\Sigma^{\tilde{m}}_{\rm HQET} = -\,i\frac{\alpha_s C_F\tilde{\mu}^{2\varepsilon}}{2^{1-2\varepsilon}\pi^{1-\varepsilon}}\frac{\Gamma(\varepsilon)}{2\varepsilon-1}\,(-v\cdot k)^{1-2\varepsilon}\;{}_2F_1\left(\varepsilon-\frac{1}{2},\varepsilon;\varepsilon+\frac{1}{2};1-\frac{\tilde{m}^2}{(-v\cdot k)^2}\right), \tag{4.18}$$

which is finite when taking $\varepsilon \to 0$. Taking the $v\cdot k \to 0$ limit we obtain for the HQET Lagrangian with massive gluons the following result

$$\begin{aligned}\mathcal{L}^{\tilde{m}}_{\rm HQET} &= \overline{h}_v\, iv\cdot D\, h_v + \overline{h}_v\,\Delta M\, h_v\,,\\ \Delta M &\equiv -\frac{\alpha_s C_F\,\tilde{m}}{2}\,.\end{aligned} \tag{4.19}$$

4.3 Jet function

In Chapter 2 we carried out the computation of the hemisphere jet function for the event shapes considered in the M-scheme through the insertion of the complete set of real states, represented by cuts in the Feynman diagrams. However, it was already mentioned that this is not the optimal way to proceed for observables in that scheme since their collinear measurement consists on the total collinear plus momentum of the hemisphere and therefore it can be integrated right away to express the jet function as twice the imaginary part (the discontinuity) of a forward-scattering matrix element. This was the form used in the original computations at one loop [24] and the most convenient for this Chapter, since otherwise the dispersive integral method needs to be adapted using phase space factorization, which is not the purpose of this thesis.

To get the computational expression just mentioned for the SCET jet function, we first introduce the respective collinear measurement [see Eq. (2.11)] into the definition given in Eq. (2.40), to obtain the following result:

$$J_n(s,\mu) = \int\frac{\mathrm{d}\ell^+}{2\pi}\,\frac{1}{4N_c}\mathrm{Tr}\int \mathrm{d}^dx\, e^{i\ell x}\,\langle 0|\,\overline{\not{n}}\chi_n(x)\,\delta(s-Q\hat{P}^+)\,\overline{\chi}_{n,Q}(0)|0\rangle\,, \tag{4.20}$$

with $\hat{P}^+$ the momentum operator in the plus direction. Since the total energy in the state has to be positive, we can rewrite the identity in Eq. (2.42) as:

$$I = \sum_{n,\,\text{spin}} \int_0^\infty \mathrm{d}t \int \frac{\mathrm{d}^d P}{(2\pi)^d}\, \theta(P^0)\, \delta(P^2 - t)\, (2\pi)^d \delta^d(P - \sum_{i=0}^{n} p_i)\, \mathrm{d}\Phi_n\, |X_n\rangle\langle X_n|\,, \tag{4.21}$$

being Φ_n the n-particles phase space [see Eq. (1.3)]. After inserting the expression for the identity in this form before the Dirac delta function appearing in Eq. (4.20), we employ the momentum operator to shift the field $\chi_{n,Q}(x)$ to $x = 0$. After integrating ℓ^+, one can express the jet function as:

$$J_n(s,\mu) = \frac{1}{4N_c Q} \int \mathrm{d}^d x \int_0^\infty \mathrm{d}t \int \frac{\mathrm{d}^d P}{(2\pi)^d}\, \theta(P^0)\, \delta(P^2 - t) e^{i(\ell - P)\cdot x} f(P)\,, \tag{4.22}$$

where we defined $\ell \equiv (s/Q, Q, 0)$ in light-cone coordinates and

$$f(P) \equiv \sum_{n,\,\text{spin}} \mathrm{Tr} \int (2\pi)^{d-1} \delta^d(P - \sum_{i=0}^{n} p_i)\, \mathrm{d}\Phi_n\, \langle 0|\, \overline{\not{n}} \chi_n(0) |X_n\rangle\langle X_n| \overline{\chi}_n(0)|0\rangle\ . \tag{4.23}$$

Finally, we can integrate x and use the resulting delta for P to get:

$$J_n(s,\mu) = \frac{1}{4N_c Q} \int_0^\infty \mathrm{d}t\, \theta(\ell^0)\, \delta(\ell^2 - t) f(\ell)\,. \tag{4.24}$$

On the other hand, if we carry out the ℓ^+ integral in Eq. (4.20), multiply by i, and take the time ordered product of the jet fields, we get the forward-scattering matrix element

$$\frac{i}{8\pi N_c Q} \mathrm{Tr} \int \mathrm{d}^d x\, e^{i\ell\cdot x}\, \langle 0|\, \mathrm{T}\left\{ \overline{\not{n}} \chi_n(x)\, \overline{\chi}_n(0) \right\} |0\rangle \equiv i J_n^T(s,\mu)\,, \tag{4.25}$$

using again $\ell = (s/Q, Q, 0)$. Applying to this quantity the same set of steps used to in the jet function we obtain

$$i J_n^T(s,\mu) = \frac{i}{4N_c Q} \int \mathrm{d}^d x \int_0^\infty \mathrm{d}t \int \frac{\mathrm{d}^d P}{(2\pi)^d}\, \theta(P^0)\, \delta(P^2 - t) e^{i\ell\cdot x} f(P) \left[\, e^{-iP\cdot x} \theta(x^0) + e^{iP\cdot x} \theta(-x^0) \right]\ . \tag{4.26}$$

In order to continue, we use the integral form of the Heaviside theta $\theta(x) \equiv \frac{1}{2\pi i} \int_{-\infty}^{\infty} \frac{\mathrm{d}\omega\, e^{i\omega x}}{\omega - i\epsilon}$, leading to

$$i J_n^T(s,\mu) = \frac{1}{8\pi N_c Q} \int_0^\infty \mathrm{d}t \int_{-\infty}^{\infty} \mathrm{d}\omega\, \frac{f(\vec{l}, t)}{2\omega_t(\omega - i\epsilon)} \left[\delta(l^0 - \omega_t + \omega) + \delta(l^0 - \omega_t + \omega) \right]\ , \tag{4.27}$$

with $\omega_t \equiv \sqrt{t + |\vec{l}|^2}$. After carrying out the ω integral and summing up the resulting terms through a common denominator we end up with

$$i J_n^T(s,\mu) = \frac{1}{8\pi N_c Q} \int_0^\infty \mathrm{d}t \frac{f(\vec{l}, t)}{t - l^2 - i\epsilon}\,. \tag{4.28}$$

The relation to the imaginary part is obtained using the Cauchy principal value relation

$$\frac{1}{t - l^2 - i\epsilon} = \mathrm{P}\left(\frac{1}{t - l^2} \right) + i\pi \delta(t - l^2)\,. \tag{4.29}$$

Comparing Eqs. (4.24) and (4.28) we obtain the final expression for the jet function:

$$J_n(s,\mu) = 2\,\mathrm{Im}\left[\frac{i}{8\pi N_c Q}\mathrm{Tr}\int \mathrm{d}^d x\, e^{i\ell\cdot x}\,\langle 0|\,\mathrm{T}\left\{\overline{\not{n}}\chi_n(x)\,\overline{\chi}_n(0)\right\}|0\rangle\right]. \tag{4.30}$$

For the bHQET jet function an analogous procedure can be followed (or one can simply match the previous expression to bHQET fields) to obtain:[3]

$$\begin{aligned} M\mathcal{B}_n(\hat{s},\mu) &= \frac{i}{4\pi N_C}\,\mathrm{Tr}\int \mathrm{d}^d x\, e^{ik\cdot x}\,\langle 0|\,\mathrm{T}\left\{\,W_n^+(x)\,h_v(x)\,\overline{h}_v(0)\,W_n(0)\right\}|0\rangle\,, \\ MB_n(\hat{s},\mu) &= \mathrm{Im}\Big[M\mathcal{B}_n(\hat{s},\mu)\Big]\,. \end{aligned} \tag{4.31}$$

where $2v\cdot k \equiv \hat{s}$.

We are now all set for carrying out the computation. Let us start considering the tree-level diagram, depicted in Fig. 4.4, to illustrate this way of calculating the jet function.

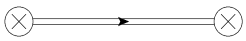

Figure 4.4: Tree-level diagram for the bHQET jet function, computed through the discontinuity of a forward-scattering matrix element.

The contribution to $\mathcal{B}_n$ is given by

$$M\mathcal{B}_n^{\mathrm{tree}}(\hat{s}) = \mathrm{Tr}\left[\frac{i}{4\pi N_C}\left(\frac{1+\not{v}}{2}\right)\frac{i}{v\cdot k + i0}\right] = -\frac{1}{\pi\hat{s}}\,, \tag{4.32}$$

where we have defined $\hat{s} \equiv \hat{s} + i0$ in the last equality. It is also worth noting that since the Dirac structure of the heavy quark propagator is simply the projector $\frac{1+\not{v}}{2}$, the trace over spin results in a factor of 2 for all Feynman diagrams.

In order to take the imaginary part of the singular terms in $\hat{s} \equiv \hat{s} + i0$ we can use the following identity:

$$\begin{aligned} \mathrm{Im}\left[\frac{\log^n(-x-i0)}{\pi(-x-i0)}\right] &= \cos^2\left(\frac{n\pi}{2}\right)\frac{(-\pi^2)^{n/2}}{n+1}\,\delta(x) \\ &\quad + \sum_{j=0}^{[(n-1)/2]} \frac{(-1)^j n!\,\pi^{2j}}{(2j+1)!\,(n-2j-1)!}\left[\frac{\theta(x)\log^{n-2j-1}(x)}{x}\right]_+\,, \end{aligned} \tag{4.33}$$

where $[(n-1)/2]$ refers to the closest integer number smaller or equal than $(n-1)/2$ (that is, $[\ldots]$ is the floor function). We may need to take into account its derivatives if higher powers of the denominator

[3] Recall that in this Chapter we use M for the primary quark and m for the secondary. Hence, we the notation $v_+ = \left(\frac{M}{Q},\frac{Q}{M},0\right)$, $v_- = \left(\frac{Q}{M},\frac{M}{Q},0\right)$ is employed. Notice that the jet function calculation carried out in this Chapter refers to the n-collinear hemisphere, therefore the relevant velocity is v_+, although we omit the subscript for clarity in the formulation. The other hemisphere computation is analogous, using v_- instead, but leading to the same result.

are involved, for instance

$$\mathrm{Im}\left[\frac{1}{\pi(x+i0)^2}\right] = \delta'(x)\,, \tag{4.34}$$

where δ' stands for the first derivative of the Dirac delta function.[4] All in all, the tree-level result reads:

$$MB_n^{\mathrm{tree}}(\hat{s}) = \mathrm{Im}\left[-\frac{1}{\pi(\hat{s}+i\epsilon)}\right] = \delta(\hat{s})\,. \tag{4.35}$$

4.3.1 Massive gluon computations

As argued in Sec. 4.1, first we need the result of the jet function with a massive gluon at one loop order to get the secondary massive quark corrections through the dispersive integral. At this order, renormalization must be already taken into account. We will carry out the computations assuming the mass of the primary heavy quark in SCET was defined in the pole-scheme. In Sec. 2.3 was already mentioned that Z_ξ does not appear directly in calculations based on Eq. (4.31). The reason is that all fields in the jet function definition are bare, but one does not need to insert a complete set of states.

Additionally, we saw in Sec. 4.2 that when considering massive gluons one gets an extra contribution to the self-energy coming from a non-zero quark bilinear term in the HQET Lagrangian that restores the position of the primary quark propagator pole at the zero off-shellness ($v\cdot k \to 0$) point.

All in all, the non-vanishing contributions[5] to the bHQET jet function with a massive gluon come from the Feynman diagrams shown in Fig. 4.5.

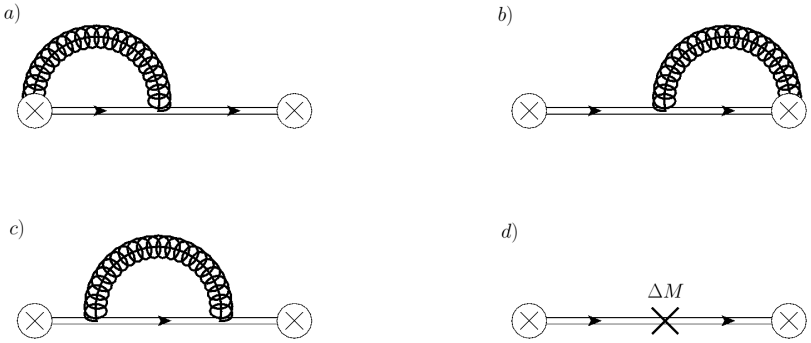

Figure 4.5: One loop diagrams with a massive gluon contributing to the Jet function, computed through the discontinuity of a forward scattering matrix element.

Quark self-energy

Applying Feynman rules for diagram c) we get:

$$M\mathcal{B}_n^c(\hat{s},\mu,\tilde{m}) = \frac{8i\alpha_s C_F \tilde{\mu}^{2\varepsilon}}{\hat{s}^2}\int \frac{\mathrm{d}^d q}{(2\pi)^d}\,\frac{1}{[q^2-\tilde{m}^2+i0][v\cdot(k-q)+i0]}\,. \tag{4.36}$$

[4] The n-th derivative of the Dirac delta is defined applying n times integration by parts.

[5] Notice that the diagram with the gluon propagator connecting both collinear Wilson lines is proportional to $n^2 = 0$ in the Feynman gauge and therefore we ignore it.

The result of the integral was already obtained in Eq. (4.17) with the replacement $v\cdot k \to \hat{s}/2$, yielding the following contribution to $\mathcal{B}$:

$$M\mathcal{B}_n^c(\hat{s},\mu,\tilde{m}) = \frac{\alpha_s C_F(\mu^2 e^{\gamma_E})^\varepsilon(-\hat{s})^{-1-2\varepsilon}}{2\pi^2}\frac{4^\varepsilon\Gamma(\varepsilon)}{1-2\varepsilon}\,{}_2F_1\left(\varepsilon-\frac{1}{2},\,\varepsilon\,;\frac{1}{2}+\varepsilon;1-\frac{4\tilde{m}^2}{(-\hat{s})^2}\right). \tag{4.37}$$

In order to take the imaginary part we split the previous expression in the following way:

$$M\mathcal{B}_n^d(\hat{s},\mu,\tilde{m}) = M\mathcal{B}_n^d(\hat{s},\mu,\tilde{m}\to\infty) + \Big[M\mathcal{B}_n^d(\hat{s},\mu,\tilde{m}) - M\mathcal{B}_n^d(\hat{s},\mu,\tilde{m}\to\infty)\Big], \tag{4.38}$$

since the decoupling limit divergences are the same and we can safely take $\varepsilon\to 0$ in the term in square brackets to obtain

$$\begin{aligned} M\mathcal{B}_n^c(\hat{s},\mu,\tilde{m}) = {}& \frac{\alpha_s C_F\Gamma(\varepsilon)(\mu^2e^{\gamma_E})^\varepsilon}{4\pi^2}\,\frac{\tilde{m}^{-2\varepsilon}}{(-\hat{s})}\left[2-\frac{4\pi^{1/2}\,\Gamma(1/2+\varepsilon)}{(2\varepsilon-1)\,\Gamma(\varepsilon)}\frac{\tilde{m}}{(-\hat{s})}\right] \\ & -\frac{\alpha_s C_F}{4\pi^2}\,\frac{1}{(-\hat{s})}\left[\frac{4\tilde{m}\pi}{(-\hat{s})}-4+4\beta[\tilde{m}^2]\,\log\left(\frac{1+\beta[\tilde{m}^2]}{2\tilde{m}/(-\hat{s})}\right)\right], \end{aligned} \tag{4.39}$$

with $\beta[x]\equiv\sqrt{1-4x/(-\hat{s})^2}$. At this point, Eq. (4.33) can be directly applied except for the last term, for which we still have to isolate the $\hat{s}\to 0$ singularities, getting in this way

$$\mathrm{Im}\left[\frac{\beta[x]}{\hat{s}}\log\left(\frac{1+\beta[x]}{2\sqrt{x}/(-\hat{s})}\right)\right] = \sqrt{x}\,\pi^2\delta'(\hat{s}) - \pi\delta(\hat{s}) - \theta(\hat{s}^2-4x)\,\pi\,\frac{\sqrt{s^2-4x}}{s^2}. \tag{4.40}$$

Finally, the contribution of the diagram to the jet function is:

$$\begin{aligned} MB_n^c(\hat{s},\mu,\tilde{m}) = {}& \frac{\alpha_s C_F}{4\pi}\left\{2\Gamma(\varepsilon)(\mu^2e^{\gamma_E})^\varepsilon\tilde{m}^{-2\varepsilon}\,\delta(\hat{s}) + \frac{(\mu^2e^{\gamma_E})^\varepsilon\tilde{m}^{1-2\varepsilon}4\pi^{1/2}\,\Gamma(1/2+\varepsilon)}{1-2\varepsilon}\,\delta'(\hat{s})\right. \\ & \left. -\,\theta(\hat{s}^2-4\tilde{m}^2)\,4\,\frac{\sqrt{\hat{s}^2-4\tilde{m}^2}}{\hat{s}^2}\right\}. \end{aligned} \tag{4.41}$$

Wilson line gluon

The result for diagrams a) and b) is identical, hence we describe the computation for a) and account for b) multiplying the result by 2. In this case, the integral given by the Feynman rules reads

$$M\mathcal{B}_n^a(\hat{s},\mu,\tilde{m}) = \frac{4i\alpha_s C_F\tilde{\mu}^{2\varepsilon}}{(-\hat{s})}\,\frac{Q}{M}\,\tilde{I}^a, \tag{4.42}$$

$$\tilde{I}^a \equiv \int\frac{\mathrm{d}^dq}{(2\pi)^d}\,\frac{1}{[v\cdot(k-q)+i0][q^2-\tilde{m}^2+i0][\overline{n}\cdot q+i0]},$$

and receives a non-vanishing 0-bin contribution [see discussion around Eq. (1.27)]:

$$\tilde{I}^a_{0-\mathrm{bin}} = \int\frac{\mathrm{d}^dq}{(2\pi)^d}\,\frac{1}{[v\cdot k-\frac{Q}{2M}q^+ + i0][q^2-\tilde{m}^2+i0][\overline{n}\cdot q+i0]}. \tag{4.43}$$

Therefore, in order to avoid double counting for the soft momentum, we have:

$$M\mathcal{B}_n^a(\hat{s},\mu,\tilde{m}) = \frac{4i\alpha_s C_F\tilde{\mu}^{2\varepsilon}}{(-\hat{s})}\,\frac{Q}{M}\,I^a \tag{4.44}$$

$$I^a \equiv \tilde{I}^a - \tilde{I}^a_{0-\mathrm{bin}} = \int\frac{\mathrm{d}^dq}{(2\pi)^d}\,\frac{\frac{M}{2Q}}{[v\cdot(k-q)+i0][v\cdot k-\frac{Q}{2M}q^+ + i0][q^2-\tilde{m}^2+i0]}.$$

To perform the computation of I^a we first integrate q^+ by residues and use a Feynman parameter to combine the resulting denominators. Subsequently, we solve the integrals of the perpendicular component in $d-2$ dimensions in first place and afterwards the one for the Feynman parameter. Lastly, changing the minus component integration variable to $\lambda = \frac{M}{Q}\, q^-$ we get:

$$I^a = \frac{i\Gamma(\varepsilon)}{2^{3-2\varepsilon}\pi^{2-\varepsilon}} \frac{M}{Q} \int_0^\infty \frac{\mathrm{d}\lambda}{\lambda} \left[\left(\lambda^2 - \hat{s}\lambda + \tilde{m}^2\right)^{-\varepsilon} - \left(-\hat{s}\lambda + \tilde{m}^2\right)^{-\varepsilon} \right]. \tag{4.45}$$

To the best of our knowledge, a closed form for the whole integral in the previous equation cannot be obtained directly and if we try to solve each term independently a rapidity divergence appears in each one of the terms. Therefore, we switch variables to $z = \frac{2\lambda}{-\hat{s}} + 1$ and introduce the analytic (massless) regulator Υ to modify the exponent of the factor $(z-1)$, responsible for such divergence. Finally, we make another change of variable $x = 1/z$ and carry out the integrals of both terms:[6]

$$\begin{aligned} I^a = \frac{i\Gamma(\varepsilon)}{2^{3-2\varepsilon}\pi^{2-\varepsilon}} \frac{M}{Q} (-\hat{s})^{-2\varepsilon}\, \Gamma(\Upsilon) \Bigg[& \frac{4^\varepsilon\, \Gamma(2\varepsilon - \Upsilon)}{\Gamma(2\varepsilon)}\, {}_2F_1\left(\varepsilon - \frac{\Upsilon}{2}, \frac{1-\Upsilon}{2} + \varepsilon\,; \frac{1}{2} + \varepsilon; 1 - \frac{4\tilde{m}^2}{(-\hat{s})^2}\right) \\ & - \frac{2^\Upsilon \left(\frac{\tilde{m}^2}{(-\hat{s})^2}\right)^{\Upsilon-\varepsilon} \Gamma(\varepsilon - \Upsilon)}{\Gamma(\varepsilon)} \Bigg]. \end{aligned} \tag{4.46}$$

It can be checked that the previous result is indeed finite when Υ goes to zero e.g. expanding around this limit. The part of the jet function corresponding to this diagram is:

$$\begin{aligned} M\mathcal{B}_n^a(\hat{s}, \mu, \tilde{m}) = -\frac{\alpha_s C_F\, \Gamma(\varepsilon)\, (\mu^2 e^{\gamma_E})^\varepsilon}{\pi^2\, (-\hat{s})} \Bigg\{ & \frac{(-\hat{s})^{-2\varepsilon}\, \Gamma(\Upsilon)}{2} \Bigg[\frac{4^\varepsilon\, \Gamma(2\varepsilon - \Upsilon)}{\Gamma(2\varepsilon)} \times \\ & \times\, {}_2F_1\left(\varepsilon - \frac{\Upsilon}{2}, \frac{1-\Upsilon}{2} + \varepsilon\,; \frac{1}{2} + \varepsilon; 1 - \frac{4\tilde{m}^2}{(-\hat{s})^2}\right) - \frac{2^\Upsilon \left(\frac{\tilde{m}^2}{(-\hat{s})^2}\right)^{\Upsilon-\varepsilon} \Gamma(\varepsilon - \Upsilon)}{\Gamma(\varepsilon)} \Bigg] \Bigg\}. \end{aligned} \tag{4.47}$$

The imaginary part can be taken following a procedure analogous to the one for diagram c), that is, adding and subtracting the $\tilde{m} \to \infty$ limit:

$$M\mathcal{B}_n^a(\hat{s}, \mu, \tilde{m}) = M\mathcal{B}_n^a(\hat{s}, \mu, \tilde{m} \to \infty) + \left[M\mathcal{B}_n^a(\hat{s}, \mu, \tilde{m}) - M\mathcal{B}_n^a(\hat{s}, \mu, \tilde{m} \to \infty) \right]. \tag{4.48}$$

However, in this case, in addition to the ε expansion of the second term, we must also set $\Upsilon \to 0$ in both. This leads to:

$$\begin{aligned} M\mathcal{B}_n^a(\hat{s}, \mu, \tilde{m}) = & \frac{\alpha_s C_F\, \Gamma(\varepsilon)\, (\mu^2 e^\gamma)^\varepsilon\, \tilde{m}^{-2\varepsilon}}{4\pi^2\, (-\hat{s})} \left[\frac{(-\hat{s})\, \pi^{1/2}\, \Gamma(1/2 + \varepsilon)}{\tilde{m}\, \Gamma(\varepsilon)} - H_{\varepsilon-1} - 2\log\left(\frac{(-\hat{s})}{\tilde{m}}\right) \right] \\ & + \frac{\alpha_s C_F}{8\pi^2\, (-\hat{s})} \left[\pi^2 - \frac{2\pi(-\hat{s})}{\tilde{m}} + 4\log^2\left(\frac{1 + \beta[\tilde{m}^2]}{2\tilde{m}/(-\hat{s})}\right) \right], \end{aligned} \tag{4.49}$$

where H_n is the harmonic number, which for non-integer argument can be related to the digamma function: $H_{\varepsilon-1} = \psi^{(0)}(\varepsilon) + \gamma_E$. We can see from the result above that we only need the following imaginary part:

$$\mathrm{Im}\left[\frac{1}{(-\hat{s})} \log^2\left(\frac{1 + \beta[\tilde{m}^2]}{2\tilde{m}/(-\hat{s})}\right) \right] = \theta\left(\hat{s}^2 - 4\tilde{m}^2\right) \frac{2\pi}{\hat{s}} \log\left(\frac{\hat{s} + \sqrt{\hat{s}^2 - 4\tilde{m}^2}}{2\tilde{m}}\right) - \frac{\pi^3}{4}\, \delta(\hat{s}), \tag{4.50}$$

[6] Notice that the last two changes of variable are the same as those in Eq. (4.16)

and Eq. (4.33) to get the contribution to the jet function, which results in:

$$MB_n^a(\hat{s},\mu,\tilde{m}) = \frac{\alpha_s C_F}{4\pi}\Bigg\{\Gamma(\varepsilon)\,(\mu^2 e_E^\gamma)^\varepsilon\,\tilde{m}^{-2\varepsilon}\left[\Big[2\log(\tilde{m}) - H_{\varepsilon-1}\Big]\delta(\hat{s}) - 2\left[\frac{\theta(\hat{s})}{\hat{s}}\right]_+\right] \\ + \theta\left(\hat{s}^2 - 4\tilde{m}^2\right)\frac{4}{\hat{s}}\log\left(\frac{\hat{s}+\sqrt{\hat{s}^2-4\tilde{m}^2}}{2\tilde{m}}\right)\Bigg\}. \tag{4.51}$$

Quark bilinear term

Feynman rules for diagram *d*) read:

$$M\mathcal{B}_n^d(\hat{s},\mu,\tilde{m}) = \mathrm{Tr}\left[\frac{i}{4\pi N_C}\left(\frac{1+\not{v}}{2}\right)\frac{i}{v\cdot k + i0}\,i\Delta M\,\frac{i}{v\cdot k + i0}\right] = \frac{2\Delta M}{\pi\hat{s}^2}\,, \tag{4.52}$$

and the corresponding part of the jet function is

$$MB_n^d(\hat{s},\mu,\tilde{m}) = 2\Delta M\delta'(\hat{s}) = -\alpha_s C_F\,\tilde{m}\,\delta'(\hat{s})\,, \tag{4.53}$$

which exactly cancels the derivative of Dirac delta term in Eq. (4.41) if we set $\varepsilon \to 0$. This is expected since ΔM is defined as the on-shell contribution to the primary quark self-energy from the massive gluon diagram with the sign reversed (see Sec. 4.2), and therefore the cancellation will happen for any value of ε provided we treat both terms on the same footing.

Massive gluon result

Combining all individual pieces we get the final result for the NLO jet function with a massive gluon:

$$MB_n^{\alpha_s}(\hat{s},\mu,\tilde{m}) = \frac{\alpha_s C_F}{4\pi}\Bigg\{2\,\Gamma(\varepsilon)\,\left(\frac{\mu^2}{\tilde{m}^2}e_E^\gamma\right)^\varepsilon\left[\Big(1 - H_{\varepsilon-1} + 2\log(\tilde{m})\Big)\delta(\hat{s})\right. \\ \left. - 2\left[\frac{\theta(\hat{s})}{\hat{s}}\right]_+ + \frac{2\tilde{m}\pi^{1/2}\,\Gamma(1/2+\varepsilon)}{(1-2\varepsilon)\,\Gamma(\varepsilon)}\,\delta'(\hat{s})\right] - 4\pi\,\tilde{m}\,\delta'(\hat{s}) \\ + \theta\left(\hat{s}^2 - 4\tilde{m}^2\right)\left[\frac{8}{\hat{s}}\log\left(\frac{\hat{s}+\sqrt{\hat{s}^2-4\tilde{m}^2}}{2\tilde{m}}\right) - \frac{4\sqrt{\hat{s}^2-4\tilde{m}^2}}{\hat{s}^2}\right]\Bigg\}. \tag{4.54}$$

Let us consider the massless limit of the previous expression as a cross-check. In this limit some other distributions may arise so we will work with the ε-expanded cumulative jet function:

$$\begin{aligned}\Sigma^{\alpha_s}(\hat{s}_c,\mu,\tilde{m}) &\equiv \int_0^{\hat{s}_c} d\hat{s}\, B_n^{\alpha_s}(\hat{s},\mu,\tilde{m}) \\ &= \frac{\alpha_s C_F}{4\pi M}\left\{\frac{2}{\varepsilon^2}+\frac{2}{\varepsilon}+\frac{4}{\varepsilon}\log(\mu)+8\log^2(\tilde{m})+4\log^2(\mu)+\frac{\pi^2}{6}+4\log(\mu)\right. \\ &\quad +16\log(2)\log(\tilde{m})+4\log^2(2)+4\log(2)+\left(-\frac{4}{\varepsilon}-8\log(\mu)-8\log(2)\right)\log\left(\hat{s}_c\right) \\ &\quad +\frac{4\sqrt{\hat{s}_c^2-4\tilde{m}^2}}{\hat{s}_c}-4\log\left(\hat{s}_c+\sqrt{\hat{s}_c^2-4\tilde{m}^2}\right)\left[1+\log\left(\hat{s}_c+\sqrt{\hat{s}_c^2-4\tilde{m}^2}\right)\right. \\ &\quad \left.\left.-2\log\left(1+\frac{\left(\hat{s}_c+\sqrt{\hat{s}_c^2-4\tilde{m}^2}\right)^2}{4\tilde{m}^2}\right)\right]+4\mathrm{Li}_2\left(-\frac{\left(\hat{s}_c+\sqrt{\hat{s}_c^2-4\tilde{m}^2}\right)^2}{4\tilde{m}^2}\right)\right\}. \end{aligned} \tag{4.55}$$

We can safely take $\tilde{m}\to 0$ in the previous expression, finding

$$\Sigma^{\alpha_s}(\hat{s}_c,\mu,\tilde{m}\to 0)=1+\frac{\alpha_s C_F}{4\pi}\left[\frac{2}{\varepsilon^2}+\frac{2}{\varepsilon}+4-\frac{\pi^2}{2}-4\log\left(\frac{\hat{s}_c}{\mu}\right)-\frac{4}{\varepsilon}\log\left(\frac{\hat{s}_c}{\mu}\right)+4\log^2\left(\frac{\hat{s}_c}{\mu}\right)\right], \tag{4.56}$$

from where we can differentiate

$$B_n^{\alpha_s}(\hat{s},\mu)=\frac{\mathrm{d}}{\mathrm{d}\hat{s}_c}\Big[\theta(\hat{s}_c)\,\Sigma^{\alpha_s}(\hat{s}_c,\mu,\tilde{m}\to 0)\Big]_{\hat{s}_c\to\hat{s}}, \tag{4.57}$$

to recover the known massless result using Eqs. (2.83) and (2.70)

$$MB_n^{\alpha_s}(\hat{s},\mu)=\frac{\alpha_s C_F}{4\pi}\left\{\left[\frac{2}{\varepsilon^2}+\frac{2}{\varepsilon}+4-\frac{\pi^2}{2}\right]\delta(\hat{s})-4\left(1+\frac{1}{\varepsilon}\right)\frac{1}{\mu}\left[\frac{\theta(\hat{s}/)}{\hat{s}}\right]_+ +\frac{8}{\mu}\left[\frac{\theta(\hat{s})\log(\hat{s}/\mu)}{\hat{s}/\mu}\right]_+\right\}. \tag{4.58}$$

4.3.2 Final result

In order to get the secondary massive quark corrections we split the integral of Eq. (4.54) involving the kernel $\mathcal{V}^{(d=4-2\varepsilon)}(\tilde{m},\tilde{\mu})\equiv\mathcal{V}^{4-2\varepsilon}$ into the different terms:

$$\int_{4m^2}^{\infty}\mathrm{d}\tilde{m}^2\;\mathcal{V}^{4-2\varepsilon}\,(\tilde{m}^2)^p=\frac{\sqrt{\pi}4^p(1-p)\left(\mu^2e^{\gamma_E}\right)^{\varepsilon}\left(m^2\right)^{p-\varepsilon}\Gamma(\varepsilon-p)}{\Gamma\left(\frac{5}{2}-p\right)};\quad p=-\varepsilon,\,1/2-\varepsilon\,, \tag{4.59}$$

$$\begin{aligned}\int_{4m^2}^{\infty}\mathrm{d}\tilde{m}^2\;\mathcal{V}^{4-2\varepsilon}\,(\tilde{m}^2)^{-\varepsilon}\log(\tilde{m}^2) &= \frac{\sqrt{\pi}4^{-\varepsilon}\left(\mu^2e^{\gamma_E}\right)^{\varepsilon}\left(m^2\right)^{-2\varepsilon}\Gamma(2\varepsilon)}{\Gamma\left(\varepsilon+\frac{5}{2}\right)} \\ &\quad\times\left[(\varepsilon+1)\log\left(4m^2\right)-(\varepsilon+1)\;\psi^{(0)}(2\varepsilon)+(\varepsilon+1)\;\psi^{(0)}\left(\varepsilon+\frac{5}{2}\right)-1\right],\end{aligned}$$

$$\int_{4m^2}^{\hat{s}^2/4}\mathrm{d}\tilde{m}^2\;\mathcal{V}^4\,\sqrt{\hat{s}^2-4\tilde{m}^2}=\frac{8\left(32m^2+3\hat{s}^2\right)}{9\hat{s}}K\left(1-\frac{16m^2}{\hat{s}^2}\right)+\frac{4\left(16m^2-11\hat{s}^2\right)}{9\hat{s}}E\left(1-\frac{16m^2}{\hat{s}^2}\right),$$

$$I[\hat{s},m]\equiv\int_{4m^2}^{\hat{s}^2/4}\mathrm{d}\tilde{m}^2\;\mathcal{V}^4\,\frac{1}{4\hat{s}}\,\log\left(\frac{\hat{s}+\sqrt{\hat{s}^2-4\tilde{m}^2}}{2\tilde{m}}\right),$$

where E and K are elliptic integrals[7] and we postpone the discussion of $I[\hat{s},m]$ to Appendix C.1 where, starting from the dispersive integrals, we work out an analytical expression along with series expansions in two different (but overlapping) regimes for the non-distributional part of the jet function. Nevertheless, we shall see that in the way we carry out the computations in the next Chapter the series and analytic results are obtained much more easily.

Note that the second line of Eq. (4.59) can be obtained from the first writing $(\tilde{m}^2)^{-\varepsilon}\log(\tilde{m}^2) = \lim_{\beta\to 0}\left[\frac{d}{d\beta}\left((\tilde{m}^2)^{-\varepsilon+\beta}\right)\right]$ and in the last two lines ε can be set to zero right away.

Since the dispersive integral corresponds to the on-shell renormalized bubble diagrams [see Eq. (4.8)] we have to add back the $\Pi_0(m^2)$ part [see Eq. (4.5)] to recover the unrenormalized $\overline{\text{MS}}$ result. And since $\Pi_0(m^2)$ appears in a term which is proportional to the (massless) gluon propagator, we account for it simply multiplying the (massless) one loop jet function by the vacuum polarization function at zero momentum, such that

$$MB_n^{m,\text{bare}}(\hat{s},\mu,m) = T_F\frac{\alpha_s}{4\pi}\int_{4m^2}^{\infty}\mathrm{d}\tilde{m}^2\;\mathcal{V}^{4-2\varepsilon}MB_n^{\alpha_s}(\hat{s},\mu,\tilde{m}) + \left[\Pi_0(m^2)+\frac{\alpha_s T_F}{3\pi\varepsilon}\right]MB_n^{\alpha_s}(\hat{s},\mu)\,, \quad (4.62)$$

with $MB_n^{m,\text{bare}}(\hat{s},\mu,m)$ the contribution of the secondary massive quark to the bare jet function.[8]

As a cross-check, we can see that the divergences obtained are canceled by the bubble terms of the $\overline{\text{MS}}$ renormalization Z-factor obtained in Ref. [42], where the 2-loop bHQET jet function was computed considering massless secondary quarks.[9]

Finally, after the convolution of the $\overline{\text{MS}}$-renormalized hemisphere jet functions [see Eq. (2.39)], the correction to the thrust bHQET jet function due to a non-vanishing secondary quark mass bubble takes the form

$$B_\tau^{(n_\ell+1)}(\hat{s},\mu,m) = B_\tau^{(n_\ell+1)}(\hat{s},\mu) + \delta B_m^{\text{dist}}(\hat{s},\mu,m) + \delta B_m^{\text{real}}(\hat{s},m)\,, \quad (4.63)$$

$$\begin{aligned}\delta B_m^{\text{dist}}(\hat{s},\mu,m) = \frac{\alpha_s^2 C_F T_F}{(4\pi)^2 M}\,2\Bigg[&\left(\frac{32}{9}L_m^3+\frac{128}{9}L_m^2+\frac{976-48\pi^2}{27}L_m+\frac{3568}{81}-\frac{64\pi^2}{27}-\frac{32}{3}\xi_3\right)\delta(\hat{s})\\ &+\left(-\frac{32}{3}L_m^2-\frac{256}{9}L_m-\frac{976}{27}+\frac{16\pi^2}{9}\right)\mathcal{L}^0(\hat{s})+\left(\frac{64}{3}L_m+\frac{256}{9}\right)\mathcal{L}^1(\hat{s})-\frac{32}{3}\mathcal{L}^2(\hat{s})\Bigg],\end{aligned}$$

$$\delta B_m^{\text{real}}(\hat{s},m) = \frac{\alpha_s^2 C_F T_F}{(4\pi)^2 M}\,64\,\theta\left(\hat{s}^2-16m^2\right)f_{\text{nd}}\,,$$

[7] Defined as

$$E(x)\equiv\int_0^1\mathrm{d}t\,\frac{\sqrt{1-xt^2}}{\sqrt{1-t^2}}\,, \qquad K(x)\equiv\int_0^1\mathrm{d}t\,\frac{1}{\sqrt{1-t^2}\sqrt{1-xt^2}}\,. \quad (4.60)$$

They can be written also in terms of hypergeometric functions

$$E(x) = \frac{\pi}{2}\,{}_2F_1\left(-\frac{1}{2},\frac{1}{2};1;x\right), \qquad K(x) = \frac{\pi}{2}\,{}_2F_1\left(\frac{1}{2},\frac{1}{2};1;x\right). \quad (4.61)$$

[8] In the previous equation we did account for the $\overline{\text{MS}}$ renormalization of the α_s parameter through the subtraction of the divergent term of $\Pi_0(m^2)$.

[9] Recall that in mass-independent renormalization schemes, divergences do not depend on infrared scales.

where n_ℓ is the number of massless flavors, $\alpha_s \equiv \alpha_s^{(n_\ell+1)}$, $L_m \equiv \log\left(\frac{m}{\mu}\right)$, $\mathcal{L}^i(\hat{s}) \equiv \frac{1}{\mu}\left[\frac{\theta(\hat{s})\log^i(\hat{s}/\mu)}{\hat{s}/\mu}\right]_+$, and

$$f_{\rm nd} = I[\hat{s},m] - \frac{32m^2+3\hat{s}^2}{9\,\hat{s}^3}K\left(1-\frac{16m^2}{\hat{s}^2}\right) - \frac{16m^2-11\hat{s}^2}{18\,\hat{s}^3}E\left(1-\frac{16m^2}{\hat{s}^2}\right). \tag{4.64}$$

The massless secondary quark jet function $B_\tau^{(n_\ell+1)}(\hat{s},\mu)$ (for $n_\ell+1$ flavors) can be found in Ref. [42]. Again, we can take the massless limit of the cumulative of the massive-bubble correction to see that indeed it vanishes but, due to the complexity of the integrals involved, the procedure was carried out numerically, finding a successful outcome.

4.4 bHQET Hard function

Another fundamental ingredient that appears in the bHQET factorization formula, see Eqs. (1.67) and (1.68), is the bHQET Hard function. It corresponds to the modulus square of the matching coefficient between the SCET and bHQET dijet quark currents [see Eq. (1.66)], whose calculation will be presented below taking the simplest possible matrix element, that is through the ratio of the so-called quark form factors in both theories:

$$C_M = \frac{\langle q,\overline{q}\,|\,J^\mu_{C\,\rm SCET}\,|0\rangle}{\langle q,\overline{q}\,|\,J^\mu_{C\,\rm bHQET}\,|0\rangle} \equiv \frac{\mathbf{F}_{\rm SCET}}{\mathbf{F}_{\rm bHQET}}\,, \tag{4.65}$$

where $\langle q,\overline{q}\,|$ stands for the quark and anti-quark on-shell final state particles. For simplicity, we have not displayed the spinors (as they cancel in the ratio) and current-type structures (the form factors coincide for vector and axial-vector currents) that appear in the matrix elements[10] and shown only the form factors themselves ($\mathbf{F}$). Furthermore, we will consider the current operators before the usual BPS field redefinition in such a way that, instead of soft Wilson lines, we will deal with collinear-soft interactions given by the Lagrangian in Eq. (1.37) and whose Feynman rule (which is the same in both EFTs) can be found in the dedicated Appendix A.

4.4.1 Massive gluon computations

The Feynman diagrams for the form factors are the same in both theories and depicted (with fields defined prior to BPS redefinition) in Fig. 4.6, where diagrams (a) and (b) correspond to collinear radiation, while (c) stands for a soft-gluon exchange between the quark legs. Since primary quarks are massive, one must include the corresponding wave function renormalization factor Z_ψ, that accounts for the fact that fields in the current are bare.

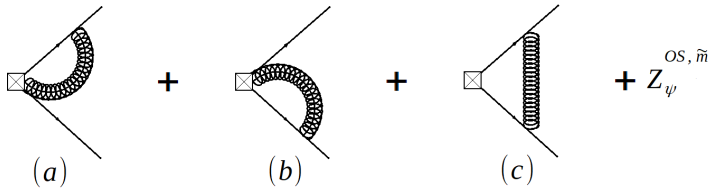

Figure 4.6: Contributions to SCET and bHQET form factors

The SCET one-loop form factor with a massive gluon is already known for massless and massive primary

[10] They result in a common factor $\overline{u}_{p_q}\Gamma^\mu_C v_{p_{\overline{q}}}$, with u, v the corresponding quark and anti-quark spinors, respectively.

quarks. The calculation for massless primary quarks can be found in Ref. [31]. To compute the different loop integrals, which contain non-vanishing 0-bin subtractions, the authors of that reference use the residue theorem on one light-cone component of the loop momentum, carry out the perpendicular integral in the usual way, finding that the remaining light-cone component integral is divergent (even with a non-zero value of epsilon). Nevertheless, these divergences cancel out when summing the contributions from all Feynman diagrams, leading to a well-defined integral. In Ref. [40], the finite corrections due to the mass of the primary quark were computed.[11] The combination of both results reads

$$\begin{aligned}\mathbf{F}^{\tilde{m}}_{\text{SCET}} = \frac{\alpha_s C_F}{2\pi}\Bigg\{&\Gamma(\varepsilon)\left(\frac{\mu^2}{\tilde{m}^2}e^{\gamma}_E\right)^{\varepsilon}\left[H_{1-\varepsilon} - (-1)^{\varepsilon}\Gamma(2-\varepsilon)\Gamma(\varepsilon-1) + \frac{1+\varepsilon-\varepsilon^2}{2-3\varepsilon+\varepsilon^2} + \log\left(\frac{\tilde{m}^2}{Q^2}\right)\right] \\ &+ \frac{6-b^3-5b}{2b(b+1)^2}\log\left(\frac{1-b}{2}\right) - \frac{b^3+5b+6}{2(1-b)^2 b}\log\left(\frac{b+1}{2}\right) \\ &+ \frac{b^2-25}{4\,(1-b^2)} + 2\log\left(\frac{1-b}{2}\right)\log\left(\frac{b+1}{2}\right) + \mathcal{O}(\varepsilon)\Bigg\},\end{aligned} \tag{4.66}$$

with $b \equiv \sqrt{1-\frac{4M^2}{\tilde{m}^2}}$. Thus, we just need to care about the bHQET form factor computation, that will be performed analogously to the procedure in Ref. [31] just described.

Collinear and Soft diagrams contribution

Applying Feynman rules to the n-collinear diagram a) we get:

$$\begin{aligned}\mathbf{F}^{\tilde{m},a}_{\text{bHQET}} &= -\,i4\pi\alpha_s C_F\tilde{\mu}^{2\varepsilon}\;\overline{n}\cdot v_+\;\tilde{I}^{\tilde{m},a}\,, \\ \tilde{I}^{\tilde{m},a} &\equiv \int\frac{\mathrm{d}^d l}{(2\pi)^d}\frac{1}{\left[l^2-\tilde{m}^2+i0\right]\left[v_+\cdot l+i0\right]\left[\overline{n}\cdot l-i0\right]}\,,\end{aligned} \tag{4.67}$$

where $\tilde{I}^{\tilde{m},a}$ has the following 0-bin subtraction:

$$\tilde{I}^{\tilde{m},a}_{0-\text{bin}} = \int\frac{\mathrm{d}^d l}{(2\pi)^d}\frac{1}{\left[l^2-\tilde{m}^2+i0\right]\left[\frac{1}{2}\overline{n}\cdot v_+\, n\cdot l+i0\right]\left[\overline{n}\cdot l-i0\right]}\,. \tag{4.68}$$

Therefore the diagram contribution reads:

$$\mathbf{F}^{\tilde{m},a}_{\text{bHQET}} = i4\pi\alpha_s C_F\tilde{\mu}^{2\varepsilon}\,\frac{1}{\overline{n}\cdot v_+}\int\frac{\mathrm{d}^d l}{(2\pi)^d}\frac{1}{\left[l^2-\tilde{m}^2+i0\right]\left[v_+\cdot l+i0\right]\left[n\cdot l+i0\right]}\,. \tag{4.69}$$

Then we use residues to integrate the minus component, keeping track of the $i0$-prescription:

$$\mathbf{F}^{\tilde{m},a}_{\text{bHQET}} = -\frac{\alpha_s C_F\tilde{\mu}^{2\varepsilon}}{2^{-2\varepsilon}\pi^{1-\varepsilon}}\,\frac{1}{\Gamma(1-\varepsilon)}\int_{-\infty}^{0}\frac{\mathrm{d}l^+}{l^+ + i0}\int_0^{\infty}\frac{\mathrm{d}\,|l_\perp|\;|l_\perp|^{d-3}}{|l_\perp|^2+\tilde{m}^2+\frac{Q^2}{M^2}\left(l^+\right)^2}\,, \tag{4.70}$$

and carry out the perpendicular integral to obtain:

$$\mathbf{F}^{\tilde{m},a}_{\text{bHQET}} = -\frac{\alpha_s C_F\tilde{\mu}^{2\varepsilon}}{2^{1-2\varepsilon}\pi^{1-\varepsilon}}\,\Gamma(\varepsilon)\int_{-\infty}^{0}\frac{\mathrm{d}l^+}{l^+ + i0}\left[\tilde{m}^2+\frac{Q^2}{M^2}\left(l^+\right)^2\right]^{-\varepsilon}\,. \tag{4.71}$$

On the other hand, Feynman rules, including 0-bin subtraction, for the $\overline{n}$-collinear diagram b) give:

$$\mathbf{F}^{\tilde{m},b}_{\text{bHQET}} = i4\pi\alpha_s C_F\tilde{\mu}^{2\varepsilon}\,\frac{1}{n\cdot v_-}\int\frac{\mathrm{d}^d l}{(2\pi)^d}\frac{1}{\left[l^2-\tilde{m}^2+i0\right]\left[v_-\cdot l+i0\right]\left[\overline{n}\cdot l+i0\right]}\,, \tag{4.72}$$

[11] Since these are finite, the computation was done in four dimensions.

and employing the same procedure, the remaining integral in this case is:

$$\mathbf{F}^{\tilde{m},b}_{\text{bHQET}} = \frac{\alpha_s C_F \tilde{\mu}^{2\varepsilon}}{2^{1-2\varepsilon}\pi^{1-\varepsilon}}\,\Gamma(\varepsilon)\int_{-\infty}^{0}\frac{\mathrm{d}l^+}{l^+ + i0}\left\{\left[\tilde{m}^2 + \frac{M^2}{Q^2}\left(l^+\right)^2\right]^{-\varepsilon} - \left[\tilde{m}^2\right]^{-\varepsilon}\right\}. \tag{4.73}$$

Finally, the soft contribution from diagram c) leads to

$$\begin{aligned}\mathbf{F}^{\tilde{m},c}_{\text{bHQET}} &= -\,i8\pi\alpha_s C_F\tilde{\mu}^{2\varepsilon}\int\frac{\mathrm{d}^d l}{(2\pi)^d}\frac{1}{[l^2-\tilde{m}^2+i0]\,[n\cdot l+i0]\,[\overline{n}\cdot l+i0]} \\ &= -\,\frac{\alpha_s C_F\tilde{\mu}^{2\varepsilon}}{2^{1-2\varepsilon}\pi^{1-\varepsilon}}\,\Gamma(\varepsilon)\,\left[\tilde{m}^2\right]^{-\varepsilon}\int_0^{\infty}\frac{\mathrm{d}l^+}{l^+ + i0}\,.\end{aligned} \tag{4.74}$$

Now we add up Eqs. (4.71), (4.73) and the second line in (4.74) to obtain

$$\begin{aligned}\mathbf{F}^{\tilde{m},a+b+c}_{\text{bHQET}} = \frac{\alpha_s C_F\tilde{\mu}^{2\varepsilon}}{2^{1-2\varepsilon}\pi^{1-\varepsilon}}\,\Gamma(\varepsilon)\Bigg\{&\int_0^{\infty}\frac{\mathrm{d}l^+}{l^+}\left[\left[\tilde{m}^2+\frac{Q^2}{M^2}\left(l^+\right)^2\right]^{-\varepsilon} - \left[\tilde{m}^2+\frac{M^2}{Q^2}\left(l^+\right)^2\right]^{-\varepsilon}\right] \\ &- \left[\tilde{m}^2\right]^{-\varepsilon}\int_{-\infty}^{\infty}\frac{\mathrm{d}l^+}{l^+ + i0}\Bigg\},\end{aligned} \tag{4.75}$$

where we also reversed the sign of the plus loop momentum $l^+ \to -l^+$ in the first integral. To solve the integral in the first line we can use an analytic regulator, modifying the exponent of l^+ in the denominator, that is through a rapidity regulation: $l^+ \to (l^+)^{1+\Upsilon}$. The integral in the last line can be carried out using the Cauchy principal value prescription $\frac{1}{l^+ + i0} = \text{P.V.}\left(\frac{1}{l^+}\right) - i\pi\delta(l^+)$. After taking $\Upsilon \to 0$ the contribution from the collinear and soft diagrams results in

$$\mathbf{F}^{\tilde{m},a+b+c}_{\text{bHQET}} = \frac{\alpha_s C_F\tilde{\mu}^{2\varepsilon}}{2^{1-2\varepsilon}\pi^{1-\varepsilon}}\,\Gamma(\varepsilon)\left[\tilde{m}^2\right]^{-\varepsilon}\log\left(\frac{M^2}{-Q^2}\right). \tag{4.76}$$

On-shell wave function renormalization constant

In Fig. 4.7 we show the 1-loop Feynman diagrams for bHQET quark self-energy due to a massive gluon, which is the same as in HQET. The diagram on the right gives just the constant term $i\Delta M$ that will not contribute to the on-shell wave function renormalization constant since it does not depend on the off-shellness [see Eq. (4.19)]. For the left one, we obtain the same as in Eq. (4.18):

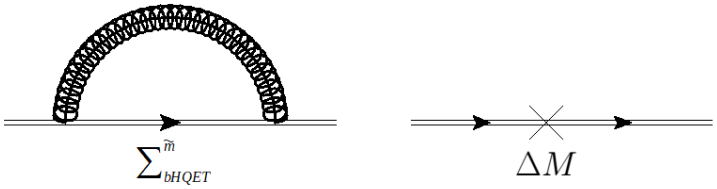

Figure 4.7: One loop massive gluon bHQET quark self-energy

$$\begin{aligned}\Sigma^{\tilde{m}}_{\text{bHQET}} &= -\,4\pi\alpha_s C_F\tilde{\mu}^{2\varepsilon}\int\frac{\mathrm{d}^d l}{(2\pi)^d}\frac{1}{[l^2-\tilde{m}^2+i0]\,[v\cdot(k+l)+i0]} \\ &= -\,i\frac{\alpha_s C_F\tilde{\mu}^{2\varepsilon}}{2^{1-2\varepsilon}\pi^{1-\varepsilon}}\frac{\Gamma(\varepsilon)}{2\varepsilon-1}\left(\frac{-\Delta^2}{2M}\right)^{1-2\varepsilon}{}_2F_1\left(\varepsilon-\frac{1}{2},\varepsilon;\varepsilon+\frac{1}{2};1-\tilde{m}^2\left(\frac{2M}{-\Delta^2}\right)^2\right),\end{aligned} \tag{4.77}$$

but where now $v\cdot k \equiv \frac{\Delta^2}{2M}$ was defined with Δ^2 the quark off-shellness. Therefore, the value for the wave function renormalization constant given by the on-shell condition is:

$$\left(Z^{\mathrm{OS},\tilde{m}}_{\psi,\mathrm{bHQET}}\right)^{1-\mathrm{loop}} = i2M\left[\frac{\mathrm{d}}{\mathrm{d}\Delta^2}\Sigma^{\tilde{m}}_{\mathrm{bHQET}}\right]_{\Delta^2\to 0} = \frac{\alpha_s C_F \tilde{\mu}^{2\varepsilon}}{2^{1-2\varepsilon}\pi^{1-\varepsilon}}\Gamma(\varepsilon)\left[\tilde{m}^2\right]^{-\varepsilon}\,. \tag{4.78}$$

From the sum of the previous equation with Eq. (4.76) we get the one loop bHQET form factor with a massive gluon

$$\mathbf{F}^{\tilde{m}}_{\mathrm{bHQET}} = \frac{\alpha_s C_F \tilde{\mu}^{2\varepsilon}}{2^{1-2\varepsilon}\pi^{1-\varepsilon}}\,\Gamma(\varepsilon)\left[\tilde{m}^2\right]^{-\varepsilon}\left[1+\log\left(\frac{M^2}{-Q^2}\right)\right]. \tag{4.79}$$

4.4.2 Final result

After taking the ratio of form factors, which at one loop is simply the difference between both $\mathcal{O}(\alpha_s)$ terms, and carrying out the dispersive integral, we must add back the subtracted $\Pi_0(m^2)$ term as in Eq. (4.62) to account for α_s renormalization in the $\overline{\mathrm{MS}}$ scheme. After this process, we find that UV divergences agree with the ones corresponding to the massless quark bubble color structure of the results obtained in Ref. [40].[12]

Squaring the renormalized matching result, that leads simply to a factor of two for the bubble part, the corrections to the bHQET hard function due to the mass of the secondary quark can be written as

$$H_M^{(n_\ell+1)}\left(M,\frac{Q}{M},\mu,m\right) = H_M^{(n_\ell+1)}\left(M,\frac{Q}{M},\mu\right) + \delta H_M\left(\frac{m}{M}\right), \tag{4.80}$$

with $H_M^{(n_\ell+1)}\left(M,\frac{Q}{M},\mu\right) \equiv \left|C_M^{(n_\ell+1)}\left(M,\frac{Q}{M},\mu\right)\right|^2$, the secondary massless quark result computed in Ref. [40], and the mass correction

$$\begin{aligned}\delta H_M\left(\frac{m}{M}\right) = \frac{\alpha_s^2 C_F T_F}{(4\pi)^2}\,2\Bigg\{&\frac{1747}{81}+\frac{52\pi^2}{27}+\left(\frac{532}{27}+\frac{16}{9}\pi^2\right)\hat{L}_m+\frac{104}{9}\hat{L}_m^2+\frac{32}{9}\hat{L}_m^3\\ &+\int_{4m^2}^{\infty}\mathrm{d}\tilde{m}^2\,\mathcal{V}^4\left[\frac{6-b^3-5b}{b(b+1)^2}\log\left(\frac{1-b}{2}\right)-\frac{b^3+5b+6}{(1-b)^2 b}\log\left(\frac{b+1}{2}\right)\right.\\ &\left.+\frac{b^2-25}{2\,(1-b^2)}+4\log\left(\frac{1-b}{2}\right)\log\left(\frac{b+1}{2}\right)\right]\Bigg\},\end{aligned} \tag{4.81}$$

where $\alpha_s \equiv \alpha_s^{(n_\ell+1)}$ and $\hat{L}_m \equiv \log\left(\frac{m}{M}\right)$.

Since the running of the hard function is just multiplicative and does not involve any distributions, the dispersive integral to be carried out in the second and third lines of the previous result does not require many numerical evaluations. Nevertheless, more efficient expressions for the whole correction will be achieved through the method developed in the next Chapter.

4.5 bHQET Variable Flavor Number Scheme

Unlike in Sec. 1.4.1, where the SCET VFNS was introduced focusing on the matrix elements participating in the factorization theorem,[13] in this Section we will present a similar discussion for bHQET

[12] These are not directly given for the divergences of the bHQET matching but for the $\overline{\mathrm{MS}}$ renormalization constants of the form factors so, in order to make the comparison, their difference must be taken.

[13] This is how it was first proposed in Ref. [56].

from the point of view of the operators appearing in the corresponding EFTs. This approach is more transparent and theoretically based on more solid grounds. As a consequence, the main object of study will be the factorization theorem building blocks, that is, the currents, whose definitions are given in Eqs. (1.9), (1.43) and (1.64) for QCD, SCET and bHQET respectively.

Let us start by the secondary massless quark case. The chain of EFTs needed is sketched in Fig. 4.8.

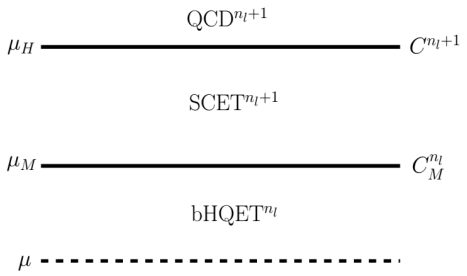

Figure 4.8: Sequence of EFTs for bHQET computations with massless secondary quarks. The horizontal lines signal energy scales, as marked on its left, and delimit the regions of validity of the various EFTs. We also show to the right of each line the matching coefficient necessary to relate two consecutive EFTs.

Since the goal is computing an observable within the bHQET framework, we need the corresponding renormalized quark current operator at the scale μ inside the theory regime.[14] Since the EFT is designed to reproduce the infrared behavior of the full theory, in order to account for the high-energy effects not accounted for in the EFT, matching onto the theory above (SCET) is necessary. The SCET-bHQET matching takes place at scale μ_M whose associated natural scale is the primary quark mass M.[15] Therefore, even though the calculation of the coefficient is carried out as the ratio of form factors in fixed-order perturbation theory, we evolve the bHQET current to a smaller scale to avoid large logarithms in the jet and soft functions, leading to the following relation[16]

$$J^{n_\ell+1}_{\rm SCET}(\mu_M) = C^{n_\ell}_M(\mu_M)\, U^{n_\ell}_{J_{\rm bHQET}}(\mu_M \leftarrow \mu)\, J^{n_\ell}_{\rm bHQET}(\mu)\,, \tag{4.82}$$

with $J^n_{\rm SCET}$ ($J^n_{\rm bHQET}$) the SCET (bHQET) dijet current operator with n active flavors. One can repeat the procedure for the SCET current at the full theory (QCD) boundary μ_H close to the center of mass energy Q

$$\mathcal{J}^{n_\ell+1}_{\rm QCD} = C^{n_\ell+1}(\mu_H)\, U^{n_\ell+1}_{J_{\rm SCET}}(\mu_H \leftarrow \mu_M)\, J^{n_\ell+1}_{\rm SCET}(\mu_M)\,. \tag{4.83}$$

It is worth mentioning that, since the primary quark mass is an infrared scale in both theories, the coefficient $C^{n_\ell+1}$ cannot depend on this parameter and only leading-order power corrections in M/Q are accounted within SCET. All in all, the starting point for the factorization theorem is:

$$\mathcal{J}^{n_\ell+1}_{\rm QCD} = C^{n_\ell+1}(\mu_H)\, U^{n_\ell+1}_{J_{\rm SCET}}(\mu_H \leftarrow \mu_M)\, C^{n_\ell}_M(\mu_M)\, U^{n_\ell}_{J_{\rm bHQET}}(\mu_M \leftarrow \mu)\, J^{n_\ell}_{\rm bHQET}(\mu)\,. \tag{4.84}$$

[14] The scheme used for the renormalization of the currents is the $\overline{\rm MS}$.

[15] The renormalization scale μ_M should not be confused with $\mu_{\mathbb{M}}$, used in Sec. 1.4.1 to denote the renormalization scale of a general matrix element $\mathbb{M}$.

[16] In this section, to alleviate the notation we only account for a superscript indicating the number of active flavors. Notice that in bHQET the primary quark is not an active flavor anymore.

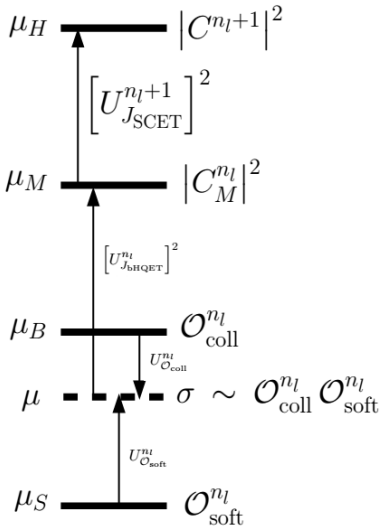

Figure 4.9: bHQET factorization theorem from the point of view of EFTs and operators.

From the previous equation, the factorization theorem is obtained by splitting the square of the bHQET current, with the insertion of the measurement delta in the theory limit, into the collinear and soft operators, whose vacuum expectation values constitute the jet and soft functions respectively

$$B(e,\mu) \equiv \langle \mathcal{O}_{\rm coll} \rangle \ , \qquad S(e,\mu) \equiv \langle \mathcal{O}_{\rm soft} \rangle \ . \tag{4.85}$$

The last step is evolving these operators to a renormalization scale close to their natural scales using the corresponding RGE equations. The setup just described for the bHQET factorization theorem with massless secondary quark is depicted in Fig. 4.9. It is completely equivalent to the one already presented in Fig. 1.8 for the matrix elements and can be argued from the fact that the QCD current operator does not depend on any renormalization scale. This implies the evolution of the matching coefficients is reversed with respect to the one for the currents. This setup, from the point of view of both operators and matrix elements, is sketched in Fig. 4.10.

Next we analyze the situation of a non-vanishing secondary quark mass m within the bHQET regime. If $Q > M > m$ one can choose a common μ larger than the renormalization scale associated to the secondary mass μ_m, we just need to consider the same EFTs setup as before but changing a light active flavor to a heavy one. The matching onto SCET is:

$$J^{n_\ell+2}_{\rm SCET}(\mu_M) = C^{n_\ell+1}_M(\mu_M, m)\, U^{n_\ell+1}_{J_{\rm bHQET}}(\mu_M \leftarrow \mu)\, J^{n_\ell+1}_{\rm bHQET}(\mu)\,, \tag{4.86}$$

where we also kept a residual dependence on the the secondary mass, even though it is an infrared scale in both theories and should not appear in matching coefficients, because this class of power corrections in m/M can be consistently incorporated in the EFT framework and makes the transition between scenarios smooth. However, its effects are not included at the QCD-SCET boundary matching since

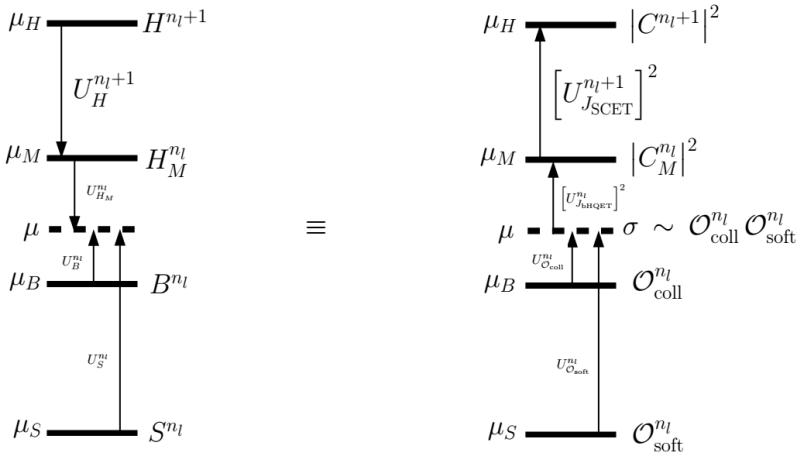

Figure 4.10: Equivalence between the bHQET matrix element setup introduced in Sec. 1.4.1 (left panel) and the corresponding EFTs operators approach followed in this section (right panel).

there is no consistent way of treating them in the presence of primary quark masses[17] so the coefficient will be identical to that in Eq. (4.83) but with the corresponding number of active flavors

$$\mathcal{J}_{\rm QCD}^{n_\ell+2} = C^{n_\ell+2}(\mu_H)\, U_{J_{\rm SCET}}^{n_\ell+2}(\mu_H \leftarrow \mu_M)\, J_{\rm SCET}^{n_\ell+2}(\mu_M)\,. \tag{4.87}$$

On the other hand, below μ_m the secondary quark must be integrated out, leading to bHQET$^{n_\ell}$. The bHQET current operators with $n_\ell+1$ and n_ℓ flavors are connected through the flavor matching condition

$$J_{\rm bHQET}^{n_\ell+1}(\mu_m) \equiv \mathcal{M}_{\rm bHQET}(\mu_m)\, J_{\rm bHQET}^{n_\ell}(\mu_m)\,, \tag{4.88}$$

which can be computed as the ratio of form factors in both theories in the limit at which both should be valid, that is, taking $m \to \infty$ (we suppress the dependence of the currents and matrix elements on the renormalization scale μ_m):

$$\mathcal{M}_{\rm bHQET} = \lim_{m\to\infty} \frac{\langle q,\overline{q}\,|\, J_{\rm bHQET}^{n_\ell+1}\,|0\rangle}{\langle q,\overline{q}\,|\, J_{\rm bHQET}^{n_\ell}\,|0\rangle} \equiv \lim_{m\to\infty} \frac{\mathbf{F}_{\rm bHQET^{n_\ell+1}}}{\mathbf{F}_{\rm bHQET^{n_\ell}}} \equiv 1 + \lim_{m\to\infty} \Big[\mathbf{F}_{\rm bHQET_{m-bubble}}^{n_\ell}\Big]_{\rm ren}\,. \tag{4.89}$$

In the previous equation we defined $\mathbf{F}_{\rm bHQET_{m-bubble}}^{n_\ell}$ as the contribution to the bHQET form factor from the secondary massive quark bubble expressed as a power series in $\alpha_s^{(n_\ell)}$, which reads:

$$\mathbf{F}_{\rm bHQET_{m-bubble}}^{n_\ell} = T_F \frac{\alpha_s}{4\pi} \int_{4m^2}^{\infty} \mathrm{d}\tilde{m}^2\; \mathcal{V}^{4-2\varepsilon} \mathbf{F}_{\rm bHQET}^{\tilde{m}} + \Big[\Pi_0(m^2) + \frac{\alpha_s T_F}{3\pi}\left(\frac{1}{\varepsilon} + \log\Big(\frac{\mu^2}{m^2}\Big)\right)\Big] \mathbf{F}_{\rm bHQET}^{\tilde{m}=0}\,, \tag{4.90}$$

where the last term comes from the $\overline{\rm MS}$ renormalization of α_s [see Eq. (4.62)] and from the strong coupling threshold condition $\alpha_s^{(n_\ell+1)}(\mu) = \alpha_s^{(n_\ell)}(\mu)\Big[1 + \frac{\alpha_s^{(n_\ell)}(\mu) T_F}{3\pi} \log\Big(\frac{\mu^2}{m^2}\Big)\Big]$. The term within square

[17] Recall that primary quark mass effects are not taken into account either, since there is no consistent way of treating them within the leading-power factorization theorem. Hence, we are strictly working at leading power in M/Q and m/Q.

brackets in Eq. (4.90) is $\mathcal{O}(\varepsilon)$ such that only the divergences in $\mathbf{F}^{\tilde{m}=0}_{\text{bHQET}}$ contribute (and coincide with those of $\mathbf{F}^{\tilde{m}}_{\text{bHQET}}$ since they do not depend on infrared scales). All in all, we can introduce Eq. (4.79) into the previous expressions to obtain the bHQET flavor matching

$$\mathcal{M}_{\text{bHQET}} = 1 + \frac{\alpha_s^2 C_F T_F}{(4\pi)^2}\,\frac{16}{27}\left[9\log^2\left(\frac{m}{\mu}\right) + 15\log\left(\frac{m}{\mu}\right) + 7\right]\left[1 - \log\left(-\frac{Q^2}{M^2}\right)\right], \tag{4.91}$$

with $\alpha_s \equiv \alpha_s^{(n_\ell)}$. The two different EFTs setups discussed for the massive secondary quark are summarized in Fig. 4.11.

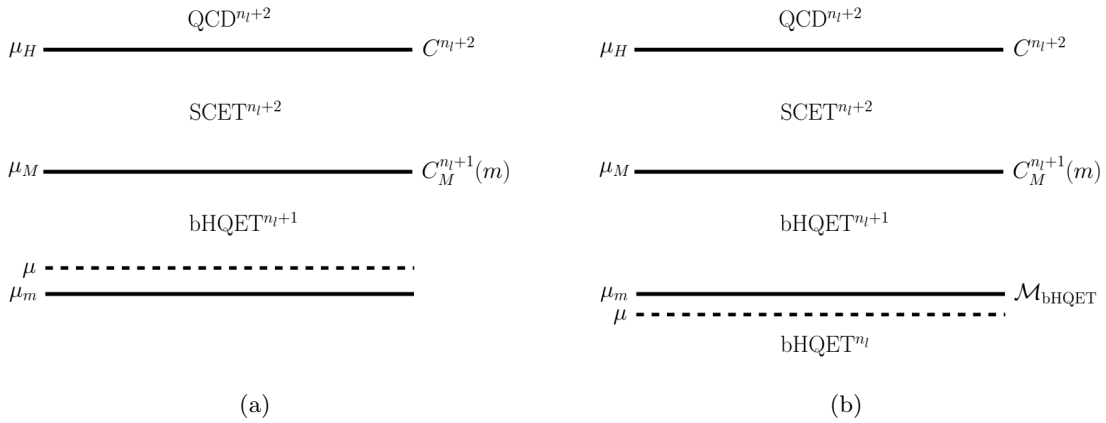

Figure 4.11: Same as Fig. 4.8 accounting for massive secondary quarks. In this case there are two different possibilities, depending on the hierarchy between μ_m and μ.

Once the factorization theorem is set up at the scale μ for the calculation of the observable, the operators $\mathcal{O}_{\text{coll}}$ and $\mathcal{O}_{\text{soft}}$ must be evolved from their natural scales (as explained before) to avoid the presence of large logarithms. The evolution will sum up those to all orders in perturbation theory. Nevertheless, depending on the choice for the common renormalization scale μ and the value of the natural scale, some threshold might be crossed in the jet or soft evolution, and therefore one needs to take into account the μ_m boundary conditions in the corresponding functions. The connection between these operators in both theories is also written as a flavor matching coefficient which can be computed through the ratio between the two vacuum expectation values[18]

$$\begin{aligned} \mathcal{O}^{n_\ell}_{\text{coll}} &= \mathcal{M}_B\,\mathcal{O}^{n_\ell+1}_{\text{coll}}\,, & \mathcal{M}_B &= \lim_{m\to\infty}\frac{\langle\mathcal{O}^{n_\ell}_{\text{coll}}\rangle}{\langle\mathcal{O}^{n_\ell+1}_{\text{coll}}\rangle} = \lim_{m\to\infty}\frac{B^{n_\ell}}{B^{n_\ell+1}}\,, \\ \mathcal{O}^{n_\ell+1}_{\text{soft}} &= \mathcal{M}_S\,\mathcal{O}^{n_\ell}_{\text{soft}}\,, & \mathcal{M}_S &= \lim_{m\to\infty}\frac{\langle\mathcal{O}^{n_\ell+1}_{\text{soft}}\rangle}{\langle\mathcal{O}^{n_\ell}_{\text{soft}}\rangle} = \lim_{m\to\infty}\frac{S^{n_\ell+1}}{S^{n_\ell}}\,. \end{aligned} \tag{4.92}$$

[18] We oversimplified here the notation for the sake of a clearer argumentation: The flavor matching for collinear and soft operators actually involves a convolution, so the ratio actually refers to the convolution with the inverse function.

The result for $\mathcal{M}_S$ is already known from Ref. [56][19] whereas for $\mathcal{M}_B$ we have, in analogy to Eqs. (4.89) and (4.90):[20]

$$\mathcal{M}_B = \delta(\hat{s}) - \lim_{m\to\infty} \left[B^{n_\ell}_{m-\text{bubble}}\right]_{\text{ren}} , \tag{4.93}$$

$$B^{n_\ell}_{m-\text{bubble}} = T_F \frac{\alpha_s}{2\pi} \int_{4m^2}^{\infty} \mathrm{d}\tilde{m}^2 \; \mathcal{V}^{4-2\varepsilon} B_n^{\alpha_s}(\hat{s},\mu,\tilde{m}) + \left[\Pi_0(m^2) + \frac{\alpha_s T_F}{3\pi}\left(\frac{1}{\varepsilon} + \log\left(\frac{\mu^2}{m^2}\right)\right)\right] 2B_n^{\alpha_s}(\hat{s},\mu)\,,$$

therefore we can use the previous equation together with Eqs. (4.54) and (4.58) to obtain the result. In addition, given that the real radiation term δB_m^{real} vanishes when taking the $m \to 0$ limit (due to the Heaviside theta), the collinear flavor matching can be expressed as

$$\mathcal{M}_B = \delta(\hat{s}) - \; B_\tau^{n_f=1} - \delta B_m^{\text{dist}} - \left[\frac{\alpha_s T_F}{3\pi} \log\left(\frac{\mu^2}{m^2}\right) 2B_n^{\alpha_s}(\hat{s},\mu)\right]_{\text{ren}} , \tag{4.94}$$

such that we can also introduce Eq. (4.58), the corresponding part of Eq. (4.63) and the value for $B_\tau^{n_f=1}$ provided in Ref. [42] into this formula to get the same result, which reads

$$\begin{aligned}\mathcal{M}_B = \delta(\hat{s}) + \frac{\alpha_s^2 C_F T_F}{(4\pi)^2 M}\, 2 \Bigg\{ \Bigg[&-\frac{32}{9}L_m^3 - \frac{128}{9}L_m^2 + \left(\frac{4\pi^2}{9} - \frac{688}{27}\right) L_m - \frac{440}{27} \\ &+ \frac{5\pi^2}{27} + \frac{28}{9}\xi_3 \Bigg] \delta(\hat{s}) + \left(\frac{32}{3}L_m^2 + \frac{160}{9}L_m + \frac{224}{27}\right) \mathcal{L}^0(\hat{s}) \Bigg\} .\end{aligned} \tag{4.95}$$

What determines all the various running possibilities given in the bHQET factorization theorem with secondary massive quarks is the hierarchy between the jet and soft scales with respect to μ_m, together with the choice of the common renormalization scale μ. They can be organized in different scenarios leading to the matrix elements setups shown in Figs. 4.12, 4.13 and 4.14. No matter what the hierarchy between μ_m and the soft/jet scales is, μ can take any value (in Fig. 4.11 we picked the most physical choice, but this is not unique). The equivalence between $\mu > \mu_m$ and $\mu < \mu_m$ within the same scenario gives the consistency conditions for the flavor matching conditions: $\mathcal{M}_S = |\mathcal{M}_{\text{bHQET}}|^2 \mathcal{M}_B$, which is indeed satisfied by Eqs. (4.91), (4.95) and the result for $\mathcal{M}_S$ provided in Ref. [56].

It is also worth mentioning that, in order to achieve a smooth transition between the different scenarios, the effects of the secondary quark mass that vanish in the decoupling limit must be kept in the computations within bHQET$^{n_\ell}$ as was done e.g. in Eq. (1.56).

4.6 Numerical results

In this section we present some phenomenological studies based on the numerical implementation of the computations carried out for the bHQET cross-section at N^{3}LL + $\mathcal{O}(\alpha_s^2)$ with massive secondary quarks. The cross section has been constructed following the procedure described in Ref. [3], where all the massless ingredients at that order are provided, to which we add the corrections discussed in this Chapter. Since the bottom mass appears for the first time at two loops, it can be considered in the pole or $\overline{\text{MS}}$ schemes. In these preliminary studies we also choose the pole mass for the top quark mass. The various plots that show the effect of the secondary bottom mass consider an unstable top

[19] Recall that the SCET and bHQET soft functions are equivalent (up to diagrams with primary quark loops) since both theories agree in the infrared. Furthermore, we choose the definitions of the respective flavor matching conditions in opposite directions for the jet and soft functions, such that they coincide with the ones given in Ref. [56].

[20] With an additional factor of 2, coming from the convolution of the two hemisphere jet functions.

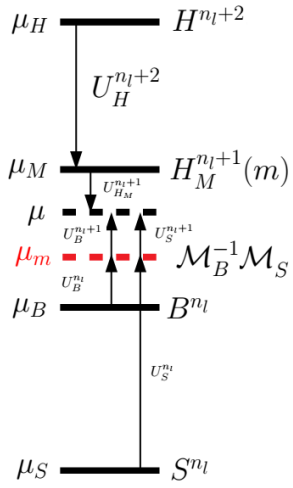

(a) $\mu > \mu_m$

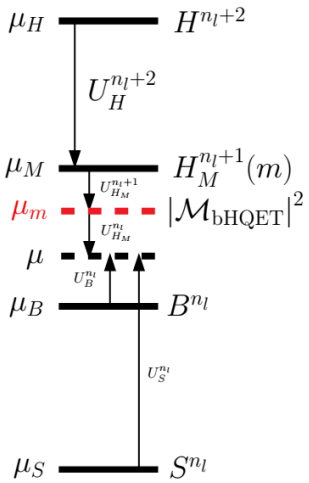

(b) $\mu < \mu_m$

Figure 4.12: bHQET factorization theorem setup with secondary mass. Scenario I.

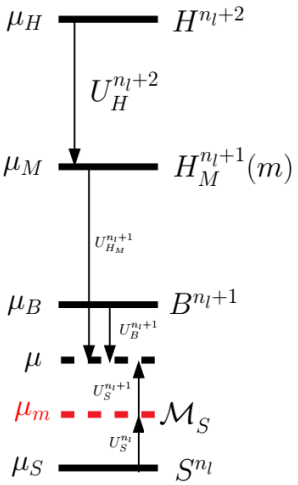

(a) $\mu > \mu_m$

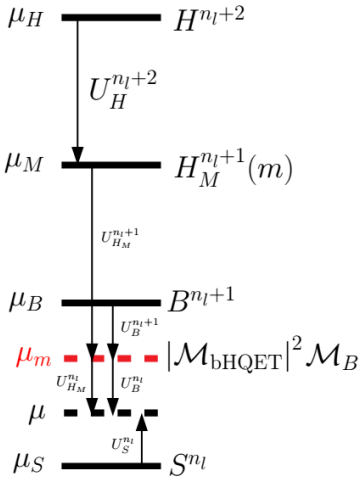

(b) $\mu < \mu_m$

Figure 4.13: bHQET factorization theorem setup with secondary mass. Scenario II.

quark thrust distribution with the standard values of the profile functions parameters. This configuration

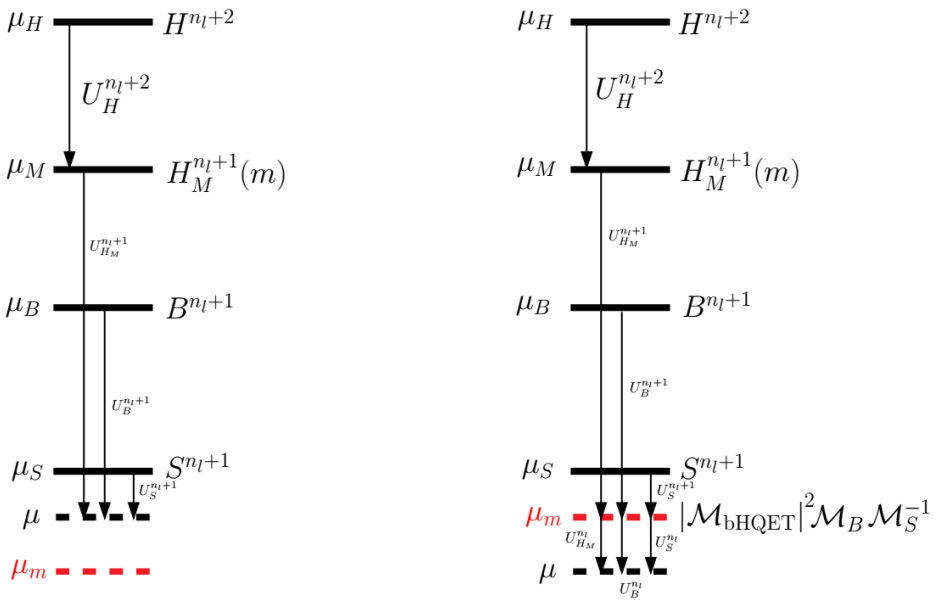

(a) $\mu > \mu_m$ (b) $\mu < \mu_m$

Figure 4.14: bHQET factorization theorem setup with secondary mass. Scenario III.

can be encompassed within scenario II throughout the peak region, which is the one we are interested in.

Our first analysis is shown in Fig. 4.15, where we compare the cases for a massless and a massive bottom quark, taking as input for the center-of-mass energy, top quark pole mass and top width the following values: $Q = 2000\,\text{GeV}$, $m_t = 170.034\,\text{GeV}$ and $\Gamma = 1.32\,\text{GeV}$.

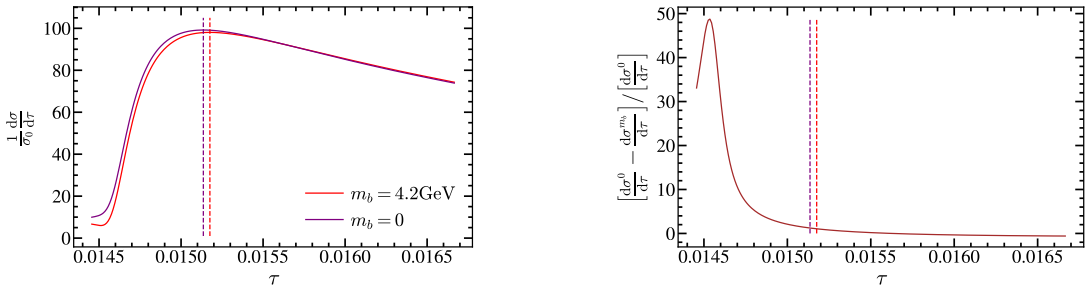

(a) Thrust distributions for massless and massive secondary quark

(b) Percentage of relative difference between massless and massive distributions.

Figure 4.15: Comparison of massive and massless bottom quark distributions for $Q = 2000\,\text{GeV}$, for unstable primary top quarks with $m_t = 170.034\,\text{GeV}$ and $\Gamma = 1.32\,\text{GeV}$. The peak positions are marked by dashed vertical lines in both panels.

In our second analysis, we scan over the bottom mass and analyze the dependence of the peak position for the corresponding distributions with this parameter, see Fig. 4.16, to get a taste of the impact it has on top mass determinations. The hemisphere jet mass associated to the thrust peak position is also indicated since it is more instructive for this purpose.

Finally, we repeat the analysis shown in Fig. 4.15 modifying one parameter at a time (COM energy, top mass or width) while the rest remain at default values. The results are shown in Fig. 4.17.

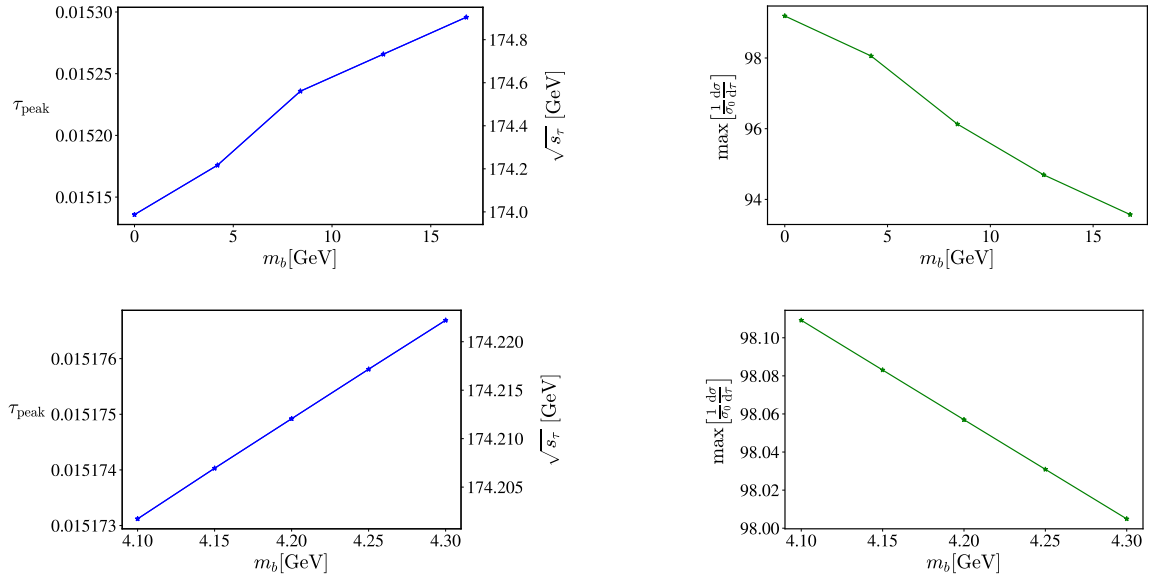

Figure 4.16: Peak position (left panels) and peak height (right panels) as a function of the bottom mass in GeV units. We also show the corresponding value for the hemisphere jet invariant mass $\sqrt{s_\tau}$.

4.7 Summary

The effects of a non-vanishing bottom quark mass must be taken into account in precise top quark mass determinations through the analysis of differential event-shape distributions in the peak region. Therefore, the goal of this Chapter has been including these corrections in the factorization theorem of bHQET, an EFT well suited to describe the process in this regime. We have computed the missing pieces: the massive quark bubble contribution to the hard and jet functions, and the threshold matching conditions. In order for that, we expressed its insertion in the gluon self-energy as an integral over the mass of an effective gluon propagator, also known as the dispersive integral method.

Before obtaining the necessary one-loop results with a massive gluon, we discussed the modification in the HQET Lagrangian due to the gluon mass. This was in fact an unknown feature of HQET, a theory that has been around for many decades now: massive gluons or secondary quarks require the addition of a quark bilinear term in the Lagrangian to keep the pole position of the propagator untouched. We have also cast the thrust jet function as the imaginary part of a forward-scattering matrix element, which facilitates the corresponding computation.

Once the matrix elements have been obtained, along with the flavor matching conditions for the hard,

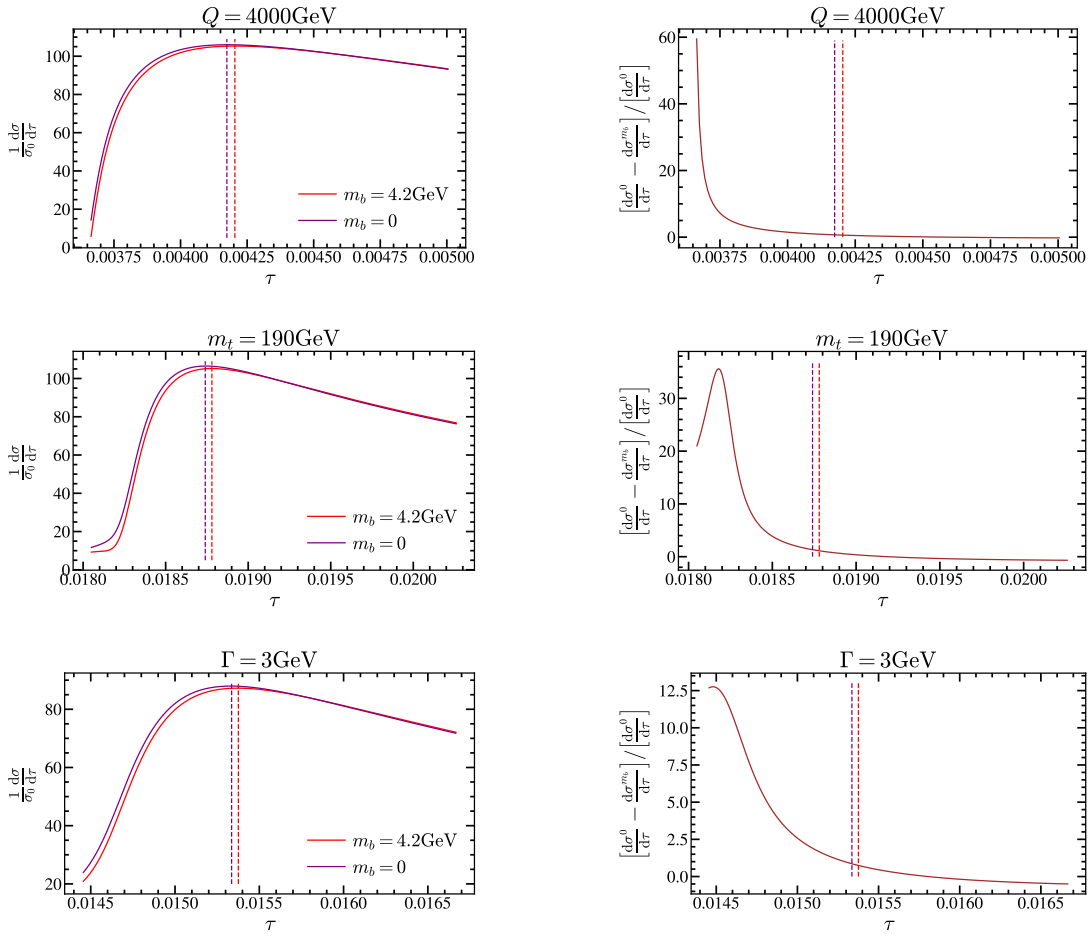

Figure 4.17: Same as Fig. 4.15 changing the value of a single parameter.

jet and soft functions, the various ingredients have been included in a numerical code in order to carry out phenomenological studies. The bottom mass contribution was added to complete the $\mathrm{N^3LL} + \mathcal{O}(\alpha_s^2)$ order of the thrust bHQET differential cross-section. The impact of these corrections has been presented through several illuminating plots.

Chapter 5

Mellin-Barnes for massive quark bubbles and massive bosons (Secondary massive quarks with the Mellin-Barnes expansion)

In Chapter 2 we used the Mellin-Barnes representation to expand the RG-evolved SCET jet function with massive primary quarks in a certain kinematic regime. In the previous Chapter we employed the dispersive integral method to compute the 2-loop secondary massive quark corrections to bHQET matrix elements. In this Chapter we combine both tools to obtain in a straightforward manner these 2-loop contributions in an expanded form. With minimal modifications, the same strategy can be also employed to compute the expansion of the 1-loop correction caused by an actual massive gauge boson. We will apply this method to a plethora of examples, in particular those relevant for factorized cross sections involving massless and massive jets, recovering previously known results and those derived for the first time in Chapter 3.

As already mentioned in Sec. 1.5, the use of Mellin-Barnes is widely extended in multi-loop calculations. The general idea is, for a given master integral, carry out all loop momenta integrals using Feynman parameters, apply the MB representation as many times as necessary, and after carrying out the remaining Feynman parameter integrals, employ the converse mapping theorem to obtain the result (which in the case of having the ratio of scales, can be an expansion in powers of a small parameter). On the contrary, in our procedure we will use the MB identity at a very early stage of the computation: right after expressing the massive polarization function in terms of an integral over a Feynman parameter x — keeping the exact dependence on $d = 4 - 2\varepsilon$ — but before any other loop integration is carried out. After applying the MB representation, the integration over x can be carried out trivially giving rise to gamma functions, such that only a single loop integral remains. This loop computation involves a modified (massless) gluon propagator which is exactly the same one employed in large-β_0 computations (that is, the denominator of the gluon propagator is raised to a non-integer power $1 - h$). This is convenient, since many existing results can be recycled, see e.g. Ref. [27].

Furthermore, one can apply the converse mapping theory after RG evolving the SCET and bHQET jet functions, such that easy-to-use expansions are obtained. An additional nice feature of this methodology is the fact that one does not really need to use any additional regulator beyond dimensional

regularization, since no rapidity divergence appears in any loop integral. Indeed, the Mellin variable h in the modified gluon propagator effectively acts as an analytic regulator which does not involve any additional energy scale. Moreover, 0-bin subtractions identically vanish.[1]

The downside of our method is that — unless some off-shellness is used — it cannot be applied to quantities afflicted by IR singularities at one-loop (with massless gluons), but it will turn out particularly good at computing matching coefficients between EFTs, since those are IR-safe. However, using consistency conditions we will be able to separate the QCD, SCET and bHQET pieces of the matching computations in all cases under study.

Finally, extracting the UV poles, taking $m \to 0$ or $m \to \infty$ limits, or figuring out the flavor matching condition between two consecutive EFTs is completely trivial in our method: these simply correspond to the residues of some poles close to the origin in the complex h plane.

5.1 Massive Quark Vacuum Polarization Function

We begin by obtaining the MB representation of the bubble insertion into the gluon self-energy that we already studied in Sec. 4.1. This can be done using the Mellin identity [Eq. (1.71)] in Eq. (4.11), which leads to

$$\begin{aligned}\Pi^{\text{OS}}(p^2,m,\mu) &= \frac{\alpha_s(\mu)}{\pi} T_F \left(\frac{\mu^2 e^{\gamma_E}}{m^2}\right)^{\varepsilon} \int_{c-i\infty}^{c+i\infty} \frac{\mathrm{d}h}{2\pi i} \left(-\frac{m^2}{p^2}\right)^{-h} G(h,\varepsilon)\,, \\ G(h,\varepsilon) &= \frac{\Gamma(h)\Gamma(1-h)\Gamma(2+h)\Gamma(h+\varepsilon)}{(3+2h)\Gamma(2h+2)}\,.\end{aligned} \tag{5.1}$$

Since, as already discussed, the method can only be applied to IR-finite quantities, $\varepsilon > 0$ in order to regulate UV divergences, hence the fundamental strip is $0 < c < 1$. From Eq. (5.1) one can read the form of the "effective" gluon propagator which will yield the MB representation from a 1-loop computation: the insertion of $\Pi^{\text{OS}}(p^2,m,\mu)/(-p^2)$ in the MB representation modifies the denominator of the gluon propagator from $(-p^2)$ to $(-p^2)^{1-h}$ and adds an overall factor.

Our expansions will become useful to compute the matching between two consecutive EFTs, one in which the secondary massive quarks are dynamic, another one in which they are not, as in Sec. 4.5. Recall that, in order to compute the matching condition we need to relate the strong coupling in the two EFTs which can be done using directly $\Pi_0^{\overline{\text{MS}}}(m^2)$ [see the definition of this quantity in Eq. (4.5)], getting:

$$\alpha_s^{(n_f+1)}(\mu) = \alpha_s^{(n_f)}(\mu)\left[1 + \frac{\alpha_s^{(n_f)}(\mu) T_F}{3\pi} \log\left(\frac{\mu^2}{m^2}\right)\right] + \mathcal{O}(\alpha_s^3) \equiv \alpha_s^{(n_f)}(\mu)\big(1+\delta_\alpha^{(n_f)}\big)\,. \tag{5.2}$$

Indeed one has that

$$\Pi_0^{\overline{\text{MS}}}(m,\mu) + \delta_\alpha = -\frac{T_F \varepsilon}{6}\frac{\alpha_s(\mu)}{\pi}\left[\log^2\left(\frac{\mu^2}{m^2}\right) + \frac{\pi^2}{6}\right] + \mathcal{O}(\varepsilon^2)\,. \tag{5.3}$$

Before discussing any further the computation of the 2-loop massive bubble diagrams, we apply the converse mapping theorem to $\Pi^{\text{OS}}(p^2,m^2)$, as it will serve as an illustration. Since the on-shell vacuum

[1] Depending on the quantity one wishes to compute, an off-shellness regulation might be necessary, but such regulator is not specific of computations with secondary masses and appears for massless quarks as well.

polarization function is UV finite, we can set $\varepsilon \to 0$ in Eq. (5.1).[2] The inverse mapping theorem is nothing less than closing the contour towards the positive or negative real axis and using the residue theorem together with Jordan's lemma, as we explained in Sec. 1.5. Moreover, we saw that to pick either side, we need to study the behavior of $G(h,0)$ for large h:

$$\lim_{h\to\infty}\left|G(h,0)\left(-\frac{m^2}{p^2}\right)^{-h}\right| = \frac{\pi^{3/2}\csc(\pi h)}{4h^{3/2}}\left(\frac{4m^2}{|p^2|}\right)^{-h}. \tag{5.4}$$

It is clear that for $|p^2| < 4m^2$ ($|p^2| > 4m^2$) the contour must be closed towards the positive (negative) real axis, resulting in an expansion for big (small) masses. This is exactly what one could have guessed from the analytic behavior of $\Pi(p^2, m^2)$: the distance from the origin of the p^2 complex plane to the branch point, which sets the convergence radius, is exactly $|p^2| = 4m^2$. For $|p^2| = 4m^2$ the contour can be closed on either side due to the damping factor $h^{3/2}$.

When closing towards $\mathrm{Re}(h) > 0$, simple poles will be found at positive integer values of $h = n$, hence no non-analytic terms will be present. This is expected, since for large m one is always below the branch cut of the vacuum polarization function. Each pole generates a term in the power expansion for large m, namely $(-p^2/m^2)^n$ with $n \geq 1$ such that $\Pi^{\mathrm{OS}}(0, m, \mu) = 0$.

On the other hand, when closing towards $\mathrm{Re}(h) < 0$ one finds double poles at all negative integer values of $h = -n$, except for $h = -1$ where the pole is simple. Logarithms are expected since, for small m and positive p^2, an imaginary part should appear. Each pole generates a term in the power expansion for small m, namely $(-m^2/p^2)^n$. Double poles generate a power of $\log(-p^2/m^2)$, whereas simple poles do not. The expansions read

$$\begin{aligned}\Pi^{\mathrm{OS}}(p^2, m, \mu) =& -\frac{\alpha_s(\mu)}{\pi}T_F\sum_{n=1}^{\infty}\frac{(n-1)!(n+1)!}{(2n+3)(2n+1)!}\left(\frac{p^2}{m^2}\right)^n \\ =&\frac{T_F\alpha_s}{\pi}\left\{\frac{1}{3}\log\left(-\frac{p^2}{m^2}\right)-\frac{5}{9}-\frac{2m^2}{p^2}+2\sum_{n=2}\left(\frac{m^2}{p^2}\right)^n\frac{(2n-2)!}{(2n-3)n!(n-2)!}\right. \\ &\left.\times\left[2(H_{2n-4}-H_{n-1})-\log\left(-\frac{p^2}{m^2}\right)+\frac{n+1}{(n-1)n}\right]\right\},\end{aligned} \tag{5.5}$$

where $H_i = \sum_{n=1}^{i} n^{-1}$ is the harmonic number. The first series can be summed up analytically and we obtain the well-known result

$$\Pi^{\mathrm{OS}}(p^2, m, \mu) = \frac{\alpha_s(\mu)}{\pi}\frac{T_F m^2}{9p^2}\left[6\sqrt{\frac{p^2-4m^2}{p^2}}\left(2+\frac{p^2}{m^2}\right)\log\left(\frac{\sqrt{4m^2-p^2}+\sqrt{-p^2}}{2m}\right)-12-\frac{5p^2}{m^2}\right]. \tag{5.6}$$

The vacuum polarization function diverges at $p^2 \to +\infty$, which is nothing less than the massless limit, not well defined due to the OS subtraction. We compare the exact form to both expansions in Fig. 5.1 where it can be seen that both series can be used at $p^2 = -4m^2$. We observe an oscillatory behavior of the large-mass expansion.

[2] If keeping a non-zero ε, the UV-finiteness is transparent when closing towards $\mathrm{Re}(h) \to +\infty$. When closing towards $\mathrm{Re}(h) \to -\infty$ the poles at $h = 0$ and $h = -\varepsilon$ generate $1/\varepsilon$ singularities which however cancel when both terms are added up.

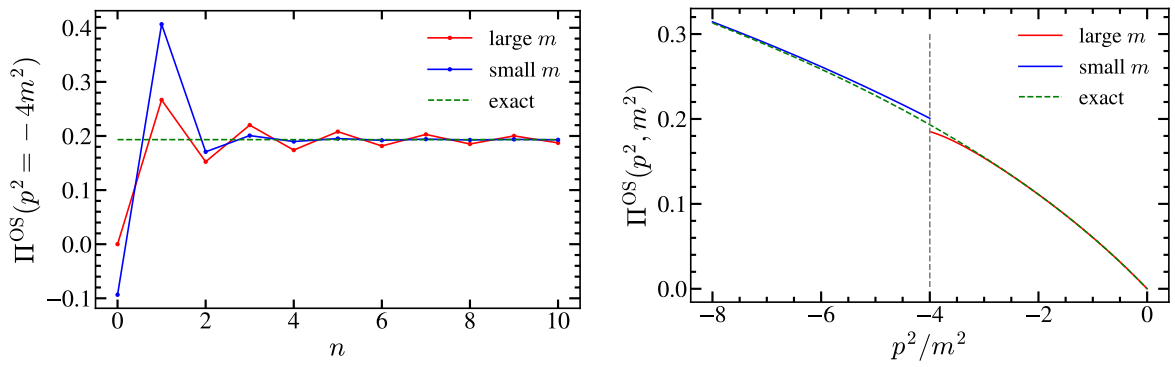

(a) (b)

Figure 5.1: On-shell subtracted vacuum polarization function for a massive quark measured in units of $\alpha_s(\mu)T_F/\pi$ in its exact form (dashed green), small- (blue) and large-mass (red) expansions. Left panel: $\Pi^{\rm OS}$ at the boundary between the mass expansions $p^2 = -4m^2$, as a function of the expansion order n of each series. Right panel: Dependence of $\Pi^{\rm OS}(p^2, m^2)$ with the ratio p^2/m^2 including 4 and 8 non-zero terms in the small- and large-mass expansions, respectively.

5.2 One-loop with a Massive Vector Boson

Before we discuss in detail the two-loop contribution from a secondary massive quark bubble, we pause to describe how the MB representation can be applied to generate large and small mass expansions to one-loop computations involving a massive vector boson. For simplicity, we consider a gluon with a non-zero mass m_g, but the method can be generalized to other massive mediators. In this case, one simply uses the MB identity Eq. (1.71) directly into the massive gluon propagator

$$\frac{1}{-p^2+m_g^2} = \frac{1}{-p^2}\int_{c-i\infty}^{c+i\infty}\frac{\mathrm{d}h}{2\pi i}\left(-\frac{m_g^2}{p^2}\right)^{-h}\Gamma(h)\Gamma(1-h)\,, \tag{5.7}$$

where the fundamental branch is $0 < c < 1$. This result again implies that for obtaining the Mellin representation one modifies the gluon propagator shifting the power of its denominator in exactly the same way, $(-p^2)$ to $(-p^2)^{1-h}$, and multiplies by the factor $\Gamma(h)\Gamma(1-h) = \pi\csc(\pi h)$ which changes sign under $h \to -h$. Let us assume that our matrix element is dimensionless: then, the 1-loop computation with a massless gluon whose propagator has been "shifted", and where $d = 4 - 2\varepsilon$ has been kept unexpanded, can be written as

$$M_1^h(\mathcal{Q}) = \frac{g_s^2 C_F}{4\pi^2}\mathcal{Q}^{2h}\left(\frac{\mu^2\varepsilon^{\gamma_E}}{\mathcal{Q}^2}\right)^{\varepsilon} m_1^h(\varepsilon)\,, \tag{5.8}$$

where $\mathcal{Q}$, with mass-dimension 1, is the only scale in the matrix element we are computing — necessary to render the 1-loop result non-zero — and g_s is the bare strong coupling constant. The function $m_1^h(\varepsilon)$ is dimensionless and does not depend on $\mathcal{Q}$, while the prefactor $\mathcal{Q}^{2h}$ accounts for the overall dimension caused by the shifted gluon propagator. All in all, the one-loop result with a massive gluon takes the

following form:

$$
\begin{aligned}
M_1(m_g,\mathcal{Q},\mu,\varepsilon) &= \frac{\alpha_s(\mu)}{\pi} C_F F_1(m_g,\mathcal{Q},\varepsilon)\,, \\
F_1(m_g,\mathcal{Q},\mu,\varepsilon) &= \left(\frac{\mu^2\varepsilon^{\gamma_E}}{\mathcal{Q}^2}\right)^{\varepsilon}\int_{c-i\infty}^{c+i\infty}\frac{\mathrm{d}h}{2\pi i}\mathcal{M}_1\!\left(h,\varepsilon,\frac{m_g}{\mathcal{Q}}\right), \\
\mathcal{M}_1\!\left(h,\varepsilon,\frac{m_g}{\mathcal{Q}}\right) &= \left(\frac{\mathcal{Q}^2}{m_g^2}\right)^{h}\Gamma(h)\Gamma(1-h)m_1^h(\varepsilon)\,,
\end{aligned}
\tag{5.9}
$$

where, at this order, $\alpha_s(\mu)$ is already the renormalized strong coupling. We will use the notation $\mathcal{M}_1(h,\varepsilon,1)=\mathcal{M}_1(h,\varepsilon)$.

Let us discuss some generic features. The function $m_1^h(\varepsilon)$ can modify the fundamental strip, and whenever the matrix element needs renormalization (that is, when the 1-loop computation with an unmodified gluon propagator generates $1/\varepsilon^n$ poles), it gets narrowed down to $0<c<\varepsilon$. This is easy to understand: since the Mellin parameter h acts as a UV-regulator, UV poles manifest themselves as singularities of the type $1/(h-\varepsilon)^n$ with $n=2$ for quantities carrying a cusp anomalous dimension, $n=1$ otherwise.[3]

The massless result $F_1(0,\mathcal{Q},\varepsilon)$ is trivial to obtain: it corresponds to the $h=0$ pole's residue.[4] Since the massless limit is manifest, there will be no logarithms of $m_g/\mathcal{Q}$ in this limit. The poles at $h=0$ and $h=\varepsilon$ contain the same (m_g-independent) UV poles, but have different finite terms. Since the correction to the massless result $\Delta_0F_1(m_g/\mathcal{Q})\equiv F_1(m_g,\mathcal{Q},\mu,\varepsilon)-F_1(0,\mathcal{Q},\mu,\varepsilon)$ is UV finite —and μ-independent as well— we can "move" the fundamental strip to $-1/2<\mathrm{Re}(h)=e<0$ and set $\varepsilon\to 0$ to obtain a closed form:

$$
\Delta_0F_1\left(\frac{m_g}{\mathcal{Q}}\right)=\int_{e-i\infty}^{e+i\infty}\frac{\mathrm{d}h}{2\pi i}\left(\frac{\mathcal{Q}^2}{m_g^2}\right)^{h}\Gamma(h)\Gamma(1-h)m_1^h(0)\,. \tag{5.10}
$$

The $m_g\to\infty$ limit corresponds to minus the residue of the $h=\varepsilon$ pole, and since the decoupling limit is not manifest in the $\overline{\mathrm{MS}}$ scheme, it will contain powers of $\log(m_g/\mathcal{Q})$. The correction to this limit $\Delta_\infty F_1(m_g/\mathcal{Q})\equiv F_1(m_g,\mathcal{Q},\mu,\varepsilon)-F_1(m_g\to\infty,\mathcal{Q},\mu,\varepsilon)$ is also UV finite and μ-independent, and can be cast in the same way as Eq. (5.10) (that is, with $\varepsilon=0$) moving the fundamental strip to $0<\mathrm{Re}(h)<1$.

Finally, the difference of the $m_g\to\infty$ and $m_g\to 0$ limits $\Delta_0^\infty F_1(m_g/\mathcal{Q})\equiv F_1(m_g\to\infty,\mathcal{Q},\mu,\varepsilon)-F_1(0,\mathcal{Q},\mu,\varepsilon)$ is once more UV-finite and μ-independent, and equals the residue at $h=0$ obtained if ε is set to zero before computing the residue. This increases the pole's multiplicity, generating the expected logs of $m_g/\mathcal{Q}$.

We will consider the matching between two EFTs: the high-energy one, containing a massive and a massless gluon, and the low-energy one, with a massless gluon only. At 1-loop, the coupling in the two theories coincides, and since there are massless gluons in both, such contributions cancel in the matching. Since the two theories should yield the same answer in the $m_g\to\infty$ limit, the relevant quantity for the matching is

$$
[F_1(m_g\to\infty,\mathcal{Q},\varepsilon)]_{\mathrm{ren}}=[F_1(0,\mathcal{Q},\varepsilon)]_{\mathrm{ren}}+\Delta_0^\infty F_1(m_g/\mathcal{Q})\,, \tag{5.11}
$$

[3] It is not hard to deduce the poles' form. Let us assume a generic scalar 1-loop bubble containing a regular and a modified gluon propagator. The d-dimensional integration measure after Wick rotation is $\mathrm{d}^d\ell=\ell^{3-2\varepsilon}\mathrm{d}\Omega\mathrm{d}\ell$, while the product of propagator denominators behaves as ℓ^{4-2h}. When combined, one has $\ell^{-1+2(h-\varepsilon)}\mathrm{d}\Omega\mathrm{d}\ell$, which upon integration diverges like $1/(h-\varepsilon)$.

[4] One trivially gets $F_1(0,\mathcal{Q},\mu,\varepsilon)=\left(\frac{\mu^2\varepsilon^{\gamma_E}}{\mathcal{Q}^2}\right)^{\varepsilon}m_1^0(\varepsilon)$ from the converse mapping theorem or directly from Eq. (5.8).

where, since the matching is performed using renormalized matrix elements, the subscript "ren" has been added to signify that the $1/\varepsilon^n$ poles have been stripped away, that is renormalized in $\overline{\rm MS}$ scheme.[5]

5.3 Two-loop massive bubble

In this section we derive the general expression for the renormalized 2-loop matrix element due to the insertion of a massive bubble. On top of the dispersive integral, which we have written as an inverse Mellin transform, one has to account for the contribution due to $\Pi_0(m^2)$ and the strong coupling renormalization as in Eq. (4.62), which can be combined as a term proportional to $\Pi_0^{\overline{\rm MS}}(m^2)$.

When inserting the vacuum polarization into the gluon internal line, the contribution from Π_0 corresponds to the replacement $1/\ell^2 \to \Pi_0(m^2)/\ell^2$ in the gluon propagator. Since $\Pi_0(m^2)$ does not depend on the loop momentum ℓ, this contribution is proportional to the 1-loop result computed with a massless gluon propagator. The two-loop result can be then written as

$$
\begin{aligned}
M_2(m,\mathcal{Q},\mu,\varepsilon) &= \left[\frac{\alpha_s(\mu)}{\pi}\right]^2 C_F T_F F_2(m,\mathcal{Q},\mu,\varepsilon)\,, \qquad (5.12)\\
F_2(m,\mathcal{Q},\mu,\varepsilon) &= H_2(m,\mathcal{Q},\mu,\varepsilon) - \frac{1}{3}F_1(0,\mathcal{Q},\mu,\varepsilon)\left[\left(\frac{\mu^2 e^{\gamma_E}}{m^2}\right)^{\varepsilon}\Gamma(\varepsilon) - \frac{1}{\varepsilon}\right],\\
H_2(m,\mathcal{Q},\mu,\varepsilon) &= \left(\frac{\mu^2 e^{\gamma_E}}{\mathcal{Q}^2}\right)^{\varepsilon}\left(\frac{\mu^2 e^{\gamma_E}}{m^2}\right)^{\varepsilon}\int_{c-i\infty}^{c+i\infty}\frac{{\rm d}h}{2\pi i}\mathcal{M}_2\left(h,\varepsilon,\frac{m_g}{\mathcal{Q}}\right),\\
\mathcal{M}_2\left(h,\varepsilon,\frac{m_g}{\mathcal{Q}}\right) &= \left(\frac{\mathcal{Q}^2}{m^2}\right)^h G(h,\varepsilon) m_1^h(\varepsilon)\,.
\end{aligned}
$$

where $G(h,\varepsilon)$ has been given in the second line of Eq. (5.1). The coupling constant $\alpha_s(\mu)$ is already renormalized and runs with $n_f = n_\ell + 1$ active flavors, where n_ℓ is the number of massless quarks. We will refer to the term H_2 as the "dispersive contribution".

Let us again discuss some generic features. As argued in Sec. 5.2, $m_1^h(\varepsilon)$ narrows the fundamental strip to $0 < h < \varepsilon$ since single or double singularities appear at $h = \varepsilon$. We denote the second term in the second line of Eq. (5.12) as "the Π_0 contribution". The UV singularities are contained in the contribution from the pole at $h = \varepsilon$ for the large m expansion, and in the sum of residues of the poles located at $h = 0$ and $h = -\varepsilon$ for the small m expansion, to which one has to add the divergent terms coming from the Π_0 insertion. Once again, the divergences for the two expansions are m independent and coincide, but the finite remainders differ.

The massless result $F_2(0,\mathcal{Q},\varepsilon)$ can be obtained as the sum of the residues of poles at $h = 0$ and $h = -\varepsilon$ plus the Π_0 contribution. Since the massless limit is manifest, no logs of $m/\mathcal{Q}$ arise. The correction to the massless limit $\Delta_0 F_2(m/\mathcal{Q}) \equiv F_2(m,\mathcal{Q},\mu,\varepsilon) - F_2(0,\mathcal{Q},\mu,\varepsilon)$ is UV-finite, μ-independent, and can be obtained moving the fundamental strip to $-1/2 < {\rm Re}(h) < 0$:

$$
\Delta_0 F_2\left(\frac{m}{\mathcal{Q}}\right) = \int_{e-i\infty}^{e+i\infty}\frac{{\rm d}h}{2\pi i}\left(\frac{\mathcal{Q}^2}{m^2}\right)^h \frac{h(h+1)\Gamma^3(h)\Gamma(1-h)}{(3+2h)\Gamma(2h+2)} m_1^h(0)\,. \qquad (5.13)
$$

The $m \to \infty$ limit is simply the Π_0 contribution minus the residue at $h = \varepsilon$. Since the decoupling limit is not manifest in the $\overline{\rm MS}$ scheme, it will contain powers of $\log(m/\mathcal{Q})$. The correction to the decoupling

[5] In previous Chapters we used that label for renormalization in any scheme.

limit $\Delta_\infty F_2(m/\mathcal{Q}) \equiv F_2(m,\mathcal{Q},\mu,\varepsilon) - F_2(m\to\infty,\mathcal{Q},\mu,\varepsilon)$ is also UV-finite and μ-independent, and can be written as in Eq. (5.13) moving the fundamental strip to $0 < \mathrm{Re}(h) < 1$.

Subtracting the $m \to \infty$ and $m \to 0$ limits yields a UV-free and μ-independent quantity denoted as $\Delta_0^\infty F_2(m/\mathcal{Q}) \equiv F_2(m\to\infty,\mathcal{Q},\mu,\varepsilon) - F_2(0,\mathcal{Q},\mu,\varepsilon)$ which again can be obtained as the residue at $h=0$ if ε is set to zero prior to computing the residue, increasing the multiplicity of the pole sitting at the origin.

The previous quantity is related to the matching between two consecutive EFTs: one where the massive secondary quark is an active degree of freedom, another one in which it is not. Let us succinctly describe how such matching condition is computed. In the theory where the massive quark is no longer active we have n_ℓ active flavors. To carry out the matching it is convenient to express the renormalized matrix elements as a series of $\alpha_s^{(n_\ell)}$. After the conversion the 2-loop term takes the form

$$F_{2,\mathrm{ren}}^{(n_\ell)}(m,\mathcal{Q},\mu) = \left\{ H_2(m,\mathcal{Q},\mu,\varepsilon) - \frac{F_1(0,\mathcal{Q},\mu,\varepsilon)}{3}\left[\left(\frac{\mu^2 e^{\gamma_E}}{m^2}\right)^\varepsilon \Gamma(\varepsilon) - \frac{1}{\varepsilon} - \log\left(\frac{\mu^2}{m^2}\right)\right]\right\}_{\mathrm{ren}}, \tag{5.14}$$

analogous to Eq. (4.90). As we already mentioned, the factor between the brackets is $\mathcal{O}(\varepsilon)$, so if $F_1(0,\mathcal{Q},\varepsilon)$ is UV-finite, the second term vanishes. Furthermore, in such cases the decoupling limit is manifest $H_2(m\to\infty,\mathcal{Q}) = 0$, and the matching condition is trivial: the effects from massive quark bubbles are fully captured in the α_s decoupling relation. If one assumes $F_1(0,\mathcal{Q},\mu,\varepsilon)$ has the following divergent structure:

$$F_1(0,\mathcal{Q},\mu,\varepsilon) = \frac{m_2}{\varepsilon^2} + \frac{m_1}{\varepsilon} + m_0\,, \tag{5.15}$$

where m_0 can potentially depend on an IR regulator, the relevant quantity for the matching coefficient

$$\begin{aligned} F_{2,\mathrm{ren}}^{(n_\ell)}(m\to\infty,\mathcal{Q}) = &\left\{ -\left(\frac{\mu^2 e^{\gamma_E}}{\mathcal{Q}^2}\right)^\varepsilon \left(\frac{\mu^2 e^{\gamma_E}}{m^2}\right)^\varepsilon \mathrm{Res}_{h=\varepsilon}\left[\mathcal{M}_2\left(h,\varepsilon,\frac{m_g}{\mathcal{Q}}\right)\right]\right\}_{\mathrm{ren}} - \frac{m_2}{18}\log^3\left(\frac{\mu^2}{m^2}\right) \\ &- \frac{m_1}{6}\log^2\left(\frac{\mu^2}{m^2}\right) - \frac{\pi^2 m_2}{36}\log\left(\frac{\mu^2}{m^2}\right) + \frac{m_2\zeta_3}{9} - \frac{\pi^2 m_1}{36}\,, \end{aligned} \tag{5.16}$$

which can be rewritten as $[F_2(0,\mathcal{Q},\varepsilon)]_{\mathrm{ren}} + \Delta_0^\infty F_2(m/\mathcal{Q}) + 2[F_1(0,\mathcal{Q},\varepsilon)]_{\mathrm{ren}}\log(\mu/m)/3$, does not depend on m_0.

5.4 Relation between the pole and $\overline{\mathrm{MS}}$ masses

Our first application is to a quantity which does not carry a cusp part in its anomalous dimension. Even though the results derived in this section are known, it is nevertheless worth re-deriving them within our formalism as it will illustrate the method on a simple example. To avoid confusion, we will also denote the primary quark mass as M in this Chapter. We start by quoting the result for $\left[\overline{M}(\mu) - M_{\mathrm{pole}}\right]/M_{\mathrm{pole}}$ at 1-loop using a modified gluon propagator, and identify $\mathcal{Q} = M_{\mathrm{pole}}$, where UV-divergences must be removed through a Z factor in the $\overline{\mathrm{MS}}$ scheme

$$m_1^h(\varepsilon) = -\frac{3-2\varepsilon}{2}\frac{(1+h-\varepsilon)\Gamma(\varepsilon-h)\Gamma(1+2h-2\varepsilon)}{\Gamma(3+h-2\varepsilon)}\,, \tag{5.17}$$

result that was computed in the form given above in Ref. [27].

5.4.1 Massive gluon

Multiplying the result in Eq. (5.17) by the factor $\Gamma(h)\Gamma(1-h)$ we obtain the corresponding Mellin transform $\mathcal{M}_1^{\overline{\rm MS}}\big(h,\varepsilon\big)$. To figure out the convergence radius of both expansions, we look at the large-h behavior of $\mathcal{M}_1^{\overline{\rm MS}}$ with $\varepsilon = 0$. Defining $\xi_g = m_g/M_{\rm pole}$ we have

$$|\mathcal{M}_1^{\overline{\rm MS}}\big(h,0,\xi_g\big)| \xrightarrow[|h|\gg 1]{} \frac{3\pi^{3/2}\csc^2(\pi h)}{2h^{3/2}}\left(\frac{\xi_g}{2}\right)^{-2h}, \tag{5.18}$$

from where we read that the small (large) gluon mass expansion works for ξ_g smaller (larger) than 2, while at $\xi_g = 2$ both expansions are convergent, as can be seen in Fig. 5.2(a). After setting $\varepsilon = 0$, if closing towards $\mathrm{Re}(h) > 0$ there are double poles at all positive integer values of h. When closing towards $\mathrm{Re}(h) < 0$, one finds simple poles at all negative integers and half-integer values of h, except for $h = -2$ where the pole is double. The divergences of both expansions coincide:

$$F_{1,\rm div}^{\overline{\rm MS}} = -\frac{3}{4\varepsilon}. \tag{5.19}$$

This result correctly yields the well-known 1-loop $\overline{\rm MS}$ mass anomalous dimension, but is removed after renormalization. The massless limit is given by the pole at $h = 0$, and after renormalization takes the form

$$F_{1,\rm ren}^{\overline{\rm MS}}(0, M_{\rm pole}, \mu, \varepsilon) = -\frac{3}{2}\log\left(\frac{\mu}{M_{\rm pole}}\right) - 1\,. \tag{5.20}$$

At this point we can compute both series expansions for the corrections to the massless gluon limit, obtaining

$$\begin{aligned}\Delta_0 F_1^{\overline{\rm MS}}(\xi_g) &= \frac{3}{8} + \frac{3}{2}\log(\xi_g) - 6\sum_{n=1}\frac{\xi_g^{-2n}\Gamma(2n)}{n(n+2)\Gamma^2(n)}\left[H_{2n-1} - H_{n-1} - \log(\xi_g) - \frac{n+1}{n(n+2)}\right] \\ &= -\frac{\xi_g^4}{24}[5 - 6\log(\xi_g)] + \frac{3}{2}\sum_{n=1}^{n\neq 4}\frac{(-\xi_g)^n\Gamma^2\left(\frac{n}{2}\right)}{(n-4)\Gamma(n)}\,.\end{aligned} \tag{5.21}$$

The bottom line can be summed up, and we find[6]

$$\Delta_0 F_1^{\overline{\rm MS}}(\xi_g) = \frac{\xi_g}{4}\left[\left(2+\xi_g^2\right)\sqrt{4-\xi_g^2}\arccos\left(\frac{\xi_g}{2}\right) + \xi_g^3\log(\xi_g) - \xi_g\right]. \tag{5.23}$$

This agrees with a direct computation whose details will be given elsewhere. To the best of our knowledge, this result has not been presented anywhere before. The large-mass expansion has only same-sign even powers. The series for small gluon mass has odd and even powers of ξ_g and is oscillatory, hence it converges slowly, as can be seen in both panels of Fig. 5.2.

Let us provide the matching coefficient between the $\overline{\rm MS}$ masses defined in the full theory, with massless gluons and a single massive gluon $\overline{M}^{(n_g)}$, and in an EFT containing only massless gluons $\overline{M}^{(n_\ell)}$. The

[6] For $\xi_g > 2$ one simply replaces

$$\sqrt{4-\xi_g^2}\arccos\left(\frac{\xi_g}{2}\right) \to \frac{1}{2}\sqrt{\xi_g^2-4}\,\log\left[\frac{\xi_g}{2}\left(\xi_g - \sqrt{\xi_g^2-4}\right) - 1\right], \tag{5.22}$$

to have every term manifestly real.

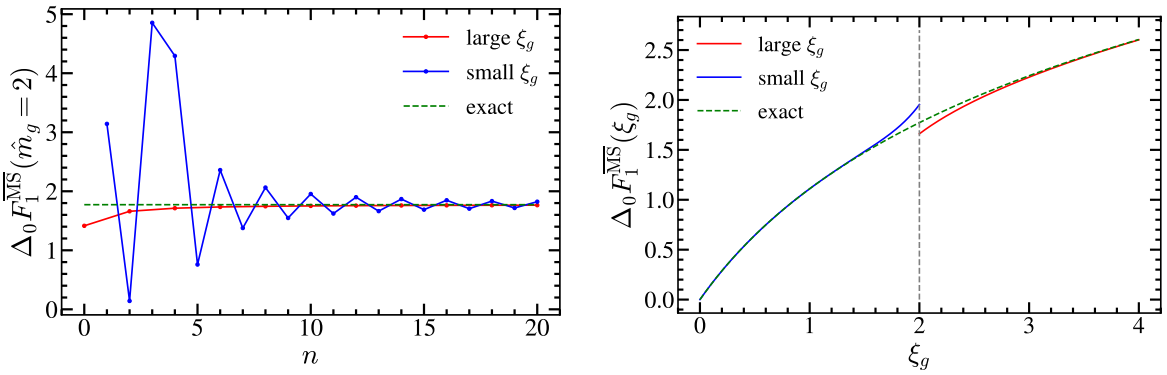

(a) (b)

Figure 5.2: Gluon mass correction to the relation between the pole and $\overline{\rm MS}$ quark masses in its exact form (dashed green), small- (blue) and large-mass (red) expansions. Left panel: $\Delta_0 F_1^{\overline{\rm MS}}$ at the boundary between the mass expansions $\xi_g = 2$, as a function of the expansion order n of each expansion. Right panel: Dependence of $\Delta_0 F_1^{\overline{\rm MS}}(\xi_g)$ with the parameter ξ_g including 10 and 3 non-zero terms in the small- and large-mass expansions, respectively.

strategy to obtain the matching coefficient is through the condition of having a universal pole mass in the limit where both theories should be valid:

$$\begin{aligned} M_{\rm pole} &= \overline{M}^{(n_g)}(\mu)\left\{1 - \frac{\alpha_s(\mu)}{\pi} C_F [2F_1^{\overline{\rm MS}}(0, M_{\rm pole}) + \Delta_0 F_1^{\overline{\rm MS}}(\xi_g \to \infty)]\right\}_{\rm ren} \\ &= \overline{M}^{(n_\ell)}(\mu)\left[1 - \frac{\alpha_s(\mu)}{\pi} C_F F_1^{\overline{\rm MS}}(0, M_{\rm pole})\right]_{\rm ren}. \end{aligned} \tag{5.24}$$

Noting that $\Delta_0 F_1^{\overline{\rm MS}}(\xi_g \to \infty) = \Delta_0^\infty F_1^{\overline{\rm MS}}(\xi_g) = 3/8 + 3/2 \log(\xi_g)$, we easily obtain the matching condition, which moreover is independent of $M_{\rm pole}$:

$$\begin{aligned} \frac{\overline{M}^{(n_g)}(\mu)}{\overline{M}^{(n_\ell)}(\mu)} &= 1 + \frac{\alpha_s}{\pi} C_F [F_{1,\rm ren}^{\overline{\rm MS}}(0, M_{\rm pole}, \mu, \varepsilon) + \Delta_0^\infty F_1^{\overline{\rm MS}}(\xi_g)] \equiv 1 + \frac{\alpha_s}{\pi} C_F \delta M^{n_g \to n_\ell}, \\ \delta M^{n_g \to n_\ell} &= -\frac{3}{2} \log\left(\frac{\mu}{m_g}\right) - \frac{5}{8}. \end{aligned} \tag{5.25}$$

5.4.2 Secondary massive quark

Multiplying Eq. (5.17) by $G(h, \varepsilon)$ we obtain $\mathcal{M}_2^{\overline{\rm MS}}(h, \varepsilon)$, and setting $\varepsilon = 0$ we can figure out the convergence radius. Defining $\xi = m/M_{\rm pole}$ one has

$$\mathcal{M}_2^{\overline{\rm MS}}(h, 0, \xi) = \frac{3\xi^{-2h}(h+1)\Gamma^2(h)\Gamma^2(1-h)}{2(h+2)h(2h+3)(2h+1)} \xrightarrow[|h|\gg 1]{} \frac{3\pi^2 \csc^2(\pi h)}{8h^3} \xi^{-2h}. \tag{5.26}$$

It is clear that the small and large m expansions work for m smaller and larger than $M_{\rm pole}$, respectively.[7] The divergences of both expansions are m-independent and coincide:

$$F_{2,\rm div}^{\overline{\rm MS}} = -\frac{1}{8\varepsilon^2} + \frac{5}{48\varepsilon}\,. \tag{5.27}$$

This result correctly reproduces the n_f color piece of the two-loop $\overline{\rm MS}$ mass anomalous dimension. From the sum of residues corresponding to the poles located at $h = 0$ and $h = -\varepsilon$ and the Π_0 contribution —after removing the UV divergences— we reproduce the known 2-loop massless result or Ref. [28], which accounts for the full μ dependence.

$$F_{2,\rm ren}^{\overline{\rm MS}}(0, M_{\rm pole}, \mu, \varepsilon) = \frac{1}{2}\log^2\left(\frac{\mu}{M_{\rm pole}}\right) + \frac{13}{12}\log\left(\frac{\mu}{M_{\rm pole}}\right) + \frac{\pi^2}{12} + \frac{71}{96}\,. \tag{5.28}$$

After setting $\varepsilon = 0$ we find double poles at all positive and negative integer values of h, except for $h = -1$, and $h = -2$ for which the pole multiplicity is 1 and 3, respectively. Furthermore, there are simple poles at $h = -1/2$ and $h = -3/2$. The difference of the massless and $m \to \infty$ limits is UV finite and μ-independent, but contains logarithms that blow up in any of those two limits. It can be computed as minus the contribution of the pole at $h = 0$ obtained setting $\varepsilon = 0$ before computing the residue

$$\Delta_0^\infty F_2^{\overline{\rm MS}}(\xi) = -\frac{1}{2}L_\xi^2 - \frac{13}{12}L_\xi - \frac{\pi^2}{12} - \frac{151}{144}\,, \tag{5.29}$$

with $L_\xi = \log(\xi)$. Since the factor containing all gamma functions in $\mathcal{M}_2(h, 0, \xi)$ is symmetric under $h \to -h$, and given that gamma functions are the only structures with an infinite number of poles, we expect that this symmetry will be manifest in the infinite sums of the 'left' and 'right' expansions. In fact that is what we find for the corrections to the massless limit:

$$\begin{aligned}
\Delta_0 F_2^{\overline{\rm MS}}(\xi) = \Delta_0^\infty F_2^{\overline{\rm MS}} + \frac{3}{2}\sum_{n=1} G_n^{\overline{\rm MS}}(\xi) &= \frac{3}{2}\xi^2 - \frac{\pi^2}{4}\xi - \frac{\pi^2}{4}\xi^3 \\
&+ \xi^4\left(\frac{1}{2}L_\xi^2 - \frac{13}{12}L_\xi + \frac{\pi^2}{12} + \frac{151}{144}\right) - \frac{3}{2}\sum_{n=3} G_{-n}^{\overline{\rm MS}}(\xi)\,, \\
G_n^{\overline{\rm MS}}(\xi) &= \frac{\xi^{-2n}}{n(n+2)(2n+1)(2n+3)}\left[\frac{2(3+10n+5n^2)}{n(2+n)(1+2n)(3+2n)} + 3 + 2(n+1)L_\xi\right].
\end{aligned} \tag{5.30}$$

For $\xi = 1$, that is, the contribution of the heavy quark to its own self-energy, we can sum up either series obtaining the known result $\Delta_0 F_2(1) = (3 - \pi^2)/4$. These expressions can be summed up to all orders, fully reproducing the known result or Ref. [28]:

$$\begin{aligned}
\Delta_0 F_2^{\overline{\rm MS}}(\xi) = -\Bigg\{ &\frac{\pi^2}{12} - \frac{1}{2}(1-\xi)(1-\xi^3)\left[{\rm Li}_2(1-\xi) + \frac{1}{2}L_\xi^2 + \frac{\pi^2}{6}\right] - \frac{\xi^2}{2}\left(L_\xi + \frac{3}{2}\right) \\
&+ \frac{1}{2}(1+\xi)(1+\xi^3)\left[{\rm Li}_2(-\xi) - \frac{1}{2}L_\xi^2 + \log(1+\xi)L_\xi + \frac{\pi^2}{6}\right] + \frac{1}{2}L_\xi^2\Bigg\}\,.
\end{aligned} \tag{5.31}$$

The small- and large-mass expansions are shown in Fig. 5.3.

We observe that the small-mass expansion is badly convergent for the first orders. After the fourth power of ξ is included (which coincides with the first appearance of L_ξ), the accuracy improves drastically.

[7] We do not assume any hierarchy between m and M since our results are general and one could consider e.g. the secondary virtual top correction to the bottom mass in QCD with six active flavors.

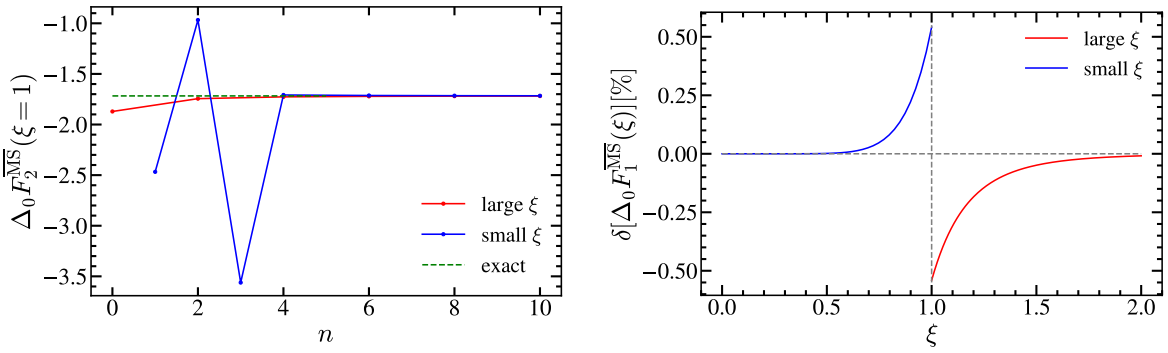

(a) (b)

Figure 5.3: Secondary mass correction to the relation between the pole and $\overline{\rm MS}$ quark masses in its exact form (dashed green), small- (blue) and large-mass (red) expansions. Left panel: $\Delta_0 F_2^{\overline{\rm MS}}$ at the boundary between the mass expansions $\xi = 1$, as a function of the expansion order n. Right panel: percent deviation of the expansions compared to the exact result as a function of the parameter ξ, using 4 and 3 non-zero terms in the small- and large-mass expansions, respectively.

The plots also reveal that the small- and large-mass expansions approach the exact result from above and below, respectively. Finally, the convergence of the small-mass expansion is much better behaved than it is for the gluon mass case. This can be understood since the gluon mass expansion contains an infinite number of odd-power corrections.

Let us compute to the $\mathcal{O}(\alpha_s^2)$ matching condition between the $\overline{\rm MS}$ masses with n_f+1 and n_f flavors, $\overline{M}^{(n_f+1)}$ and $\overline{M}^{(n_f)}$, respectively, following the same strategy as in the previous section. Using Eq. (5.16), or equivalently the relation underneath, we find

$$\frac{\overline{M}^{(n_f+1)}(\mu)}{\overline{M}^{(n_f)}(\mu)} \equiv 1 + \left[\frac{\alpha_s^{(n_f)}(\mu)}{\pi}\right]^2 T_F C_F \delta M^{n_f\to n_\ell}\,, \tag{5.32}$$

$$\begin{aligned}\delta M^{n_f\to n_\ell} &= F_2(M_{\rm pole},0,\varepsilon) + \Delta_0 F_2(\xi\to\infty) + \frac{2}{3}F_1(M_{\rm pole},0,\varepsilon)\log\left(\frac{\mu}{m}\right)\\ &= -\frac{1}{2}\log^2\left(\frac{\mu}{m}\right) + \frac{5}{12}\log\left(\frac{\mu}{m}\right) - \frac{89}{288}\,,\end{aligned}$$

independent of $M_{\rm pole}$ and in agreement with Ref. [11].

5.5 SCET Computations

We turn our attention now to the computation of matrix elements which enter the SCET factorization theorem with massless primary quarks, see Eq. (1.48). Since our formalism as it stands now only applies to virtual massive bubbles, we will be able to compute only the corrections to the general (event-shape independent) hard matching coefficient and to the hemisphere jet function, which enters the factorized expressions for thrust, heavy jet mass and C-parameter in the M-scheme because, as we already discussed in Sec. 4.3, it can be computed as the discontinuity of a forward-scattering matrix element.

Even though both results have been already computed in closed form, to the best of our knowledge, the small and large secondary mass expansions were not known. Furthermore, the RG evolved jet function was not known in closed form, and in that respect our result in terms of expansions can be regarded as a new analytic result.

5.5.1 Hard Matching Coefficient

In this section we compute the corrections to the Wilson coefficient appearing when matching QCD and SCET due to a massive vector boson or a massive quark bubble. To write expressions as simple as possible, it will be useful to define the reduced mass also for the vector boson $\hat{m}_g^2 = m_g^2/Q^2$.

For contributions of either massive vector bosons or secondary massive bubbles, the non-zero mass acts as an IR regulator and neither the QCD nor the SCET loop-level form factors vanish any more if dimreg is used —in fact, they are IR finite and no regulator is needed.[8] Furthermore, in either case the SCET form factors are finite only after soft bin subtractions are included, requiring regulators in individual Feynman diagrams due to rapidity divergences.

However, with our computational strategy we bypass all problems at once: only the QCD Feynman diagrams contribute, soft bin subtractions identically vanish and there are no rapidity singularities. On the other hand, the calculation does not disentangle the QCD and SCET IR-finite contributions. As we will see, consistency conditions can be used to obtain these separately. For the 1-loop computation with a shifted gluon propagator we have $\mathcal{Q}^2 = -Q^2$, and the following result was found in Ref. [27]:

$$m_1^h(\varepsilon) = -\frac{1}{2}\frac{\Gamma^2(h-\varepsilon)\Gamma(1-h+\varepsilon)}{\Gamma(3+h-2\varepsilon)}\{2-\varepsilon[3+h^2+h(2-3\varepsilon)-\varepsilon(3-2\varepsilon)]\}\,, \tag{5.33}$$

from which we observe a double pole sits at $h=\varepsilon$.

Massive gluon

We quote the relevant results for the QCD to SCET matching coefficient before showing the expansions. We use the superscript H since from this coefficient the hard factor can be obtained:

$$\begin{aligned}
\mathcal{M}_1^H(h,\hat{m}_g,0) &= -\frac{\Gamma^2(h)\Gamma^2(1-h)}{h(h+1)(h+2)}(-\hat{m}_g^2)^{-h} \xrightarrow[|h|\gg 1]{} -\frac{\pi^2\csc^2(\pi h)}{h^3}(-\hat{m}_g^2)^{-h}\,, \\
F_{1,\text{div}}^H(Q^2,\mu,\varepsilon) &= -\frac{1}{2\varepsilon^2}-\frac{1}{4\varepsilon}\big(2L_\mu+3\big)\,, \\
F_{1,\text{ren}}^H(0,Q,\mu) &= -\frac{1}{4}L_\mu^2-\frac{3}{4}L_\mu+\frac{\pi^2}{24}-2\,, \\
\Delta_0^\infty F_1^H(\hat{m}_g) &= \frac{1}{4}\log^2(-\hat{m}_g^2)+\frac{3}{4}\log(-\hat{m}_g^2)+\frac{\pi^2}{6}+\frac{7}{8}\,,
\end{aligned} \tag{5.34}$$

where $L_\mu = \log(-\mu^2/Q^2)$ and we have displayed the 1-loop massless limit already renormalized, which agrees with the well-known result of Ref. [23]. The divergences shown in the second line make clear the result does not correspond to the full-theory computation, since a massive gluon yields a UV- and IR-finite result and does not need any regulator. As for the convergence radius, $\hat{m}_g$ smaller or larger than 1 call for small- or large-mass expansions. This result can be confirmed using the Cauchy root criteria on the general terms shown in Eq. (5.35). As shown in Fig. 5.4(a), at the boundary one can use

[8] The computation with a massive vector boson is IR finite. For the massive bubble, the Π^{OS} insertion is also IR finite, but that proportional to $\Pi_0^{\overline{\text{MS}}}$ needs regularization.

either expansion, and both series converge equally fast.

The two expansions for the correction to the massless limit are computed easily noting that there are double poles at all negative and positive integer values of h, except for $h=-1$ and $h=-2$ that are triple. Once again, the factor containing all gamma functions in $\mathcal{M}_1$ is symmetric under reversing the sign of h, thence a symmetry between the infinite sums will be manifest. We found

$$\begin{aligned}\Delta_0 F_1^H(\hat{m}_g) &= \Delta_0^\infty F_1^H - \sum_{n=1} G_n^H(\hat{m}_g) = \sum_{n=3} G_{-n}^H(\hat{m}_g) - \hat{m}_g^2\left[\frac{1}{2}\log^2(-\hat{m}_g^2) + \frac{\pi^2}{3} + 1\right] \\ &\quad - \hat{m}_g^4\left[\frac{1}{4}\log^2(-\hat{m}_g^2) - \frac{3}{4}\log(-\hat{m}_g^2) + \frac{\pi^2}{6} + \frac{7}{8}\right], \\ G_n^H(\hat{m}_g) &= \frac{(-\hat{m}_g^2)^{-n}}{n(n+1)(n+2)}\left[\log(-\hat{m}_g^2) + \frac{3n^2+6n+2}{n(n+1)(n+2)}\right].\end{aligned} \tag{5.35}$$

The infinite sum can be carried out analytically:

$$\Delta_0 F_1^H(\hat{m}_g) = \frac{\pi^2}{12} - \frac{1}{2}\big(1+\hat{m}_g^2\big)^2\,\mathrm{Li}_2\big(1+\hat{m}_g^2\big) - \frac{\hat{m}_g^2}{2}\big[\log(-\hat{m}_g^2)+1\big] - \frac{\hat{m}_g^2}{12}\big(2+\hat{m}_g^2\big)\big[\pi^2+3\log^2(-\hat{m}_g^2)\big]. \tag{5.36}$$

For $\hat{m}_g > 0$ the expression above develops an imaginary term. To take the real part, relevant to obtain the hard factor, one simply has to make the following replacements:

$$\begin{aligned}\mathrm{Li}_2\big(1+\hat{m}_g^2\big) &\to \frac{\pi^2}{6} - \mathrm{Li}_2\big(-\hat{m}_g^2\big) - \log(1+\hat{m}_g^2)\log(\hat{m}_g^2)\,, \\ \log^n(-\hat{m}_g^2) &\to \big\{\mathrm{Re}\big[\log^n(\hat{m}_g^2) + i\pi\big]\big\}^n\,.\end{aligned} \tag{5.37}$$

The plots for the exact result and expansions are shown in Fig. 5.4. The respective approximations can be made arbitrarily precise adding more and more terms. Obtaining expansions for the hard matching coefficient poses no difficulty, but to avoid cluttering we do not show them.

At this point we can split the Wilson coefficient in the QCD and SCET terms. In order for that, we use that the QCD form factor must vanish in the decoupling limit $m_g \to \infty$. Hence we have $\mathbf{F}_1^{\mathrm{QCD}}(\hat{m}_g) = \Delta_\infty F_1^H(\hat{m}_g) = \Delta_0 F_1^H(\hat{m}_g) - \Delta_0^\infty F_1^H$, and using the result in Eq. (5.36) we find full agreement with Refs. [34, 35, 47]. Note that the $m_g \to 0$ limit of $\mathbf{F}_1^{\mathrm{QCD}}$ diverges, signaling the need for an IR regulator.

Finally, we can obtain the bare SCET form factor that should contain all UV divergences but is otherwise IR finite. It takes the following simple form $\mathbf{F}_1^{\mathrm{SCET}} = \mathbf{F}_1^{\mathrm{QCD}} - F_1^H = -\Delta_0^\infty F_1^H - F_1^H(0,Q,\mu) = -F_1^H(m_g\to\infty, Q, \mu)$, and corresponds to the contribution of the residue at $h=\varepsilon$:

$$\begin{aligned}\mathbf{F}_1^{\mathrm{SCET}} &= \frac{\Gamma(\varepsilon)}{2}\left(\frac{\mu^2 e^{\gamma_E}}{m_g^2}\right)^\varepsilon\left[H_{1-\varepsilon} + \log\big(-\hat{m}_g^2\big) + \pi\cot(\pi\varepsilon) + \frac{1+\varepsilon-\varepsilon^2}{(1-\varepsilon)(2-\varepsilon)}\right] \\ &= -\mathbf{F}_1^{\mathrm{div}} + \mathbf{F}_{1,\mathrm{ren}}^{\mathrm{SCET}}\,, \\ \mathbf{F}_{1,\mathrm{ren}}^{\mathrm{SCET}} &= -\frac{1}{4}\log^2\big(-\hat{m}_g^2\big) - \frac{3}{4}\log\big(-\hat{m}_g^2\big) + \frac{1}{4}\log^2\left(-\frac{\mu^2}{Q^2}\right) + \frac{3}{4}\log\left(-\frac{\mu^2}{Q^2}\right) - \frac{5\pi^2}{24} + \frac{9}{8}\,,\end{aligned} \tag{5.38}$$

where the harmonic number with a non-integer argument can be expressed in terms of the digamma function $\psi^{(0)}$ — the derivative of the logarithm of the gamma function — as follows: $H_{1-\varepsilon} = \psi^{(0)}(2-\varepsilon)+\gamma_E$. One can also relate the cotangent to digamma functions: $\pi\cot(\pi\varepsilon) = \psi^{(0)}(1-\varepsilon) - \psi^{(0)}(\varepsilon)$. Our unexpanded result agrees with Eq. (321) of Ref. [29], and our expanded result agrees with Ref. [12].

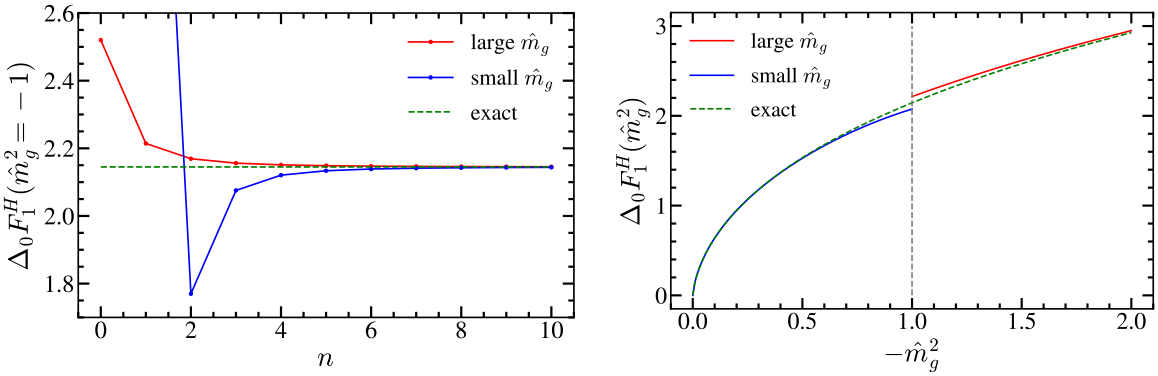

Figure 5.4: Gluon mass correction to the massless SCET Wilson coefficient in its exact form (dashed green), small- (blue) and large-mass (red) expansions. Left panel: $\Delta_0 F_1^H$ at the boundary between the mass expansions $\hat{m}_g^2 = -1$, as a function of the expansion order n of each series. Right panel: Dependence of $\Delta_0 F_1^H(\hat{m}_g^2)$ with the reduced gluon mass, including 3 and 2 non-zero terms in the small- and large-mass expansions, respectively.

We close the section computing the QCD and SCET "gluonic flavor" matching coefficients relating the renormalized quark currents in the theories with massive and massless gluons (operators labeled with a superscript n_g) and with only massless gluons (operators labeled with a superscript n_ℓ). That is, analogously to Eq. (4.88), we have:

$$\begin{aligned} \mathcal{J}_{\rm QCD}^{n_g} &\equiv \mathcal{M}_{\rm QCD}^{n_g \to n_\ell}\, \mathcal{J}_{\rm QCD}^{n_\ell}\,, \\ J_{\rm SCET}^{n_g} &\equiv \mathcal{M}_{\rm SCET}^{n_g \to n_\ell}\, J_{\rm SCET}^{n_\ell}\,. \end{aligned} \tag{5.39}$$

Since the contribution of massless gluons is the same in both theories, the result of the ratio between renormalized form factors keeping all the dependence is simply the massive gluon contribution (the strong coupling is the same in both theories at 1-loop):

$$\begin{aligned} \mathcal{M}_{\rm QCD}^{n_g \to n_\ell} &= 1 + \frac{\alpha_s(\mu)}{\pi} C_F \mathbf{F}_1^{\rm QCD}(\hat{m}_g)\,, \\ \mathcal{M}_{\rm SCET}^{n_g \to n_\ell} &= 1 + \frac{\alpha_s(\mu)}{\pi} C_F \mathbf{F}_{1,\rm ren}^{\rm SCET}(m_g, Q, \mu)\,. \end{aligned} \tag{5.40}$$

On the other hand, if one takes the decoupling limit, the only non-trivial contribution for the strict matching will be the SCET one, which agrees with Eq. (29) of Ref. [31].

Secondary massive bubble

The relevant results for the QCD to SCET matching coefficient with massive corrections are in this case

$$\begin{aligned}
\mathcal{M}_2^H(h,\hat{m},0) &= -\big(-\hat{m}^2\big)^{-h}\frac{4(h+1)\Gamma^2(1-h)\Gamma^4(h)}{\Gamma(2h+5)} \xrightarrow[|h|\gg 1]{} -\frac{\pi^{5/2}\csc^2(\pi h)}{4h^{9/2}}\big(-4\hat{m}^2\big)^{-h}\,, \qquad (5.41)\\
F_{2,\text{div}}^H(Q,\mu,\varepsilon) &= -\frac{1}{8\varepsilon^3}-\frac{1}{\varepsilon^2}\left(\frac{1}{12}L_\mu+\frac{1}{18}\right)+\frac{1}{\varepsilon}\left(\frac{5}{36}L_\mu+\frac{\pi^2}{48}+\frac{65}{432}\right),\\
F_{2,\text{ren}}^H(0,Q,\mu,\varepsilon) &= \frac{1}{36}L_\mu^3+\frac{19}{72}L_\mu^2+\left(\frac{209}{216}+\frac{\pi^2}{36}\right)L_\mu+\frac{\zeta_3}{36}+\frac{23\pi^2}{432}+\frac{4085}{2592}\,,\\
\Delta_0^\infty F_2^H(\hat{m}) &= -\frac{1}{36}L_m^3-\frac{19}{72}L_m^2-\left(\frac{265}{216}+\frac{\pi^2}{36}\right)L_m+\frac{\zeta_3}{3}-\frac{19\pi^2}{216}-\frac{3355}{1296}\,.
\end{aligned}$$

with $L_m = \log(-\hat{m}^2)$. Our results for the massless limit and the renormalization factor agree with Ref. [53]. From the top line result it becomes clear that the small- and big-mass expansions converge for $4m^2 \le |Q|^2$ and $4m^2 \ge |Q|^2$, respectively. Fast convergence at $4m^2 = |Q|^2$ is expected from any of the two expansions, as can be seen in Fig. 5.5(a).

After removing the massless limit one can set $\varepsilon = 0$ and examine the pole structure of the Mellin transform. On the positive real axis there are double poles at all integer values of h. On the negative real axis one has a quartic pole at $h = -2$ and triple poles at $h = -n$ with $n \neq 2$. We can use the inverse mapping theorem to obtain the corresponding expansions for $\Delta_0 F_2$:

$$\begin{aligned}
\Delta_0 F_2^H(\hat{m}) =& \Delta_0^\infty F_2^H(\hat{m}) + 4\sum_{n=1}\frac{(n+1)[(n-1)!]^2}{(2n+4)!}(-\hat{m}^2)^{-n}\left[2(H_{n-1}-H_{2n+1})-L_m-\frac{7+4n}{(n+2)(2n+3)}\right]\\
=& \hat{m}^2\left(L_m^2+2L_m+8+\frac{\pi^2}{3}\right)+\hat{m}^4\left(L_m^2-\frac{1}{6}L_m^3-\frac{33+2\pi^2}{12}L_m+\frac{13}{4}+\frac{\pi^2}{3}+2\zeta_3\right)\\
&+2\sum_{n=3}^{\infty}\frac{(2n-2)!}{(n-2)(2n-3)(n!)^2}\big(-\hat{m}^2\big)^n\left[\frac{2(4n-7)}{(n-2)(2n-3)}\left(H_{2n-2}-H_n+\frac{1}{2}L_m\right)\right.\\
&\left.-2\left(H_{2n-2}-H_n+\frac{1}{2}L_m\right)^2+2H_{2n-2}^{(2)}-H_n^{(2)}-\frac{\pi^2}{6}-\frac{37-42n+12n^2}{(n-2)^2(2n-3)^2}\right], \qquad (5.42)
\end{aligned}$$

where $H_k^{(2)} = \sum_{i=1}^k n^{-2}$ is the harmonic number of order 2. The infinite sum for the large-mass expansion can be summed up and we obtain the following result:

$$\begin{aligned}
\Delta_0 F_2^H(\hat{m}) =& \left(\frac{23r^2}{72}+\frac{5}{24}\right)r\left[\text{Li}_2\left(\frac{r-1}{r+1}\right)-\text{Li}_2\left(\frac{r+1}{r-1}\right)\right]+\left(\frac{55r^2}{72}+\frac{25}{54}\right)L_m \qquad (5.43)\\
&+\left(\frac{5}{48}-\frac{r^4}{16}+\frac{r^2}{8}\right)\left[\text{Li}_3\left(\frac{r-1}{r+1}\right)+\text{Li}_3\left(\frac{r+1}{r-1}\right)-2\zeta_3\right]+\frac{119r^2}{72}\\
&-\frac{L_m^3}{36}-\frac{19L_m^2}{72}-\left(\frac{265}{216}+\frac{\pi^2}{36}\right)L_m+\frac{\zeta_3}{3}-\frac{19\pi^2}{216}-\frac{119}{72}\,,
\end{aligned}$$

with $r = \sqrt{1+4\hat{m}^2}$, in agreement with Ref. [46, 35]. In the equation above all terms are manifestly real for $0 > \hat{m}^2 > -1/4$. For $\hat{m}^2 < -1/4$ some terms develop imaginary parts, but $\Delta_0 F_2^H(\hat{m})$ is still

real-valued. To have every term explicitly real in this case we simply make the following substitutions:

$$\begin{aligned} r\left[\mathrm{Li}_2\left(\frac{r-1}{r+1}\right)-\mathrm{Li}_2\left(\frac{r+1}{r-1}\right)\right] &\to -2\sqrt{-1-4\hat{m}^2}\,\mathrm{Cl}_2\left[\arccos\left(\frac{r^2+1}{r^2-1}\right)\right], \\ \mathrm{Li}_3\left(\frac{r-1}{r+1}\right)+\mathrm{Li}_3\left(\frac{r+1}{r-1}\right) &\to 2\,\mathrm{Cl}_3\left[\arccos\left(\frac{r^2+1}{r^2-1}\right)\right], \end{aligned} \tag{5.44}$$

where the Clausen functions are defined as

$$\mathrm{Cl}_2(\alpha)=\sum_{k=1}\frac{\sin(k\alpha)}{k^2}\,,\quad \mathrm{Cl}_3(\alpha)=\sum_{k=1}\frac{\cos(k\alpha)}{k^3}\,. \tag{5.45}$$

For $\hat{m}^2>0$ a genuine imaginary part is generated. To obtain the real part (which is most relevant to compute the hard factor), one has to do the following replacements:

$$\begin{aligned} \mathrm{Li}_2\left(\frac{r-1}{r+1}\right)-\mathrm{Li}_2\left(\frac{r+1}{r-1}\right) &\to 2\mathrm{Li}_2\left(\frac{r-1}{r+1}\right)+\frac{1}{2}\log^2\left(\frac{r-1}{r+1}\right)-\frac{\pi^2}{3}\,, \\ \mathrm{Li}_3\left(\frac{r-1}{r+1}\right)+\mathrm{Li}_3\left(\frac{r+1}{r-1}\right) &\to 2\mathrm{Li}_3\left(\frac{r-1}{r+1}\right)-\frac{1}{6}\log^3\left(\frac{r+1}{r-1}\right)+\frac{\pi^2}{3}\log\left(\frac{r+1}{r-1}\right), \\ L_m^n &\to \mathrm{Re}[\log(\hat{m}^2)+i\pi]^n\,. \end{aligned} \tag{5.46}$$

Obtaining the expansions for the SCET hard factor is trivial from the results quoted in this section and to avoid cluttering these will not be explicitly shown.

A comparison of the small- and large-mass expansions to the summed-up result is shown in Fig. 5.5, where one can observe that both expansions converge very fast, specially for large masses, where including only two terms is enough to achieve sub-percent accuracy everywhere the sum converges.

The dispersive contribution to the two-loop QCD form factor is IR-finite and given by the difference $\mathbf{F}_{2,\mathrm{disp}}^{\mathrm{QCD}}=F_2^H(\hat{m})-F_2^H(\hat{m}\to\infty)$. The dispersive contribution to the SCET form factor is also IR finite and obtained as $\mathbf{F}_{2,\mathrm{disp}}^{\mathrm{SCET}}=F_2^H(\hat{m}\to\infty)$, which is simply the pole at $h=\varepsilon$ of the H_2 contribution.

$$\begin{aligned} \mathbf{F}_{2,\mathrm{disp}}^{\mathrm{SCET}} =& \frac{1}{8\varepsilon^3}+\frac{1}{\varepsilon^2}\left(\frac{L_\mu}{4}-\frac{L_m}{6}+\frac{1}{18}\right)+\frac{1}{\varepsilon}\left[\frac{L_\mu^2}{4}+\frac{L_m^2}{12}+L_\mu\left(\frac{1}{9}-\frac{L_m}{3}\right)-\frac{L_m}{4}-\frac{\pi^2}{144}-\frac{65}{432}\right] \\ &+\frac{L_\mu^3}{6}+L_\mu\left(\frac{L_m^2}{6}-\frac{L_m}{2}-\frac{\pi^2}{72}-\frac{65}{216}\right)+\frac{7L_m^2}{18}+L_\mu^2\left(\frac{1}{9}-\frac{L_m}{3}\right) \\ &+L_m\left(\frac{121}{216}+\frac{\pi^2}{36}\right)-\frac{5\zeta_3}{12}+\frac{\pi^2}{18}+\frac{875}{864}\,. \end{aligned} \tag{5.47}$$

Our result agrees with Ref. [29].

We can obtain the flavor matching SCET decoupling coefficient analogously to Eq. (4.89) for the bHQET case, leading to:

$$\begin{aligned} \mathcal{M}_{\mathrm{SCET}} =& 1+\left[\frac{\alpha_s(\mu)}{\pi}\right]^2 C_F T_F\left[\frac{L_\mu^3}{18}+\frac{1}{36}L_m^3-L_\mu^2\left(\frac{L_m}{12}+\frac{1}{72}\right)-L_\mu\left(\frac{L_m}{4}+\frac{65}{216}+\frac{\pi^2}{24}\right)\right. \\ &\left.+\frac{19}{72}L_m^2+\frac{1}{216}\left(121+9\pi^2\right)L_m-\frac{13\zeta_3}{36}+\frac{875}{864}+\frac{5\pi^2}{144}\right], \end{aligned} \tag{5.48}$$

in agreement with Ref. [56] if setting $\mu_m=\mu_H$.

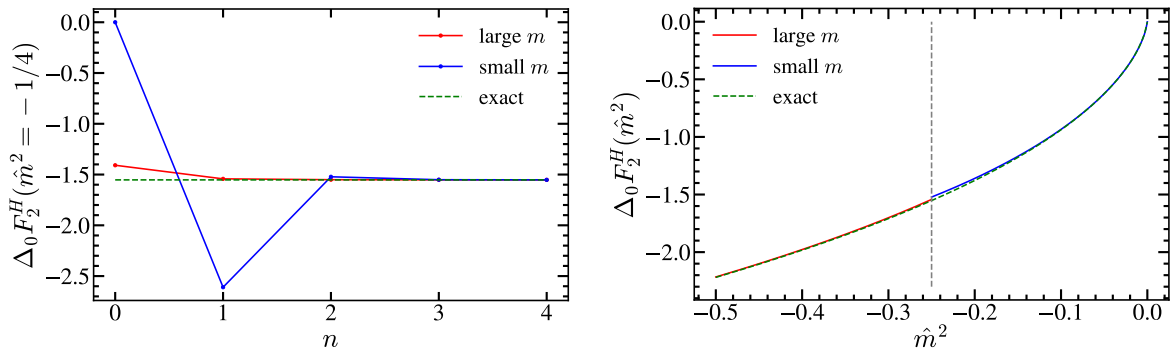

(a) (b)

Figure 5.5: Secondary mass correction to the massless SCET Wilson coefficient in its exact form (dashed green), small- (blue) and large-mass (red) expansions. Left panel: $\Delta_0 F_2^H$ at the boundary between the mass expansions $\hat{m}^2 = -1/4$, as a function of the expansion order n of each series. Right panel: Dependence of $\Delta_0 F_2^H(\hat{m}^2)$ with the reduced secondary quark mass, including 2 non-zero terms in each expansion.

5.5.2 Jet function

In this section we present results for the SCET single-hemisphere jet function, which appears in the factorization theorems for 2-jettiness and C-jettiness. The distributions contained in the momentum-space jet function might get obscured when expanding in big and small masses, therefore we compute its cumulative version, defined as

$$\Sigma_J(s_c, \mu) = \int_0^{s_c} \mathrm{d}s\, J(s, \mu)\,, \tag{5.49}$$

to obtain those, and provide the expansions for the non-distributional terms of the differential jet function.

For either secondary quarks or massive vector bosons, the jet function has real and virtual radiation contributions. The virtual contains only distributions that become singular at $s = 0$, while the real radiation has only non-distributional terms. The virtual correction is easy to obtain since for large (gluon or secondary quark) masses one cannot radiate a massive particle any more. Hence, the expansion for large masses will be given by the residue of a single pole sitting at $h = \varepsilon$. The non-distributional terms (which are proportional to a Heaviside theta function) are simply obtained as the sum of residues on the real non-positive axis, from which one must subtract the radiative tails of the plus distributions coming from the virtual diagrams.

For the 1-loop computation of Σ_J with a shifted gluon propagator we have $\mathcal{Q}^2 = s_c$, and the following result was found in Ref. [27]:

$$m_1^h(\varepsilon) = \frac{1}{2}\frac{\Gamma(2-\varepsilon)}{(h-\varepsilon)\Gamma(1-h)\Gamma(3+h-2\varepsilon)}\left[5-\varepsilon+\frac{2(2-h)}{h-\varepsilon}\right], \tag{5.50}$$

from which we observe a double pole sits at $h = \varepsilon$. We label quantities related with the differential and cumulative jet functions with J and Σ_J superscripts, respectively.

Massive gluon

To simplify the notation we define the dimensionless and positive-definite variable $\hat{s}_g = s/m_g^2$, which will be used in the differential and cumulative versions. The relevant results for these are

$$\begin{aligned}
\mathcal{M}_1^{\Sigma_J}(h,\hat{s}_g,0) &= \frac{(3h+4)\hat{s}_g^h}{2h^3(2+h)(1+h)} \xrightarrow[|h|\gg 1]{} \frac{3\hat{s}_g^h}{2h^4}\,, \\
F_{1,\mathrm{div}}^J(s,\mu,\varepsilon) &= \left(\frac{1}{\varepsilon^2}+\frac{3}{4\varepsilon}\right)\delta(s) - \frac{1}{\varepsilon}\frac{1}{\mu^2}\left[\frac{\mu^2}{s}\right]_+\,, \\
F_{1,\mathrm{ren}}^J(0,s,\mu) &= \frac{1}{\mu^2}\left[\frac{\mu^2}{s}\log\left(\frac{s}{\mu^2}\right)\right]_+ - \frac{3}{4}\frac{1}{\mu^2}\left[\frac{\mu^2}{s}\right]_+ + \left(\frac{7}{4}-\frac{\pi^2}{4}\right)\delta(s)\,, \\
\Delta_0^\infty F_1^J(\hat{s}_g) &= -\frac{1}{m_g^2}\left[\frac{m_g^2}{s}\log(\hat{s}_g)\right]_+ + \frac{3}{4}\frac{1}{m_g^2}\left[\frac{m_g^2}{s}\right]_+ - \frac{5}{8}\delta(s)\,.
\end{aligned} \tag{5.51}$$

The Mellin-Barnes transform for the differential jet function is trivially obtained applying a derivative: $\mathcal{M}_1^J(h,\hat{s}_g,0) = h\mathcal{M}_1^{\Sigma_J}(h,\hat{s}_g,0)/s$. Interestingly, after setting $\varepsilon = 0$ there is finite number of poles on each side of the real axis. The virtual contribution is simply the pole at $h=\varepsilon$, and prior to renormalization we find

$$\begin{aligned}
F_{1,\mathrm{virt}}^J &= \frac{\Gamma(\varepsilon)}{2}\left(\frac{\mu^2 e^{\gamma_E}}{m_g^2}\right)^\varepsilon\left\{\left[2\pi\cot(\pi\varepsilon) - 2\log\left(\frac{\mu^2}{m_g^2}\right) + \frac{3-\varepsilon^2}{(2-\varepsilon)(1-\varepsilon)}\right]\delta(s) - \frac{2}{\mu^2}\left[\frac{\mu^2}{s}\right]_+\right\} \\
&= F_{1,\mathrm{div}}^J(s,\mu,\varepsilon) + F_{1,\mathrm{virt,ren}}^J + \mathcal{O}(\varepsilon)\,, \\
F_{1,\mathrm{virt,ren}}^J &= \frac{1}{8}\left[6\log\left(\frac{\mu^2}{m_g^2}\right) - 4\log^2\left(\frac{\mu^2}{m_g^2}\right) + 9 - 2\pi^2\right]\delta(s) - \log\left(\frac{\mu^2}{m_g^2}\right)\frac{1}{\mu^2}\left[\frac{\mu^2}{s}\right]_+\,.
\end{aligned} \tag{5.52}$$

The unexpanded result agrees with Eq. (365) of Ref. [29][9] and $F_{1,\mathrm{virt,ren}}^J$ in the expanded expression reproduces Eq. (33) of Ref. [31] up to a global factor of 2 that accounts for the fact that in that article jet function accounts for the two hemispheres combined. Besides, since the pole at $h=\varepsilon$ moves to zero when taking four dimensions in the Mellin plane, $F_{1,\mathrm{virt,ren}}^J$ can be obtained equivalently through the sum of $F_{1,\mathrm{ren}}^J(0,s,\mu)$ and $\Delta_0^\infty F_1^J(\hat{s}_g)$.

The real-radiation part is then obtained simply as the sum of residues of $\mathcal{M}_1^J(h,\hat{s}_g,0)$ to the left of the origin minus the radiative tail of the virtual contribution and it must vanish for $\hat{s}_g < 1$ as can be deduced from the top line in Eq. (5.51). The calculation can be done through the sum of the residues at $h=0$ (double), -1 and -2 (simple) setting $\varepsilon = 0$ before computing them:

$$F_{1,\mathrm{real}}^J = \frac{1}{s}\left[\frac{(1-\hat{s}_g)(1+3\hat{s}_g)}{4\hat{s}_g^2} + \log(\hat{s}_g)\right]\theta(\hat{s}_g - 1)\,, \tag{5.53}$$

again in agreement with Eq. (34) of Ref. [31] (once more up to the factor of two already mentioned). The one-loop correction to jet matching coefficient relating the jet functions in the theories with and without massive gluons is given by

$$J_n^{n_\ell}(s) = \int_0^s \mathrm{d}s'\mathcal{M}_J^{n_\ell\to n_g}(s-s')\,J_n^{n_g}(s')\,, \qquad \mathcal{M}_J^{n_\ell\to n_g} = \delta(s) - \frac{\alpha_s(\mu)}{\pi}C_F F_{1,\mathrm{virt,ren}}^J\,, \tag{5.54}$$

in agreement with Eq. (37) of Ref. [31] (once again we account for the factor of two). The gluon mass correction to the massless jet function can be written as

$$\Delta_0 F_1^J(s,m_g^2) \equiv \frac{1}{s}\tilde{F}_1^J(\hat{s}_g)\,, \tag{5.55}$$

[9] There is indeed a typo in that equation: there should be a minus sign in front of $H_{1-d/2}$.

From that, we define the following RG-evolved jet function that is the relevant object to carry out large-log resummation in differential and cumulative cross sections:

$$\tilde{F}_1^{\tilde{\omega}}(\hat{s}_g) = \int_0^{\hat{s}_g} \frac{\mathrm{d}s'}{s'} \left(1 - \frac{s'}{\hat{s}_g}\right)^{-1-\tilde{\omega}} \tilde{F}_1^J(s') = \int_{c-i\infty}^{c+i\infty} \frac{\mathrm{d}h}{2\pi i} \frac{(3h+4)\Gamma(h)\hat{s}_g^h}{2h^2(2+h)(1+h)(-\omega)_h}\,, \tag{5.56}$$

with $-1 < c < 0$ and where $(a)_n = \Gamma(a+n)/\Gamma(a)$ is the Pochhammer symbol. The convergence regions are identical as for the fixed-order case. Closing to the right one encounters only the triple pole at $h = 0$. Closing to the left there are double poles at $h = -1, -2$ and simple poles at $h = -k$ with $k \geqslant 3$. All in all, we find

$$\begin{aligned}\tilde{F}_1^{\tilde{\omega}}(\hat{s}_g) &= \frac{1}{2\hat{s}_g}\left\{[L_g - \psi^{(0)}(-\tilde{\omega})](\tilde{\omega}+1) + 5\tilde{\omega} + 4\right\} + \frac{1}{2}\sum_{n=3} \frac{1}{\hat{s}_g^n} \frac{(4-3n)(\tilde{\omega}+1)_n}{(n-2)(n-1)n^2 n!} \\ &\quad + \frac{1}{8\hat{s}_g^2}\left\{[L_g - \psi^{(0)}(-\tilde{\omega})](\tilde{\omega}+1)_2 + 2\tilde{\omega}(\tilde{\omega}+2) + 1\right\}, \\ &= L_g\left[\psi^{(0)}(-\omega) + \frac{3}{4}\right] - \frac{L_g^2}{2} - \frac{\psi^{(0)}(-\tilde{\omega})^2}{2} - \frac{3\psi^{(0)}(-\tilde{\omega})}{4} + \frac{\psi^{(1)}(-\tilde{\omega})}{2} - \frac{\pi^2}{12} - \frac{5}{8}\,,\end{aligned} \tag{5.57}$$

where $L_g = \log(\hat{s}_g) - \gamma_E$ and the trigamma function $\psi^{(1)}$ is the derivative of the digamma $\psi^{(0)}$. The series can be summed up and we find a closed form for the RG-evolved jet function:

$$\begin{aligned}\tilde{F}_1^{\tilde{\omega}}(\hat{s}_g) &= \frac{1}{2\hat{s}_g}\left\{[L_g - \psi^{(0)}(-\tilde{\omega})](\tilde{\omega}+1) + 5\tilde{\omega} + 4\right\} + \frac{1}{8\hat{s}_g^2}\left\{[L_g - \psi^{(0)}(-\tilde{\omega})](\tilde{\omega}+1)_2 + 2\tilde{\omega}(\tilde{\omega}+2) + 1\right\} \\ &\quad + \frac{(\tilde{\omega}+1)_3}{216\hat{s}_g^3}\left[4\,{}_4F_3\left(1,1,3,\tilde{\omega}+4;4,4,4;\hat{s}_g^{-1}\right) - 9\,{}_3F_2\left(1,1,\tilde{\omega}+4;4,4;\hat{s}_g^{-1}\right)\right].\end{aligned} \tag{5.58}$$

Plots for the exact result and the small-mass expansion are shown in Fig. 5.6. Nice convergence is achieved for any value of $\hat{s}_g$ (in particular, at threshold) and various values of the resummation parameter $\tilde{\omega}$.

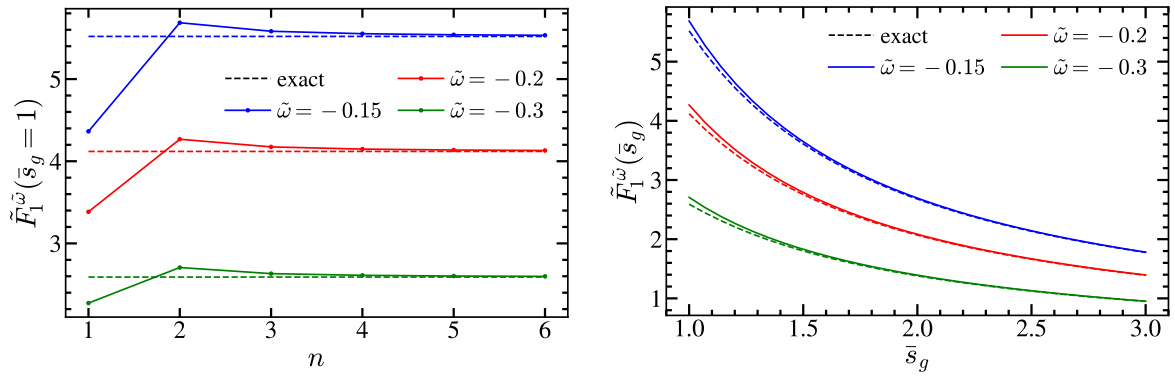

(a) (b)

Figure 5.6: Gluon mass correction to the massless RG-evolved jet function in its exact form (dashed), and expansions for small masses (solid lines) for three values of $\tilde{\omega}$: -0.15 (blue), -0.2 (red) and -0.3 (green). Left panel: small mass expansion of $\tilde{F}_1^{\tilde{\omega}}$ at threshold $\hat{s}_g = 1$ as a function of the expansion order n. Right panel: Dependence of $\tilde{F}_1^{\tilde{\omega}}$ with $\hat{s}_g$, including 2 non-zero terms in the small-mass expansion.

Secondary massive bubble

We proceed in the same way as in the previous section, switching between cumulative or differential to identify distributions and virtual corrections. To simplify expressions as much as possible, we define $\hat{s} = s/m^2$. In this case we also compute the expansion for the differential jet function prior to its RG evolution. The most relevant results before we discuss any expansion are the following:

$$\begin{aligned}
\mathcal{M}_2^{\Sigma_J}(h,\hat{s}_c,0) &= \frac{2(3h+4)(h+1)\Gamma^2(h)}{h^2\Gamma(2h+5)}\hat{s}_c^h \xrightarrow[|h|\gg 1]{} \frac{3\sqrt{\pi}}{8}\frac{1}{h^{11/2}}\left(\frac{\hat{s}_c}{4}\right)^h, \qquad (5.59)\\
F_{2,\text{div}}^J(s,\mu,\varepsilon) &= \left[\frac{1}{4\varepsilon^3}-\frac{1}{72\varepsilon^2}-\frac{1}{\varepsilon}\left(\frac{\pi^2}{72}+\frac{121}{432}\right)\right]\delta(s)+\left(\frac{5}{18\varepsilon}-\frac{1}{6\varepsilon^2}\right)\frac{1}{\mu^2}\left[\frac{\mu^2}{s}\right]_+,\\
F_{2,\text{ren}}^J(0,s,\mu,\varepsilon) &= \left(\frac{\zeta_3}{9}+\frac{17\pi^2}{108}-\frac{4057}{2592}\right)\delta(s)-\left(\frac{\pi^2}{18}-\frac{247}{216}\right)\frac{1}{\mu^2}\left[\frac{\mu^2}{s}\right]_+\\
&\quad -\frac{29}{36}\frac{1}{\mu^2}\left[\frac{\mu^2}{s}\log\left(\frac{s}{\mu^2}\right)\right]_+ + \frac{1}{6}\frac{1}{\mu^2}\left[\frac{\mu^2}{s}\log^2\left(\frac{s}{\mu^2}\right)\right]_+,\\
\Delta_0^\infty F_2^J(\hat{s}) &= -\frac{1}{6}\frac{1}{m^2}\left[\frac{1}{\hat{s}}\log^2(\hat{s})\right]_+ + \frac{29}{36}\frac{1}{m^2}\left[\frac{1}{\hat{s}}\log(\hat{s})\right]_+ - \left(\frac{359}{216}-\frac{\pi^2}{18}\right)\frac{1}{m^2}\left[\frac{1}{\hat{s}}\right]_+\\
&\quad +\left(\frac{4325}{1296}-\frac{2\zeta_3}{3}-\frac{29\pi^2}{216}\right)\delta(s).
\end{aligned}$$

From the first line we see that the expansion for small masses converges if $\hat{s} > 4$, that is, above threshold. Much as happened for the massive vector boson, below threshold one only has the contribution from the virtual diagrams, captured by the residue of the only pole with $h > 0$, sitting at $h = \varepsilon$ [after removing the massless limit and setting $\varepsilon = 0$, the pole moves to $h = 0$, making it of multiplicity 4, and one is left with the last line of Eq. (5.59)].

We can split the virtual and real-radiation contributions again, and compare to known results. In fact, the virtual terms of the massive corrections to the 2-loop massless jet function are given by $\Delta_0^\infty F_2^J(\hat{s})$, in agreement Ref. [56].[10] The non-distributional (or real-radiation) part is the sum of poles in the negative real axis minus the radiative tail, which is simply the sum of residues corresponding to all poles with $h \leqslant 0$ having set $\varepsilon = 0$ prior to its computation. The extra factor of h in $\mathcal{M}_2^J(h,\hat{m},0)$ makes the pole at $h = 0$ triple. The pole at $h = -2$ is double, while the rest of poles sitting at negative integer values of h are all simple. The result quoted below is valid only for $\hat{s} > 4$, since otherwise it identically vanishes, and the series is convergent in its whole domain of validity, as can be observed in Fig. 5.7(b):

$$\begin{aligned}
s\Delta_0 F_{2,\text{real}}^J &= \left\{\frac{359}{216}-\frac{\pi^2}{18}+\frac{1}{6}\log^2(\hat{s})-\frac{29}{36}\log(\hat{s})-\frac{\log(\hat{s})+1}{2\hat{s}^2}+\sum_{n=1}^{n\neq 2}\frac{4-3n}{3-2n}\frac{(2n-2)!}{\hat{s}^n(n-2)n(n!)^2}\right\}\theta(\hat{s}-4)\\
&= \left\{\frac{359}{216}-\frac{\pi^2}{18}+\frac{1}{6}\log^2(\hat{s})-\frac{29}{36}\log(\hat{s})-\frac{1}{\hat{s}}-\frac{\log(\hat{s})+1}{2\hat{s}^2}+\frac{1}{\hat{s}^3}\left[{}_3F_2\left(1,1,\frac{3}{2};3,4;\frac{4}{\hat{s}}\right)\right.\right.\\
&\quad \left.\left.-\frac{7}{9}\,{}_3F_2\left(1,1,\frac{3}{2};4,4;\frac{4}{\hat{s}}\right)+\frac{4}{27}\,{}_4F_3\left(1,1,\frac{3}{2},3;4,4,4;\frac{4}{\hat{s}}\right)\right]\right\}\theta(\hat{s}-4) \qquad (5.60)
\end{aligned}$$

where to get to the last equality we have summed up the infinite series. This result is equivalent to Eq. (42) of Ref. [56], which is expressed in terms of logarithms and a dilogarithm. As can be seen in

[10] Despite appearances, Eq. (41) of Ref. [56] is μ-independent as it should: the dependence on the renormalization scale is entirely contained in the massless jet function.

Fig. 5.7(a), indeed our result for $\Delta_0 F^J_{1,\text{real}}$ exactly vanishes at $\hat{s} = 4$.

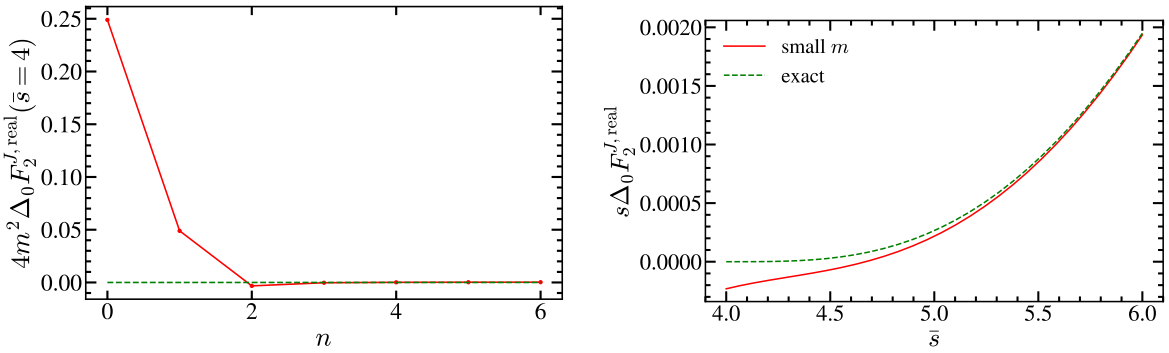

(a) (b)

Figure 5.7: Secondary mass corrections to the jet function: real radiation part. We show exact results as a green dashed line, and the expansions for small masses as a red solid line. Left panel: small mass expansion of $m^2\Delta_0 F^J_{1,\text{real}}$ at threshold $\hat{s} = 4$ as a function of the expansion order n. Right panel: Dependence of $m^2\Delta_0 F^J_{1,\text{real}}$ with $\hat{s}$, including 6 non-zero terms in the expansion.

The jet matching condition, defined as in Eq. (4.92) for the bHQET case, is obtained using Eq. (5.14), and the obtained result

$$\mathcal{M}_J = \delta(s) + \left[\frac{\alpha_s(\mu)}{\pi}\right]^2 T_F\, C_F \mathcal{M}_J^{(2)}(m,s,\mu)\,, \tag{5.61}$$

$$\begin{aligned}\mathcal{M}_J^{(2)}(m,s,\mu) = &\left[\frac{29}{72}\log^2\left(\frac{\mu^2}{m^2}\right) - \frac{1}{18}\log^3\left(\frac{\mu^2}{m^2}\right) - \left(\frac{233}{216} + \frac{\pi^2}{36}\right)\log\left(\frac{\mu^2}{m^2}\right) - \frac{5\zeta_3}{9}\right.\\ &\left. + \frac{5\pi^2}{216} + \frac{1531}{864}\right]\delta(s) + \left[\frac{5}{9}\log\left(\frac{\mu^2}{m^2}\right) - \frac{1}{6}\log^2\left(\frac{\mu^2}{m^2}\right) - \frac{14}{27}\right]\frac{1}{\mu^2}\left[\frac{\mu^2}{s}\right]_+,\end{aligned}$$

in agreement with Eq. (46) of Ref. [56] if setting $\mu_m = \mu_J$ after accounting for the factor of 2 explained already.

We discuss next the RG-evolved jet function, defined as in Eqs. (5.55) and (5.56), and considering once more only the evolution of the correction to the massless result. From the inverse Mellin transform we find for the jet function:

$$\tilde{F}_2^{\tilde{\omega}}(\hat{s}) = \int_0^{\hat{s}} \frac{\mathrm{d}s'}{s'}\left(1 - \frac{s'}{\hat{s}}\right)^{-1-\tilde{\omega}} \tilde{F}_2^J(s') = \int_{c-i\infty}^{c+i\infty} \frac{\mathrm{d}h}{2\pi i} \frac{2(h+1)(3h+4)\Gamma^3(h)\hat{s}^h}{h\Gamma(2h+5)(-\omega)_h}\,, \tag{5.62}$$

where the convergence radius does not depend on $\tilde{\omega}$. Once again, closing to right for $\hat{s} < 4$ one picks only the multiplicity-4 pole at $h = 0$ corresponding to the virtual radiation contribution. For $\hat{s} > 4$ one closes to the left, finding an infinite number of poles sitting at integer negative values of h: double at

$h=-2$, simple otherwise. Defining $L=\log(\hat{s})-\gamma_E-\psi^{(0)}(-\tilde{\omega})$ we obtain the following results:

$$\begin{aligned}\tilde{F}_2^{\tilde{\omega}}(\hat{s}) &= \frac{29L^2}{72}-\frac{L^3}{18}+\frac{L}{216}\left[36\psi^{(1)}(-\tilde{\omega})+6\pi^2-359\right] \\ &\quad+\frac{1}{1296}\left[72\psi^{(2)}(-\tilde{\omega})-522\psi^{(1)}(-\tilde{\omega})-720\zeta_3-87\pi^2+4325\right] \\ &= -\frac{1}{8\hat{s}^2}\left\{\left[L^2-\frac{\pi^2}{6}-\psi^{(1)}(-\tilde{\omega})\right](\tilde{\omega}+1)_2+L[\tilde{\omega}(5\tilde{\omega}+11)+4]+\tilde{\omega}(7\tilde{\omega}+11)+1\right\} \\ &\quad+\sum_{n=1}^{n\neq 2}\frac{(3n-4)(2n-2)!(\tilde{\omega}+1)_n}{\hat{s}^n n(n-2)(2n-3)(n!)^3}\left[L+3H_n-2H_{2n-2}+\psi^{(0)}(-\tilde{\omega})-\psi^{(0)}(-n-\tilde{\omega})\right. \\ &\quad\left.+\frac{12n^3-45n^2+56n-24}{n(n-2)(2n-3)(3n-4)}\right].\end{aligned} \tag{5.63}$$

The infinite sum can be carried out and one obtains an analytic expression in terms of MeijerG functions. We find it more convenient to carry out the sum, adding as many terms as necessary to achieve the desired numerical accuracy. For efficient computer implementations, it is convenient to express $\psi^{(0)}(-n-\tilde{\omega})$ in terms of $\psi^{(0)}(-\tilde{\omega})$ as follows:

$$\psi^{(0)}(-n-\tilde{\omega})=\psi^{(0)}(-\tilde{\omega})+\sum_{i=1}^{n}\frac{1}{i+\tilde{\omega}}\,. \tag{5.64}$$

In Fig. 5.8 we show the good convergence of the small-mass expansion, and how it agrees with the single term corresponding to the virtual radiation contribution at $\hat{s}=4$. The agreement of the two series is a strong cross-check on our results.

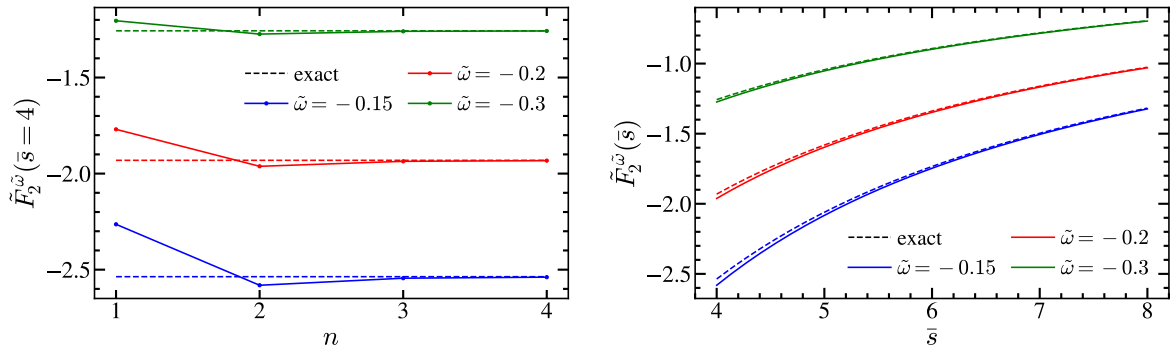

(a) (b)

Figure 5.8: Secondary mass correction to the massless RG-evolved jet function in its exact form (dashed), and expansions for small masses (solid lines) for three values of $\tilde{\omega}$: -0.15 (blue), -0.2 (red) and -0.3 (green). Left panel: small mass expansion of $\tilde{F}_2^{\tilde{\omega}}$ at threshold $\hat{s}=4$ as a function of the expansion order n. Right panel: Dependence of $\tilde{F}_2^{\tilde{\omega}}$ with $\hat{s}$, including two non-zero terms in the small-mass expansion.

If applying the strict EFT philosophy, when the secondary quark is no longer active (that is, if $\mu_m>\mu_J$), the secondary quark simply and plainly does not participate in the jet function. The matching condition

$\mathcal{M}_J$ accounts for the discrepancy of the two EFTs in the UV. Since the two theories are required to agree for $m \to \infty$, the matching condition takes into account only the virtual radiation, as real emissions cannot occur in this limit. However, as already discussed in Sec. 1.4.1 (and Sec. 4.5 for bHQET), one can make the transition between the two scenarios smoother by including the mass-suppressed real-radiation contribution not accounted for in $\mathcal{M}_J$, which will naturally become increasingly small as $\hat{s}$ decreases. This "improved" n_ℓ-flavored jet function is simply:

$$J_n^{(n_\ell)}(s,\mu,m) = J_n^{(n_\ell)}(s,\mu,0) + \left[\frac{\alpha_s^{(n_\ell)}(\mu)}{\pi}\right]^2 C_F T_F \Delta_\infty F_2^J(\hat{s})\,, \tag{5.65}$$

that agrees with the EFT result $J_n^{(n_\ell)}(s,\mu,0)$ in the limit $m \to \infty$. In Ref. [56], this mass-modified jet function is obtained from the n_f jet function computation using an OS renormalization factor $Z_J^{\rm OS}$. Even if different in spirit, the results are of course equivalent.

5.6 bHQET computations

We consider now the situation of jets produced by boosted heavy primary quarks [see Eq. (1.67)]. We will compute the mass corrections from secondary quarks to the matching between SCET and bHQET and the bHQET hemisphere jet function. Even though these results were already obtained in the previous Chapter, in this section we apply the Mellin-Barnes procedure developed in this Chapter which, as we shall see, turns out to be much easier. It also leads to much more efficient expressions for numerical evaluations than the ones we could get from the dispersive integral method (see appendix C.1), and allows for an analytic evolution of the bHQET jet function, which could only be carried out numerically if the exact results were used.

Therefore, in this section, instead of just taking the one loop results with a modified gluon propagator first obtained in Ref. [27], as we have done in previous sections, we will carry out those computations anew. As we will see, it will be instructive to compare those with the corresponding dispersive integral method as carried out in Chapter 4. Additionally we will calculate the contribution from massive gluons to those matrix elements as an expansion.

5.6.1 bHQET Hard function

One loop computations

As was done in previous Chapters, we take the ratio of form factors in SCET and bHQET to obtain the matching coefficient, as those are the simplest matrix elements one can come up with. If using dimensional regularization to take care of IR and collinear singularities, since our gluon is massless even for a modified propagator, all Feynman diagrams for the form factor in bHQET are scaleless and vanish. Therefore, the matching coefficient is simply the SCET form factor in dimensional regularization.

For a change, in this section we will regulate IR divergences with off-shellness $\Delta^2 \equiv p^2 - M^2 \equiv \bar{p}^2 - M^2$, (with p, $\bar{p}$ the quark, anti-quark momentum) since in this way we can see explicitly the cancellation of IR divergences, and these results, to the best of our knowledge, have not been provided before. Additionally, they can be used to get the individual SCET and bHQET contributions directly from the inverse Mellin without relying on consistency conditions, but we shall not follow this path to avoid duplicating the computations.[11]

[11] One just needs to consider the poles corresponding to $\Delta \to 0$ limit.

The Feynman diagrams that contribute both in SCET and bHQET (albeit with different Feynman rules) are shown in Fig. 4.6, where one has to use the appropriate gluon propagator. We will denote the quantities related to the form factors with **F** as in Sec. 4.4. This should not be confused with F from Eq. (5.9).

- **Collinear Contribution:**

  Applying SCET Feynman rules to diagram 4.6(a) leads to:

$$\begin{aligned}\mathbf{F}^{h,(a)}_{\text{SCET}} &= -\,i8\pi\alpha_s C_F\tilde{\mu}^{2\varepsilon}\, I^{h,a}\,, \\ I^{h,a} &\equiv \int \frac{\mathrm{d}^d l}{(2\pi)^d\,(-1)^{1-h}}\,\frac{\bar{n}\cdot(p-l)}{[l^2+i0]^{1-h}\,[\bar{n}\cdot l+i0]\,[(p-l)^2-M^2+i0]}\,,\end{aligned} \tag{5.66}$$

  where in this case the 0-bin subtraction integral is zero, as can be seen through Georgi parameters:

$$\begin{aligned}I^{h,a}_{0-\text{bin}} &= \int \frac{\mathrm{d}^d l}{(2\pi)^d\,(-1)^{1-h}}\,\frac{1}{[l^2+i0]^{1-h}\,[\bar{n}\cdot l+i0]\left[-n\cdot l+\frac{\Delta^2}{Q}+i0\right]} \\ &= -\,\frac{i\Gamma(1+\varepsilon-h)}{2^{2-2\varepsilon}\pi^{2-\varepsilon}\Gamma(1-h)}\int_0^\infty \mathrm{d}\lambda_2\,\left[-2\frac{\Delta^2}{Q}+4\lambda_2\right]^{h-\varepsilon-1}\int_0^\infty \mathrm{d}\lambda_1\,\lambda_1^{h-\varepsilon-1}=0\,.\end{aligned} \tag{5.67}$$

  Using the residue theorem to carry out the l^+ integration, followed by the integration of the perpendicular component, we obtain:

$$I^{h,(a)} = \frac{-i}{2^{4-2\varepsilon}\pi^{2-\varepsilon}}\frac{\Gamma(\varepsilon-h)}{\Gamma(1-h)}\int_0^1 \mathrm{d}z\,(1-z)^{1-h}\,z^{h-\varepsilon-1}\left[(\Delta^2+M^2)z-\Delta^2\right]^{h-\varepsilon}\,, \tag{5.68}$$

  which yields a Gaussian hypergeometric function that must be power expanded in Δ^2 to get:

$$\begin{aligned}\mathbf{F}^{h,(a)}_{\text{SCET}} = -\,\frac{\alpha_s C_F\tilde{\mu}^{2\varepsilon}}{2^{1-2\varepsilon}\pi^{1-\varepsilon}}\left(M^2\right)^{h-\varepsilon}\Bigg\{&\frac{\Gamma(h-\varepsilon)\Gamma(2\varepsilon-2h)}{\Gamma(1-h)}\left(-\frac{\Delta^2}{M^2}\right)^{2(h-\varepsilon)} \\ &+\frac{2^{2(h-\varepsilon)}(1-h)}{2\sqrt{\pi}}\,\frac{\Gamma(\varepsilon-h)\Gamma(h-\varepsilon)\Gamma(h-\varepsilon+1/2)}{\Gamma(2+h-2\varepsilon)}\Bigg\}\,.\end{aligned} \tag{5.69}$$

  The bHQET counterpart for this diagram is:

$$\begin{aligned}\mathbf{F}^{h,(a)}_{\text{bHQET}} &= i4\pi\alpha_s C_F\tilde{\mu}^{2\varepsilon}\,(\bar{n}\cdot v_+)\;I^{h,a}\,, \\ I^{h,a} &\equiv \int \frac{\mathrm{d}^d l}{(2\pi)^d\,(-1)^{1-h}}\,\frac{1}{[l^2+i0]^{1-h}\,[\bar{n}\cdot l-i0]\left[v_+\cdot l+\frac{\Delta^2}{2M}+i0\right]}\,.\end{aligned} \tag{5.70}$$

  We first use Georgi parameters to again show that 0-bin subtractions identically vanish:

$$\begin{aligned}I^{h,a}_{0-\text{bin}} &= \int \frac{\mathrm{d}^d l}{(2\pi)^d\,(-1)^{1-h}}\,\frac{1}{[l^2+i0]^{1-h}\,[\bar{n}\cdot l-i0]\left[\frac{Q}{2M}\,n\cdot l+\frac{\Delta^2}{2M}+i0\right]} \\ &= \frac{i\Gamma(1+\varepsilon-h)}{2^{2-2\varepsilon}\pi^{2-\varepsilon}\Gamma(1-h)}\int_0^\infty \mathrm{d}\lambda_2\,\left[-\frac{\Delta^2}{M}+2\lambda_2\frac{Q}{M}\right]^{h-\varepsilon-1}\int_0^\infty \mathrm{d}\lambda_1\,\lambda_1^{h-\varepsilon-1}=0\,,\end{aligned} \tag{5.71}$$

and then to solve the integral:

$$\mathbf{F}^{h,(a)}_{\text{bHQET}} = -\frac{\alpha_s C_F \tilde{\mu}^{2\varepsilon}\,(\bar{n}\cdot v_+)}{2^{-2\varepsilon}\pi^{1-\varepsilon}}\frac{\Gamma(1+\varepsilon-h)}{\Gamma(1-h)}\int_0^\infty \mathrm{d}\lambda_1\,\mathrm{d}\lambda_2\;(\lambda_2)^{h-\varepsilon-1}\left[2\lambda_1\,(\bar{n}\cdot v_+)+\lambda_2-\frac{\Delta^2}{M}\right]^{h-\varepsilon-1}$$
$$= -\frac{\alpha_s C_F \tilde{\mu}^{2\varepsilon}}{2^{1-2\varepsilon}\pi^{1-\varepsilon}}\left(M^2\right)^{h-\varepsilon}\frac{\Gamma(h-\varepsilon)\Gamma(2\varepsilon-2h)}{\Gamma(1-h)}\left(-\frac{\Delta^2}{M^2}\right)^{2(h-\varepsilon)}. \tag{5.72}$$

We double these results to account also for diagram (b). We can take the difference of SCET and bHQET results already at this stage, and we observe that the IR divergent terms exactly cancel for any value of h and ε, as expected. We keep them apart since we aim to isolate the form factor for each EFT separately.

- **Soft Contribution:**

The contribution form the exchange of a soft gluon between the two collinear sectors coincides in both EFTs as expected, hence cancels in the difference. The result will nevertheless be important to isolate each form factor. We obtain

$$\mathbf{F}^{h,(c)}_{\text{th}} = -i8\pi\alpha_s C_F\tilde{\mu}^{2\varepsilon}\,I^{h,c}, \tag{5.73}$$
$$I^{h,c} \equiv \int\frac{\mathrm{d}^d l}{(2\pi)^d\,(-1)^{1-h}}\frac{1}{[l^2+i0]^{1-h}\left[\bar{n}\cdot l+\frac{\Delta^2}{Q}+i0\right]\left[-n\cdot l+\frac{\Delta^2}{Q}+i0\right]},$$

with $\text{th} = \text{SCET}, \text{bHQET}$. The resulting integral can be solved once more through Georgi parametrization:

$$\mathbf{F}^{h,(c)}_{\text{th}} = \frac{\alpha_s C_F\tilde{\mu}^{2\varepsilon}}{2^{-1-2\varepsilon}\pi^{1-\varepsilon}}\frac{\Gamma(1+\varepsilon-h)}{\Gamma(1-h)}\int_0^\infty \mathrm{d}\lambda_1\,\mathrm{d}\lambda_2\left[-4\lambda_1\lambda_2-2(\lambda_1+\lambda_2)\frac{\Delta^2}{Q}\right]^{h-\varepsilon-1} \tag{5.74}$$
$$= -\frac{\alpha_s C_F\tilde{\mu}^{2\varepsilon}}{2^{1-2\varepsilon}\pi^{1-\varepsilon}}(Q^2)^{h-\varepsilon}\frac{\Gamma^2(\varepsilon-h)\Gamma(1+h-\varepsilon)(-1)^{h-\varepsilon}}{\Gamma(1-h)}\left(\frac{\Delta^2}{Q^2}\right)^{2(h-\varepsilon)}.$$

- **On-shell wave function renormalization constant:**

Since we are using an off-shellness, self-energy diagrams will contribute in both EFTs, and

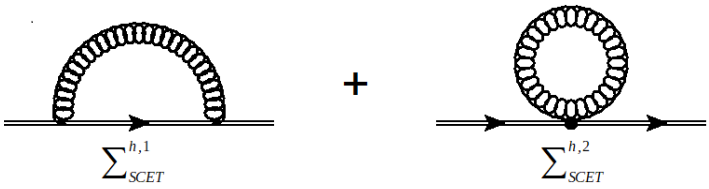

Figure 5.9: SCET quark self-energy

since the UV behavior of both theories differs, they will not coincide. The diagrams contributing

to the SCET quark self-energy are depicted in Fig. 5.9 and read:

$$\begin{aligned}\Sigma^{h,1}_{\text{SCET}} &= i4\pi\alpha_s C_F\tilde{\mu}^{2\varepsilon}\int\frac{\mathrm{d}^d l}{(2\pi)^d\,(-1)^{1-h}}\frac{1}{\left[l^2+i0\right]^{1-h}\left[(p-l)^2-M^2+i0\right]} \\ &\quad\times\left[2dM^2-\frac{(d-2)\,M^2\,\bar{n}\cdot(p-l)}{\bar{n}\cdot p}+\frac{(d-2)\,\bar{n}\cdot p\,(l_\perp^2-M^2)}{\bar{n}\cdot(p-l)}\right] \\ \Sigma^{h,2}_{\text{SCET}} &= -\,i4\pi\alpha_s C_F\tilde{\mu}^{2\varepsilon}\int\frac{\mathrm{d}^d l}{(2\pi)^d\,(-1)^{1-h}}\frac{(d-2)\,\bar{n}\cdot p}{\left[l^2+i0\right]^{1-h}\left[\bar{n}\cdot(p-l)\right]}\,.\end{aligned} \tag{5.75}$$

Taking into account that 0-bin subtractions are power suppressed and hence do not contribute, the sum of both gives:

$$\begin{aligned}\Sigma^{h}_{\text{SCET}} &= \Sigma^{h,1}_{\text{SCET}}+\Sigma^{h,2}_{\text{SCET}} \\ &= i4\pi\alpha_s C_F\tilde{\mu}^{2\varepsilon}\int\frac{\mathrm{d}^d l}{(2\pi)^d\,(-1)^{1-h}}\frac{1}{\left[l^2+i0\right]^{1-h}\left[(p-l)^2-M^2+i0\right]} \\ &\quad\times\left[2dM^2-\frac{(d-2)\,M^2\,\bar{n}\cdot(p-l)}{\bar{n}\cdot p}-(d-2)\,\bar{n}\cdot p\;\;n\cdot(p-l)\right] \\ &= -\,\frac{\alpha_s C_F\tilde{\mu}^{2\varepsilon}}{2^{2-2\varepsilon}\pi^{1-\varepsilon}}\frac{\Gamma(\varepsilon-h)}{\Gamma(1-h)}\int_0^1\mathrm{d}z\,(1-z)^{-1-h}\left\{\frac{2(1-\varepsilon)^2}{\varepsilon-h-1}\left[M^2z^2+\Delta^2(z-1)z\right]^{h-\varepsilon+1}\right. \\ &\quad\left.+\left[M^2z^2+\Delta^2(z-1)z\right]^{h-\varepsilon}\left[(8-4\varepsilon)M^2(z-1)+2(1-\varepsilon)M^2(z-1)^2+2(1-\varepsilon)M^2\right]\right\}\end{aligned} \tag{5.76}$$

where we first integrated the plus component by residues and then carried out the perp integral. After taking the derivative with respect to the off-shellness, solving the last integral and expanding the result in Δ^2 we obtain for the renormalization constant at one loop the following result:

$$\begin{aligned}Z^{\text{OS},h}_{\psi,\text{SCET}} = \left[\frac{\mathrm{d}\Sigma^h_{\text{SCET}}}{\mathrm{d}\Delta^2}\right]_{\Delta^2\to 0} &= \frac{\alpha_s C_F\tilde{\mu}^{2\varepsilon}}{2^{2-2\varepsilon}\pi^{1-\varepsilon}}\frac{\Gamma(\varepsilon-h)}{\Gamma(1-h)}\left(M^2\right)^{h-\varepsilon}\left\{4(2h-2\varepsilon+1)\Gamma(1+h-\varepsilon)\right. \\ &\quad\times\left(\frac{\Delta^2}{M^2}\right)^{2(h-\varepsilon)}\left[\frac{\Gamma(2\varepsilon-2h-1)}{\Gamma(\varepsilon-h)}+\frac{(-1)^{h-\varepsilon}\Gamma(1+h-\varepsilon)}{\Gamma(2+2h-2\varepsilon)}\right] \\ &\quad\left.-\,\frac{2(2\varepsilon-3)(\varepsilon-h-1)\Gamma(2-h)\Gamma(-2\varepsilon+2h+1)}{\Gamma(-2\varepsilon+h+3)}\right\}.\end{aligned} \tag{5.77}$$

The bHQET quark self-energy diagrams were already shown in Fig. 4.7 but since our gluon is massless, the quark bilinear term ΔM vanishes[12]

$$\begin{aligned}\Sigma^h_{\text{bHQET}} &= 4\pi\alpha_s C_F\tilde{\mu}^{2\varepsilon}\int\frac{\mathrm{d}^d l}{(2\pi)^d\,(-1)^{1-h}}\frac{1}{\left[l^2+i0\right]^{1-h}\left[v\cdot l+\frac{\Delta^2}{2M}+i0\right]} \\ &= \frac{-i\alpha_s C_F\tilde{\mu}^{2\varepsilon}}{2^{1-2\varepsilon}\pi^{1-\varepsilon}}\frac{\Gamma(\varepsilon-h)}{\Gamma(1-h)}\Gamma(1+h-\varepsilon)\left(\frac{\Delta^2}{M}\right)^{2(h-\varepsilon)+1} \\ &\quad\times\left[\frac{\Gamma(2\varepsilon-2h-1)}{\Gamma(\varepsilon-h)}+\frac{(-1)^{h-\varepsilon}\Gamma(1+h-\varepsilon)}{\Gamma(2+2h-2\varepsilon)}\right].\end{aligned} \tag{5.78}$$

[12]The off-shellness in not an actual scale but a regulator.

Georgi parametrization was again used to solve the integral. Applying the on-shell condition we end up with:

$$\begin{aligned} Z^{\mathrm{OS},h}_{\psi,\mathrm{bHQET}} &= 2iM\left[\frac{\mathrm{d}}{\mathrm{d}\Delta^2}\Sigma^h_{\mathrm{bHQET}}\right]_{\Delta^2\to 0} \\ &= \frac{\alpha_s C_F \tilde{\mu}^{2\varepsilon}}{2^{-2\varepsilon}\pi^{1-\varepsilon}}(2h-2\varepsilon+1)\left(M^2\right)^{h-\varepsilon}\frac{\Gamma(\varepsilon-h)\Gamma(1+h-\varepsilon)}{\Gamma(1-h)}\left(\frac{\Delta^2}{M^2}\right)^{2(h-\varepsilon)} \\ &\quad\times\left[\frac{\Gamma(2\varepsilon-2h-1)}{\Gamma(\varepsilon-h)}+\frac{(-1)^{h-\varepsilon}\Gamma(1+h-\varepsilon)}{\Gamma(2+2h-2\varepsilon)}\right]. \end{aligned} \tag{5.79}$$

As expected, the difference of self-energies is also finite in the $\Delta \to 0$ limit. This comes at no surprise, since this cancellation already occurred in the difference of collinear contributions and the soft diagrams are identical in both EFTs.

Altogether, the one-loop results for the form factors with modified massless gluon propagator and regularization of IR singularities through an off-shellness are:

$$\begin{aligned} \mathbf{F}^h_{\mathrm{SCET}} &= \frac{\alpha_s C_F\left(\mu^2 e^{\gamma_E}\right)^{\varepsilon}}{2\pi}\left(M^2\right)^{h-\varepsilon}\left\{2(h-1)\left(1+\frac{(3-2\varepsilon)(\varepsilon-h-1)(\varepsilon-h)}{2+h-2\varepsilon}\right)\frac{\Gamma(\varepsilon-h)\Gamma(2h-2\varepsilon)}{\Gamma(2+h-2\varepsilon)}\right. \\ &\quad+\frac{2^{1+2(\varepsilon-h)}(-1)^{2(h-\varepsilon)}(1+\varepsilon-h)\pi^{3/2}\csc\left[2(\varepsilon-h)\pi\right]}{(\varepsilon-h)\Gamma(1-h)\Gamma(1/2-\varepsilon+h)}\left(\frac{\Delta^2}{M^2}\right)^{2(h-\varepsilon)} \\ &\quad\left.-\frac{\Gamma^2(\varepsilon-h)\Gamma(1+h-\varepsilon)(-1)^{h-\varepsilon}}{\Gamma(1-h)}\left(\frac{\Delta^4}{M^2Q^2}\right)^{h-\varepsilon}\right\}, \end{aligned} \tag{5.80}$$

and

$$\begin{aligned} \mathbf{F}^h_{\mathrm{bHQET}} &= \frac{\alpha_s C_F\left(\mu^2 e^{\gamma_E}\right)^{\varepsilon}}{2\pi}\left(M^2\right)^{h-\varepsilon}\left\{\frac{2^{1+2(\varepsilon-h)}(-1)^{2(h-\varepsilon)}(1+\varepsilon-h)\pi^{3/2}\csc\left[2(\varepsilon-h)\pi\right]}{(\varepsilon-h)\Gamma(1-h)\Gamma(1/2-\varepsilon+h)}\left(\frac{\Delta^2}{M^2}\right)^{2(h-\varepsilon)}\right. \\ &\quad\left.-\frac{\Gamma^2(\varepsilon-h)\Gamma(1+h-\varepsilon)(-1)^{h-\varepsilon}}{\Gamma(1-h)}\left(\frac{\Delta^4}{Q^2M^2}\right)^{h-\varepsilon}\right\}. \end{aligned} \tag{5.81}$$

In the previous expressions, as long as h and ε are kept arbitrary, one can take $\Delta^2 \to 0$, and in dimensional regularization the limit simply kills all non-analytic terms in Δ, recovering the same result found in Ref. [27]. Notice that bHQET form factor only contains terms depending on the IR regulator, so it indeed vanishes in dimreg, and cancels all the SCET Δ^2-terms when taking the difference of the two to render the matching coefficient.

On the other hand, one can also plug these results into Eqs. (5.9) and (5.12), and take $\Delta^2 \to 0$ limit after computing the Mellin inverse to obtain the corresponding form factor contributions in each theory. However, in order to stick to the line argument of this Chapter, this possibility is left for future work and we will consider only the difference of the one-loop results to compute directly the matching. We then employ consistency conditions to obtain each EFT part separately. Therefore, the input for our Mellin procedure will be $\mathcal{Q}^2 = M^2$ and

$$\begin{aligned} m_1^h(h,\varepsilon) &= \frac{1}{2}\frac{(1-h)\Gamma(1-h+\varepsilon)\Gamma(1+2h-2\varepsilon)}{\Gamma(3+h-2\varepsilon)(h-\varepsilon)^2} \\ &\quad\times\left\{2+h^2(3-2\varepsilon)+4h(1-\varepsilon)^2-\varepsilon[5-(5-2\varepsilon)\varepsilon]\right\}, \end{aligned} \tag{5.82}$$

where we spot a double pole at $h = \varepsilon$, expected due to the presence of Wilson lines.

Massive gluon

In this section we use again the dimensionless variable $\xi_g = m_g/M$ defined in Sec. 5.4.1. The most relevant results to be presented before turning to the small- and large-m_g expansions are the following:

$$\begin{aligned}
\mathcal{M}_1^m(h,0,\xi_g) &= \frac{[2+h(3h+4)]\Gamma^2(2-h)\Gamma(2h)\xi_g^{-2h}}{h^2(1-h^2)(h+2)} \xrightarrow[|h|\gg 1]{} -\frac{3\pi^{\frac{3}{2}}\csc^2(\pi h)}{2\sqrt{h}}\left(\frac{\xi_g}{2}\right)^{-2h}, \qquad (5.83)\\
F_{1,\text{div}}^m(M,\mu,\varepsilon) &= \frac{1}{2\varepsilon^2}+\frac{1}{4\varepsilon}\left[2\log\left(\frac{\mu^2}{M^2}\right)+1\right],\\
F_{1,\text{ren}}^m(0,M,\mu) &= 1+\frac{\pi^2}{24}+\frac{1}{4}\log^2\left(\frac{\mu^2}{M^2}\right)+\frac{1}{4}\log\left(\frac{\mu^2}{M^2}\right),\\
\Delta_0^\infty F_1^m(\xi_g) &= \frac{1}{8}-\frac{\pi^2}{4}-\log^2(\xi_g)-\frac{1}{2}\log(\xi_g).
\end{aligned}$$

The form of the $1/\varepsilon^n$ terms on the second line makes clear the result cannot correspond to a SCET computation, since in this EFT the primary mass is an infrared scale and UV divergences can only depend on UV physics. The result in the second line agrees with the known 1-loop result, computed for the first time in Ref. [24], see Eq. (131) therein.

The result in the last line of Eq. (5.83) comes from the triple pole at $h = 0$. From the first line of Eq. (5.83) one can see that the small and large gluon mass expansions will converge for m_g smaller or larger that $2M$, respectively. On the negative real axis there are double poles at $h = -1$ and -2, and simple poles in all other negative integer and half-integer values of h. The pole sitting at $h = -1/2$ reflects a linear sensitivity to IR momentum and is directly related to the $u = 1/2$ renormalon found in Ref. [27]. On the positive real axis one finds a triple pole at $h = 1$ and double poles at all other integer values of h. All in all, we find

$$\begin{aligned}
\Delta_0 F_1^m(\xi_g) &= -\xi_g^2\left[\log(\xi_g)+\frac{1}{4}\right]+\frac{3}{16}\xi_g^4\big[4\log(\xi_g)-3\big]-\sum_{n=1}^{n\neq 2,n\neq 4}\big(-\xi_g\big)^n\,\frac{(n+2)(3n^2-8n+8)\Gamma^2\big(\frac{n}{2}+1\big)}{(n-4)(n-2)n^3(n-1)!}\\
&= \Delta_0^\infty F_1^m+\frac{3}{2}\xi_g^{-2}+\sum_{n=2}\xi_g^{-2n}\,\frac{(2n-1)!}{[(n+2)!]^2}\left\{\frac{8+22n+20n^2+9n^3-2n^4-3n^5}{n}\right.\\
&\quad\left.-2(n^2-1)(n+2)(3n^2+4n+2)\big[\log(\xi_g)+H_{n-1}-H_{2n-1}\big]\right\}. \qquad (5.84)
\end{aligned}$$

The expansion for small m_g can be summed up and we find the following analytic result:

$$\Delta_0 F_1^m = \frac{10\xi_g^2-4-3\xi_g^4}{4r_g}\xi_g\log\left(\frac{\xi_g+r_g}{2}\right)-\log^2\left(\frac{\xi_g+r_g}{2}\right)-\frac{\pi^2+3\xi_g^2+\xi_g^2(4-3\xi_g^2)\log(\xi_g)}{4}, \qquad (5.85)$$

with $r_g = \sqrt{\xi_g^2-4}$. The expression above has all terms manifestly real for $\xi_g \geq 2$. For $\xi_g < 2$ the result is also real-valued, but to have all terms manifestly real one has to make the following replacements: $r_g \to \hat{r}_g = \sqrt{\xi_g^2-4}$, $\log^2[(\xi_g+r_g)/2] \to -\arctan^2(\hat{r}_g\xi_g)$ and $\log[(\xi_g+r_g)/2]/r_g \to \arctan(\hat{r}_g/\xi_g)/\hat{r}_g$. At the limiting value one gets of course a finite result, $\Delta_0 F_1^m(\xi_g = 2) = 8\log(2)-6-\pi^2/4$.

In Fig. 5.10 we study the convergence of the small and large gluon mass series. The small mass expansion has an oscillatory behavior, and converges at a slower pace than its large-mass counterpart. We observe that the latter needs many terms to approach the exact value at the limiting value $\xi_g = 2$, hence it is

also slowly convergent.

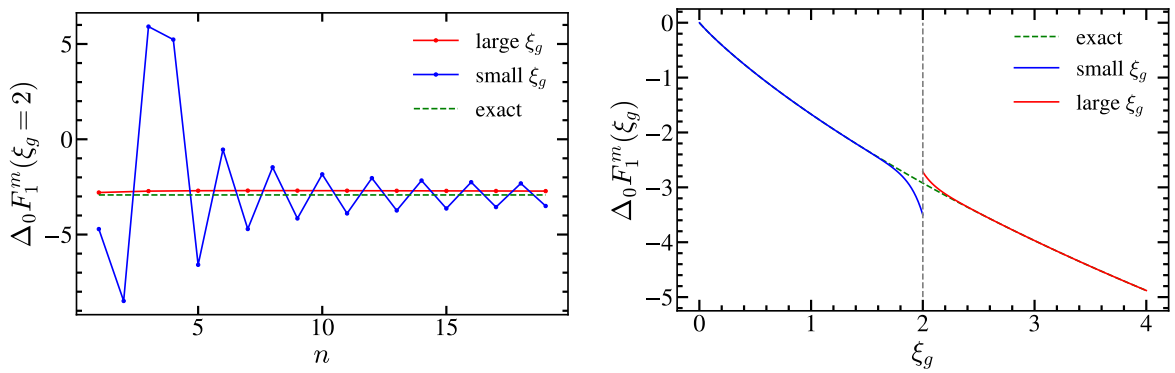

(a) (b)

Figure 5.10: Gluon mass correction to the massless Wilson coefficient relating the dijet operators in SCET and bHQET in its exact form (dashed green), small- (blue) and large-mass (red) expansions. Left panel: $\Delta_0 F_1^m$ at the boundary between the mass expansions $\xi_g = 2$, as a function of the expansion order n of each series. Right panel: Dependence of $\Delta_0 F_1^m(\xi_g)$ with the reduced gluon mass, including 20 and 10 non-zero terms in the small- and large-mass expansions, respectively.

Next we compute the matching condition $\mathcal{M}_{\rm bHQET}^{n_g \to n_\ell}$ at one loop, which coincides with the bHQET massive gluon form factor $\mathbf{F}_1^{\rm bHQET}$ and is obtained from the $m_g \to \infty$ limit of the SCET to bHQET Wilson coefficient. This is due to the fact that within bHQET there is only one remaining dynamic (not hard) scale, in such a way that the dependence of the form factor on this scale m_g must be logarithmic.[13] In SCET, the primary mass is not integrated out yet so we have two scales: M and m_g leading to the equivalence: $(m_g \to \infty) \leftrightarrow (M \to 0)$ in the corresponding form factor.[14] Therefore, we can add to the SCET form factor with massless primary quark, that we already computed in Eq. (5.38), the decoupling limit $(m_g \to \infty)$ of the Wilson coefficient to recover the bHQET part:

$$\begin{aligned} \mathcal{M}_{\rm bHQET}^{n_g \to n_\ell} &= 1 + C_F \frac{\alpha_s(\mu)}{\pi} \mathbf{F}_1^{\rm bHQET}(M, Q, m_g, \mu)\,, \\ \mathbf{F}_1^{\rm bHQET}(M, Q, m_g, \mu) &= \mathbf{F}_{1,\rm ren}^{\rm SCET}(0, Q, m_g, \mu) - F_{1,\rm ren}^m(0, M, \mu) - \Delta_0^\infty F_1^m(\xi_g) \\ &= \log\Big(\frac{\mu}{m_g}\Big)\big[\log(-\hat{M}^2) + 1\big]\,. \end{aligned} \tag{5.86}$$

The presence of powers of $\log(\mu/m_g)$ makes clear that the gluon mass is acting as a regulator for IR divergences. The dependence on the renormalization scale agrees with that of Eq. (130) in Ref. [24], where off-shellness was used as a regulator. We finish this section by computing the primary-mass-corrected matching condition $\mathcal{M}_{\rm SCET}^{n_g \to n_\ell}$ at one loop, which coincides with the SCET form factor for

[13] Notice that the dependence of any EFT form factor on hard scales can only be logarithmic since any other kind would suppose a power correction to the EFT and we work at leading (fixed) order in the power counting.

[14] As a consequence of the fact that the non-logarithmic dependence can only consist on a power series on the ratio of the two dynamic scales.

massive primary quarks and a massive virtual gluon, adding $\mathbf{F}_1^{\text{bHQET}}$ and $F^m_{1,\text{ren}}$:

$$\begin{aligned}\mathcal{M}^{n_g\to n_\ell}_{\text{SCET}} &= 1 + C_F\frac{\alpha_s(\mu)}{\pi}\mathbf{F}_1^{\text{SCET}}(M,Q,m_g,\mu)\,,\\ \mathbf{F}_1^{\text{SCET}}(M,Q,m_g,\mu) &= \mathbf{F}^{\text{SCET}}_{1,\text{ren}}(0,Q,m_g,\mu) + \Delta_0 F_1^m(\xi_g) - \Delta_0^\infty F_1^m(\xi_g)\,.\end{aligned} \tag{5.87}$$

It can be shown that all these massive gluon results just obtained are equivalent to the ones provided in Sec. 4.4.1.

Secondary massive bubble

In this section we will write the expressions in terms of the dimensionless parameter ξ defined in Sec. 5.4.2. The most relevant results prior to discussing any expansions are

$$\begin{aligned}\mathcal{M}_2^m(h,\xi,0) &= -\frac{(h-1)[h(3h+4)+2]\pi^2\csc^2(\pi h)\xi^{-2h}}{2h^2(h+2)(2h+1)(2h+3)} \xrightarrow[|h|\gg 1]{} -\frac{3\pi^2\csc^2(\pi h)}{8h^2}\xi^{-2h}\,,\\ F^m_{2,\text{div}}(M,\mu,\varepsilon) &= \frac{1}{8\varepsilon^3}+\frac{1}{12\varepsilon^2}\left(L_M-\frac{1}{3}\right)-\frac{1}{\varepsilon}\left(\frac{5}{36}L_M+\frac{\pi^2}{48}+\frac{5}{432}\right),\\ F^m_{2,\text{ren}}(0,M,\mu,\varepsilon) &= -\frac{1}{36}L_M^3-\frac{13}{72}L_M^2-L_M\left(\frac{\pi^2}{18}+\frac{77}{216}\right)-\frac{13\zeta_3}{36}-\frac{37\pi^2}{432}-\frac{1541}{2592}\,,\\ \Delta_0^\infty F_2^m(\xi) &= \frac{2}{9}\log^3(\xi)+\frac{13}{18}\log^2(\xi)+\frac{133+12\pi^2}{108}\log(\xi)+\frac{1747+156\pi^2}{1296}\,.\end{aligned} \tag{5.88}$$

with $L_M \equiv \log(\mu^2/M^2)$. From the first line we see that the boundary between expansions is $\xi = 1$, and they overlap at this point, where both converge due to the h^{-2} overall dependence of $\mathcal{M}_2^m(h,\xi,0)$ for large h. The divergent pieces and massless part agree with the results found in Ref. [40].

Let us study now the different series for the mass corrections: there are double poles at all integer values of h except for $h = 1$, which is simple, and $h = -2$ with multiplicity equal to 3. Additionally, we have simple poles located at $h = -1/2, -3/2$. Since the factor containing gamma functions in $\mathcal{M}_2^m(h,\xi,0)$ is invariant under the replacement $h \to 1-h$, one expects some symmetry in the infinite sums appearing in the expansions for small and large mass. Indeed, after applying the converse mapping theorem, we get the following expansions:

$$\begin{aligned}\Delta_0 F_2^m(\xi) &= \Delta_0^\infty F_2^m(\xi) - \sum_{n=1} A_n(\xi)\\ &= \frac{3\pi^2\xi}{8}-\frac{55\pi^2\xi^3}{72}+\xi^4\left(\frac{3}{2}L_\xi^2-3L_\xi+\frac{\pi^2}{4}+\frac{145}{48}\right)+\sum_{n=1}^{n\neq 2}A_{-n}(L_\xi)\\ A_n(\xi) &= \frac{\xi^{-2n}(2+4n+3n^2)}{n^2(n+2)(2n+1)(2n+3)}\Bigg[(n-1)L_\xi\\ &\quad+\frac{3\big(8n^6+20n^5-45n^3-68n^2-42n-8\big)}{2n(n+2)(2n+1)(2n+3)\,(3n^2+4n+2)}\Bigg].\end{aligned} \tag{5.89}$$

where $L_\xi = \log(\xi)$. For $\xi = 1$ one finds $\Delta_0 F_2^m(1) = \frac{\zeta_3}{3} + \frac{83}{36} - \frac{\pi^2}{108}$. The series for large ξ can be summed up and we find the following expression, in which all terms are manifestly real for $\xi > 1$:

$$\begin{aligned}\Delta_0 F_2^m(\xi) = &\frac{\pi^2\xi^4}{8} - \frac{55\pi^2\xi^3}{108} + \frac{83\xi^2}{36} + \frac{13}{18}L_\xi^2 + \left(\frac{14\xi^2}{9} + \frac{\pi^2}{6}\right)L_\xi + \frac{\pi^2\xi}{4} - \frac{10}{9}L_\xi^3 + \frac{13\pi^2}{216} \\ &+ \frac{1}{3}\left[\mathrm{Li}_3\left(\frac{1}{\xi^2}\right) + 2L_\xi^2\log\left(\xi^2-1\right)\right] + \left(\frac{13}{36} - \frac{3\xi^4}{4} - \frac{L_\xi}{3}\right)\mathrm{Li}_2\left(1-\frac{1}{\xi^2}\right) \\ &+ \left(\frac{3\xi}{4} - \frac{55\xi^3}{36}\right)\left[L_\xi\log(\xi+1) - \frac{1}{2}\log^2(\xi+1) + \mathrm{Li}_2(1-\xi) - \mathrm{Li}_2\left(\frac{\xi}{\xi+1}\right)\right].\end{aligned} \tag{5.90}$$

For $\xi < 1$ the expression is still real, but the individual pieces on the term in square brackets in the second line become complex. To have each term manifestly real, the following substitution should be implemented:

$$\mathrm{Li}_3\left(\frac{1}{\xi^2}\right) + 2L_\xi^2\log\left(\xi^2-1\right) \to \mathrm{Li}_3\left(\xi^2\right) + 2L_\xi^2\log\left(1-\xi^2\right) + \frac{4}{3}L_\xi^3 - \frac{2}{3}\pi^2 L_\xi\,. \tag{5.91}$$

In Fig. 5.11, a comparison of the exact expression and both expansions is shown at various orders. We see that at $\xi = 1$ both expansions converge very quickly, although the large-mass one is accurate already at very low orders, and the small-mass series exhibits an oscillatory behavior related to the poles at half-integer values: after the third power of xi is included, the sign alternating behavior disappears. Both expansions excel reproducing the exact result in their respective convergence domains, but the large-mass expansion is particularly fast at reproducing the all-order result.

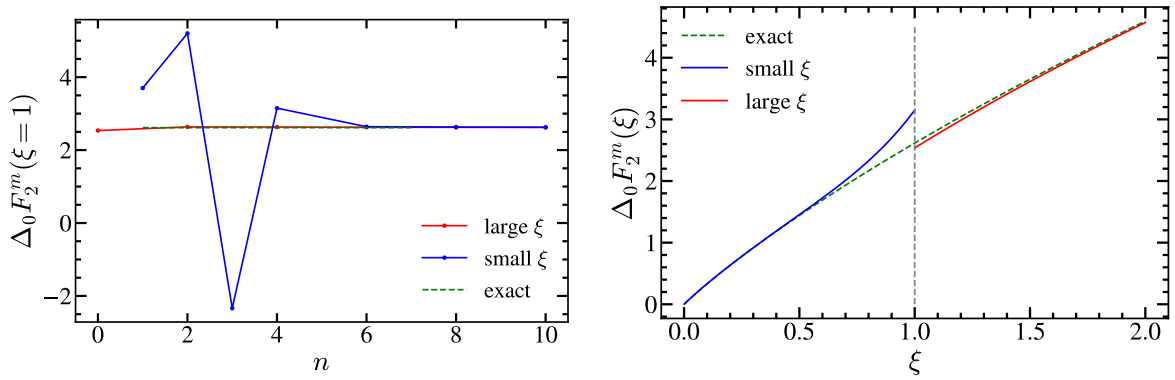

(a) (b)

Figure 5.11: Secondary mass correction to the 2-loop massless Wilson coefficient relating the dijet operators in SCET and bHQET in its exact form (dashed green), small- (red) and large-mass (blue) expansions. Left panel: $\Delta_0 F_2^m$ at the boundary between the mass expansions $\xi = 1$, as a function of the expansion order n of each series. Right panel: Dependence of $\Delta_0 F_2^m(\xi)$ with the reduced gluon mass, including 4 and 1 non-zero terms in the small- and large-mass expansions, respectively.

An additional cross-check was made with the results of Chapter 4 in the following form:

$$\Delta_0 F_2^m(\xi) = \frac{\pi^2}{\alpha_s^2 C_F T_F}\,\frac{1}{2}\,\delta H_M(\xi)\,, \tag{5.92}$$

with $\delta H_M(\xi)$ given in Eq. (4.81).

To recover the expression of each EFT form factor independently, we can follow a procedure analogous to the one for the massive gluon, that is, we can subtract from the result in Eq. (5.47) for the dispersive part of the massless primary SCET form factor, the decoupling limit of the dispersive term of the matching, given by just the pole $h = \varepsilon$ contribution. In this way, we obtain the part corresponding to the unrenormalized bHQET form factor:

$$\begin{aligned}\mathbf{F}_{2,\text{disp}}^{\text{bHQET}} = \left[\log\left(\frac{M^2}{-Q^2}\right)+1\right]\left\{\frac{1}{12\varepsilon^2}-\frac{1}{36\varepsilon}\left[5-6\log\left(\frac{\mu^2}{m^2}\right)\right]\right. \\ \left.+\frac{1}{216}\left[36\log^2\left(\frac{\mu^2}{m^2}\right)-60\log\left(\frac{\mu^2}{m^2}\right)+3\pi^2+56\right]\right\},\end{aligned} \tag{5.93}$$

and adding the $\Pi_0^{\overline{\text{MS}}}$ contribution together with the term coming from the flavor threshold condition in α_s (all of them proportional to the one loop bHQET form factor) we arrive again to Eq. (4.91) for the flavor matching.[15] Finally, the dispersive part of the SCET form factor with massive primary and secondary quarks is given by the sum of the previous result and the dispersive part of the matching results, that is, one must subtract the $\Pi_0^{\overline{\text{MS}}}$ contribution from the corresponding expressions in Eq. (5.88).

The secondary massive bubble part of the bHQET and SCET form factors was also compared to the corresponding results obtained with the dispersive integral method, discussed in Sec. 4.4.1 and agreement (analytical for bHQET and numerical for SCET) was found.

5.6.2 Jet function

One loop computations

Since the measurement function is completely inclusive, we will perform the calculation of the bHQET jet function as the discontinuity of a forward-scattering matrix element, in a way analogous to the calculation carried out in Sec. 4.3. Therefore, we need to consider the diagrams shown in Fig. 4.5 with the quark bilinear contribution set yo zero.

- **Quark self-energy:**

$$M\mathcal{B}_n^{c,\,h}(\hat{s},\mu) = -\frac{8i\alpha_s C_F\tilde{\mu}^{2\varepsilon}}{\hat{s}^2}\int\frac{\mathrm{d}^d l}{(2\pi)^d\,(-1)^{1-h}}\frac{1}{[l^2+i0]^{1-h}\,[v\cdot(k+l)+i0]}\,. \tag{5.94}$$

  The result of the integral can be read from Eq. (5.78), which can be rewritten to obtain the following result for this contribution to the forward-scattering matrix element:

$$M\mathcal{B}_n^{c,\,h}(\hat{s},\mu) = \frac{\alpha_s\,C_F}{\pi^2}\left(\mu^2 e^{\gamma_E}\right)^{\varepsilon}\frac{2\Gamma(2+h-\varepsilon)\Gamma(-2-2h+2\varepsilon)}{\Gamma(1-h)}(-\hat{s})^{-1+2h-2\varepsilon}\,, \tag{5.95}$$

  a form more convenient to take the imaginary part since we can use the identity

$$\mathrm{Im}\,(-\hat{s})^{-a} = \mathrm{Im}\,(-\hat{s}-i0)^{-a} = \mathrm{Im}\left(\hat{s}^{-a}e^{i\pi a}\right) = \frac{\pi\hat{s}^{-a}}{\Gamma(a)\Gamma(1-a)}\,, \tag{5.96}$$

  right away, obtaining for the contribution coming from the self-energy diagram to the jet function the following expression:

$$MB_n^{c,\,h}(\hat{s},\mu) = -C_F\frac{\alpha_s}{\pi}\frac{\Gamma(1+h-\varepsilon)\hat{s}^{-1+2h}e^{\varepsilon\gamma_E}}{\Gamma(1-h)\Gamma(2+2h-2\varepsilon)}\left(\frac{\mu}{\hat{s}}\right)^{2\varepsilon}\,. \tag{5.97}$$

[15] Recall that only the divergent pieces contribute when multiplied by log-subtracted $\Pi_0^{\overline{\text{MS}}}$ vacuum polarization function.

- **Wilson line gluon:** The contribution to the forward-scattering matrix element from the Feynman diagram in which the gluon is radiated directly from the gluon line and absorbed in the heavy-quark propagator is

$$M\mathcal{B}_n^{a,\,h}(\hat{s},\mu) = \frac{4i\alpha_s C_F \tilde{\mu}^{2\varepsilon}}{(-\hat{s})}\frac{Q}{M}\int \frac{\mathrm{d}^d l}{(2\pi)^d\,(-1)^{1-h}}\frac{1}{[l^2+i0]^{1-h}\,[\bar{n}\cdot l - i0]\,[v\cdot(k+l)+i0]}\,. \quad (5.98)$$

  This integral was also computed previously and its value can be deduced from Eq. (5.72). Using again Eq. (5.96) to determine the imaginary part, we end up with

$$MB_n^{a,\,h}(\hat{s},\mu) = -C_F\frac{\alpha_s}{2\pi}\frac{\Gamma(1+h-\varepsilon)\hat{s}^{-1+2h}e^{\varepsilon\gamma_E}}{(\varepsilon-h)\Gamma(1-h)\Gamma(1+2h-2\varepsilon)}\left(\frac{\mu}{\hat{s}}\right)^{2\varepsilon}. \quad (5.99)$$

Adding all contributions one gets

$$MB_n^{h}(\hat{s},\mu) = -C_F\frac{\alpha_s}{\pi}\frac{\Gamma(2+h-\varepsilon)\hat{s}^{-1+2h}e^{\varepsilon\gamma_E}}{(\varepsilon-h)\Gamma(1-h)\Gamma(2+2h-2\varepsilon)}\left(\frac{\mu}{\hat{s}}\right)^{2\varepsilon}. \quad (5.100)$$

For the Mellin calculations of the massive gluon and secondary quark corrections we will work with the cumulative Σ_B as in the SCET case so we identify $\mathcal{Q} = \hat{s}_c$, and use the following 1-loop modified expression

$$m_1^h(\varepsilon) = \frac{1}{2}\frac{\Gamma(2+h-\varepsilon)}{(\varepsilon-h)^2\Gamma(1-h)\Gamma(2+2h-2\varepsilon)}\,. \quad (5.101)$$

Massive gluon

Let us apply the previous equation first to the massive gluon contribution, for which we have:

$$\begin{aligned}
\mathcal{M}_1^{\Sigma_B}(h,\tilde{s}_g,0) &= \frac{\Gamma(h)\Gamma(h+2)\tilde{s}_g^{2h}}{2h^2\Gamma(2h+2)} \xrightarrow[|h|\gg 1]{} \frac{\sqrt{\pi}}{4h^{5/2}}\left(\frac{\tilde{s}_g}{2}\right)^{2h}, \quad (5.102)\\
F^B_{1,\mathrm{div}}(\hat{s},\mu,\varepsilon) &= \left(\frac{1}{2\varepsilon^2}+\frac{1}{2\varepsilon}\right)\delta(\hat{s}) - \frac{1}{\varepsilon}\frac{1}{\mu}\left[\frac{\mu}{\hat{s}}\right]_+,\\
F^B_{1,\mathrm{ren}}(0,\hat{s},\mu) &= \frac{2}{\mu}\left[\frac{\mu}{\hat{s}}\log\left(\frac{\hat{s}}{\mu}\right)\right]_+ - \frac{1}{\mu}\left[\frac{\mu}{\hat{s}}\right]_+ + \left(1-\frac{\pi^2}{8}\right)\delta(\hat{s})\,,\\
\Delta_0^\infty F_1^B(\tilde{s}_g) &= -\frac{2}{m_g}\left[\frac{m_g}{\hat{s}}\log(\tilde{s}_g)\right]_+ + \frac{1}{m_g}\left[\frac{m_g}{\hat{s}}\right]_+ - \left(1-\frac{\pi^2}{12}\right)\delta(\hat{s})\,,
\end{aligned}$$

where we defined $\tilde{s}_g \equiv \hat{s}/m_g$, variable which is used also for the cumulative related quantities (that is, $\tilde{s}_g \equiv \hat{s}_c/m_g$ in the first line). This is analogous to the variable defined in the corresponding SCET computation, but in this case we placed a *tilde* instead of a *hat* to remark that they are different variables. The second and third lines agree with the results given in Ref. [24] .

We can also isolate the virtual part from the residue of the double pole sitting at $h = \varepsilon$, that constitutes the only contribution from the right side of the fundamental strip, and after renormalization also coincides with the sum of $F^B_{1,\mathrm{ren}}(0,\hat{s},\mu)$ and $\Delta_0^\infty F_1^B(\tilde{s}_g)$:

$$F^B_{1,\mathrm{virt,ren}} = \frac{1}{24}\left[-6\log^2\left(\frac{\mu^2}{m_g^2}\right)+12\log\left(\frac{\mu^2}{m_g^2}\right)-\pi^2\right]\delta(\hat{s}) - \log\left(\frac{\mu^2}{m_g^2}\right)\frac{1}{\mu}\left[\frac{\mu}{\hat{s}}\right]_+. \quad (5.103)$$

For the real radiation part, which is μ independent, since it does not involve any distribution, we can safely apply the inverse Mellin transform direct to the differential jet function. This can be extracted from Eq. (5.100) or from the derivative of the cumulative's Mellin transform. We have to consider the double pole at zero, and the simple poles for all the negative integers smaller than -1 that appear when setting $\varepsilon \to 0$.

$$\begin{aligned} F^B_{1,\text{real}} =& \frac{1}{\hat{s}}\left[2\log(\tilde{s}_g) - 1 - 2\sum_{n=2}\frac{\Gamma(2n-1)\tilde{s}_g^{-2n}}{n\,n!\Gamma(n-1)}\right]\theta(\tilde{s}_g - 2) \\ =& \frac{1}{\hat{s}}\left[2\log\left(\sqrt{1-\frac{4}{\tilde{s}_g^2}}+1\right) + 2\log\left(\frac{\tilde{s}_g}{2}\right) - \sqrt{1-\frac{4}{\tilde{s}_g^2}}\right]\theta(\tilde{s}_g - 2)\,. \end{aligned} \tag{5.104}$$

The Heaviside theta condition comes from the large h behavior shown in Eq. (5.102), and to get to the second line we just sum up the series. Adding up real and virtual results one gets the same result as the ε-expanded and renormalized version of Eq. (4.54). In Fig. 5.12 we compare the series expansion of the real-radiation contribution for small gluon masses with the exact result. We observe an excellent convergence everywhere except for $\hat{s}_g = 2$ where convergence is rather slow.

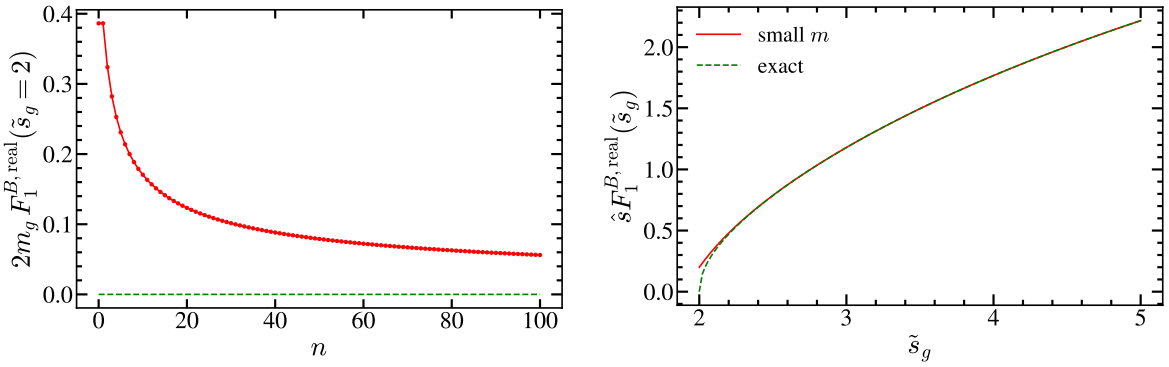

(a) (b)

Figure 5.12: Real-radiation term of the 1-loop massive gluon bHQET jet function. We show exact results as green dashed line, and the expansions for small masses as a red solid line. Left panel: small mass expansion of $2m_g\Delta_0 F_1^{B,\text{real}}$ at threshold $\tilde{s}_g = 2$ as a function of the expansion order n. Right panel: Dependence of $\hat{s}\Delta_0 F_1^{B,\text{real}}$ with $\tilde{s}_g$, including 6 non-zero terms in the expansion.

The one-loop correction to the jet matching coefficient relating the jet functions in the theories with and without massive gluons is given by

$$B_n^{n_\ell}(\hat{s}) = \int_0^{\hat{s}} \mathrm{d}\hat{s}'\,\mathcal{M}_B^{n_\ell\to n_g}(\hat{s}-\hat{s}')\,B_n^{n_g}(\hat{s}')\,, \qquad \mathcal{M}_B^{n_\ell\to n_g} = \delta(\hat{s}) - \frac{\alpha_s(\mu)}{\pi}C_F F^B_{1,\text{virt,ren}}\,. \tag{5.105}$$

Next, we study the series for the RG evolved gluon mass corrections following the same procedure as in SCET. Therefore, we have to consider

$$\begin{aligned} &\Delta_0 F_1^B(\hat{s}, m_g^2) \equiv \frac{1}{\hat{s}}\tilde{F}_1^B(\tilde{s}_g)\,, \\ &M\tilde{B}_1^{\tilde{\omega}}(\tilde{s}_g) = \int_0^{\tilde{s}_g}\frac{\mathrm{d}s'}{s'}\left(1-\frac{s'}{\tilde{s}_g}\right)^{-1-\tilde{\omega}}\tilde{F}_1^B(s') = \int_{c-i\infty}^{c+i\infty}\frac{\mathrm{d}h}{2\pi i}\frac{\tilde{s}_g^{2h}\Gamma(h)\Gamma(h+2)}{2h^2(2h+1)(-\tilde{\omega})_{2h}}\,, \end{aligned} \tag{5.106}$$

with $-1/2 < c < 0$, in such a way that the only pole to the right is triple and located at $h = 0$, whereas to the left simple poles appear at $h = -1/2$ and $h = -1$, and double poles for the rest of integers on that side. The expansions can be written as:

$$\begin{aligned} M\tilde{B}_1^{\tilde{\omega}}(\tilde{s}_g) &= \tilde{L}_g - \tilde{L}_g^2 + \psi^{(1)}(-\tilde{\omega}) - \frac{\pi^2}{12} - 1 \\ &= \frac{\pi(\tilde{\omega}+1)}{\tilde{s}_g} + \frac{(\tilde{\omega}+1)_2}{2\tilde{s}_g^2} - \sum_{n=2} \frac{(n-1)(\tilde{\omega}+1)_{2n}\tilde{s}_g^{-2n}}{n(2n-1)(n!)^2}\Bigg[\tilde{L}_g + H_n \\ &\quad + \frac{2n^2-4n+1}{2n(n-1)(2n-1)} + \psi^{(0)}(\tilde{\omega}+1) - \psi^{(0)}(2n+\tilde{\omega}+1)\Bigg], \end{aligned} \tag{5.107}$$

where $\log(\tilde{s}_g) - \gamma_E - \psi^{(0)}(-\tilde{\omega})$. We have not been able to sum up the previous series, therefore we consider "exact" the sum of the first 140 terms. In Fig. 5.13 we study the convergence of the series for the RG-evolved bHQET jet function for three values of the running parameter $\tilde{\omega}$. We observe that, analogously to our findings for the real-radiation bHQET jet function, convergence is not great at $\tilde{s}_g = 2$, although it becomes better for values $\tilde{\omega}$ further away from zero. Likewise, the series converges rapidly for $\tilde{s}_g > 2$, and the further $\tilde{\omega}$ is from zero, the faster it converges.

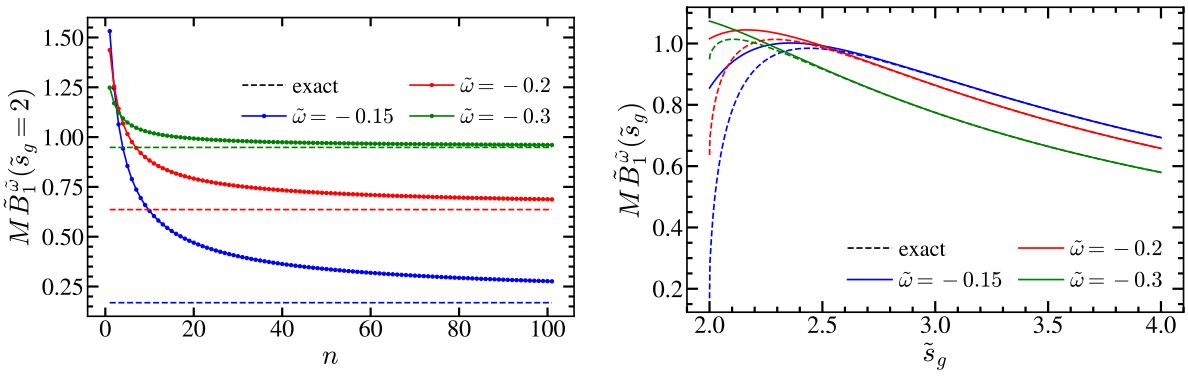

(a) (b)

Figure 5.13: Gluon mass correction to the massless RG-evolved bHQET jet function in its exact form (dashed), and expansions for small masses (solid lines) for three values of $\tilde{\omega}$: -0.15 (blue), -0.2 (red) and -0.3 (green). Left panel: small mass expansion of $M\tilde{B}_1^{\tilde{\omega}}$ at threshold $\tilde{s}_g = 2$ as a function of the expansion order n. Right panel: Dependence of $M\tilde{B}_1^{\tilde{\omega}}$ with $\tilde{s}_g$, including 6 non-zero terms in the small-mass expansion.

Secondary massive bubble

As a final application of this thesis, we compute the 2-loop secondary massive quark correction to the bHQET jet function, therefore we multiply Eq. (5.101) by the kernel $G(h,\varepsilon)$, leading to

$$\begin{aligned}
\mathcal{M}_2^{\Sigma_B}(h,\tilde{s}_c,0) &= \frac{(1+h)^2\Gamma^4(h)\tilde{s}_c^{2h}}{2(2h+3)\Gamma^2(2h+2)} \xrightarrow[|h|\gg 1]{} \frac{\pi}{16h^4}\left(\frac{\tilde{s}_c}{4}\right)^{2h}, \qquad (5.108)\\
F^B_{2,\text{div}}(\hat{s},\mu,\varepsilon) &= \left[\frac{1}{8\varepsilon^3}+\frac{1}{72\varepsilon^2}+\frac{1}{\varepsilon}\left(\frac{\pi^2}{144}-\frac{29}{108}\right)\right]\delta(\hat{s})+\left(\frac{5}{18\varepsilon}-\frac{1}{6\varepsilon^2}\right)\frac{1}{\mu}\left[\frac{\mu}{\hat{s}}\right]_+,\\
F^B_{2,\text{ren}}(0,\hat{s},\mu,\varepsilon) &= \left(\frac{17\zeta_3}{36}+\frac{59\pi^2}{432}-\frac{281}{162}\right)\delta(\hat{s})-\left(\frac{\pi^2}{9}-\frac{47}{27}\right)\frac{1}{\mu}\left[\frac{\mu}{\hat{s}}\right]_+\\
&\quad -\frac{16}{9}\frac{1}{\mu}\left[\frac{\mu}{\hat{s}}\log\left(\frac{\hat{s}}{\mu}\right)\right]_+ +\frac{2}{3}\frac{1}{\mu}\left[\frac{\mu}{\hat{s}}\log^2\left(\frac{\hat{s}}{\mu}\right)\right]_+,\\
\Delta_0^\infty F_2^B(\tilde{s}) &= -\frac{2}{3}\frac{1}{m}\left[\frac{1}{\tilde{s}}\log^2(\tilde{s})\right]_+ +\frac{16}{9}\frac{1}{m}\left[\frac{1}{\tilde{s}}\log(\tilde{s})\right]_+ -\left(\frac{61}{27}-\frac{\pi^2}{9}\right)\frac{1}{m}\left[\frac{1}{\tilde{s}}\right]_+\\
&\quad +\left(\frac{223}{81}-\frac{2\zeta_3}{3}-\frac{4\pi^2}{27}\right)\delta(\hat{s})\,.
\end{aligned}$$

where we defined $\tilde{s}=\hat{s}/m$ and $\tilde{s}_c=\hat{s}_c/m$ to point out the difference with the analogous SCET variable. The limit taken on the first line establishes the boundary for the small mass expansion convergence at $\hat{s}=4m$. The second and third lines agree with the massless result provided in Ref. [42] and the last line can be compared (once we account for the color, α_s/π and $M/2$ factors) to δB_m^{dist} given in Eq. (4.63).

Therefore we are left with the calculation of the real-radiation contribution to the mass corrections and the residues to be considered for that purpose, once we set $\varepsilon=0$ in the Mellin transform of the jet function, are the triple pole at $h=0$ along with the double poles for all $h=-n$ with $n\geq 2$, ending up with:

$$\begin{aligned}
\hat{s}\,\Delta_0 F^B_{2,\text{real}} =& \left\{\frac{61}{27}-\frac{\pi^2}{9}-\frac{16}{9}\log(\tilde{s})+\frac{2}{3}\log^2(\tilde{s})+32\sum_{n=2}^{\infty}\frac{(2n-3)[(2n-4)!]^2\tilde{s}^{-2n}}{n^3[(n-2)!]^4}\right.\qquad (5.109)\\
&\left.\times\left[\log(\tilde{s})+2H_n-2H_{2n-2}+\frac{-3+9n-4n^2}{2n(n-1)(2n-3)}\right]\right\}\theta(\tilde{s}-4)\,,
\end{aligned}$$

where the Heaviside theta condition can be derived from the large h limit we took in Eq. (5.108). This expansion can be cross-checked by implementing numerically the dispersive integral in the result of Chapter 4, that is by the comparison:

$$\left[\frac{\alpha_s(\mu)}{\pi}\right]^2 C_F T_F\,\Delta_0 F^B_{2,\text{real}} = M\delta B_m^{\text{real}}(\hat{s},m)/2\,, \qquad (5.110)$$

with $\delta B_m^{\text{real}}(\hat{s},m)$ as appears in Eq. (4.63). The outcome of this comparison is depicted in Fig. 5.14 where the dispersive integral result is marked with a label to indicate numerical output (*num*). Notice that if one considers instead Eq. (C.10) for this comparison both sides are completely equivalent so we just reproduce, through this simpler procedure, the main result of the previous Chapter for the bHQET jet function. Likewise, we can also use Eq. (5.14) to recover the flavor matching in Eq. (4.95).

We can take advantage of the flexibility of our MB representation and go one step further by providing a fast convergent series also for the convolution with the running kernel. The Mellin transform

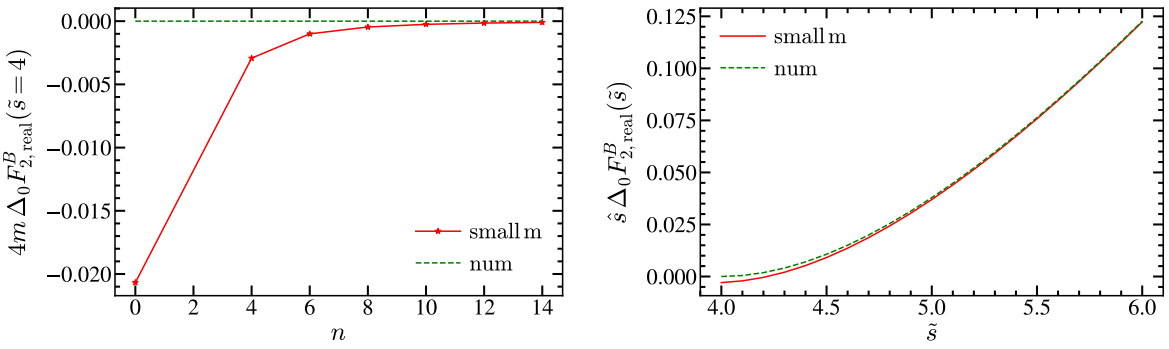

(a) (b)

Figure 5.14: Secondary mass corrections to the bHQET jet function: real radiation part. We show dispersive integral results as green dashed, and the expansion for small masses as a red solid line. Left panel: small mass expansion of $\tilde{s}\Delta_0 F^B_{2,\mathrm{real}}$ at threshold $\tilde{s}=4$ as a function of the expansion order n. Right panel: Dependence of $\tilde{s}\Delta_0 F^B_{2,\mathrm{real}}$ with $\tilde{s}$, including two non-zero terms in the expansion.

of the RG-evolved mass corrections is:

$$M\tilde{B}_2^{\tilde{\omega}}(\tilde{s}) = \int_0^{\tilde{s}} \frac{\mathrm{d}s'}{s'}\left(1-\frac{s'}{\tilde{s}}\right)^{-1-\tilde{\omega}} \tilde{F}_2^B(s') = \int_{c-i\infty}^{c+i\infty} \frac{\mathrm{d}h}{2\pi i}\, \frac{\sqrt{\pi}(h+1)^2\Gamma(h)^3\left(\frac{\tilde{s}}{2}\right)^{2h}}{8h\,(1+2h)\,\Gamma\left(h+\frac{5}{2}\right)(-\tilde{\omega})_{2h}}\,, \tag{5.111}$$

with $-1/2 < c < 0$ and the same condition for convergence found before holds, despite appearances. The configuration of singularities is simple: one has a fourth-order pole sitting at the origin, while to the left of this point simple poles at $h=-1/2,-1$ and triple poles at integers below -1 are found. All in all we obtain:

$$\begin{aligned}
M\tilde{B}_2^{\tilde{\omega}}(\tilde{s}) =& \frac{8}{9}\tilde{L}^2 - \frac{2}{9}\tilde{L}^3 + \frac{\tilde{L}}{3}\left[2\psi^{(1)}(-\tilde{\omega}) - \frac{61}{9}\right] - \frac{8}{9}\psi^{(1)}(-\tilde{\omega}) + \frac{2}{9}\psi^{(2)}(-\tilde{\omega}) + \frac{223}{81} - \frac{2\zeta_3}{9} \\
=& -\frac{\pi^2(\tilde{\omega}+1)}{2\tilde{s}} + \sum_{n=1}\frac{(2n)!(\tilde{\omega}+1)_{2n}\tilde{s}^{-2n}}{n(1-2n)^2(2n-3)(n!)^4}\Big\{(n-1)^2\big\{\big[\tilde{L}+K_n(\tilde{\omega})\big]^2 + H_n^{(2)} \\
&- H_{2n}^{(2)} + \psi^{(1)}(2n+\tilde{\omega}+1) - \psi^{(1)}(\tilde{\omega}+1) - \psi^{(1)}(-\tilde{\omega})\big\} \\
&+ \frac{(n-1)(8n^3-22n^2+19n-3)}{n(2n-3)(2n-1)}[\tilde{L}+K_n(\tilde{\omega})] \\
&+ \frac{48n^6-264n^5+596n^4-670n^3+372n^2-90n+9}{2n^2(2n-3)^2(2n-1)^2}\Big\}\,, \\
K_n(\tilde{\omega}) =& 2H_n - H_{2n} - \sum_{i=1}^{2n}\frac{1}{\tilde{\omega}+i}\,,
\end{aligned} \tag{5.112}$$

with $\tilde{L}\equiv\log(\tilde{s})-\psi^{(0)}(-w)-\gamma_E$. Again, we verified numerically this series through the analysis plotted in Fig. 5.15.

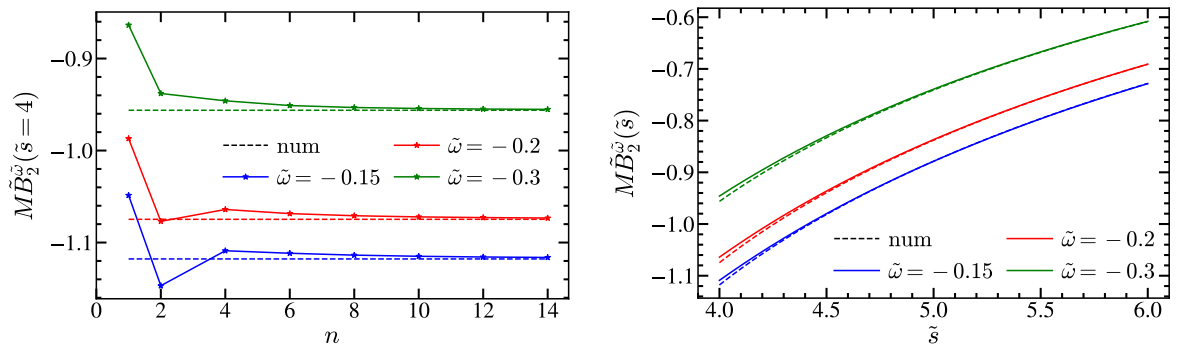

(a) (b)

Figure 5.15: Secondary mass correction to the massless RG-evolved bHQET jet function in its numerical form (dashed), and expansions for small masses (solid lines) for three values of $\tilde{\omega}$: -0.5 (blue), -0.6 (red) and -0.7 (green). Left panel: small mass expansion of $M\tilde{B}_2^{\tilde{\omega}}$ at threshold $\tilde{s}=4$ as a function of the expansion order n. Right panel: Dependence of $M\tilde{B}_2^{\tilde{\omega}}$ with $\tilde{s}$, including 3 non-zero terms in the small-mass expansion.

5.7 Summary

In order to obtain the expansion for small and large masses to arbitrary high order in processes involving massless or massive quarks at lowest order, we reorganize the usual sequence of steps carried out when solving multi-loop integrals through the Mellin-Barnes procedure, and derive a simple way of computing the massive virtual quark bubble contributions to any given matrix element (not necessarily within QCD), which can also be adapted to virtual massive vector bosons.

This was achieved through an inspection of the integrals involved in the corrections from massive quark bubbles in the gluon self-energy, that lead to the conclusion that we can expand away the mass very early in the calculation by working in the Mellin plane. This, in turn, implies that we do not have to deal with additional scales in the remaining loop integrals and once they are solved one is left with the Mellin transform of the final result. From this representation, the application of the converse mapping theorem, that basically is nothing else than carrying out the corresponding integral using the residue theorem and Jordan's lemma, leads to small- and large-mass expansions, whose convergence radius can be inferred from the behavior of the Mellin transform at infinity.

After analyzing the massive quark bubble insertion on the gluon self-energy from the Mellin plane, we applied this method to the difference between the pole and $\overline{\text{MS}}$ mass schemes and to matrix elements in the factorization theorems for the processes we are interested in this thesis, that is, event shape differential distributions in the context of $e^+e^- \to$ hadrons, both in SCET and bHQET. We reproduced without much effort all known results, including those first derived in Chapter 4.

We conducted numerical investigations of the convergence for each series and obtained closed expressions in the cases in which the expansions can be summed to all orders. Finally, for the jet functions in both EFTs, we convolve with the running kernel already using their original representation in Mellin space, and invert at the very end in order to have access to a series for the RG-evolved results. These turn out to be much more efficient than the direct numerical implementation of the corresponding integral.

Conclusions

The particle physics community is currently making a big effort in the quest for finding new physics that could overcome the theoretical less sound aspects of the Standard Model, and that could explain some tensions found between Standard Model predictions and experimental data. Since no clear signals of new physics have been found in high-energy colliders such as the LHC, the search has to be more subtle. Reducing the theoretical uncertainties is then crucial to search for small deviations that could be overlooked if the precision is not high enough.

The slow convergence of perturbative series in powers of the strong coupling α_s and the non-perturbative effects inherent to the strong sector of the Standard Model (QCD) makes it hard to get a grip on the actual theoretical accuracy. Additionally since the coupling of particles to the Higgs boson is proportional to their own mass, the top quark can be used as a gate to explore physics beyond the Standard Model.

Having this in mind, the research carried out in this thesis has focused on NLO and NNLO computations for observables called event shapes with massive quarks, either primary or secondary, necessary for precise determinations of QCD parameters and to distinguish standard and non-standard experimental signals. Our interest has not been limited to fixed-order computations, but also has dealt with resummed perturbation theory, with special focus on jets involving massive particles.

We have developed new calculation methods that can be applied in EFTs or full QCD to optimally expand the results for various hierarchies between the (primary or secondary) mass with respect to the kinematic variable (jet mass, center-of-mass energy, primary quark mass, etc...). As a result, higher precision for these observables was obtained in several ways:

- Exploring the sensitivity to quark masses through different choices for the event shape definition (E-, P- and Massive schemes). We worked out the resummed expression at NLO + $\mathrm{N^2LL}$ for boosted tops and no-so-boosted bottom and top quarks. To that end, we computed the missing jet functions in the corresponding factorization theorem of each EFT (SCET and bHQET) using cut Feynman diagrams instead of the discontinuity of a forward-scattering matrix element due to the non-inclusive nature of the observables. We have also worked out the RG-evolved version of each jet function. For the SCET setup, the results have been implemented as fast-converging series expansions (to arbitrary order) for the resummation of the new non-distributional parts, which would otherwise involved high-order hypergeometric functions, which are not easy to code (neither fast) in standard high-level computer languages such as `Fortran`, `C++` or `Python`. The three expansions that we worked out have overlapping convergence radius and cover the whole physical domain. Therefore they are equivalent to the exact result, but much faster and convenient.
- Computing oriented event-shape distributions for massive quarks at NLO. Measuring the orientation of the event with respect to the beam axis permits gaining further sensitivity to the strong

coupling and quark masses while, in the case of a total cross section, decreasing hadronization effects. The fixed-order computation at NLO requires projecting out the angular distribution from the regularized cross section differential in two energies and two angles, and requires using multi-differential phase-space integrals in $d = 4 - 2\varepsilon$ dimensions. It involves a delicate cancellation of infrared singularities between real and virtual radiation, that we worked out analytically. Our results can be used to obtain the strong coupling from the total oriented cross section, and this has left for future work.

- Through the calculation of secondary massive quark corrections to massless and massive resummed cross sections at NNLO. We have establishing a new variable-flavor number scheme (VFNS) for boosted tops in the resonance region. The results of the secondary bubble diagrams were obtained first with the usual dispersive integral method in which the massive bubble is expressed as an integral over a massive gluon propagator. In order to obtain series expansions for small and large secondary masses to arbitrarily high order, we used the Mellin-Barnes representation to replace the secondary massive bubble insertion by a massless gluon with a modified exponent. This novel strategy, which can be used only for IR-finite quantities, significantly simplifies the calculations since the additional mass scale is expanded away at early stages of the computation. The method can be trivially adapted to compute 1-loop matrix elements with massive vector bosons. We have employed this novel technique to a plethora of examples: the relation between the pole and $\overline{\text{MS}}$ masses, and the hard and jet functions of SCET and bHQET. Furthermore, we have obtained fast converging expansions for the RG-evolved versions of the corresponding jet functions, which so far could be obtained only numerically.

Conclusiones

La comunidad de física de partículas está haciendo actualmente un gran esfuerzo en la búsqueda de nueva física para poder explicar las tensiones encontradas entre las predicciones del Modelo Estándar y los datos experimentales. Reducir las incertidumbres teóricas ayudaría a esclarecer las discrepancias y por tanto acotaría dicha búsqueda.

La lenta convergencia de las series perturbativas y los efectos no perturbativos en el sector de QCD dificultan el control de la precisión teórica. Además, debido a que el acoplo al Higgs es proporcional a la masa del quark, el quark top se usa como una puerta de exploración a la física más allá del Modelo Estándar.

Con esto en mente, la investigación llevada a cabo durante este trabajo se ha centrado en cálculos NLO y NNLO para observables llamados *formas de evento* con quarks masivos, primarios o secundarios, para ayudar a la determinación de los parámetros de QCD.

Hemos desarrollado nuevas técnicas de cálculo que pueden ser aplicadas a teorías efectivas o a QCD para expandir de forma óptima los resultados para varias jerarquías de las masas con respecto a las variables cinéticas. Como resultado, se ha obtenido mayor precisión para estos observables de varias maneras:

- Explorando la sensibilidad a las masas de los quarks a través de diferentes elecciones para la definición de la *forma de evento* (esquemas E, P y Masivo). Hemos hallado la expresión resumada a NLO + $\mathrm{N^2LL}$ para quarks top *impulsados* y para quarks bottom y top menos *impulsados*. Para dicho fin, hemos calculado las funciones *chorro* restantes en el teorema de factorización correspondiente de cada teoría efectiva usando diagramas con cortes en lugar de mediante la discontinuidad de un elemento de matriz de *dispersión hacia adelante* debido a la naturaleza no inclusiva de los observables. Los resultados se han implementado como expansiones en serie de convergencia rápida (a un orden arbitrario) para la resumación de las nuevas partes no distribucionales. Las tres expansiones halladas tienen un radio de convergencía solapado y cubren todo el rango físico. Por tanto, son equivalentes al resultado exacto pero mucho más convenientes y rápidas.
- Calculando las distribuciones de *forma de evento* orientadas para quarks masivos a NLO. Medir la orientación del evento con respecto al eje del haz permite ganar mayor sensibilidad al parámetro de acoplo fuerte y a las masas de los quarks, a la vez que se disminuyen los efectos de hadronización. El cálculo de *orden fijo* a NLO requiere proyectar la distribución angular desde la sección eficaz regularizada diferencial en dos energías y dos ángulos. Tiene lugar una delicada cancelación de singularidades infrarrojas entre la radiación real y virtual que hemos llevado a cabo analíticamente. Nuestros resultados se pueden emplear para obtener el parámetro de acoplo fuerte a partir de la sección eficaz total orientada.
- A través de la determinación de las correcciones de masa del quark secundario a la sección eficaz resumada para la producción de quarks masivos y sin masa a NNLO, estableciendo un *esquema de*

número de sabores variable para tops *impulsados*. Los resultados de los diagramas *burbuja* se obtuvieron mediante la modificación del método de integral dispersiva usual en el que la *burbuja* masiva se expresa como una integral sobre un propagador de gluón masivo. Usamos la representación de Mellin-Barnes para reemplazar este propagador por el correspondiente a un gluon sin masa con el exponente modificado. Esta innovadora estrategia, la cual se puede aplicar a cantidades finitas en el infrarrojo, simplifica significativamente los cálculos ya que carece de una escala adicional.

Appendix A

Appendix Feynman rules

In this Appendix we collect all the Feynman rules necessary of carrying out all EFTs computations presented in this thesis. The momentum q is always outgoing.

A.1 SCET

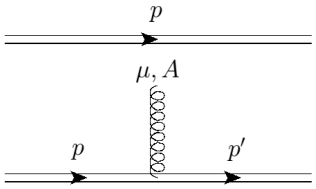

$$i\frac{\not{n}}{2}\frac{p^-}{p^2-m^2+i0}$$

$$(igT^A)n^\mu\frac{\not{\overline{n}}}{2}$$

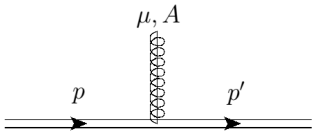

$$(igT^A)\left[n^\mu+\frac{\gamma_\perp^\mu(\not{p}_\perp+m)}{p^-}+\frac{(\not{p}'_\perp-m)\gamma_\perp^\mu}{p'^-}-\frac{(\not{p}'_\perp-m)(\not{p}_\perp+m)}{p^-p'^-}\overline{n}^\mu\right]\frac{\not{\overline{n}}}{2}$$

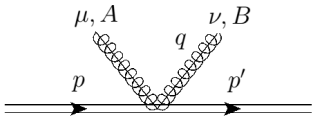

$$\frac{ig^2T^AT^B}{p^- - q^-}\left[\gamma_\perp^\mu\gamma_\perp^\nu-\frac{\gamma_\perp^\mu(\not{p}_\perp+m)}{p^-}\overline{n}^\nu-\frac{(\not{p}'_\perp-m)\gamma_\perp^\nu}{p'^-}\overline{n}^\mu+\frac{(\not{p}'_\perp-m)(\not{p}_\perp+m)}{p^-p'^-}\overline{n}^\mu\overline{n}^\nu\right]\frac{\not{\overline{n}}}{2}$$

$$+\frac{ig^2T^BT^A}{p'^- + q^-}\left[\ \mu\leftrightarrow\nu\ \right]$$

A.2 bHQET

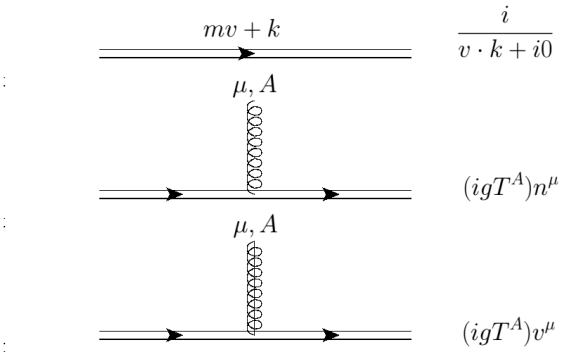

A.3 Wilson Lines

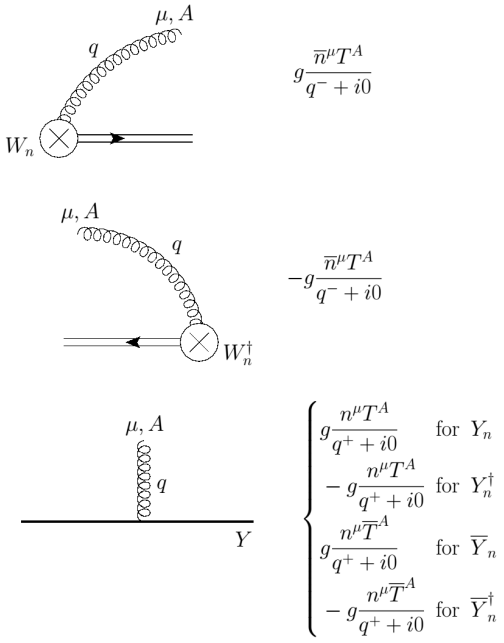

For the $\overline{n}$-collinear Wilson lines one just has to replace $n \leftrightarrow \overline{n}$ and $q^+ \leftrightarrow q^-$.

Appendix B

Appendix Event-Shape schemes

B.1 Sector Decomposition

The direct ε expansion of $J^{\rm real}_{a,P}$ becomes much simpler if one does not have to deal with distributions, therefore we consider the cumulative jet function, and to that end we define

$$\Sigma_a(s_c,\mu) \equiv \int_0^{s_c} \mathrm{d}s\, J^{\rm real}_{a,P}(s,\mu)\,. \tag{B.1}$$

Switching variables to $s = y s_c$ in Eq. (B.1) and $x \to 1-x$ in Eq. (2.57) we get

$$\begin{aligned}\Sigma_a(s_c,\mu) &= \frac{C_F\alpha_s}{2\pi\Gamma(1-\varepsilon)}\left(\frac{s_c}{\mu^2}\right)^{-\varepsilon} I_3\left(\frac{m^2}{s_c}\right), \\ I_3(t) &\equiv \int_0^1 \mathrm{d}y\, y^{-\varepsilon}\int_0^1 \mathrm{d}x\, \frac{(1-x)^{2-\varepsilon}x^{-1-\varepsilon}}{y(1-x)+t\,x}\,.\end{aligned} \tag{B.2}$$

We apply sector decomposition by splitting the x integration in two segments: $(0,y)$ and $(y,1)$. In the former we switch variables to $x = zy$ and in the latter we reverse the order of integration, which is followed by the change of variables $y = z\,x$, to find

$$\begin{aligned}I_3(t) &= \int_0^1 \mathrm{d}y\, y^{-1-2\varepsilon}\int_0^1 \mathrm{d}z\, \frac{(1-zy)^{2-\varepsilon}z^{-1-\varepsilon}}{(1-zy)+t\,z} + \int_0^1 \mathrm{d}x\, x^{-1-2\varepsilon}(1-x)^{2-\varepsilon}\int_0^1 \frac{\mathrm{d}z\, z^{-\varepsilon}}{(1-x)z+t} \\ &\equiv I_3^\alpha(t) + I_3^\beta(t)\,.\end{aligned} \tag{B.3}$$

Since the original singularities at $x = 0, 1$ have been properly separated, mapping the former at $y = 0$ and the latter at $x = 0$, one can expand in ε before integrating. Let us solve I_3^β first, which has a single pole only, such that we can use Eq. (2.59) on $x^{-1-2\varepsilon}$ to obtain

$$\begin{aligned}I_3^\beta(t) &= -\frac{1}{2\varepsilon}\int_0^1 \frac{\mathrm{d}z}{z+t}\big[1-\varepsilon\log(z)\big] + \int_0^1 \mathrm{d}x\int_0^1 \mathrm{d}z\, \frac{2t-tx-xz+z}{(t+z)(xz-t-z)} \\ &= -\frac{1}{2\varepsilon}\log\left(1+\frac{1}{t}\right) + \frac{1}{2}\mathrm{Li}_2\left(-\frac{1}{t}\right) - (1+t)\log\left(1+\frac{1}{t}\right) - \mathrm{Li}_2\left(\frac{1}{1+t}\right) + 1\,.\end{aligned} \tag{B.4}$$

For I_3^α one must start applying Eq. (2.59) to $y^{-1-2\varepsilon}$ in order to regulate the pole of the z-integral. Taking into account the plus-function prescription and that the upper integration limit is 1 we get

$$I_3^\alpha(t) = -\frac{1}{2\varepsilon}\int_0^1 \mathrm{d}z\, \frac{z^{-1-\varepsilon}}{1+t\,z} - \int_0^1 \mathrm{d}y\int_0^1 \mathrm{d}z\, \frac{1+tz(2-yz)-yz}{(1+tz)(1+tz-yz)}\,, \tag{B.5}$$

where in the second term we have already set $\varepsilon = 0$. Using again Eq. (2.59) to expand $z^{-1-\varepsilon}$ in ε and solving the resulting integrals we arrive at

$$I_3^{\alpha}(t) = \frac{1}{2\varepsilon^2} + \frac{1}{2\varepsilon}\log(1+t) + \frac{1}{2}\,\mathrm{Li}_2(-t) - \mathrm{Li}_2(1-t) + \mathrm{Li}_2\Big(\frac{1}{1+t}\Big) \\ - \frac{t}{t-1}\log(t) + t\log(1+t) + \log(1+t) - 1\,. \tag{B.6}$$

Thus, summing I_3^{α} and I_3^{β} we obtain:

$$I_3(t) = \frac{1}{2\varepsilon^2} + \frac{1}{2\varepsilon}\log(t) + \mathrm{Li}_2\Big(\frac{1}{1-t}\Big) + \frac{1}{2}\log^2(t-1) - \frac{1}{4}\log^2(t) - \frac{1}{t-1}\log(t) + \frac{\pi^2}{12}\,. \tag{B.7}$$

To obtain this expression, which facilitates taking the $t \to \infty$ limit (that corresponds to $s_c \to 0$), we have applied the following identities of dilogarithms:

$$\mathrm{Li}_2(z) = -\mathrm{Li}_2(1-z) - \log(1-z)\log(z) + \frac{\pi^2}{6}\,, \qquad \mathrm{Li}_2(z) = -\mathrm{Li}_2\Big(\frac{1}{z}\Big) - \frac{1}{2}\log^2(-z) - \frac{\pi^2}{6}\,, \tag{B.8}$$

where the second line holds for $z \notin (0,1)$ only. Now we insert Eq. (B.7) into (B.2) and expanding again in ε becomes trivial. To compute $J^{\mathrm{real}}_{a,P}$ we have to take the derivative of $\Sigma_a(s_c)$ with respect to s_c taking into account that it has support only for $s_c > 0$:

$$J^{\mathrm{real}}_{a,P}(s,\mu) = \frac{\mathrm{d}}{\mathrm{d}s}\Big[\theta(s)\,\Sigma_a(s,\mu)\Big]. \tag{B.9}$$

Using the relations in Eq. (2.83) [1] and the identity given in Eq. (2.70) one arrives at the result quoted in Eq. (2.66).

B.2 Alternative Analytic Expression of I^P_{nd} for $s > m^2$

In this appendix we present an alternative form of I^P_{nd} in which all terms are manifestly real for $y > 1$ and where no numerical derivatives are involved. In a first step we express ${}_2F_1(1, 1+\varepsilon, 2+\tilde{\omega}, 1-y)$ in Eq. (2.115) in terms of ${}_2F_1(1, 1+\varepsilon, 1-\tilde{\omega}+\varepsilon, y)$ through Eq. (2.113), and then use that for $y > 1$ one has [2]

$${}_2F_1(1, 1+\varepsilon, 1-\tilde{\omega}+\varepsilon, y) = -\frac{\tilde{\omega}\,\pi(y-1)^{-1-\tilde{\omega}}\,[\cot(\pi\varepsilon) + i\,]\,y^{\tilde{\omega}-\varepsilon}\,\Gamma(1-\tilde{\omega}+\varepsilon)}{\Gamma(1-\tilde{\omega})\Gamma(\varepsilon+1)} \\ + \frac{(\tilde{\omega}-\varepsilon)}{y\varepsilon}\,{}_2F_1\Big(1, 1+\tilde{\omega}-\varepsilon, 1-\varepsilon, \frac{1}{y}\Big). \tag{B.12}$$

[1] To use these relations the functions multiplying $\theta(x)$ should be either $\log^n(x)$ or regular at $x = 0$. Therefore it is convenient to write $\log(t-1)$ as $\log(t) - \log(1-1/t)$.

[2] To obtain this relation one simply has to divide the integration path in Eq. (2.60) into the segments $(0, 1/y)$ and $(1/y, 1)$. Using

$$[1 - z(y \pm i\varepsilon)]^{-a} = \theta(1-zy)(1-yz)^{-a} + \theta(zy-1)(yz-1)^{-a}[\cos(a\pi) \pm i\sin(a\pi)]\,, \tag{B.10}$$

remapping each segment back to $(0,1)$ by a change of variables ($z \to z/y$ in the first segment and $z \to [1-(1-1/y)x]$ in the second), and carrying out the integrals one finds the following identity:

$${}_2F_1(a, b, c, y \pm i\varepsilon) = \frac{\Gamma(1-a)y^{-b}\Gamma(c)}{\Gamma(1-a+b)\Gamma(c-b)}\,{}_2F_1\Big(b, 1+b-c, 1-a+b, \frac{1}{y}\Big) \\ + \frac{e^{\pm i\pi a}\Gamma(1-a)\Gamma(c)y^{b-c}(y-1)^{-a-b+c}}{\Gamma(b)\Gamma(1-a-b+c)}\,{}_2F_1\Big(1-b, c-b, 1-a-b+c, \frac{y-1}{y}\Big). \tag{B.11}$$

The only involved computation left is finding an analytic expression for the derivative of the hypergeometric function ${}_2F_1(1,1+\tilde{\omega}-\varepsilon,1-\varepsilon,1/y)$ with respect to ε in the $\varepsilon\to 0$ limit. The complication here arises because there are poles in $1/\varepsilon$ such that one also needs the second derivative, which as we shall see implies the appearance of the ${}_4F_3$ function. A practical way of doing the derivative is by Taylor expanding. The first derivative reads

$$\frac{\mathrm{d}}{\mathrm{d}\varepsilon}{}_2F_1(1,1+\tilde{\omega}-\varepsilon,1-\varepsilon,y)=\frac{y\,\tilde{\omega}(1-y)^{-1-\tilde{\omega}}}{(1-\varepsilon)^2}\,{}_3F_2(1-\tilde{\omega},1-\varepsilon,1-\varepsilon,2-\varepsilon,2-\varepsilon,y)\,. \tag{B.13}$$

For the second one needs the first derivative of the ${}_3F_2$ function:

$$\begin{aligned}&\frac{\mathrm{d}}{\mathrm{d}\varepsilon}\,{}_3F_2(1-\tilde{\omega},1-\varepsilon,1-\varepsilon,2-\varepsilon,2-\varepsilon,y)= \\ &\quad -\frac{2y(1-\tilde{\omega})(1-\varepsilon)}{(2-\varepsilon)^3}\,{}_4F_3(2-\tilde{\omega},2-\varepsilon,2-\varepsilon,2-\varepsilon,3-\varepsilon,3-\varepsilon,3-\varepsilon,y)\,.\end{aligned} \tag{B.14}$$

With these results one can obtain the Taylor expansion of ${}_2F_1(1,1+\tilde{\omega}-\varepsilon,1-\varepsilon,1/y)$, which allows to compute the first derivative of ${}_2F_1(1,1+\varepsilon,1-\tilde{\omega}+\varepsilon,y)$

$$\begin{aligned}&\frac{\mathrm{d}}{\mathrm{d}\varepsilon}{}_2F_1(1,1+\varepsilon,1-\tilde{\omega}+\varepsilon,y)\Big|_{\varepsilon\to 0} \\ &=\frac{\tilde{\omega}(y-1)^{-\tilde{\omega}-1}y^{\tilde{\omega}-1}}{12}\Bigg\{12\,\tilde{\omega}\,{}_4F_3\Big(1,1,1,1-\tilde{\omega},2,2,2,\frac{1}{y}\Big)-12\,{}_3F_2\Big(1,1,1-\tilde{\omega},2,2,\frac{1}{y}\Big) \\ &\quad y\Big[6(H_{-\tilde{\omega}}-\log(y))(2i\pi-H_{-\tilde{\omega}}+\log(y))-6\psi^{(1)}(1-\tilde{\omega})+5\pi^2\Big]\Bigg\}.\end{aligned} \tag{B.15}$$

Using this result we arrive at the alternative expression for I^P_{nd}

$$\begin{aligned}&I^P_{\mathrm{nd}}(\tilde{\omega},y)=\frac{\tilde{\omega}[(2\tilde{\omega}+5)y+\tilde{\omega}(3\tilde{\omega}+7)-4y^2]}{\Gamma(1-\tilde{\omega})(1+\tilde{\omega})(1-y)^2}\Big[H_{1-\tilde{\omega}}-\frac{1}{1-\tilde{\omega}}-\log(y)\Big]{}_2F_1(1,1,\tilde{\omega}+2,1-y) \\ &+\frac{3\tilde{\omega}^2y+3\tilde{\omega}^2-5\tilde{\omega}y+14\tilde{\omega}+y-7}{\Gamma(2-\tilde{\omega})(y-1)^2}+(y-1)^{-3-\tilde{\omega}}y^{\tilde{\omega}-1}[4y^2-2(\tilde{\omega}+5)y-\tilde{\omega}(3\tilde{\omega}+7)] \\ &\times\Bigg\{\tilde{\omega}^2{}_4F_3\Big(1,1,1,1-\tilde{\omega},2,2,2,\frac{1}{y}\Big)-\tilde{\omega}\,{}_3F_2\Big(1,1,1-\tilde{\omega},2,2,\frac{1}{y}\Big) \\ &\times\frac{\tilde{\omega}\,y}{12}\Big[5\pi^2-6\Big(H_{1-\tilde{\omega}}-\frac{1}{1-\tilde{\omega}}-\log(y)\Big)^2-6\psi^{(1)}(1-\tilde{\omega})\Big] \\ &+y\cos(\pi\tilde{\omega})\Gamma(1-\tilde{\omega})\Gamma(1+\tilde{\omega}){}_2F_1(1,1,2+\tilde{\omega},1-y)\Big[H_{1-\tilde{\omega}}-\frac{1}{1-\tilde{\omega}}-\log(y)\Big]\Bigg\}.\end{aligned} \tag{B.16}$$

Appendix C

Appendix Massive secondary quark corrections to bHQET cross-section

C.1 Non-distributional term

From the result obtained for the contribution of a secondary massive quark bubble to the bHQET jet function applying the dispersive integral method —that is, an integral that cannot be solved analytically— we were able to get neither the Fourier transform of the non-distributional part of the jet function, nor a closed from for its RG-evolved version. Therefore, the running of the cross section needs to be done, for these non-distributional terms, in momentum space. This involves another integration, as in Chapter 2, which might again be numerical in the worst cases.[1] In addition, if we convolve the result with a Breit-Wigner distribution to account for the finite width of the primary quark (in the case of top production) we have to confront the numerical evaluation of a triple integral.

To improve the efficiency of the numerical implementations necessary to build up a computer code for the differential cross-section, we will provide in this Appendix a closed form and series expansions in two different (but overlapping) regimes for $f_{\rm nd}$. Since the properties and expansions of the elliptic integrals are well known and there are internal routines in different packages and programming languages for their evaluation (such as `Mathematica` [63] and the `Scipy` module [61] in `Python` [58]), the previous task amounts to get a suitable form for $I[\hat{s}, m]$.

Closed expression

Starting from its integral expressions as provided in the last line of Eq. (4.59) we carry out three consecutive changes of variables:

$$\begin{aligned} \tilde{m}^2 &\longrightarrow b = \sqrt{\tilde{m}^2 - 4m^2}\,, \\ b &\longrightarrow x = \frac{b}{\sqrt{\hat{s}^2/4 - 4m^2}}\,, \\ x &\longrightarrow z = \sqrt{1 - x^2}\,, \end{aligned} \tag{C.1}$$

[1] One could try to get an analytical expression for the convolution of the kernel with the one loop massive gluon result and then take the dispersive integral numerically.

to get to the following expression

$$I[\hat{s},m]=\frac{a^3}{3\hat{s}}\left[\frac{1-a^2}{2}\int_0^1 dz\frac{z\sqrt{1-z^2}}{\left(1-a^2z^2\right)^{5/2}}\log\left(\frac{1+az}{1-az}\right)+\int_0^1 dz\frac{z\sqrt{1-z^2}}{\left(1-a^2z^2\right)^{3/2}}\log\left(\frac{1+az}{1-az}\right)\right], \quad \text{(C.2)}$$

where we defined $a\equiv\sqrt{1-16m^2/\hat{s}^2}$. Then we apply integration by parts once to the first term and twice to the second in order to get always the derivative of the logarithms involved in the resulting integrals, which leads to

$$I[\hat{s},m]=\frac{1}{3\hat{s}}\left[\frac{16-2a^2}{9}E\left(a^2\right)-\frac{16-a^2}{9}K\left(a^2\right)+\underbrace{\int_0^1 dz\,\frac{az}{\sqrt{1-z^2}\sqrt{1-a^2z^2}}\log\left(\frac{1+az}{1-az}\right)}_{\equiv f(a)}\right], \quad \text{(C.3)}$$

with a remaining logarithmic type integral. Taking its derivative with respect to a

$$f'(a)=\int_0^1 dz\,\frac{z}{\sqrt{1-z^2}}\frac{2az+\log\left(\frac{1+az}{1-az}\right)}{\left(1-a^2z^2\right)^{3/2}}=\frac{2a}{1-a^2}\,K\big(a^2\big)\,, \quad \text{(C.4)}$$

we can write the auxiliary function $f(a)$ as

$$f(a)=\int_{a_0}^{a}d\tilde{a}\,\frac{2\tilde{a}}{1-\tilde{a}^2}\,K\big(\tilde{a}^2\big)+f(a_0)\,. \quad \text{(C.5)}$$

Since the integral in the previous form for $f(a)$ is divergent in the massless ($a\to 1$) limit, we subtract the corresponding contribution at this boundary, that can be inferred from the result in Ref. [42],[2] to express the function as

$$f(a)=\int_1^a d\tilde{a}\,\frac{\tilde{a}}{1-\tilde{a}^2}\,\left[2K\left(\tilde{a}^2\right)+\log\left(\frac{1-\tilde{a}^2}{16}\right)\right]+\log^2\left(\frac{\sqrt{1-a^2}}{4}\right)-\frac{\pi^2}{6}\,. \quad \text{(C.6)}$$

Now we can replace the elliptic integral by its series expansion

$$K\left(a^2\right)=\sum_{k=0}^{\infty}\frac{\left[\left(\frac{1}{2}\right)_k\right]^2\left[\psi^{(0)}(k+1)-\psi^{(0)}\left(k+\frac{1}{2}\right)\right]}{(k!)^2}\left(1-a^2\right)^k-\frac{\log(1-a^2)}{2}\sum_{k=0}^{\infty}\frac{\left(\left(\frac{1}{2}\right)_k\right)^2}{(k!)^2}\left(1-a^2\right)^k\,, \quad \text{(C.7)}$$

valid in the whole range we need to consider,[3] solve the integral, and cast the infinite sum of the resulting terms into hypergeometric functions. This procedure leads to the following closed expression, which can be used in the entire regime, for the non-distributional part[4]

$$\begin{aligned}3\hat{s}f_{\rm nd}=&\left[\frac{61}{18}+\frac{8}{9}\frac{m^2}{\hat{s}^2}\right]E\left(1-\frac{16m^2}{\hat{s}^2}\right)-\frac{8}{9}\left[\frac{14m^2}{\hat{s}^2}+3\right]K\left(1-\frac{16m^2}{\hat{s}^2}\right) \quad \text{(C.8)}\\ &-\frac{2m^2}{\hat{s}^2}{}_5F_4\left(1,1,1,\frac{3}{2},\frac{3}{2};2,2,2,2;\frac{16m^2}{\hat{s}^2}\right)+\frac{2m^2}{\hat{s}^2}\left[2+\log\left(\frac{m^2}{\hat{s}^2}\right)\right]{}_4F_3\left(1,1,\frac{3}{2},\frac{3}{2};2,2,2;\frac{16m^2}{\hat{s}^2}\right)\\ &+\frac{4m^2}{\hat{s}^2}\frac{\mathrm{d}}{\mathrm{d}\epsilon}\left[{}_4F_3\left(1,1,\frac{3}{2},\frac{3}{2}+\epsilon;2,2,2+\epsilon;\frac{16m^2}{\hat{s}^2}\right)\right]_{\epsilon=0}+\frac{1}{4}\log^2\left(\frac{m^2}{\hat{s}^2}\right)-\frac{\pi^2}{6}\,.\end{aligned}$$

Even though having a closed expression seems advantageous, the evaluation of the high order hypergeometric functions involved is computationally time consuming, in particular when their last arguments approach the value of 1. Therefore, we will consider now the expansions around this limit and also around the massless one.

[2] We carried out a numerical cross-check of the massless limit in our expression to be sure that we can trust this result.

[3] Notice that the Heaviside theta forces $\hat{s}\geq 4m\Rightarrow 0\leq a\leq 1$.

[4] The value of the hypergeometric derivative can be obtained in a numerical way analogously to Eq. (2.114), through finite differences.

Expansion around $m/\hat{s} \to 0$

This series expansion can be directly obtained from the outcome of introducing Eq. (C.7) into Eq. (C.6) and the corresponding series for the elliptic integrals already given for K in Eq. (C.7), whereas for the expansion of the E elliptic function we have

$$\begin{aligned} E\left(a^2\right) =& 1-\frac{1}{4}(1-a^2)\log(1-a^2)\sum_{k=0}^{\infty}\frac{\left(\frac{1}{2}\right)_k\left(\frac{3}{2}\right)_k}{k!(k+1)!}\left(1-a^2\right)^k \\ &-\frac{1}{4}(1-a^2)\sum_{k=0}^{\infty}\frac{\left(\frac{1}{2}\right)_k\left(\frac{3}{2}\right)_k\left[\frac{1}{2k^2+3k+1}-2\psi^{(0)}(k+1)+2\psi^{(0)}\left(k+\frac{1}{2}\right)\right]}{k!(k+1)!}\left(1-a^2\right)^k. \end{aligned} \tag{C.9}$$

On the other hand, one could also use the elliptic and hypergeometric expansions in Eq. (C.8). The series expansion for the non-distributional coefficient in this limit is

$$\begin{aligned} f_{\rm nd} =& \frac{1}{\hat{s}}\left[\frac{61}{54}-\frac{\pi^2}{18}+\frac{8}{9}\log\left(\frac{m}{\hat{s}}\right)+\frac{1}{3}\log^2\left(\frac{m}{\hat{s}}\right)+\sum_{n=0}^{\infty}\frac{\left(\left(\frac{1}{2}\right)_n\right)^2}{32(n!)^2(n+2)^3}\times\right. \\ &\left.\times\left(\frac{4n-1}{n+2}+2(1+2n)\left[\psi^{(0)}(n+1)-\psi^{(0)}(n+1/2)-\log\left(\frac{4m}{\hat{s}}\right)\right]\right)\left(\frac{16m^2}{\hat{s}^2}\right)^{n+2}\right]. \end{aligned} \tag{C.10}$$

Expansion around $\hat{s} \to 4m$

In this regime we were only able to get a double series and cast it as a Kampé de Fériet type [18] and, for some cases, as Appell generalized hypergeometric series. The expansion for the elliptic integrals is

$$E\left(a^2\right)=\frac{\pi}{2}\sum_{k=0}^{\infty}\frac{\left(-\frac{1}{2}\right)_k\left(\frac{1}{2}\right)_k}{(k!)^2}a^{2k}\;; \qquad\qquad K\left(a^2\right)=\frac{\pi}{2}\sum_{k=0}^{\infty}\frac{\left(\frac{1}{2}\right)_k\left(\frac{1}{2}\right)_k}{(k!)^2}a^{2k}. \tag{C.11}$$

And for $f(a)$ we can consider its definition in Eq. (C.3) or the form in Eq. (C.5). The former procedure consists in the insertion of the inverse hyperbolic tangent series expression $\tanh^{-1}(az)=\sum_{n=1}^{\infty}\frac{(az)^{2n-1}}{2n-1}$ into

$$f(a)=2\int_0^1 dz\,\frac{az}{\sqrt{1-z^2}\sqrt{1-a^2z^2}}\,\tanh^{-1}(az)\,, \tag{C.12}$$

leading to a sum of hypergeometric functions which can be reexpanded and identify as Kampé de Fériet

$$f(a)=\sum_{n=1}^{\infty}\sum_{k=0}^{\infty}\frac{\Gamma\left(\frac{1}{2}+k\right)}{\Gamma\left(1+n+k\right)}\frac{\Gamma\left(\frac{1}{2}+n+k\right)}{(2n-1)\,k!}\left(a^2\right)^{n+k}=\frac{\pi}{2}\,a^2\,F^{1,2,1}_{1,1,0}\left[\begin{matrix}\frac{3}{2}\,;\,1,\frac{1}{2}\,;\,\frac{1}{2}\\ 2\,;\,\frac{3}{2}\,;\,-\end{matrix}\;\middle|\;a^2,a^2\right]. \tag{C.13}$$

On the other hand, if we do not reexpand the hypergeometric functions from the direct integration but apply the identity

$${}_2F_1(a,b;c;z)=(1-z)^{-a}\,{}_2F_1\left(a,c-b;c;\frac{z}{z-1}\right), \tag{C.14}$$

to then write those as a power series, the result, valid only for $a^2<1/2$, is an Appell function

$$\begin{aligned} f(a) =& \frac{1}{2\sqrt{\pi}\sqrt{1-a^2}}\sum_{n=1}^{\infty}\sum_{k=0}^{\infty}\frac{\Gamma\left(n-\frac{1}{2}\right)\Gamma\left(k+\frac{1}{2}\right)\Gamma\left(k+\frac{1}{2}\right)}{\Gamma(k+n+1)\,k!}\left(\frac{a^2}{a^2-1}\right)^k\left(a^2\right)^n \\ =& \frac{\pi\,a^2}{2\sqrt{1-a^2}}\,F_3\left(1/2\,,\,1/2\,;\,1/2\,,\,1\,;\,2\,;\frac{a^2}{a^2-1},a^2\right). \end{aligned} \tag{C.15}$$

If we begin instead from Eq. (C.5), we can replace the denominator by the geometric series or use Eq. (C.11) to get[5]

$$f(a) = \frac{1}{2}\sum_{n=0}^{\infty}\sum_{k=0}^{\infty}\frac{\Gamma\left(k+\frac{1}{2}\right)^2}{(1+n+k)\,(k!)^2}\,(a^2)^{k+n+1} = \frac{\pi}{2}\,a^2\,F^{1,2,1}_{1,1,0}\left[\begin{array}{c} 1\,;\,\frac{1}{2},\frac{1}{2}\,;\,1 \\ 2\,;\,1\,;\,- \end{array}\;\middle|\; a^2, a^2\right], \tag{C.16}$$

which again can be transformed into an Appell series for $a^2 < 1/2$ following the same procedure as before

$$\begin{aligned} f(a) &= \frac{a^2}{2(1-a^2)}\sum_{n=0}^{\infty}\sum_{k=0}^{\infty}\frac{\Gamma\left(\frac{1}{2}+k\right)^2\Gamma\left(1+n\right)}{\Gamma(2+n+k)\,k!}\left(\frac{a^2}{a^2-1}\right)^n a^{2k} \\ &= \frac{\pi\,a^2}{2(1-a^2)}\,F_3\left(1\,,\,1/2\,;\,1\,,\,1/2\,;\,2\,;\frac{a^2}{a^2-1}, a^2\right). \end{aligned} \tag{C.17}$$

All in all, the expansions given by the different approaches for $f_{\rm nd}$ are:

$$\begin{aligned} f_{\rm nd} = \frac{1-\frac{16m^2}{\hat{s}^2}}{3\hat{s}}\sum_{n=0}^{\infty}\Bigg\{ &\frac{\pi}{36}\frac{\left[\left(\frac{1}{2}\right)_n\right]^2}{(n!)^2}\left(\frac{31}{1+n}+\frac{1}{2n-1}-48\right) \\ &+\frac{1}{2n+1}\sum_{k=0}^{\infty}\frac{\Gamma\left(\frac{1}{2}+k\right)\Gamma\left(\frac{3}{2}+n+k\right)}{\Gamma\left(2+n+k\right)k!}\left(1-\frac{16m^2}{\hat{s}^2}\right)^k\Bigg\}\left(1-\frac{16m^2}{\hat{s}^2}\right)^n, \end{aligned} \tag{C.18}$$

from the first one and

$$\begin{aligned} f_{\rm nd} = \frac{1-\frac{16m^2}{\hat{s}^2}}{3\hat{s}}\sum_{n=0}^{\infty}\Bigg\{ &\frac{\pi}{36}\frac{\left[\left(\frac{1}{2}\right)_n\right]^2}{(n!)^2}\left(\frac{31}{1+n}+\frac{1}{2n-1}-48\right) \\ &+\frac{1}{2(1+n+k)}\sum_{k=0}^{\infty}\frac{\Gamma\left(k+\frac{1}{2}\right)^2}{(k!)^2}\left(1-\frac{16m^2}{\hat{s}^2}\right)^k\Bigg\}\left(1-\frac{16m^2}{\hat{s}^2}\right)^n, \end{aligned} \tag{C.19}$$

from the latter.

[5] The constant term satisfies $f(0) = 0$.

Bibliography

[1] Riccardo Abbate, Michael Fickinger, Andre H. Hoang, Vicent Mateu, and Iain W. Stewart. Thrust at N^{3}LL with Power Corrections and a Precision Global Fit for $\alpha_s(m_Z)$. *Phys. Rev.*, D83:074021, 2011.

[2] Riccardo Abbate, Michael Fickinger, Andre H. Hoang, Vicent Mateu, and Iain W. Stewart. Precision Thrust Cumulant Moments at N^3LL. *Phys. Rev. D*, 86:094002, 2012.

[3] Brad Bachu, André H. Hoang, Vicent Mateu, Aditya Pathak, and Iain W. Stewart. Boosted top quarks in the peak region with NL3L resummation. *Phys. Rev. D*, 104(1):014026, 2021.

[4] Christian W. Bauer, Sean P. Fleming, Christopher Lee, and George F. Sterman. Factorization of e^+e^- Event Shape Distributions with Hadronic Final States in Soft Collinear Effective Theory. *Phys. Rev. D*, 78:034027, 2008.

[5] Christian W. Bauer, Dan Pirjol, and Iain W. Stewart. Soft-collinear factorization in effective field theory. *Phys. Rev. D*, 65:054022, Feb 2002.

[6] T. Binoth and G. Heinrich. An automatized algorithm to compute infrared divergent multiloop integrals. *Nucl. Phys. B*, 585:741–759, 2000.

[7] R.P. Brent. *Algorithms for minimization without derivatives*. Prentice-Hall, 1973.

[8] Mathias Butenschoen, Bahman Dehnadi, Andre H. Hoang, Vicent Mateu, Moritz Preisser, and Iain W. Stewart. Top Quark Mass Calibration for Monte Carlo Event Generators. *Phys. Rev. Lett.*, 117(23):232001, 2016.

[9] T. Chandramohan and L. Clavelli. Consequences of Second Order QCD for Jet Structure in e^+e^- annihilation. *Nucl.Phys.*, B184:365, 1981.

[10] Junegone Chay, Chul Kim, Yeong Gyun Kim, and Jong-Phil Lee. Soft wilson lines in the soft-collinear effective theory. *Phys. Rev. D*, 71:056001, Mar 2005.

[11] K. G. Chetyrkin, Bernd A. Kniehl, and M. Steinhauser. Decoupling relations to $\mathcal{O}(\alpha_s^3)$ and their connection to low-energy theorems. *Nucl. Phys. B*, 510:61–87, 1998.

[12] Jui-yu Chiu, Andreas Fuhrer, Andre H. Hoang, Randall Kelley, and Aneesh V. Manohar. Soft-Collinear Factorization and Zero-Bin Subtractions. *Phys. Rev. D*, 79:053007, 2009.

[13] L. Clavelli. Jet Invariant Mass in Quantum Chromodynamics. *Phys. Lett.*, B85:111, 1979.

[14] L. Clavelli and D. Wyler. Kinematica Bounds on Jet Variables and the Heavy Jet Mass Distribution. *Phys. Lett.*, B103:383, 1981.

[15] Timothy Cohen. As scales become separated: Lectures on effective field theory, 2020.

[16] Csaba Csáki, Salvator Lombardo, and Ofri Telem. *TASI Lectures on Non-supersymmetric BSM Models*, pages 501–570. WSP, 2018.

[17] Mrinal Dasgupta and Gavin P. Salam. Event shapes in e^+e^- annihilation and deep inelastic scattering. *J. Phys. G*, 30:R143, 2004.

[18] MJ Kampé de Fériet. Sciences mathématiques. 1937.

[19] D. de Florian et al. Handbook of LHC Higgs Cross Sections: 4. Deciphering the Nature of the Higgs Sector. 2/2017, 10 2016.

[20] John F. Donoghue, F.E. Low, and So-Young Pi. Tensor Analysis of Hadronic Jets in Quantum Chromodynamics. *Phys. Rev.*, D20:2759, 1979.

[21] F. Englert and R. Brout. Broken symmetry and the mass of gauge vector mesons. *Phys. Rev. Lett.*, 13:321–323, Aug 1964.

[22] Edward Farhi. A QCD Test for Jets. *Phys. Rev. Lett.*, 39:1587–1588, 1977.

[23] Sean Fleming, Andre H. Hoang, Sonny Mantry, and Iain W. Stewart. Jets from massive unstable particles: Top-mass determination. *Phys. Rev.*, D77:074010, 2008.

[24] Sean Fleming, Andre H. Hoang, Sonny Mantry, and Iain W. Stewart. Top Jets in the Peak Region: Factorization Analysis with NLL Resummation. *Phys. Rev.*, D77:114003, 2008.

[25] Samuel Friot, David Greynat, and Eduardo De Rafael. Asymptotics of Feynman diagrams and the Mellin-Barnes representation. *Phys. Lett. B*, 628:73–84, 2005.

[26] Sheldon L. Glashow. Partial-symmetries of weak interactions. *Nuclear Physics*, 22(4):579–588, 1961.

[27] Néstor G. Gracia and Vicent Mateu. Toward massless and massive event shapes in the large-β_0 limit. *JHEP*, 07:229, 2021.

[28] N. Gray, David J. Broadhurst, W. Grafe, and K. Schilcher. Three Loop Relation of Quark (Modified) Ms and Pole Masses. *Z. Phys. C*, 48:673–680, 1990.

[29] S. Gritschacher. Massive gluino effects in event shape distributions. Master's thesis, TU Munich, 2011.

[30] Simon Gritschacher, Andre Hoang, Ilaria Jemos, and Piotr Pietrulewicz. Two loop soft function for secondary massive quarks. *Phys. Rev. D*, 89(1):014035, 2014.

[31] Simon Gritschacher, Andre H. Hoang, Ilaria Jemos, and Piotr Pietrulewicz. Secondary Heavy Quark Production in Jets through Mass Modes. *Phys. Rev. D*, 88:034021, 2013.

[32] B. W. Harris and J. F. Owens. The Two cutoff phase space slicing method. *Phys. Rev.*, D65:094032, 2002.

[33] Peter W. Higgs. Broken symmetries and the masses of gauge bosons. *Phys. Rev. Lett.*, 13:508–509, Oct 1964.

[34] A. H. Hoang, Johann H. Kuhn, and T. Teubner. Radiation of light fermions in heavy fermion production. *Nucl. Phys. B*, 452:173–187, 1995.

[35] Andre Hoang. Applications of two loop calculations in the standard model and its minimal supersymmetric extension. Other thesis, 12 1995.

[36] Andre H. Hoang, Ambar Jain, Christopher Lepenik, Vicent Mateu, Moritz Preisser, Ignazio Scimemi, and Iain W. Stewart. The MSR mass and the $\mathcal{O}(\Lambda_{\rm QCD})$ renormalon sum rule. *JHEP*, 04:003, 2018.

[37] Andre H. Hoang, Ambar Jain, Ignazio Scimemi, and Iain W. Stewart. Infrared Renormalization Group Flow for Heavy Quark Masses. *Phys. Rev. Lett.*, 101:151602, 2008.

[38] André H. Hoang, Daniel W. Kolodrubetz, Vicent Mateu, and Iain W. Stewart. C-parameter distribution at N^{3}LL' including power corrections. *Phys. Rev. D*, 91(9):094017, 2015.

[39] Andre H. Hoang, Christopher Lepenik, and Vicent Mateu. REvolver: Automated running and matching of couplings and masses in QCD. *Comput. Phys. Commun.*, 270:108145, 2022.

[40] Andre H. Hoang, Aditya Pathak, Piotr Pietrulewicz, and Iain W. Stewart. Hard Matching for Boosted Tops at Two Loops. *JHEP*, 12:059, 2015.

[41] Tobias Huber and Daniel Maitre. HypExp 2, Expanding Hypergeometric Functions about Half-Integer Parameters. *Comput. Phys. Commun.*, 178:755–776, 2008.

[42] Ambar Jain, Ignazio Scimemi, and Iain W. Stewart. Two-loop Jet-Function and Jet-Mass for Top Quarks. *Phys. Rev. D*, 77:094008, 2008.

[43] Matthias Jamin and Markus E. Lautenbacher. TRACER: Version 1.1: A Mathematica package for gamma algebra in arbitrary dimensions. *Comput. Phys. Commun.*, 74:265–288, 1993.

[44] J. Jersak, E. Laermann, and P. M. Zerwas. Electroweak Production of Heavy Quarks in e^+e^- Annihilation. *Phys. Rev.*, D25:1218, 1982. [Erratum: Phys. Rev.D36,310(1987)].

[45] Stefan Kluth. Tests of Quantum Chromo Dynamics at e^+e^- Colliders. *Rept. Prog. Phys.*, 69:1771–1846, 2006.

[46] Bernd A. Kniehl. Two Loop QED Vertex Correction From Virtual Heavy Fermions. *Phys. Lett. B*, 237:127–129, 1990.

[47] Bernd A. Kniehl, M. Krawczyk, Johann H. Kuhn, and R. G. Stuart. Hadronic Contributions to $\mathcal{O}(\alpha^2)$ Radiative Corrections in e^+e^- Annihilation. *Phys. Lett. B*, 209:337–342, 1988.

[48] Christopher Lepenik and Vicent Mateu. NLO Massive Event-Shape Differential and Cumulative Distributions. *JHEP*, 03:024, 2020.

[49] Zoltan Ligeti, Iain W. Stewart, and Frank J. Tackmann. Treating the b quark distribution function with reliable uncertainties. *Phys. Rev. D*, 78:114014, 2008.

[50] Aneesh V. Manohar. Introduction to effective field theories, 2018.

[51] Vicent Mateu and Germán Rodrigo. Oriented Event Shapes at N^{3}LL$+\mathcal{O}(\alpha_s^2)$. *JHEP*, 1311:030, 2013.

[52] Vicent Mateu, Iain W. Stewart, and Jesse Thaler. Power Corrections to Event Shapes with Mass-Dependent Operators. *Phys. Rev. D*, 87(1):014025, 2013.

[53] T. Matsuura and W. L. van Neerven. Second Order Logarithmic Corrections to the Drell-Yan Cross-section. *Z. Phys.*, C38:623, 1988.

[54] G. Parisi. Super Inclusive Cross-Sections. *Phys. Lett.*, B74:65, 1978.

[55] Antonio Pich. The Standard model of electroweak interactions. In *2006 European School of High-Energy Physics*, pages 1–49, 2007.

[56] Piotr Pietrulewicz, Simon Gritschacher, Andre H. Hoang, Ilaria Jemos, and Vicent Mateu. Variable Flavor Number Scheme for Final State Jets in Thrust. *Phys. Rev. D*, 90(11):114001, 2014.

[57] A. Pomarol. Beyond the Standard Model. In *2010 European School of High Energy Physics*, pages 115–151, 2 2012.

[58] Guido Rossum. Python reference manual. Technical report, Amsterdam, The Netherlands, The Netherlands, 1995.

[59] G. P. Salam and D. Wicke. Hadron masses and power corrections to event shapes. *JHEP*, 05:061, 2001.

[60] Iain W Stewart and Christian W Bauer. Lectures on the soft-collinear effective theory, 2013.

[61] Pauli Virtanen et al. SciPy 1.0–Fundamental Algorithms for Scientific Computing in Python. 2019.

[62] Steven Weinberg. A Model of Leptons. *Phys. Rev. Lett.*, 19:1264–1266, 1967.

[63] Inc Wolfram Research. *Mathematica Edition: Version 10.0*. Wolfram Research, Inc., Champaign, Illinois, 2014.

[64] C. N. Yang and R. L. Mills. Conservation of isotopic spin and isotopic gauge invariance. *Phys. Rev.*, 96:191–195, Oct 1954.